Poul M. F. Nielsen · Martyn P. Nash ·
Xinshan Li · Karol Miller ·
Adam Wittek *Editors*

Computational Biomechanics for Medicine

Towards Translation and Better Patient Outcomes

Springer

Computational Biomechanics for Medicine

Poul M. F. Nielsen · Martyn P. Nash · Xinshan Li ·
Karol Miller · Adam Wittek
Editors

Computational Biomechanics for Medicine

Towards Translation and Better Patient Outcomes

Springer

Editors
Poul M. F. Nielsen
Auckland Bioengineering Institute
University of Auckland
Auckland, New Zealand

Xinshan Li
Department of Mechanical Engineering
University of Sheffield
Sheffield, UK

Adam Wittek
Intelligent Systems for Medicine
Laboratory
The University of Western Australia
Perth, WA, Australia

Martyn P. Nash
Auckland Bioengineering Institute
University of Auckland
Auckland, New Zealand

Karol Miller
Intelligent Systems for Medicine
Laboratory
The University of Western Australia
Perth, WA, Australia

ISBN 978-3-031-09326-5 ISBN 978-3-031-09327-2 (eBook)
https://doi.org/10.1007/978-3-031-09327-2

This Springer imprint is published by the registered company Springer Nature Switzerland AG
The registered company address is: Gewerbestrasse 11, 6330 Cham, Switzerland

Preface

Computational biomechanics exploits our knowledge of physics and physiological and biological processes, to enable quantitative predictions of outcomes resulting from the complex interactions that occur in living systems. Biomechanical models increasingly provide valuable tools to improve the diagnosis, treatment, and monitoring of many diseases, as well as enhancing our understanding of how healthy bodies function.

The first volume in the Computational Biomechanics for Medicine book series was published in 2010. Since then, the book has become an annual forum for specialists in computational sciences to describe their latest results and discuss the application of their techniques to computer-integrated medicine. The twelfth volume in the Computational Biomechanics for Medicine book series comprises fifteen of the latest developments in continuum biomechanics and patient-specific computations, by researchers from New Zealand, Australia, Serbia, Denmark, France, the United Kingdom, Argentina, and the United States of America. Topics covered in this book include:

- Tissue biomechanics;
- Patient-specific modelling;
- Vessel fluid mechanics;
- Biomedical instrumentation;
- Medical image analysis.

The Computational Biomechanics for Medicine book series provides the community with the most up-to-date source of information for both researchers and practitioners.

Auckland, New Zealand — Poul M. F. Nielsen
Auckland, New Zealand — Martyn P. Nash
Perth, Australia — Karol Miller
Perth, Australia — Adam Wittek
Sheffield, UK — Xinshan Li

The original version of this chapter has been revised. "All authors contributed equally to the manuscript" has been incorporated in Chapter https://doi.org/10.1007/978-3-031-09327-2_4

Contents

Solid Mechanics

Towards Accurate Measurement of Abdominal Aortic Aneurysm Wall Thickness from CT and MRI

Andy T. Huynh and Karol Miller

Abstract Abdominal Aortic Aneurysm (AAA) is the focal dilation or widening of the infrarenal artery. It is a vascular disease commonly found in older adults with prevalence increasing steadily with age. The disease is often discovered by unrelated medical examinations and screenings due to its asymptomatic nature. People unaware of their condition may only find out after the catastrophic event of a ruptured AAA, where most patients will not survive if left untreated. The current clinical rupture risk indicator for AAA repair is a AAA diameter exceeding 5.5 cm. There are many limitations with the clinical rupture risk indicator due to its derivation coming from population statistics and not patient-specific circumstances. Computation of AAA wall stress using three-dimensional (3D) reconstructions of patient CT scans have often been used by researchers as a potential patient-specific rupture risk indicator. A property that has a great influence on the stress distribution and magnitude is the aortic wall thickness. Unfortunately, there are no validated, non-invasive methods for measuring aortic wall thickness of patients with AAA. Researchers have utilised either CT or MRI as input into their custom wall detection algorithms, however, there has not yet been a study which utilises both. Therefore, this study aims to develop a non-invasive, and patient-specific method of detecting aortic wall thickness utilising both CT and MRI scans.

Keywords Abdominal aortic aneurysm · Aortic wall thickness · Measurement · Patient-specific · Computed tomography · Magnetic resonance imaging

A. T. Huynh (✉) · K. Miller
Intelligent Systems for Medicine Laboratory, The University of Western Australia, Perth, WA, Australia
e-mail: andy.huynh@research.uwa.edu.au

K. Miller
e-mail: karol.miller@uwa.edu.au

K. Miller
Harvard Medical School, Boston, MA, USA

P. M. F. Nielsen et al. (eds.), *Computational Biomechanics for Medicine*,
https://doi.org/10.1007/978-3-031-09327-2_1

1 Introduction

Abdominal Aortic Aneurysm (AAA) is the focal dilation or widening of the infrarenal artery and is most commonly fusiform in shape [1]. It is a vascular disease commonly found in older adults with prevalence increasing steadily with age [2]. Although the prevalence and incidence of AAA has declined globally, there have been rising AAA rates in many regional areas around the world, including the Oceanic region [2]. In Australia, approximately 7% of elderly men aged 65 years and above suffer from AAA—equating to about 114,000 Australian men [3]. This highlights the need for improved disease surveillance and prevention.

Due to the asymptomatic nature of the disease, it is often discovered by unrelated medical examinations and screening [1]. People unaware of their condition may only find out after the catastrophic event of a ruptured AAA. The majority of patients with a ruptured AAA will not survive if left untreated, having an overall mortality rate of approximately 80–90% [4]. Unfortunately, even with immediate surgery by experienced vascular surgeons, the mortality remains high between 41 and 55% [5]. As such, it is crucial for doctors to identify the location on the AAA vessel at highest risk of rupturing prior to the catastrophic event.

There are many limitations to the current clinical rupture risk indicator due to its derivation coming from population statistics and not patient-specific circumstances. Clinical rupture risk indicator for elective repair only factors the AAA diameter size (>5.5 cm for men and >5 cm for women), growth rate (>1 cm/year) and some patient symptoms [1]. This is insufficient as there are many other patient-specific factors such as age, smoking, atherosclerosis, hypertension, ethnicity, and family history [1]. Further evidence indicates that 60% of AAAs that were recommended for elective repair often remained stable [6] and 20% of small AAA have ruptured [7]. Research is currently being undertaken to visualise and understand patient-specific biomechanics of AAA. This novel approach aims to develop a non-invasive and patient-specific biomechanical rupture risk assessment for AAA.

Computation of AAA wall stress using three-dimensional (3D) reconstructions of patient CT scans have often been used by researchers as a potential rupture risk indicator [8–10]. Although it was recently discovered that neither stress magnitude nor stress distribution alone had any noticeable relationship with AAA symptoms [11], wall stress calculations still holds great practical importance in research. Wall thickness is a property that has a great influence on the stress distribution and magnitude [8, 12]. Unfortunately, there are no validated, non-invasive methods for measuring aortic wall thickness [13]. Additionally, the poor soft tissue contrast of CT scans alone limit the visibility and measurement of the aortic wall, resulting in a majority of AAA rupture risk studies assuming a uniform wall thickness [14]. BioPARR is a software system used for estimating the rupture potential index (RPI) for AAA [14]. The software only requires the segmentation of the AAA and wall thickness specification as manual user inputs with all other steps being automated. Unfortunately, the wall thickness specification is applied either by assuming uniform wall thickness or manually measuring wall thickness at sparse locations and using them to generate

the walls through interpolation and smoothing [14]. As such, substantial research efforts are needed to investigate patient-specific aortic wall thickness measurement techniques for reliable estimates of AAA wall stress.

Researchers have utilised either CT or MRI as input into their custom wall detection algorithms, however, there has yet been a study which utilises both. Semi-automatic wall detection from CT has been developed based on common image analysis techniques using image intensity and contours [13, 15]. Similarly, MRI has also been studied to detect wall contours based on image gradient measurements [16].

In our method, both CT and MRI are used to detect aortic wall thickness with the assistance of common image processing techniques. Utilising both modalities, advantages such as cross-checking measurements and having improved visibility of the aortic walls can be achieved. Exact methods to achieve this have not been clearly outlined in existing literature. This study therefore aims to develop a non-invasive, and patient-specific method of detecting aortic wall thickness utilising both CT and MRI scans.

2 Methods

The aortic walls were detected from patient CT and MRI data using image processing techniques included in the MATLAB software. Our method involves registering the CT and MRI scans of the patients using open-source software 3D Slicer [17] to align the datasets. This is followed by importing the data into an in-house MATLAB script to detect the aortic walls using Canny edges. Canny edges use adaptive thresholding with hysteresis to detect edges based on the intensity gradients of the image [18]. The edges produced from the CT and MRI slices are overlaid to give an improved structural visibility of the wall thickness for measurement. This process simplifies the analysis of the images by reducing the amount of data to be processed while preserving useful structural information [18].

2.1 Patient Data

A pilot cohort of four patient CT and MRI scans were used in this study. Patient data were acquired randomly from the MRI in AAA to predict Rupture or Surgery (MA^3RS) study [19]. The patients were under surveillance for AAA with maximum diameter greater than 4 cm [14]. The scans were previously used by Joldes et al. and is described in their BioPARR paper [14].

2.2 Registration of Patient CT and MRI Scans

Image registration is the process of aligning two or more images and has many applications in the medical field. The patient's MRI and CT data sets were registered using open-source software 3D Slicer. The automatic registration of inter-modality images is difficult since different image modalities reveal and represent different information about the organ [14]. To overcome this difficulty, a label map registration algorithm outlined in the BioPARR paper was followed in this study [14]. A disadvantage of using this registration method is that it cannot account for local deformations [14]. A summary of the steps is shown below [14].

Manual segmentation of the AAA was applied to both the CT and MRI scans using the 'Editor' module within the 3D Slicer software. Labels of the segmented AAA were produced for each modality and are used to acquire the registration transformation.

The general registration and resampling algorithm (BRAINSFit and BRAINSResample) were used to register the CT and MRI images. This involved using the resulting transformation acquired from the label map registration to register the MRI and CT images and bring them to the same coordinate system. The deformed MRI and CT images (Fig. 1) will be used for further image processing to detect the aortic walls.

2.3 Detection of Aortic Wall from CT and MRI

The aortic wall detection algorithm was developed using MATLAB and the Image Processing Toolbox included. The Image Processing Toolbox allows users to use a variety of different algorithms for image processing, visualisation, and analysis.

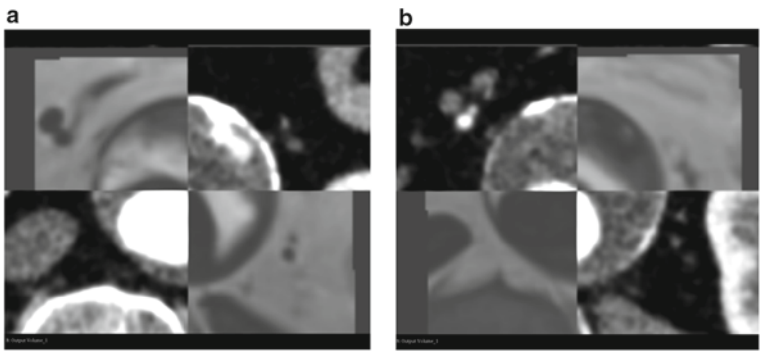

Fig. 1 The registration of the CT and MRI dataset using 3D slicer **a** checkerboard with MRI top-left **b** checkerboard with CT top-left

The CT and deformed (registered) MRI scans were read into the MATLAB script. The files were in '.nrrd' format and required adjustment to the coordinate system in order to visualise and save the images. Users can specify the number of sample of slices to analyse from the patient's CT/MRI volume and scale of the image size that the wall detection algorithm will be applied. In this experiment, a sample size of 50 image slices and scale factor of 4 was used. The size of the sample will be subject to the time available to the user (depending on the clinical workflow) and the computational hardware available. The scale factor will depend on the quality/resolution of the scans. Further parameters are specified by the user for semi-automatic segmentation of the aortic walls based on the contrast and quality of the image being assessed. This includes in-built MATLAB functions such as low-light image enhancement and edge detection using the Canny method. The algorithm first enhances the visibility of the aortic walls using low-light image enhancement techniques and then produces edges using Canny edge detection. Figure 2 shows the aortic walls from the CT and MRI.

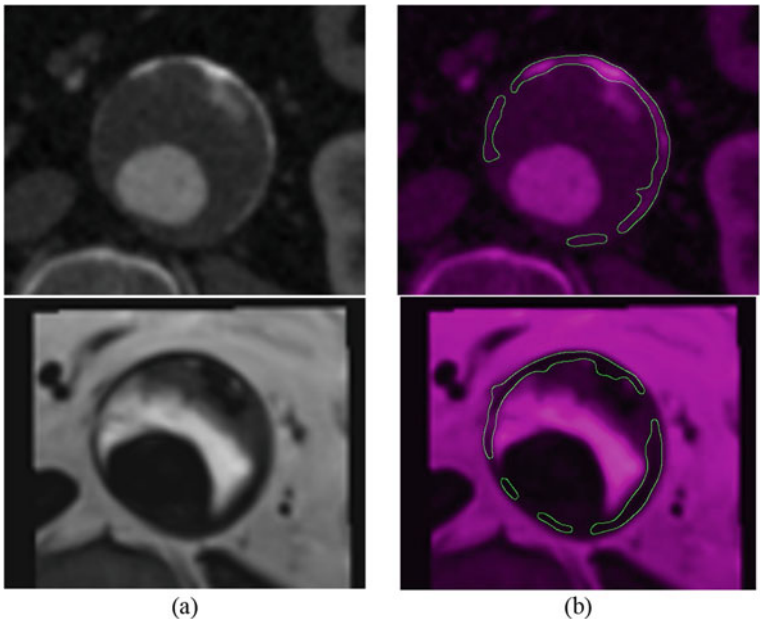

Fig. 2 Detection of aortic walls, Top = CT and Bottom = MRI **a** original image **b** aortic wall detection using our algorithm

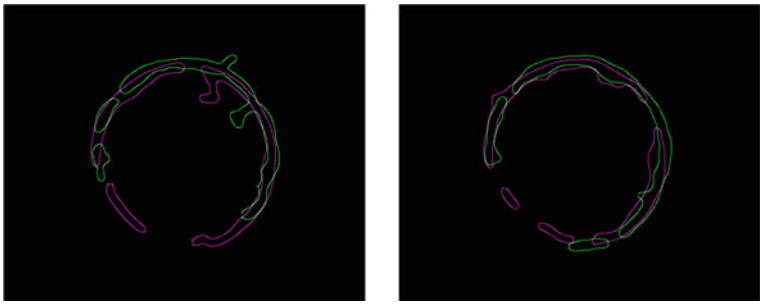

Fig. 3 Samples of overlaying wall edges detected from CT and MRI. Green = CT and magenta = MRI

2.4 Overlaying Wall Edges of CT and MRI

By overlaying the edges detected from the CT and MRI scans, an improved visualisation of the aortic walls can be produced. From Fig. 3, a sample of aortic wall edges detected using our algorithm is displayed. The images include both edges detected from CT (in green) and MRI (in magenta).

2.5 Measurement of Aortic Wall Thickness

Measurement of the aortic wall thickness was done manually using open-source software, ImageJ. The software allows for users to define the spatial scale so measurements can be presented in millimetres. A total of 50 axial slices were analysed for each patient in which 10 of the best quality edges produced by our algorithm were selected for measurement. For each slice, four approximately equidistant aortic wall measurements were taken by measuring the shortest distance between the outer wall and inner wall. This totals to 80 measurements per patient. Additionally, only measurements where both the CT and MRI edges are aligned at either the inner or outer wall were taken as this has a higher chance for the edges to represent the aortic wall. It is also used as a reference point to compare measurements from the CT edges and MRI edges. Alignment of edges is represented as white, edges from CT is represented as green and edges from MRI is represented as magenta (Fig. 4). It should be noted that this method may overestimate the wall thickness measurements due to the slices not being perpendicular to the aortic axis.

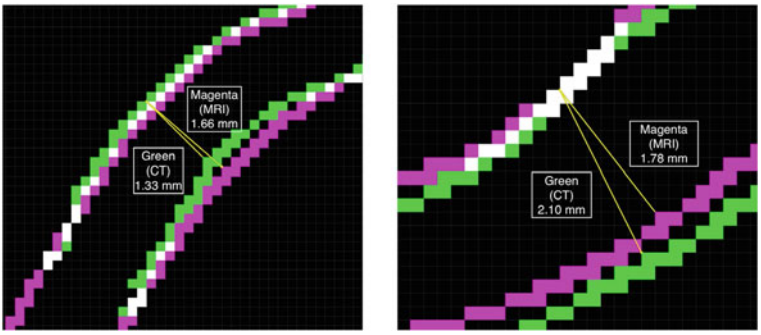

Fig. 4 Example measurement of aortic wall thickness for CT (green) and MRI (magenta) pair

Table 1 Summary of overall aortic wall thickness measurements for each patient

Patient	Modality	Mean (mm)	SD (mm)	Minimum (mm)	Maximum (mm)
1	CT MRI	2.05 1.88	0.28 0.29	1.44 1.54	2.58 2.97
2	CT MRI	1.97 2.05	0.36 0.31	1.56 1.56	3.25 2.81
3	CT MRI	1.97 1.77	0.29 0.16	1.34 1.47	2.54 2.10
4	CT MRI	1.92 1.75	0.25 0.13	1.42 1.44	2.59 2.03

3 Results

3.1 Summary of Results

For each patient, pairs of CT and MRI aortic wall thickness were measured, totalling to 80 measurements per patient (40 for CT and 40 for MRI). The summary of results of aortic wall thickness measurements from CT and MRI for each patient are summarised below (Table 1).

3.2 Statistical Analysis

The mean ± standard error of the aortic wall measurements from edges created by CT and MRI are displayed below (Fig. 5). For each patient, a sample size of 10 slices was used. Each slice was used to manually measure 4 pairs (CT and MRI)

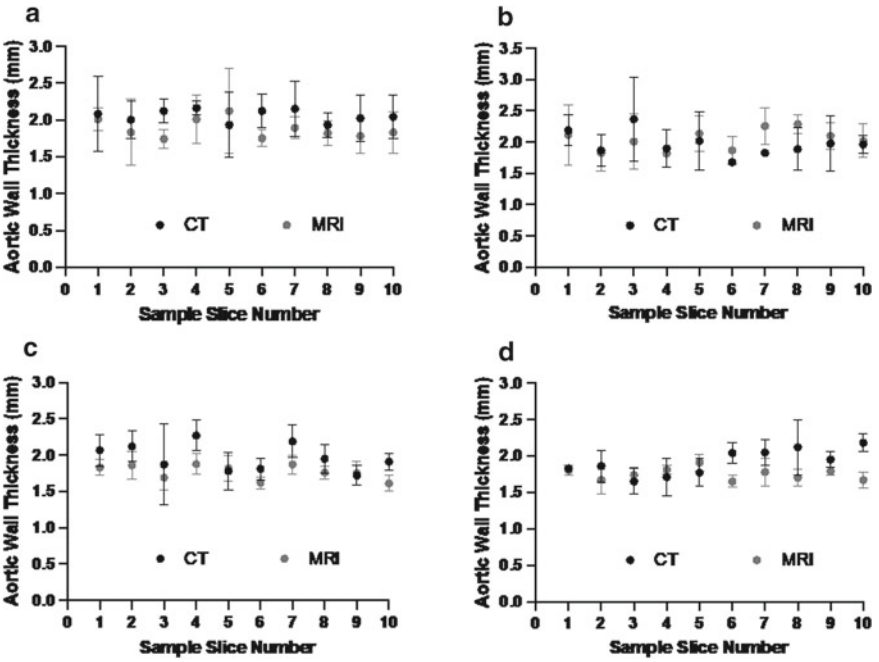

Fig. 5 Plots showing mean ± standard error of aortic wall measurement from CT and MRI for each sample slice **a** Patient 1 **b** Patient 2 **c** Patient 3 **d** Patient 4

of approximately equidistant aortic wall thickness. The results show thickness variability depending on the location of the aneurysm in both axial and coronal/sagittal planes.

Bland–Altman plots were used to assess the agreement between the aortic wall thickness measurements from edges created using CT and edges created using MRI. This graphical assessment uses an approach based on quantifying the variation of the differences between measurements by two different methods on the same subject [20]. We use this method of analysis to see if measuring wall thickness from edges created from CT and MRI are comparable and if they can be used interchangeably. This is important as one of the main advantages of using our method for wall thickness measurements is the increased visibility of the surrounding wall over methods which uses only one or the other modality.

The plots display the difference between the measurements by the CT and MRI for each subject against their average (Fig. 6). For patient 1, the plot shows a positive bias of 0.18 mm ± 0.3 mm, suggesting that on average the CT measures 0.18 mm more than the MRI measures. Additionally, the 95% limits of agreement (LOA) ranged from −0.41 mm (mean +1.96 SD) to 0.76 mm (mean −1.96 SD). Patient 2 shows a negative bias of −0.08 mm ± 0.38 mm with 95% LOA ranging from − 0.82 mm to 0.67 mm. Patient 3 shows a positive bias of 0.20 mm ± 0.26 mm with

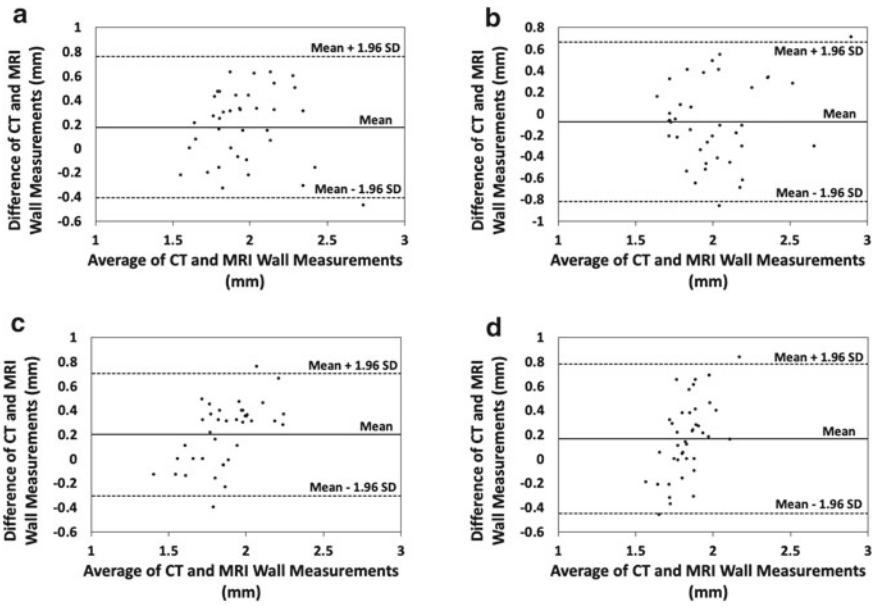

Fig. 6 Bland–Altman plots of the difference between the paired aortic wall thickness measurements from CT and MRI **a** Patient 1 **b** Patient 2 **c** Patient 3 **d** Patient 4. The difference between CT and MRI-based measurement can be as much as 0.6 mm, approximately a pixel size (0.625 mm) in the original images. This shows that it is difficult to obtain accuracies better than the pixel size of the original image

95% LOA ranging from −0.30 mm and 0.70 mm. Lastly, patient 4 shows a positive bias of 0.17 mm ± 0.31 mm and 95% LOA of −0.45 mm to 0.78 mm.

4 Discussion and Conclusions

In this study, we present a patient specific and non-invasive method to measure the aortic wall thickness by overlaying patient CT and MRI data. This was achieved using an in-house script incorporating image processing techniques included in the MATLAB software. Most researchers have used either CT or MRI for measuring wall thickness, however, the lack of information from using one or the other may be compensated by overlaying both modalities.

The need for modelling non-uniform wall thickness in abdominal aortic aneurysm biomechanics has been a problem for many researchers. The comparison between assuming uniform wall thickness and variable wall thickness for tension and stress field computation was presented by Joldes et al. [8]. The paper suggested that incorporating wall thickness measurements is necessary for a reliable estimation of AAA stress field.

Using our method, local measurements of the aortic wall thickness can be achieved. By overlaying CT and MRI, an improved 'completeness' of the aortic wall is produced allowing researchers to conduct more local wall thickness measurements to reliably describe their AAA geometric model. Our results show that aortic wall thickness varies along both axial and coronal/sagittal planes (Fig. 5). This gives the possibility for researchers to develop geometric biomechanical models with varying local thickness. Unlike raw CT or MRI, Canny edges allows users to measure the wall thickness based on the pixel edges reflecting the outer and inner wall boundaries. This avoids the random error associated with measuring wall thickness using raw CT or MRI where users are required to distinguish between the unclear boundaries of the inner and outer wall.

Currently, using both CT and MRI to measure aortic wall thickness may not be common practice, as it is an expensive process to acquire both modalities. However, it should be noted that the processes used to detect the aortic walls from these images are both computationally and financially feasible. If the quality of the CT is sufficient for the user to detect the walls, then an additional MRI may not be necessary, lowering the cost of the process. There are studies which use either CT or MRI to detect and measure aortic wall thickness but use interpolation algorithms [15] or mean distance [21]. With the expense of requiring both modalities, the method presented here allows users to locally measure wall thickness without any interpolation algorithms to estimate the wall boundaries.

A limitation in our study is that the measurement results are not compared to ground truth as it is not available. Bland–Altman plots were used to assess the agreement of using aortic wall thickness measurements using edges created between CT and MRI. The plots show that the bias (or mean difference) was close to the ideal zero value across all four patients, ranging between −0.08 to 0.20 mm. Additionally, plots across all patients only have 1–2 values lying outside the 95% LOA. It is also observed that depending on the modality, measurement of wall thickness may vary by as much as 1 pixel size of the original image.

Another limitation is the uncertainty of measurements due to several factors. Image resizing was incorporated in the script as the original CT and MRI resolution quality was too low for the algorithm to detect and produce Canny edges. The nearest neighbour interpolation was used to resample the pixels and scale the image by a factor of 4. This may introduce noise and jagged boundaries [22] which can affect accuracy of measurements as aortic walls are rounded in shape. Registration of CT and MRI was also a necessary step to produce overlayed edges. Accuracy of registration methods determines the reliability of the aortic wall thickness measurements. Since the method of registration has not yet been validated for our application, the registration error may have significant effects on our results.

We believe the next step to progress this novel technique of patient specific, non-invasive detection of local aortic wall thickness is to introduce a larger cohort of patient data and validating our method using ground truth wall thickness measurements. Additionally, the method could be simplified by automating the significant step of manually measuring the aortic wall thickness, improving both the repeatability and accuracy of this approach.

Acknowledgements The authors wish to acknowledge help of Dr. Grand Roman Joldes and funding from National Health and Medical Research Council (Australia) through an Ideas Grant no. APP2001689.

References

1. Wanhainen, A., et al. (2019). Editor's choice—European Society for Vascular Surgery (ESVS) 2019 clinical practice guidelines on the management of abdominal aorto-iliac artery aneurysms. *European Journal of Vascular and Endovascular Surgery, 57*(1), 8–93.
2. Sampson, U. K. A., et al. (2014). Estimation of global and regional incidence and prevalence of abdominal aortic aneurysms 1990 to 2010. *Global Heart, 9*(1), 159–170.
3. Norman, P. E., et al. (2004). Population based randomised controlled trial on impact of screening on mortality from abdominal aortic aneurysm. *BMJ (Clinical Research ed.), 329*(7477), 1259–1259.
4. Hoornweg, L. L., et al. (2008). Meta analysis on mortality of ruptured abdominal aortic aneurysms. *European Journal of Vascular and Endovascular Surgery, 35*(5), 558–570.
5. Bown, M. J., et al. (2002). A meta-analysis of 50 years of ruptured abdominal aortic aneurysm repair. *British Journal of Surgery, 89*(6), 714–730.
6. Farotto, D., et al. (2018). The role of biomechanics in aortic aneurysm management: Requirements, open problems and future prospects. *Journal of the Mechanical Behavior of Biomedical Materials, 77*, 295–307.
7. De Rango, P., & Verzini, F. (2010). Rupture in small abdominal aortic aneurysms: Beyond the rates. *European Journal of Vascular and Endovascular Surgery, 41*(1), 11–12.
8. Joldes, G. R., et al. (2016). A simple, effective and clinically applicable method to compute abdominal aortic aneurysm wall stress. *Journal of the Mechanical Behavior of Biomedical Materials, 58*, 139–148.
9. Zelaya, J. E., et al. (2014). Improving the efficiency of abdominal aortic aneurysm wall stress computations. *PLoS ONE, 9*(7), e101353–e101353.
10. Raghavan, M. L., et al. (1999). *Mechanical wall stresses on three-dimensionally reconstructed models of abdominal aortic aneurysm* (Vol. 1, p. 210). IEEE.
11. Miller, K., et al. (2020). Is there a relationship between stress in walls of abdominal aortic aneurysm and symptoms? *The Journal of Surgical Research, 252*, 37–46.
12. Conlisk, N., et al. (2016). Patient-specific modelling of abdominal aortic aneurysms: The influence of wall thickness on predicted clinical outcomes. *Medical Engineering & Physics, 38*(6), 526–537.
13. Shang, E. K. M. D., et al. (2015). Validation of semiautomated and locally resolved aortic wall thickness measurements from computed tomography. *Journal of Vascular Surgery, 61*(4), 1034–1040.
14. Joldes, G. R., et al. (2017). BioPARR: A software system for estimating the rupture potential index for abdominal aortic aneurysms. *Scientific Reports, 7*(1), 4641–4715.
15. Shum, J., et al. (2010). Semiautomatic vessel wall detection and quantification of wall thickness in computed tomography images of human abdominal aortic aneurysms: Wall thickness quantification of human abdominal aortic aneurysms. *Medical Physics (Lancaster), 37*(2), 638–648.
16. Adame, I. M., et al. (2006). Automatic vessel wall contour detection and quantification of wall thickness in in-vivo MR images of the human aorta. *Journal of Magnetic Resonance Imaging, 24*(3), 595–602.
17. Fedorov, A., et al. (2012). 3D Slicer as an image computing platform for the quantitative imaging network. *Magnetic Resonance Imaging, 30*(9), 1323–1341.

18. Canny, J. (1986). A computational approach to edge detection. *IEEE Transactions on Pattern Analysis and Machine Intelligence, PAMI-8*(6), 679–698.
19. McBride, O. M. B., et al. (2015). MRI using ultrasmall superparamagnetic particles of iron oxide in patients under surveillance for abdominal aortic aneurysms to predict rupture or surgical repair: MRI for abdominal aortic aneurysms to predict rupture or surgery—The MA3RS study. *Open Heart, 2*(1), e000190.
20. Bland, J. M., & Altman, D. G. (1999). Measuring agreement in method comparison studies. *Statistical Methods in Medical Research, 8*(2), 135–160.
21. Rosero, E. B., et al. (2009). Agreement between methods of measurement of mean aortic wall thickness by MRI. *Journal of Magnetic Resonance Imaging, 29*(3), 576–582.
22. Dianyuan, H. (2013). Comparison of commonly used image interpolation methods. In *Proceedings of the 2nd International Conference on Computer Science and Electronics Engineering (ICCSEE 2013).* Atlantis Press.

Patient-Specific Finite Element Modeling of Aneurysmal Dilatation After Chronic Type B Aortic Dissection

Shaojie Zhang, Joan D. Laubrie, S. Jamaleddin Mousavi, Sabrina Ben Ahmed, and Stéphane Avril

Abstract Progressive aneurysmal dilatation is a well-recognized complication in patients with chronic type B aortic dissection (cTBAD), which may lead to a delayed rupture and create a life-threatening condition. However, our understanding of such aortic expansion in cTBAD remains weak. In the present paper, we propose to use numerical simulations to study the role of growth and remodeling (G&R) in aneurysmal dilatation after cTBAD. We set up a 3D finite-element model of G&R for aortic dissection within an open-source code. Constitutive equations, momentum balance equations, and equations related to the mechanobiology of the artery were formulated based on the homogenized constrained mixture theory. The model was first applied to an idealized cylindrical aortic geometry to demonstrate its feasibility and efficiency. The model was then applied to a patient-specific aortic segment to show its potential in more relevant and complex patient-specific clinical applications. It was found that the G&R tends to naturally trigger the aneurysmal dilatation after dissection, in order to restore its tensional equilibrium. Our results indicated that the value of the gain parameter, related to collagen G&R, plays an important role in the stability of aortic expansion after cTBAD. A small gain parameter will induce an excessive aneurysmal degeneration whilst a large gain parameter helps to recover a stabilized state of the artery after dissection. Finally, it was found that other mechanobiology-related parameters, such as the circumferential length of the dissection, as well as the pressure in the false lumen, may also be a determinant for the stability of aneurysmal dilatation after cTBAD. Both a wide tear and an elevated false lumen pressure favor an unstable development of aortic expansion after cTBAD. As future work, the present model will be validated through predictions of aneurysmal dilatation in patient-specific clinical cases, in comparison with datasets followed over a significant period of time.

S. Zhang · J. D. Laubrie · S. J. Mousavi · S. Avril (✉)
Mines Saint-Etienne, University of Lyon, Université Jean Monnet, INSERM, U1059 Sainbiose, Centre CIS, 42023 Saint-Etienne, France
e-mail: avril@emse.fr

S. B. Ahmed
Université Jean Monnet, INSERM, U1059 Sainbiose and University Hospital of Saint-Etienne, 42000 Saint-Etienne, France

P. M. F. Nielsen et al. (eds.), *Computational Biomechanics for Medicine*,
https://doi.org/10.1007/978-3-031-09327-2_2

Keywords Growth and re-modelling · Aortic aneurysm · Dissection · EVAR · Collagen · Patient-specific simulation

1 Introduction

Chronic type B aortic dissection (cTBAD) is defined when a tear originates in the descending aorta and remains 3 months after its onset [1]. Patients with uncomplicated cTBAD are preferentially treated medically with periodic clinical and imaging surveillance, regarding the acceptable survival rate generally observed in a short-term follow-up [2, 3]. However, the long-term outcome of such conservative management remains questionable mainly due to the progressive aneurysmal dilatation [4]. Invasive surgical interventions, such as endovascular repair or open surgery are then needed [5]. Up to now, little is known about the aneurysmal dilatation after cTBAD, either it is stable with a moderated progression rate or there is an excessive aneurysmal degeneration. It is of crucial importance for surgeons to be able to assess the risk of aortic expansions in patients with early-stage cTBAD to choose the optimal treatment approach. Patients identified at high risk for aortic enlargement may therefore benefit from early surgical interventions and reduce mortality from delayed aneurysm ruptures.

Published studies on this topic remain scarce. It has been widely accepted that the presence of an excessive aortic diameter, typically greater than 40 mm, and a patent false lumen are two high-risk factors for late aneurysm development after cTBAD [6, 7, 8]. Besides, older age and elevated mean blood pressure were also found to promote aneurysmal degeneration in cTBAD [6]. Tsai et al. reported that the size, the number, as well as location of tears have significant impacts on the pressure in the false lumen, and therefore influencing the false lumen expansion [9]. Recently, Trimarchi et al. revealed that there are many other factors that may affect aneurysmal dilatation after cTBAD, including demographic, clinical, pharmacologic, and radiologic variables, such as connective tissues disorders, gender, the presence of thrombus in the false lumen, etc. [10]. However, all the above researches were based on observational studies or clinical trials with data collected over a long follow-up period.

Considering the recent advances in computational mechanics of arteries [11, 12] and more specifically the growth and remodeling (G&R) models [13–17], numerical models can be an interesting alternative option for studying these influencing factors. However, to the author's best knowledge, G&R after cTBAD has never been modeled so far. There is still an important potential for G&R models to understand vascular adaptation in chronic type B aortic dissection, where the patient can undergo a long-term process of G&R after breaking the initial mechanical equilibrium due to tear opening.

In this specific context, we developed a 3D finite-element model of vascular adaptation to study the aneurysmal dilatation after cTBAD, within an open-source code written in python and C++ [18–20]. The G&R model of the arterial wall is based on the homogenized constrained mixture theory (CMT) and the aortic dissection is

modeled through an original two-continuum arterial wall concept. We also performed a sensitivity analysis to evaluate the influence of several selected mechanobiological parameters on the aneurysmal dilatation after cTBAD.

Details of the model are given in this book chapter, by first introducing the mathematical framework of the CMT method for G&R with respect to cTBAD, then describing the two-continuum aortic dissection model, and finally showing potentials of the model, from a simple validation test case to academic applications with idealized geometries, until a more relevant patient-specific application.

2 Material and Methods

2.1 Constitutive and Balance Equations

The CMT was first proposed by Humphrey and Rajagopal as a hybrid method to describe mechano-regulated G&R of arteries [21]. It was then largely used for modeling aneurysm formation [13–17]. In this work, we employ the homogenized CMT [17] to model arterial G&R after cTBAD. Basic equations formulated under the homogenized CMT framework are briefly introduced in this section. Readers can refer to reference publications for more detailed mathematical formulations and their interpretations [15, 17, 21].

First, we assume that the arterial wall can be modeled as a homogenized mixture comprising a matrix containing a network of elastic fibers, passive reinforcements represented by 4 collagen fiber families (respectively oriented in circumferential, axial and $\pm 45°$ diagonal direction) and active reinforcements accounting for the contractility of smooth muscle cells (SMCs) in the circumferential direction. Let $\Omega_R \subset \mathbb{R}^3$ and $\Omega_t \subset \mathbb{R}^3$ denote, respectively, the initial traction-free reference configuration at time $t = 0$ and current deformed configuration at time $t > 0$ of the arterial wall. According to homogenized CMT, we assume that all constituents in the arterial wall deform together with a same deformation gradient $\mathbf{F}$:

$$\mathbf{F} = \frac{\partial \boldsymbol{x}}{\partial \boldsymbol{X}} \tag{1}$$

where $\boldsymbol{X}$ represents a material point in Ω_R and $\boldsymbol{x}$ represents the associated spatial point in Ω_t. Moreover, based on the theory of Rodriguez and Hoger [22], this deformation gradient tensor $\mathbf{F}$ can be split into an elastic part and an inelastic part for each constituent $i \in [e, c_j, m]$, such as

$$\mathbf{F} = \mathbf{F}^i_{el}\mathbf{F}^i_{gr} \tag{2}$$

where e, c_j, m represents respectively the elastic matrix, the jth collagen fiber family and smooth muscle cells. More precisely, $\mathbf{F}^i_{el}$ represents the elastic deformation tensor

related to stresses that balance external mechanical loads over the arterial wall, while $\mathbf{F}^i_{gr}$ represents the inelastic deformation tensor related to G&R, i.e. related to the continuous mass turnover of each constituent. Besides, we assume that G&R is a fully stress-mediated process. Other non-mechanical effects related to the mass turnover, such as immune-mediated chemical remodeling, damage, or mechanical fatigue, are neglected in this work. Therefore, the temporal homogenized mass deposition or degradation rate of each constituent can be expressed as

$$\dot{\rho}^i_R = \rho^i_R k^i_\sigma \frac{\sigma^i - \sigma^i_h}{\sigma^i_h} \tag{3}$$

where ρ^i_R is the reference mass density of constituent i, related to the reference configuration of the arterial wall. The right-hand side term of Eq. 3 describes the mass turnover due to the stress difference between the current stress σ^i and the homeostatic stress σ^i_h, where k^i_σ is a regularization parameter (named gain parameter) with respect to each constituent.

The homogenized CMT consists in the decomposition of the inelastic deformation gradient $\mathbf{F}^i_{gr}$ through two sub-gradient tensors

$$\mathbf{F}^i_{gr} = \mathbf{F}^i_g \mathbf{F}^i_r \tag{4}$$

where $\mathbf{F}^i_g$ is the growth-related tensor describing volume changes to due to mass turnover, and $\mathbf{F}^i_r$ is the remodeling-related tensor describing how the prestretch of each constituent is updated through continuous extant mass degradation and new mass production. As suggested by Braeu et al. [15], we assume that the growth deformation is the same for all constituents in the arterial wall, such as

$$\mathbf{F}^i_g = \mathbf{F}_g = \mathbf{I} + \frac{\rho_R}{\rho_{R0}} \boldsymbol{a}^\perp_0 \otimes \boldsymbol{a}^\perp_0 - \boldsymbol{a}^\perp_0 \otimes \boldsymbol{a}^\perp_0 \tag{5}$$

where ρ_R is the current reference mass density, ρ_{R0} is the initial reference mass density (at time $t = 0$), $\mathbf{I}$ is the second order identity and $\boldsymbol{a}^\perp_0$ the growth direction [17]. The remodeling process of elastin can be generally neglected ($\mathbf{F}^e_r = \mathbf{I}$) considering its slow mass degradation rate (typically several decades for elastin half-life time). We assume that the remodeling process of collagen fibers and SMCs occurs at a constant volume and along the fiber direction, which can be expressed as [23]

$$\mathbf{F}^i_r = \lambda^i_r \boldsymbol{a}^i_0 \otimes \boldsymbol{a}^i_0 + \frac{1}{\sqrt{\lambda^i_r}} \left(\mathbf{I} - \boldsymbol{a}^i_0 \otimes \boldsymbol{a}^i_0\right) \tag{6}$$

where λ^i_r is the respective remodeling stretch of fiber $i \in \left[c_j, m\right]$ along its fiber direction $\boldsymbol{a}^i_0$ with its time evolution $\dot{\lambda}^i_r$ given by [13]

$$\dot{\lambda}_r^i = \left(\frac{\dot{\rho}_R^i}{\rho_R^i} + \frac{1}{T^i}\right)\frac{\lambda^i}{\left(\lambda_{el}^i\right)^2}\left(\frac{\partial \sigma^i}{\partial \lambda_{el}^i}\right)^{-1} \times \left(\sigma^i - \sigma_h^i\right) \tag{7}$$

where T^i is the average mass turnover time during which old mass increment is degraded and replaced by a new mass increment. λ_{el}^i is the elastic stretch of fiber i defined as $\lambda_{el}^i = \sqrt{\left(\mathbf{F}_{el}^i\right)^t \mathbf{F}_{el}^i : \boldsymbol{a}_0^i \otimes \boldsymbol{a}_0^i}$ and λ^i is the total stretch of fiber i defined as $\lambda^i = \sqrt{(\mathbf{F})^t \mathbf{F} : \boldsymbol{a}_0^i \otimes \boldsymbol{a}_0^i}$.

Finally, considering that the homeostatic configuration of the arterial wall is achieved at time $t = t_0$ and defining the initial traction-free geometry of the arterial wall at time $t = 0$ as the same geometry as its homeostatic configuration, the initial elastic prestretch of each constituent $\mathbf{G}_h^i$ corresponding to the homeostatic configuration at time t_0 can simply satisfy

$$\mathbf{F}_r^i(t_0) = \left(\mathbf{G}_h^i\right)^{-1} \tag{8}$$

since $\mathbf{I} = \mathbf{F}(t_0) = \mathbf{F}_e^i(t_0)\mathbf{F}_g^i(t_0)\mathbf{F}_r^i(t_0) = \mathbf{G}_h^i\mathbf{F}_g^i(t_0)\mathbf{F}_r^i(t_0) = \mathbf{G}_h^i\mathbf{F}_r^i(t_0)$. The detailed expressions of $\mathbf{G}_h^i$ are hereby given for each constituent $\in \left[e, c_j, m\right]$, with respect to a cylindrical coordinate system

$$\mathbf{G}_h^e = \mathbf{diag}\left(\frac{1}{\lambda_\theta^e \lambda_z^e}, \lambda_\theta^e, \lambda_z^e\right) \tag{9}$$

$$\boldsymbol{G}_h^{c_i} = \lambda_h^{c_i} \boldsymbol{a}_0^{c_i} \otimes \boldsymbol{a}_0^{c_i} + \frac{1}{\sqrt{\lambda_h^{c_i}}}\left(\boldsymbol{I} - \boldsymbol{a}_0^{c_i} \otimes \boldsymbol{a}_0^{c_i}\right) \tag{10}$$

$$\boldsymbol{G}_h^m = \lambda_h^m \boldsymbol{a}_0^m \otimes \boldsymbol{a}_0^m + \frac{1}{\sqrt{\lambda_h^m}}\left(\boldsymbol{I} - \boldsymbol{a}_0^m \otimes \boldsymbol{a}_0^m\right) \tag{11}$$

where λ_θ^e and λ_z^e are the initial deposition stretches of elastin, respectively in the circumferential and axial direction, uniform over the whole arterial wall. $\lambda_h^{c_i}$ and λ_h^m are respectively the initial deposition stretches of collagen fibers (same deposition stretch for all four directions) and SMCs.

Based on CMT, the strain energy density function of the arterial wall can be given by

$$\Psi = \rho_R^e W^e + \sum_{j=1}^{4} \rho_R^{c_j} W^{c_j} + \rho_R^m W^m \tag{12}$$

where ρ_R^e, $\rho_R^{c_j}$ and ρ_R^m are respectively the reference mass densities of the elastic matrix, of the j^{th} collagen fiber family and of SMCs, and W^e, W^{c_j} and W^m are the specific strain energy density functions with respect to each constituent. Moreover, the strain energy density function W^i of each constituent $i \in \left[e, c_j, m\right]$, can be

expressed as a function of its elastic deformation tensor $\mathbf{F}^i_{el}$, or equivalently, its elastic right Cauchy-Green tensor $\mathbf{C}^i_{el}$, defined as $\mathbf{C}^i_{el} = \left(\mathbf{F}^i_{el}\right)^t \mathbf{F}^i_{el}$. In the present work, the elastic matrix is considered as a quasi-incompressible Neo-Hookean hyperelastic material with its specific strain energy density function W^e given by [24, 25]

$$W^e = \frac{\mu^e}{2}\left(\mathrm{tr}\left(\overline{\mathbf{C}}^e_{el}\right) - 3\right) + \kappa\left(\left|\mathbf{F}^e_{el}\right| - 1\right)^2 \tag{13}$$

where μ^e is a material parameter characterizing the shear stiffness of elastin and κ is an arbitrary but sufficiently high penalty parameter ensuring quasi incompressibility. $\overline{\mathbf{C}}^e_{el}$ is the isochoric elastic right Cauchy-Green tensor of elastin, defined as $\overline{\mathbf{C}}^e_{el} = \left(\overline{\mathbf{F}}^e_{el}\right)^t \overline{\mathbf{F}}^e_{el}$ and $\overline{\mathbf{F}}^e_{el} = \mathbf{F}^e_{el}/\left|\mathbf{F}^e_{el}\right|^{1/3}$. The specific strain energy density function of collagen fiber families is modeled by an anisotropic Fung-type exponential function [26, 27],

$$W^{c_j} = \frac{k_1^{c_j}}{2k_2^{c_j}}\left(e^{k_2^{c_j}\left(I_{4^{c_j}_{el}}-1\right)^2} - 1\right) \tag{14}$$

We also use the same anisotropic Fung-type exponential function to model the passive behavior of SMCs [15], while an additional term is added for the active tone contribution such as,

$$W^m = \frac{k_1^m}{2k_2^m}\left(\boldsymbol{e}^{k_2^m\left(I_{4^m_{el}}-1\right)^2} - 1\right) + \frac{\sigma_{max}}{\rho_{R0}}\left(\lambda_{act} + \frac{1}{3}\frac{\left(\lambda^m_{max} - \lambda_{act}\right)^3}{\left(\lambda^m_{max} - \lambda^m_0\right)^2}\right) \tag{15}$$

where $k_1^{c_j}$ and k_1^m are stress-like material parameters, and $k_2^{c_j}$ and k_2^m are dimensionless material parameters. $I_{4^{c_j}_{el}}$ and $I_{4^m_{el}}$ are pseudo-invariants, which are additional invariants defined in case of anisotropic materials such as $\lambda^i_{el} = \mathbf{C}^i_{el} : \boldsymbol{a}^i_0 \otimes \boldsymbol{a}^i_0$ with $i \in \left[c_j, m\right]$ [25]. λ_{act} is the active stretch in the circumferential direction, σ_{max} is the maximum active Cauchy stress, ρ_{R0} is the reference total mass density of the arterial wall at time $t = 0$, and λ^m_{max} and λ^m_0 are the active stretches respectively at maximum and zero active stress for SMCs.

The second Piola–Kirchhoff stress tensor $\mathbf{S}$ and the fourth order elasticity tensor of the arterial wall $\mathbb{C}$ are then deduced by performing the first and second derivatives of the strain energy function Ψ with respect to the total Green–Lagrange strain $\mathbf{E}$

$$\mathbf{S} = \frac{\partial \Psi}{\partial \mathbf{E}} = \varphi^e \mathbf{S}^e + \sum\nolimits_i \varphi^{c_j} \mathbf{S}^{c_j} + \varphi^m \mathbf{S}^m \tag{16}$$

$$\mathbb{C} = \frac{\partial^2 \mathbf{S}}{\partial \mathbf{E} \partial \mathbf{E}} = \varphi^e \mathbb{C}^e + \sum\nolimits_i \varphi^{c_j} \mathbb{C}^{c_j} + \varphi^m \mathbb{C}^m \tag{17}$$

where φ^i, $\mathbf{S}^i$ and $\mathbb{C}^i$ are the mass fraction, second Piola–Kirchhoff stress and forth order elasticity tensor with respect to each constituent $i \in \left[e, c_j, m\right]$ in the arterial

wall, defined as

$$\varphi^i = \frac{\rho_R^i}{\rho_R} \tag{18}$$

$$\mathbf{S}^i = \rho_R \frac{\partial W^i}{\partial \mathbf{E}} \tag{19}$$

$$\mathbb{C}^i = \rho_R \frac{\partial^2 W^i}{\partial \mathbf{E} \partial \mathbf{E}} \tag{20}$$

with $\rho_R = \rho_R^e + \rho_R^{c_j} + \rho_R^m$ the reference total mass density of the arterial wall. Finally, assuming that the G&R occurs at a slow time scale and can be considered as a quasi-static process, the dynamics effects such as inertia or viscoelasticity of the arterial wall can be neglected. Therefore, the momentum balance equations of the arterial wall can be simply written as

$$\nabla \cdot \boldsymbol{\sigma} + \rho \boldsymbol{b} = 0 \tag{21}$$

ρ is the spatial density of the arterial wall, related to its reference density ρ_R, as $\rho = \rho_R/|\mathbf{F}|$, $\boldsymbol{b}$ is the body force vector given in the spatial configuration, $\boldsymbol{\sigma}$ is the Cauchy stress derived from the previous second Piola-Kirchoff stress as

$$\boldsymbol{\sigma} = \frac{\mathbf{1}}{|\mathbf{F}|} \mathbf{F}\mathbf{S}\mathbf{F}^t \tag{22}$$

The boundary conditions applied on the arterial wall can be Dirichlet boundary conditions, assigning the predefined displacement field over the mesh nodes or Robin boundary conditions, which are applied over the mesh surface, such as

$$\boldsymbol{\sigma} \cdot \boldsymbol{n} = P_{TL} \boldsymbol{n} + \boldsymbol{p}_{dissection} + \boldsymbol{F}_{spring} \tag{23}$$

where P_{TL} denotes the true luminal pressure of the artery due to blood flow, applied on the inner surface of the media layer. $\boldsymbol{n}$ is the outward pointing unit vector normal to the arterial inner media surface. $\boldsymbol{p}_{dissection}$ is the pressure in the false lumen after cTBAD. $\boldsymbol{F}_{spring}$ is an additional spring-based elastic force, related to the two-contInnumm arterial wall concept proposed in this work. Details of the two-continuum arterial wall concept, as well as, $\boldsymbol{F}_{spring}$, $\boldsymbol{p}_{dissection}$, will be given in the next section.

2.2 Dissection Model

In this section, we will firstly present the two-continuum arterial wall concept, dedicated to the modeling of G&R in the case of cTBAD. It is worth noting that the mechanism of the initial tear formation or the subsequent tear progression is currently not of primary interest in this paper. Under this specific context, we propose to model the initial healthy arterial wall without dissection with two continuum bodies. As shown in Fig. 1a, the arterial wall is made up of two layers, respectively the inner media layer and the outer adventitia layer. The two layers are perfectly connected by high stiffness elastic springs. More precisely, each spring connects two adjacent mesh surfaces S^a and S^m, at the inner surface of the adventitia and the outer surface of media, respectively. The force applied on each surface is computed on the relative displacement of the two connecting surfaces, as given in Eq. (24)

$$\boldsymbol{F}_{dissection} = \begin{cases} -k_{spring}(d_{S^a} - d_{S^m})\boldsymbol{n}_{S^a}, & adventitia \\ k_{spring}(d_{S^a} - d_{S^m})\boldsymbol{n}_{S^m}, & media \end{cases} \tag{24}$$

where k_{spring} is the stiffness of the interfacial spring. d_{S^a} and d_{S^m} the nodal-averaged displacement of the mesh surface located respectively in the inner adventitia and outer media surfaces. $\boldsymbol{n}_{S^a}$ and $\boldsymbol{n}_{S^m}$ are the outward pointing unit vectors normal to the respective mesh. It is worth noting that displacement of one layer is transmitted to the other layer with low distortions due to the high stiffness of the springs. Finally, we assume that this initial configuration of the arterial wall is at its homeostatic state with a reference luminal pressure P_{TL}. To validate this new concept, a simple validation

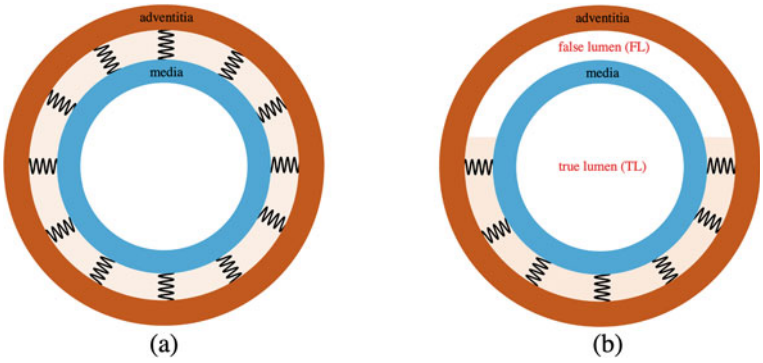

Fig. 1 **a** Illustration of the two-continuum arterial wall model, with the adventitia layer and the media layer connected by high stiffness elastic springs, representing a healthy arterial wall under its homeostatic state. **b** Initial configuration of the arterial wall after cTBAD. The false lumen is created by breaking interfacial elastic springs in a selected region between the media and adventitia layers

test case has been proposed in this work, in comparison with the conventional arterial wall model with a single continuum body [13–17].

Based on this new concept of a two-continuum arterial wall, the initial configuration of cTBAD with false lumen can be obtained by simply removing interfacial springs. As shown in Fig. 1b, the false lumen (FL), as well as the free surfaces (i.e. inner side of adventitia layer and outer side of media layer), is created by removing springs in a selected region where tears are assumed to be present. The force induced by the pressure in the false lumen is then applied on each mesh surface, $S^{dissection}$, of the newly created free surfaces

$$\boldsymbol{p}_{dissection} = P_{FL}\boldsymbol{n}_{S^{dissection}} \tag{25}$$

where P_{FL} is the constant pressure in the false lumen and $\boldsymbol{n}_{S^{dissection}}$ is the outward pointing unit vector normal to the free mesh surfaces in the false lumen. Finally, it is worth noting that the presence of such pressurized false lumen will break the mechanical equilibrium of the arterial initial homeostatic state, and therefore trigging the G&R of the arterial wall over a long period of time in case of cTBAD, until the achievement of a new preferred mechanical state or eventually an excessive aneurysmal degeneration.

2.3 Finite Element Implementation

The proposed model was implemented within an open-source finite element code, written in Python and C++ [18, 19]. Three different steps, are defined in the model:

- **1st step**: Computation of the healthy arterial wall at homeostasis. The initial arterial wall is loaded with a constant luminal pressure, P_{TL}, on its entire inner surface of media.
- **2nd step**: Opening of the arterial wall. Interfacial springs are removed in a selected region between the adventitia layer and media layer, creating the initial dissection tear of cTBAD. The same luminal pressure in the true lumen, P_{TL}, is maintained as in the previous step, applied on the entire inner surface of the media. In the meantime, the false lumen will be loaded with a constant pressure, P_{FL}, applied on the newly created surfaces related to the tear-open region.
- **3rd step**: Adaptation of the arterial wall with G&R after cTBAD, i.e., after the creation of a pressurized false lumen.

Note that there is only one time increment in the first two steps while the third step is composed of several time increments to obtain relevant results of a long-term arterial wall adaptation after cTBAD. For each time increment, the same set of momentum balance and constitutive equations is solved with the Newton–Raphson method. Finally, at the end of each time increment, we obtain the displacement field and the associated stress–strain information on each mesh node of the arterial wall.

3 Numerical Applications

In order to show the potentials of the present dissection model, three different simulations were performed in this paper:

- **Validation test case**: It consists of a simple test case to validate the spring-connected two-continuum arterial wall concept proposed in this work. The validation was achieved through the comparison with reference results in the literature [13–17] where the conventional single continuum arterial wall model was employed to simulate the aneurysm formation in response to external stimuli.
- **Application to a cylindrical artery**: The second application is to study the G&R after cTBAD in the case of an idealized cylindrical artery.
- **Application to a patient-specific artery**: In this last application, we demonstrate the feasibility of our dissection model for further more complex and relevant clinical patient-specific applications, by modeling the G&R on a dissected patient-specific human descending aortic segment.

3.1 Validation Test Case

An idealized two-layered cylindrical artery is considered. The geometry was the same as that used in the work of Braeu et al. [15], with an inner arterial radius of 10 mm and a constant arterial thickness of 1.41 mm. We assume that each layer of the arterial wall, i.e. adventitia layer and media layer, has the same thickness of 0.705 mm. Moreover, it should be mentioned that a constant gap of 0.01 mm is defined between the two layers, allowing the presence of interfacial connecting springs with respect to the two-continuum arterial wall concept. The mesh is hexahedral and composed of $6 \times 40 \times 25$ elements (thickness $\times$ circumferential $\times$ length). Finally, the whole geometry is assumed to be at a homeostatic state, related to a reference luminal pressure of 13.3 kPa.

Following Braeu et al. [15], we apply a sudden degradation of the elastic matrix such as

$$\dot{D}^e = -\frac{\rho_R^e}{T^e} - \frac{D_{dam}}{t_{dam}} \rho_{R0}^e e^{-0.5\left(\frac{z}{L_{dam}}\right)^2 - \frac{t}{t_{dam}}} \tag{26}$$

where L_{dam} and t_{dam} are respectively the spatial and the temporal damage spread parameter, D_{dam} is the maximum damage, ρ_{R0}^e is the initial reference mass density of elastin, z is the axial position of the cylinder. Noting that due to the symmetry of the problem, only half of the cylinder is modeled in this simulation with z varying from 0 to 90 mm. The first term at the right-hand side (RHS) of Eq. 26 describes the natural elastin degradation by aging effect. The second term of the RHS is related to sudden external stimuli, causing a maximum elastin degradation at the center of the cylinder, i.e. $z = 0$ mm. Material properties used in this validation test case are

Table 1 Material properties used in the validation test case

Symbol	Value	Unit
μ^e	72	J kg^{-1}
κ	720	J kg^{-1}
$k_1^{c_j}$	568	J kg^{-1}
$k_2^{c_j}$	11.2	–
k_1^m	7.6	J kg^{-1}
k_2^m	11.4	–
ρ_{R0}^e	241.5	kg m^{-3}
$\rho_{R0}^{c_1} = \rho_{R0}^{c_2}$	65.1	kg m^{-3}
$\rho_{R0}^{c_3} = \rho_{R0}^{c_4}$	260.4	kg m^{-3}
ρ_{R0}^m	157.5	kg m^{-3}
λ_z^e	1.25	–
λ_θ^e	1.34	–
$\lambda_h^{c_j}$	1.062	–
λ_h^m	1.1	–
T^e	101.16	Years
T^{c_j}	101	Days
T^m	101	Days
L_{dam}	8	mm
t_{dam}	40	Days
D_{max}	0.5	–
σ_{actmax}	54	kPa
λ_0	0.8	–
λ_m	1.4	–
k_{spring}	1000	kPa mm^{-1}

taken from the 3D model of Braeu et al. [15] and are summarized in Table 1 together with other simulation parameters. The simulation results obtained in this simulation are compared to the reference results in the literature [13], by using three different values of collagen gain parameter $k_\sigma^{c_i}$.

3.2 Application to a Cylindrical Artery

After the validation of the two-continuum arterial wall model, we first apply the G&R after cTBAD in the case of an idealized two-layered cylindrical artery as shown in Fig. 2. The same geometry as in the previous validation case was used, except that the length of the artery is reduced from 90 to 50 mm. The mesh was hexahedral and composed of 6 × 60 × 20 elements (thickness × circumferential × length).

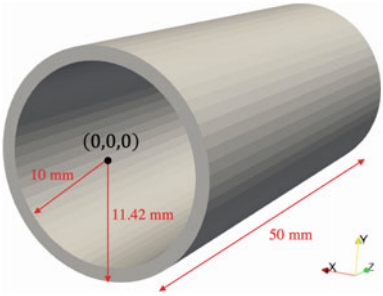

Fig. 2 Schematic representation of the idealized cylindrical artery on which the presented dissection model is applied for modeling G&R after cTBAD

Similarly, we assume that this geometry was related to a homeostatic state under an inner true lumen pressure of 13.3 kPa (100 mmHg). The initial tear of the dissection is created by breaking springs in regions where $x \leq 10$ mm and $z \leq 50$ mm, to model a representative initial tear of cTBAD. A pure sliding boundary condition is assigned on the cross-section at two extremities. The outer surface of the adventitia is free. The reference pressure in the false lumen is assumed to be the same as in the true lumen. The same material properties as reported in Table 1 has been used, considering additionally the layered distribution of different material constituents as suggested by Mousavi et al. [16] for human ascending thoracic aorta, i.e., the media has 97% of the total elastin, 15% of the total axial and diagonal collagen fibers, and 100% of the total SMCs, while the adventitia has 3% of the total elastin, 85% of the total axial and diagonal collagen and 100% of the total circumferential collagen.

3.3 Application to a Patient-Specific Artery

In this last test case, our dissection model was applied to a patient-specific human descending thoracic aortic segment, as shown in Fig. 3a. It was taken from a patient-specific aortic arch geometry, reconstructed from a patient's CT scan [16], as shown in Fig. 3b. The exact location of the modeled aortic segment is shown in Fig. 3b with the blue mesh. The thickness of the adventitia and media was assumed to be equal with the two layers separated with a constant gap of 0.01 mm. The mesh was hexahedral and composed of $6 \times 48 \times 42$ elements (thickness $\times$ circumferential $\times$ length). Similar to previous test cases, we assumed that this initial geometry was related to a homeostatic state, with an inner true lumen pressure of 10.7 kPa (80 mmHg). The reference pressure in the false lumen was assumed to be the same as in the true lumen. However, this value may change as a sensitivity study was performed on the false lumen pressure in this patient-specific case test, which is detailed in the results section. Moreover, it should be mentioned that the pure sliding boundary condition was applied on the cross-section at the two extremities and the outer surface of the adventitia was let free.

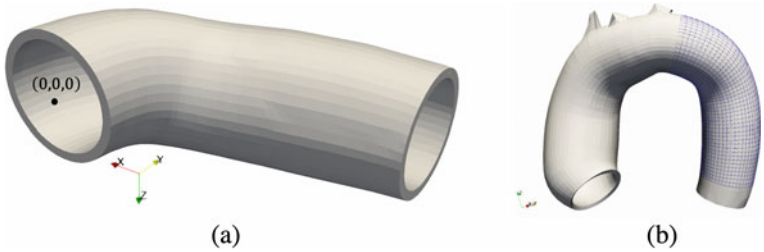

Fig. 3 **a** Schematic representation of the patient-specific human descending thoracic aortic segment on which the presented dissection model was applied for modeling G&R after cTBAD. **b** Illustration of the modeled aortic segment location, i.e., regions covered by the blue mesh, with respect to the whole patient-specific aortic arch

Mechanical parameters, as well as simulation parameters, are reported in Table 2, based on Laubrie et al. [28] Finally, it is worth noting that the non-uniform prestretches were used in this patient-specific artery, which was computed based on an iterative method previously developed by Laubrie et al. [28].

In order to better describe the initial dissection tear of cTBAD, we introduce a numerical parameter, α, for each circumferential cross-section of the arterial segment, as shown in Fig. 4. Note that the unit vector normal to this cross-section is computed from the arterial centerline points. The unit vertical direction of the cross-section is approximately defined as the averaged projection vector of this section on the xy plane. After the definition of directions, we define α for each interfacial connecting spring

$$\alpha = \frac{l}{D} \tag{27}$$

where l is the length of averaged spring positions, projected on the cross-section's vertical direction. The tear opening criterion is thus defined as $\alpha \geq \alpha_{min}$. Therefore, with $\alpha_{min} = 0$, all interfacial springs between the adventitia and media layers will be broken, creating a full separation of the two layers. While if α_{min} is equal to 1, no interfacial springs will be broken and thus no presence of the tear. In this patient-specific simulation, the effect of the tear opening length to the G&R after cTBAD was considered, by varying the values of α_{min} from 0.8 (a narrow tear) to 0.5 (a wide tear).

Table 2 Material properties and simulation parameters used for the patient-specific artery simulation

Symbol	Value	Unit
μ^e	80	J kg^{-1}
κ	800	J kg^{-1}
$k_1^{c_j}$	292.0	J kg^{-1}
$k_2^{c_j}$	5.6	–
k_1^m	13.8	J kg^{-1}
k_2^m	6.0	–
ρ_{R0}^e (media)	169.0	kg m^{-3}
$\rho_{R0}^{c_1} = \rho_{R0}^{c_2}$ (media)	14.6	kg m^{-3}
$\rho_{R0}^{c_3} = \rho_{R0}^{c_4}$ (media)	58.4	kg m^{-3}
ρ_{R0}^m (media)	735.0	kg m^{-3}
ρ_{R0}^e (adventitia)	565.0	kg m^{-3}
$\rho_{R0}^{c_1} = \rho_{R0}^{c_2}$ (adventitia)	48.5	kg m^{-3}
$\rho_{R0}^{c_3} = \rho_{R0}^{c_4}$ (adventitia)	194.0	kg m^{-3}
ρ_{R0}^m (adventitia)	0.0	kg m^{-3}
$\lambda_h^{c_j}$	11	–
λ_h^m	1.1	–
T^e	101.16	Years
T^{c_j}	101	Days
T^m	101	Days
σ_{actmax}	54	kPa
λ_0	0.8	–
λ_m	1.4	–
k_{spring}	1000	kPa mm^{-1}

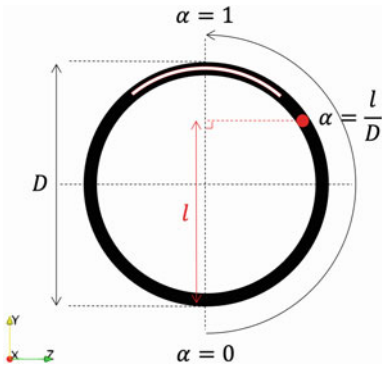

Fig. 4 Description of the initial tear opening criteria defined on each circumferential cross-section of the aortic segment

3.4 Computational Details

All simulations were performed on a Macbook Pro with Intel Core i5 and 8 GB of memory. The computation time for each simulation takes around 2 h. The low computation resources prove the computational efficiency of our dissection model.

4 Results

4.1 Validation Test Case

Results of the validation test case are shown in Fig. 5, illustrating the aneurysmal expansion of the arterial wall due to elastin loss. The evolution of the maximum inner radius of the aneurysm is shown, in comparison with the reference results [13], over a period of 10 years. The results indicated that the current two-continuum arterial wall model is in good agreement with the conventional single continuum arterial wall model. The aneurysmal expansion tends to recover its stability with a large gain parameter while a small gain parameter promotes an uncontrolled expansion of the

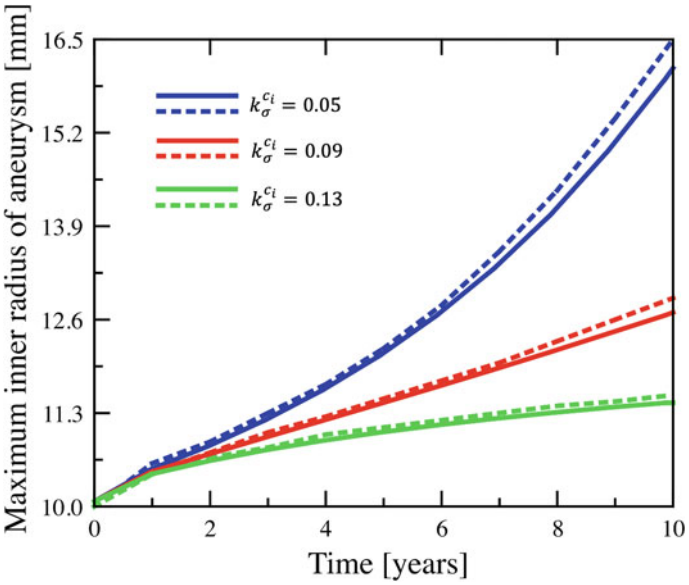

Fig. 5 Evolution of the maximum arterial inner radius over 10 years in response to an initial sudden elastin loss for both the two-continuum arterial wall model (solid lines) and the reference single-continuum arterial wall model (dash lines), with three different values of gain parameter related to collagen G&R [13]

aneurysm. With this validation test case, we justified the use of such a two-continuum arterial wall concept for G&R problems.

4.2 Application to a Cylindrical Artery

We first show the reference simulation results in the case of a cylindrical artery, as illustrated in Fig. 6, with respect to a reference value of gain parameter $k_\sigma^{c_j} = k_\sigma^m = 0.05$. It can be seen that the dissected part of the artery, especially the outer adventitia layer, continues to dilate due to the effect of G&R after the initial tear opening. This aneurysmal dilatation tends to be unstable, with an increasing growth rate over time. The maximum stress, which is located at the vicinity of the tear edge, also increases rapidly over time.

Previous studies on G&R, which modeled aneurysm progression but disregarded effects of the dissection, reported that gain parameters have a determinant effect on the stability of aneurysmal dilatation [15, 16]. To investigate the effect of this gain parameter in the specific context of cTBAD, we considered three different values of gain parameters, ranging between 0.05 and 0.15, with results illustrated in Fig. 7, showing the temporal evolution of the maximum outer diameter of the dissected cylindrical artery. It can be seen that the same tendency as previously reported in the

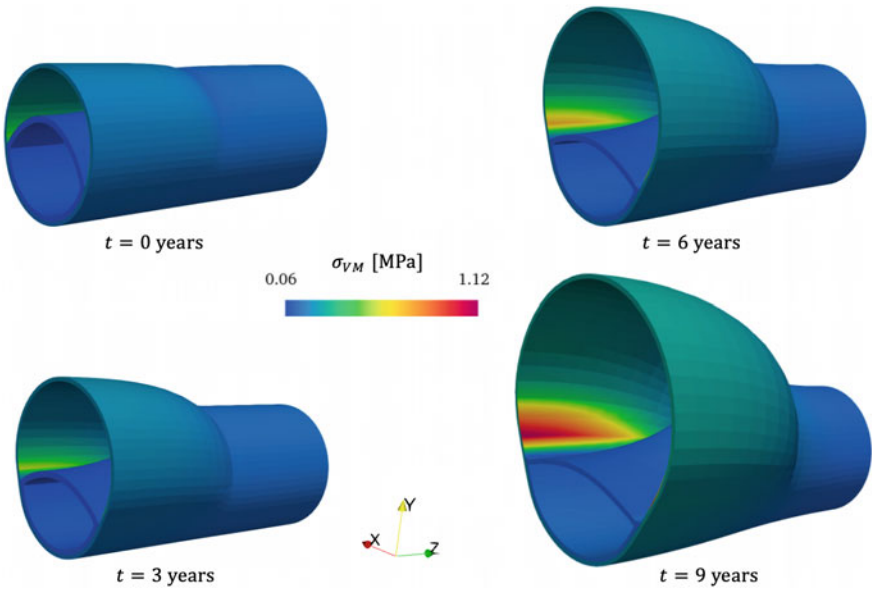

Fig. 6 Reference results of the cylindrical artery with respect to a reference value of gain parameter $k_\sigma^{c_j} = k_\sigma^m = 0.05$, showing geometrical and equivalent von Mises stress evolutions after cTBAD over 9 years

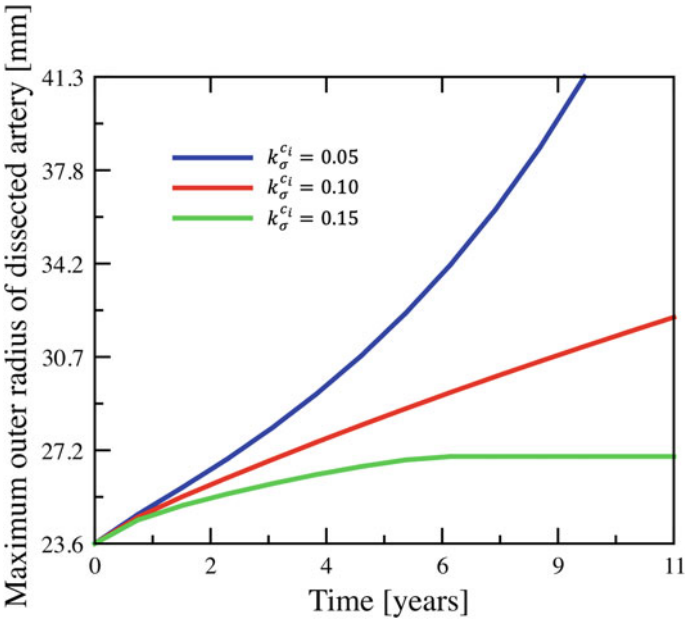

Fig. 7 Influence of the gain parameter to aneurysmal dilatation after cTBAD, showing the temporal evolution of the maximum outer diameter of the dissected cylindrical artery

literature has been observed for G&R after cTBAD. A small gain parameter tends to induce an unstable aneurysmal degeneration while a large gain parameter tends to favor the stability of aneurysmal dilatation.

4.3 Application to a Patient-Specific Artery

The reference simulation results in the case of a patient-specific artery, more precisely, a patient-specific human descending aortic segment, are shown in Fig. 8, with respect to a reference value of gain parameter $k_\sigma^{c_j} = k_\sigma^m = 0.05$. The results illustrate the geometrical and stress evolutions of the aortic segment, and also the circumferential cross-section at its dissected extremity. We found that the dissected aortic segment undergoes continuous aneurysmal dilatation over time after the initial tear opening. It can be seen that there is a significant increase of stress over time, mostly on the dissected part of the outer adventitia layer.

Similarly, the effect of the gain parameter on aneurysmal dilatation after cTBAD was investigated. Results obtained confirm the same tendency as observed in previous test cases: a large gain parameter tends to stabilize the aneurysmal dilatation of the dissected artery while a small gain parameter promotes an excessive aneurysmal degeneration after cTBAD (Fig. 9).

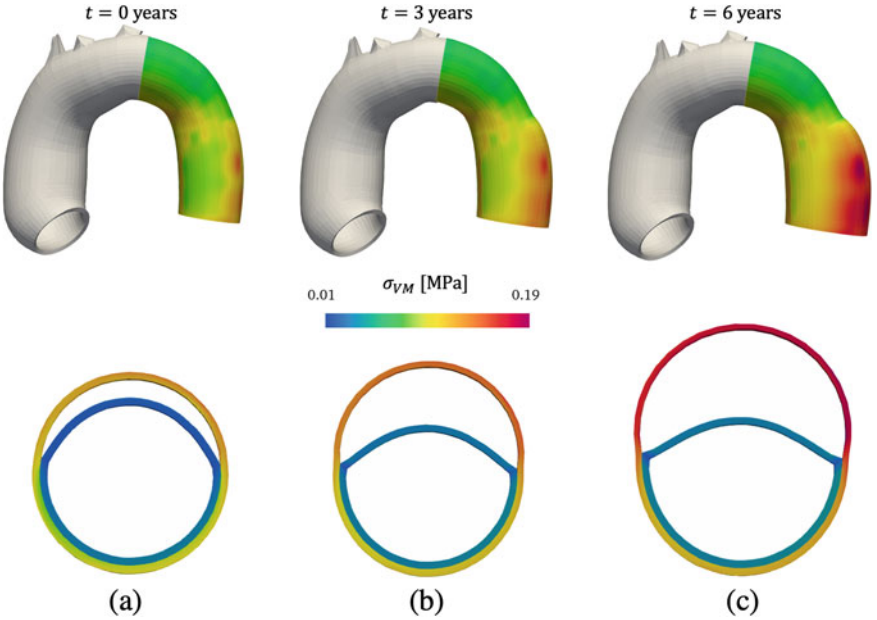

Fig. 8 Reference results of the patient-specific artery with respect to a reference value of gain parameter $k_\sigma^{c_j} = k_\sigma^m = 0.05$, showing geometrical and equivalent von Mises stress evolutions after cTBAD over 6 years, as well as the dilated circumferential cross-section at its dissected maximum extremity, respectively at **a** 0 year of G&R, **b** 3 year of G&R and 6 year of G&R

Apart from the gain parameter, it has also been reported in the literature that the tear size may have a significant influence on aneurysmal dilatation after cTBAD [9, 29]. The effects of the tear size are very complex, which depend not only on the position of the tear but also on its irregular shape, involving generally measures in three dimensions. In this paper, we studied only the circumferential length of the tear, with four different values of α_{min} ranging from 0.8 to 0.5, i.e., from narrow circumferential tear to wide circumferential tear. Results obtained are shown in Fig. 10, describing the temporal evolution of the maximum outer diameter of the dissected artery. It can be seen that a wider tear promotes an uncontrolled aneurysmal dilatation after cTBAD, while a narrow tear tends to favor a stable aneurysmal dilatation with a moderate growth rate. This provides a mechanical evidence to the commonly accepted clinical risk assessment of dissected aneurysm by its size [6–8].

Finally, in this patient-specific simulation, we also investigated the effect of the pressure as it has been identified as a high-risk factor in cTBAD, especially in the false lumen where the pressure may impact directly on the stress distribution of the most weakened outer adventitia layer [6, 30, 31]. In order to evaluate the effect of the pressure in the false lumen, three different values of false lumen pressure are considered, respectively higher than the true lumen pressure ($p_{FL}/p_{TL} > 1$), equal to the true lumen pressure ($p_{FL}/p_{TL} = 1$), and lower than the true lumen pressure

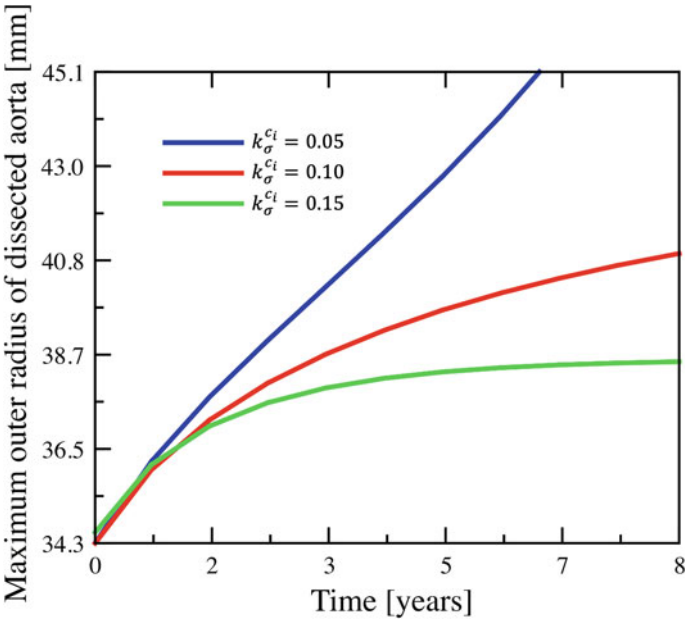

Fig. 9 Influence of the gain parameter to the aneurysmal dilatation after cTBAD, showing the temporal evolution of the maximum outer diameter of the dissected patient-specific artery

($p_{FL}/p_{TL} < 1$). Note that pressure in the true lumen is assumed to be constant. Results are shown in Fig. 11, showing the temporal evolution of the maximum outer diameter of the dissected artery. It can be seen that a higher pressure promotes aneurysmal dilatation after cTBAD. More precisely, regarding the aneurysmal dilatation rate at 3 years, a 10% pressure increase in the false lumen induces an "enlarging" growth of the dissected artery ($\geq$3 mm/year) while for false lumen pressure equal or below the true lumen pressure, aneurysmal dilatation can be considered as "stable" ($<$3 mm/year) [1].

5 Discussion

cTBAD is associated with poor long term outcomes, mainly as a result of excessive aneurysmal dilatations. Consequently, a significant fraction of patients with cTBAD will require ultimately surgical interventions such as endovascular repair or open surgery [32, 33]. However, there is a serious lack of risk assessment tools because our current understanding of the aneurysmal dilatation mechanism after cTBAD remains weak.

In this chapter, we proposed a numerical approach to study the role of G&R in aneurysmal dilatation in cTBAD. We found that the G&R process naturally triggers

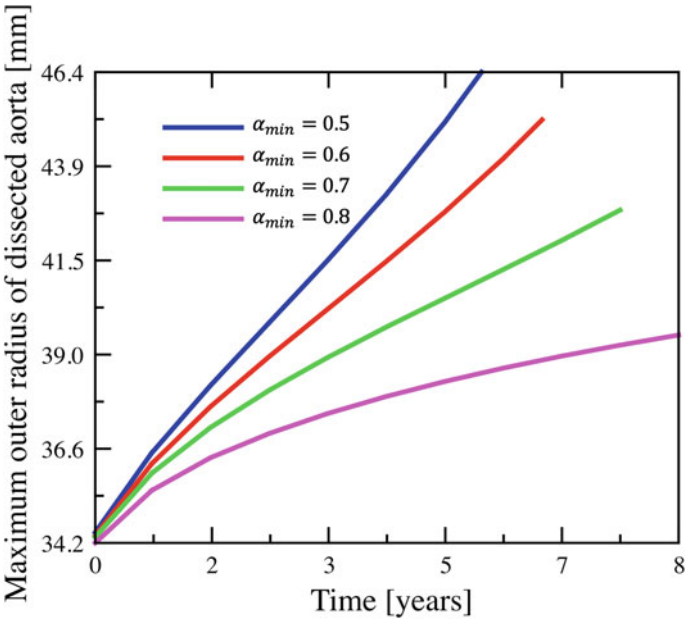

Fig. 10 Influence of the initial circumferential opening length of dissecting tear to the aneurysmal dilatation after cTBAD, showing the temporal evolution of the maximum outer diameter of the dissected patient-specific artery

the aneurysmal dilatation. Moreover, it was found that with a large gain parameter related to collagen G&R, the aneurysmal dilatation tends to be stable while with a small gain parameter, there would be an excessive aneurysmal degeneration. It is interesting to note that the results obtained are in agreement with clinical evidence reported by Juvonen et al. [6], where older patients present a higher risk of aneurysmal rupture in case of cTBAD. In fact, this gain parameter describes the capacity of arteries to restore its tensional equilibrium state in case of a disturbance of its mechanobiological equilibrium [14] and it has been reported that age may affect this gain parameter with older patients generally having an impaired stress-regulated repair mechanism compared to young patients [34].

Based on sensitivity analysis performed on patient-specific simulations, we found that the circumferential tear length also has a significant influence on the G&R process after cTBAD. A wide tear promotes an unstable development of aneurysmal dilatation while a narrow tear reduces the risk of uncontrolled aneurysmal dilatation. The reason could be twofold. First, a wide initial opening tear means naturally a larger initial dissected arterial diameter once the false lumen is pressurized compared to a narrow initial tear. Secondly, the consequence of a larger initial dissected arterial diameter is that the deformation and stress will be much higher, especially in the dissected outer adventitia layer, accelerating the G&R process of the artery. Indeed, the results remained very limited, considering the irregular three-dimensional tear shape and

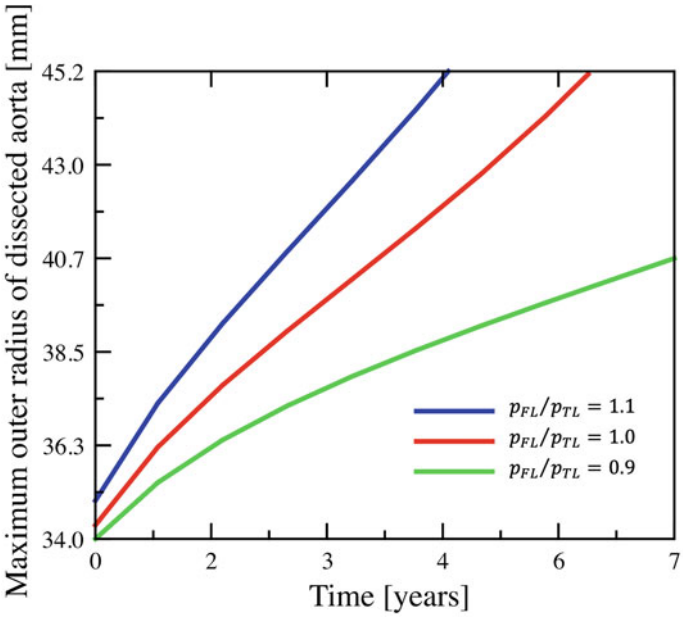

Fig. 11 Influence of the pressure in the false lumen to the aneurysmal dilatation after cTBAD, showing the temporal evolution of the maximum outer diameter of the dissected patient-specific artery

other complex mechanobiological phenomena neglected. However, it provides a mechanical proof that the tear size is also an important influencing factor that needs to be considered in the risk assessment of patients with cTBAD.

Finally, our results indicated that the pressure in the false lumen has a determinant role in the aneurysmal progression rate of the dissected artery. We found that a relative 10% increase of pressure in the false lumen, compared to that of the true lumen, is sufficient to promote an "unstable" growth of the dissecting aneurysm. This can be critical for patients, as surgical interventions are usually recommended for such situations [1].

Despite the above promising results, the current model still has some shortcomings that could be addressed in the future. First, in the present model, the tear configuration remains fixed after its initial creation. However, with the continuous aneurysmal dilatation and accumulation of stress especially near the edge of the tear, the initial tear may propagate due to high-stress concentration and thus alter the G&R process. Therefore, integration of the tear propagation models, such as that reported in the literature [35–38], could be an essential step to build a more reliable dissection model for evaluating the G&R effect to aneurysmal dilatation after cTBAD.

Secondly, the dissection model is relatively simplified. Intraluminal thrombus, which was often reported to have an important role in dissecting aneurysm pathologies and rupture [39, 40], was literally neglected in this work. The effects of

surrounding tissues were also neglected although it has already been reported in the literature that the surrounding connective tissues or vertebral column may impact regional adaptation of aortic walls by changing the local wall stress distribution or even more directly the aneurysmal aortic shape [41, 42]. Moreover, potential dynamic effects of the blood flow inside the arterial wall are currently not taken into consideration, despite its non-negligible effect directly on the wall stress distribution, as reported in the literature [29, 43].

Finally, the initial tear configuration was restricted to its circumferential length. Location of the tear, number of the tears or other dimensions related to the tears are currently neglected. For further patient-specific simulations, these parameters should be carefully considered as they may directly impact the pressure in both the false lumen and the true lumen [9].

6 Conclusions

In summary, we introduced an efficient 3D finite-element model, based on an open-source in-house code, to model the aneurysmal dilatation due to G&R after cTBAD. We showed the potential of this dissection model to simulate G&R process after cTBAD, from simple test cases with idealized arterial geometries to a more relevant case with a patient-specific geometry. The effects of different parameters on aneurysmal dilatation were assessed through a comprehensive sensitivity analysis. It was found that the gain parameter related to collagen G&R as well as the circumferential initial tear length, has an undeniable impact on the stability of the dissecting aneurysm. Moreover, our results indicated that the stability of the dissecting aneurysm is very sensitive to the intraluminal false lumen pressure. A relative pressure increase of 10% in the false lumen may induce an excessive aneurysmal degeneration in patients with cTBAD.

Future work is threefold. The first one is coupling the present dissection model with tear propagation models, for applications to more reliable patient-specific simulations. The second one is to account for a more accurate configuration of opening tears while considering the potential dynamic effects of the blood flow inside the dissected arteries. The third one is to perform a more thorough and extensive investigation of mechanobiological parameters that may influence aneurysmal dilatation after cTBAD.

References

1. Erbel, R., et al. (2014). 2014 ESC guidelines on the diagnosis and treatment of aortic diseases: Document covering acute and chronic aortic diseases of the thoracic and abdominal aorta of the adult the task force for the diagnosis and treatment of aortic diseases of the European Society of Cardiology (ESC). *European Heart Journal, 35*(41), 2873–2926.
2. Elefteriades, J. A., et al. (1999). Management of descending aortic dissection. *Annals of Thoracic Surgery, 67*(6), 2002–2005.
3. Hagan, P. G., et al. (2000). The International Registry of Acute Aortic Dissection (IRAD): New insights into an old disease. *JAMA, 283*(7), 897–903.
4. Peterss, S., et al. (2016). Changing pathology of the thoracic aorta from acute to chronic dissection: Literature review and insights. *Journal of the American College of Cardiology, 68*(10), 1054–1065.
5. Masuda, Y., et al. (1991). Prognosis of patients with medically treated aortic dissections. *Circulation, 84*(5 Suppl), III7–13.
6. Juvonen, T., et al. (1999). Risk factors for rupture of chronic type B dissections. *Journal of Thoracic and Cardiovascular Surgery, 117*(4), 776–786.
7. Onitsuka, S., et al. (2004). Long-term outcome and prognostic predictors of medically treated acute type B aortic dissections. *Annals of Thoracic Surgery, 78*(4), 1268–1273.
8. Sueyoshi, E., et al. (2004). Growth rate of aortic diameter in patients with type B aortic dissection during the chronic phase. *Circulation, 110*(11_suppl_1), II-256.
9. Tsai, T. T., et al. (2008). Tear size and location impacts false lumen pressure in an ex vivo model of chronic type B aortic dissection. *Journal of Vascular Surgery, 47*(4), 844–851.
10. Trimarchi, S., et al. (2014). Predicting aortic enlargement in type B aortic dissection. *Annals of Cardiothoracic Surgery, 3*(3), 285.
11. Holzapfel, G. A., Gasser, T. C., & Ogden, R. W. (2000). A new constitutive framework for arterial wall mechanics and a comparative study of material models. *Journal of Elasticity, 61*(1), 1–48.
12. Humphrey, J. D., & Holzapfel, G. A. (2012). Mechanics, mechanobiology, and modeling of human abdominal aorta and aneurysms. *Journal of Biomechanics, 45*(5), 805–814.
13. Cyron, C. J., Aydin, R. C., & Humphrey, J. D. (2016). A homogenized constrained mixture (and mechanical analog) model for growth and remodeling of soft tissue. *Biomechanics and Modeling in Mechanobiology, 15*(6), 1389–1403.
14. Cyron, C. J., & Humphrey, J. D. (2017). Growth and remodeling of load-bearing biological soft tissues. *Meccanica, 52*(3), 645–664.
15. Braeu, F. A., et al. (2017). Homogenized constrained mixture models for anisotropic volumetric growth and remodeling. *Biomechanics and Modeling in Mechanobiology, 16*(3), 889–906.
16. Mousavi, S. J., Farzaneh, S., & Avril, S. (2019). Patient-specific predictions of aneurysm growth and remodeling in the ascending thoracic aorta using the homogenized constrained mixture model. *Biomechanics and Modeling in Mechanobiology, 18*(6), 1895–1913.
17. Laubrie, J. D., Mousavi, J. S., & Avril, S. (2020). A new finite-element shell model for arterial growth and remodeling after stent implantation. *International Journal for Numerical Methods in Biomedical Engineering, 36*(1), e3282.
18. Poya, R., Gil, A. J., & Ortigosa, R. (2017). A high performance data parallel tensor contraction framework: Application to coupled electro-mechanics. *Computer Physics Communications, 216*, 35–52.
19. Poya, R., et al. (2018). A curvilinear high order finite element framework for electromechanics: From linearised electro-elasticity to massively deformable dielectric elastomers. *Computer Methods in Applied Mechanics and Engineering, 329*, 75–117.
20. https://github.com/szhang-cis/Kuru_Mac.git
21. Humphrey, J. D., & Rajagopal, K. R. (2002). A constrained mixture model for growth and remodeling of soft tissues. *Mathematical Models and Methods in Applied Sciences, 12*(03), 407–430.

22. Rodriguez, E. K., Hoger, A., & McCulloch, A. D. (1994). Stress-dependent finite growth in soft elastic tissues. *Journal of Biomechanics, 27*(4), 455–467.
23. Cyron, C. J., & Humphrey, J. D. (2014). Vascular homeostasis and the concept of mechanobiological stability. *International Journal of Engineering Science, 85*, 203–223.
24. Cardamone, L., et al. (2009). Origin of axial prestretch and residual stress in arteries. *Biomechanics and Modeling in Mechanobiology, 8*(6), 431–446.
25. Holzapfel, G. A. (2002). Nonlinear solid mechanics: A continuum approach for engineering science. *Meccanica, 37*(4), 489–490.
26. Riveros, F., et al. (2013). A pull-back algorithm to determine the unloaded vascular geometry in anisotropic hyperelastic AAA passive mechanics. *Annual Review of Biomedical Engineering, 41*(4), 694–708.
27. Mousavi, S. J., & Avril, S. (2017). Patient-specific stress analyses in the ascending thoracic aorta using a finite-element implementation of the constrained mixture theory. *Biomechanics and Modeling in Mechanobiology, 16*(5), 1765–1777.
28. Laubrie, J. D., Mousavi, S. J., & Avril, S. (2022). About prestretch in homogenized constrained mixture models simulating growth and remodeling in patient-specific aortic geometries. *Biomechanics and Modeling in Mechanobiology*. https://doi.org/10.1007/s10237-021-01544-3
29. Zadrazil, I., et al. (2020). A combined experimental and computational study of the flow characteristics in a type B aortic dissection: Effect of primary and secondary tear size. *Chemical Engineering Research and Design, 160*, 240–253.
30. Vogt, B. A., et al. (1999). Aortic dissection in young patients with chronic hypertension. *American Journal of Kidney Diseases, 33*(2), 374–378.
31. Marlevi, D., et al. (2021). False lumen pressure estimation in type B aortic dissection using 4D flow cardiovascular magnetic resonance: Comparisons with aortic growth. *Journal of Cardiovascular Magnetic Resonance, 23*(1), 1–13.
32. Parsa, C. J., et al. (2010). Midterm results for endovascular repair of complicated acute and chronic type B aortic dissection. *Annals of Thoracic Surgery, 89*(1), 97–104.
33. Parsa, C. J., et al. (2011). Midterm results with thoracic endovascular aortic repair for chronic type B aortic dissection with associated aneurysm. *Journal of Thoracic and Cardiovascular Surgery, 141*, 322–327.
34. Ungvari, Z., et al. (2010). Mechanisms of vascular aging: New perspectives. *Journals of Gerontology Series A Biological Sciences and Medical Sciences, 65*(10), 1028–1041.
35. Gasser, T. C., & Holzapfel, G. A. (2006). Modeling the propagation of arterial dissection. *European Journal of Mechanics; A/Solids, 25*(4), 617–633.
36. Ferrara, A., & Pandolfi, A. N. N. A. (2010). A numerical study of arterial media dissection processes. *International Journal of Fracture, 166*(1), 21–33.
37. Wang, L., et al. (2017). Propagation of dissection in a residually-stressed artery model. *Biomechanics and Modeling in Mechanobiology, 16*(1), 139–149.
38. Wang, L., et al. (2018). Modelling peeling-and pressure-driven propagation of arterial dissection. *Journal of Engineering Mathematics, 109*(1), 227–238.
39. Tsai, T. T., et al. (2007). Partial thrombosis of the false lumen in patients with acute type B aortic dissection. *New England Journal of Medicine, 357*(4), 349–359.
40. Trimarchi, S., et al. (2013). Importance of false lumen thrombosis in type B aortic dissection prognosis. *Journal of Thoracic and Cardiovascular Surgery, 145*(3), s208–s212.
41. Kim, J., et al. (2013). Influence of surrounding tissues on biomechanics of aortic wall. *International Journal of Experimental and Computational Biomechanics, 2*(2), 105–117.
42. Kwon, S. T., et al. (2015). Interaction of expanding abdominal aortic aneurysm with surrounding tissue: Retrospective CT image studies. *Journal of Natural Sciences, 1*(8), e150.
43. Karmonik, C., et al. (2012). Longitudinal computational fluid dynamics study of aneurysmal dilatation in a chronic DeBakey type III aortic dissection. *Journal of Vascular Surgery, 56*(1), 260–263.

Characterizing the Biomechanics of an Endovascular Intervention in Cerebral Aneurysms Using Kirchhoff–Love Shells of Nonuniform Thickness

Nicolás Muzi, Francesco Camussoni, Luis G. Moyano, and Daniel Millán

Abstract Rupture of intracranial aneurysms is the most common cause of spontaneous subarachnoid bleeding, related to high morbidity and mortality rates. However, intracranial aneurysms have a higher prevalence than that due to their spontaneous rupture rate, exacerbated by the risks associated with occlusion intervention, which motivates the development of technological tools to support clinical diagnosis and endovascular occlusion intervention planning. In particular, the aneurysm dome is sensitive to applied loads in the contiguous surroundings to the aneurysm neck. Indeed, this region shows high complexity due to the arterial wall nature of the pathology. This work presents preliminary statistical analysis results of a thin shell model, with varying material and geometrical parameters, under a localized load emulating the effect of a microcatheter pressing the neck area. In a selection of 34 cases, we show that dimensionality reduction techniques such as Isomap can help determine non-trivial regions of interest under concentrated loads, leading to more general machine learning classification models for sensitive area identification.

Keywords Endovascular planning · Computational biomechanics · Forward jump · Dimensionality reduction

N. Muzi · L. G. Moyano · D. Millán (✉)
Consejo Nacional de Investigaciones Científicas y Técnicas (CONICET), C1425FQB CABA, Argentina
e-mail: dmillan@fcai.uncu.edu.ar

N. Muzi · D. Millán
Facultad de Ciencias Aplicadas a la Industria, Universidad Nacional de Cuyo, 5600 San Rafael, Mendoza, Argentina

F. Camussoni · L. G. Moyano
Grupo de Física Estadística e Interdisciplinaria, Centro Atómico Bariloche, Comisión Nacional de Energía Atómica, 8400 San Carlos de Bariloche, Río Negro, Argentina

Instituto Balseiro - Universidad Nacional de Cuyo, 8400 San Carlos de Bariloche, Río Negro, Argentina

P. M. F. Nielsen et al. (eds.), *Computational Biomechanics for Medicine*,
https://doi.org/10.1007/978-3-031-09327-2_3

1 Introduction

When an unruptured intracranial aneurysm (UIA) is diagnosed, the most common response is its treatment. However, endovascular treatment and microsurgical intervention show a non-negligible morbidity (5–7%) and mortality (1–2%) risk [1]. Indeed, UIAs are relatively common, with an estimated prevalence of up to 6% [2, 3] and, given that many of them never break (only 1/3 in a life-long follow-up cohort [1]), physicians frequently find themselves in the dichotomy of treating them or not [4].

External forces applied by instruments near the aneurysm neck can alter the structural stability during the endovascular intervention. Increased tension on the microcatheter during the intervention may lead to a sudden "forward jump" [5]. The uncontrolled advancement of the microcatheter can lead to complications in the embolization procedure such as rupture of the parent artery, intimal injury and procedure-related thromboembolic complications [6], or perforation of the aneurysm dome, which is a more devastating effect than perforation by a coil [7, 8]. Furthermore, the endovascular treatment challenges the physicians between occlusion success and intervention time. The study of this issue is challenging due to the need to model the arterial wall's biomechanics, which offers a complex multi-layered structure of composite materials, each with different mechanical behavior [9, 10]. Furthermore, the aneurysm wall exhibits several differences to the healthy parent vessel at the dome and the transition region on the aneurysm neck. The wall gets thinner and presents an irregular thickness, loses its layered organization, and becomes stiffer [11–14].

However, some publications show impressive technical achievements in modeling the biomechanics of aneurysms and blood vessels, for instance, considering incompressible nonlinear material models such as Mooney-Rivlin solid multi-layered materials or incorporating fiber orientations [15, 16]. Unfortunately, these works consider either simple theoretical geometries (dome = sphere, vessel = cylinder) or a low number of cases (1–2). Nowadays, the lack of a systematic study in a statistically relevant population is noteworthy due to the model's high-resource demand, the difficulties of specifying a broad set of parameters to perform patient-specific simulations, or both.

On the road towards developing a plausible analysis capable of dealing with a number of statistically meaningful cases, we describe the deformation kinematics using a geometrically nonlinear thin shell model under Kirchhoff–Love's assumptions in conjunction with a simpler Saint–Venant's hyperelastic material model. Though it cannot assess the artery's complexity, it allows us to exercise the application of a localized load in multiple sites for a given aneurysm model. We apply such workflow to several real aneurysm models of the AneuriskWeb database (Sect. 2.1). Also, as proof of concept, we consider a larger thickness in the artery relative to the aneurysm dome, as well as different Young's modulus in both regions to mimic the nonuniformity of the real problem. Given the uncertainty and heterogeneity of material parameters reported in the literature, we considered values from works

with similar approaches [17–20]. The lack of reliable parameters hampers the use of material models that take into account the anisotropic behavior of the aneurysm and the blood vessel in patient-specific three-dimensional models. Nevertheless, the proposed approach can help determine non-trivial zones of interest when a significant number of cases is under study. In summary, the structural stability of the aneurysm could be sensitive to a localized load in the parent vessel close to the neck, a possible situation during the endovascular intervention. Our ultimate goal is to enhance endovascular treatment planning by studying the mechanical behavior of the aneurysm-vessel structure under different combinations of reported wall thickness and concentrated load location.

The present work is organized as follows. Section 2 describes the database used for this study, the nonlinear thin shell model and its numerical implementation. Section 3 explains the treatment of the geometrical models acquired from the database, to obtain the meshes for the simulation. In Sect. 4, we analyze the results of experiments across several cases. We show that dimensionality reduction techniques can help determine non-trivial areas of interest for a selection of case studies. Finally, we collect some conclusions in Sect. 5.

2 Materials and Methods

2.1 AneuriskWeb Database

The database used as starting point is a compilation of aneurysm medical images and associated data retrieved from the Aneurisk project between 2005 and 2008, funded by SIEMENS Medical Solutions in collaboration with several medical institutions, and carried out by the Laboratory for Modeling and Scientific Computing (MOX), Department of Mathematics at Politecnico di Milano [21].

The database contains 103 geometrical models (triangular meshes) of intracranial aneurysms of 99 different patients, retrieved from 3D rotational angiograms (23 available in the database) with an isotropic spatial resolution of 0.3 mm ($256 \times 256 \times 256$) and segmented through a semi-automated process validated by an expert. These cases also include the ostium (polygon describing the neck), the parent vessel's centerlines and some geometrical parameters of the aneurysms such as location, classification (lateral or terminal), and rupture status (Fig. 1). We examined the 46 cases located in the internal carotid artery (ICA). From these cases, we discarded those presenting fusiform aneurysms or saccular aneurysms with two or more domes, resulting in 40 final subjects.

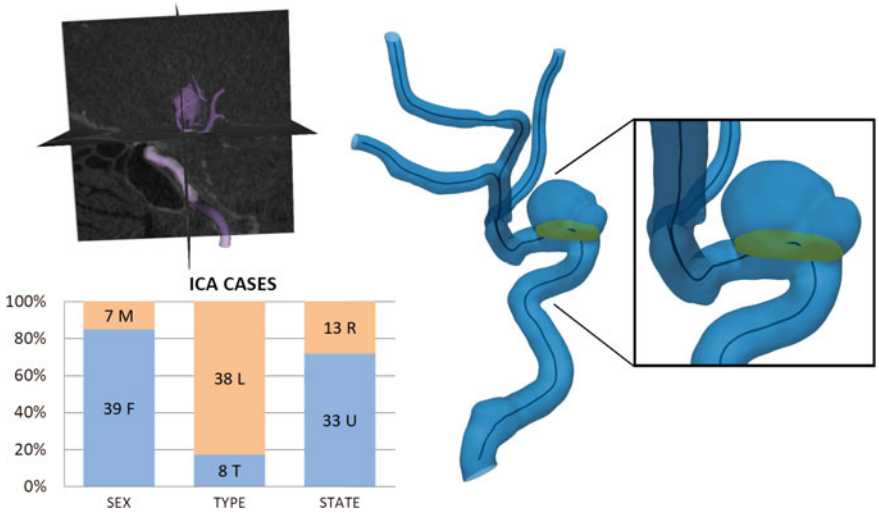

Fig. 1 Left: Stacked barplot showing three characteristic variables in the Aneurisk database, (only ICA cases): *Sex*: M: masculine, F: feminine; *Type*: L: lateral, T: terminal; *State*: R: ruptured, U: unruptured. Right: Geometrical model describing the lumen, centerlines, and the ostium (in green)

2.2 Geometrically Nonlinear Thin Shells Elastic Model

In this section, we concisely describe the mechanics of thin shells, based on a geometrically exact formulation [22]. We restrict our attention to the Kirchhoff–Love theory of shells, i.e. we neglect the shearing and stretching deformation normal to the shell mid-surface. In this theory, the shell director remains normal to the mid-surface during the deformation, see [23] and references therein.

We assume that this body can be described by the pair $(\boldsymbol{\varphi}, \mathbf{t})$, where the mapping $\boldsymbol{\varphi}$ defines the middle surface Ω of the shell, and $\mathbf{t}$ is a field of unitary vectors (director field). We assume a varying thickness h, and also that the change in shell thickness after the deformation is negligible. The subscript 0 indicates quantities in the reference configuration; for example, $\boldsymbol{\varphi}_0$ parametrizes the reference middle surface. We follow the usual convention for Latin and Greek indices (i.e. $i = 1, 2, 3; \alpha = 1, 2$), a comma denotes partial differentiation, subscripts refer to covariant components, and superscripts denote contravariant components.

The thin shell body $\mathscr{S}$ is given by

$$\mathscr{S} = \left\{ \boldsymbol{\Phi} \subset \mathbb{R}^3 | \boldsymbol{\Phi} = \boldsymbol{\varphi}(\xi^\alpha) + \xi \boldsymbol{t}(\xi^\alpha), -\frac{\mathrm{h}(\xi^\alpha)}{2} \leq \xi \leq \frac{\mathrm{h}(\xi^\alpha)}{2}, (\xi^1, \xi^2) \in \mathscr{A} \right\}, \tag{1}$$

where $\mathscr{A} \subset \mathbb{R}^2$ is s the parametric space for the middle surface. Hence, we view a configuration $\boldsymbol{\Phi}$ as a mapping from a parametric domain $\mathscr{A} \times [-h/2, h/2]$ into

$\mathbb{R}^3$. The parametric domain is described by the coordinates $\{\xi^1, \xi^2, \xi^3\}$ (where we identify $\xi = \xi^3$), whose corresponding dual basis is $\{\boldsymbol{E}^i\}$. The area element of the deformed middle surface can be computed as $d\Omega = \overline{J} d\xi^1 d\xi^2$, where $\overline{J} = \|\boldsymbol{\varphi}_{,1} \times \boldsymbol{\varphi}_{,2}\|$, and the unit normal is $\boldsymbol{t} = (\boldsymbol{\varphi}_{,1} \times \boldsymbol{\varphi}_{,2})/\overline{J}$. The membrane strain tensor is defined as $\varepsilon_{\alpha\beta} = \frac{1}{2}\left(\boldsymbol{\varphi}_{,\alpha} \cdot \boldsymbol{\varphi}_{,\beta} - \boldsymbol{\varphi}_{0,\alpha} \cdot \boldsymbol{\varphi}_{0,\beta}\right)$ which measures changes in the in-plane metric tensor. The bending strain tensor, measuring changes in the second fundamental form, is given by $\rho_{\alpha\beta} = \boldsymbol{\varphi}_{,\alpha} \cdot \boldsymbol{t}_{,\beta} - \boldsymbol{\varphi}_{0,\alpha} \cdot \boldsymbol{t}_{0,\beta}$. Also, strain is expressed in terms of the kinematics of the middle surface. For an elastic lamina the potential energy is expressed exclusively in terms of the kinematics of the middle surface, that is the mapping $\boldsymbol{\varphi}$, and is written in the parametric space as

$$\prod_{\text{tot}}[\boldsymbol{\varphi}] = \prod_{\text{int}}[\boldsymbol{\varphi}] - \prod_{\text{ext}}[\boldsymbol{\varphi}] = \int_{\Omega_0} W(\boldsymbol{\varepsilon}, \boldsymbol{\rho}) d\Omega_0 + \int_{\Omega_0} \boldsymbol{q} \cdot (\boldsymbol{\varphi} - \boldsymbol{\varphi}_0) d\Omega_0, \tag{2}$$

where W is the strain energy density per surface unit, Ω_0 is the reference middle surface of the shell, and $\boldsymbol{q}$ is the external body load per unit area. Here we consider an isotropic Kirchhoff-St. Venant model as the elastic material model.

2.3 Localized Force

The effect of a localized force is modeled by a plateau function, which decays as a function of the geodesic distance on the middle surface reference configuration to the application point. This function is given as

$$\widehat{q}(r) = \frac{\widehat{\mathrm{C}}}{2\pi\sigma^2} \frac{\exp\left[-\frac{1}{4}\left(\frac{\mathrm{r}}{\sigma}\right)^4\right]}{1 + \exp\left[-\frac{1}{4}\left(\frac{\mathrm{r}}{\sigma}\right)^4\right]}, \tag{3}$$

where r is the radial distance, σ is a given parameter that controls the function width and $\widehat{C}$ is a constant computed such that the integral of $\widehat{q}(r)$ equals one.

2.4 Numerical Implementation

To compute the total energy, second order derivatives for the deformations of the shell $\boldsymbol{\varphi}$ are required, needing an approximation with C^1 continuity in order to use a straightforward Galerkin discretization approach. To this end, we use subdivision surfaces finite elements [24] to approximate. A Lagrangian approach was followed, with the same space of basis functions for both the deformed and the reference

configurations. Being $\boldsymbol{\varphi}_0$ the mapping of the reference configuration

$$\boldsymbol{\varphi}_{0h}\left(\xi^1, \xi^2\right) = \sum_{a=1}^{N} B_a(\xi^1, \xi^2)\boldsymbol{\varphi}_{0a}, \tag{4}$$

where $B_a\left(\xi^1, \xi^2\right)$ are subdivision surfaces basic functions, N the number of nodes in the mesh, and $\boldsymbol{\varphi}_{0a}$ the position in the tridimensional space of the a-th control point defining the middle surface of the undeformed shell.

It is noteworthy that it is possible to make use of a prescribed shell thickness, discretized as follows

$$h_h\left(\xi^1, \xi^2\right) = \sum_{a=1}^{N} B_a\left(\xi^1, \xi^2\right)h_a, \tag{5}$$

where h_a represents predefined values of the shell thickness at the reference nodes. It is known that at the aneurysm neck, the thickness decreases dramatically. Nevertheless, this transition hasn't been defined yet with certainty [13, 25]. We will assume that the thickness of the shell varies according to the arctangent of the geodesic distance on the aneurysm from the node to the neck curve. The function used to assign a thickness value for each node is

$$h_a = \frac{(h_v - h_d)}{\pi}\left(\arctan\left(\frac{d_{Ga}}{w}\right) + \frac{\pi}{2}\right) + h_d, \tag{6}$$

where h_v and h_d are the thickness in the blood vessel and the dome (from reported values), w is the width of the transition zone, and d_{Ga} the value of the geodesic distance between the a-th node and the curve defining the aneurysm neck. This geodesic distance is calculated by the CGAL library [26]. We provide further information about this in Sect. 3.

When using the load function given by Eq. (3) for a curved surface the distance r is replaced by the geodesic distance d_{Ga}, while the load is $\boldsymbol{q} = Q\widehat{q}(d_G)\boldsymbol{t}_0$, where Q is the load value, whereas $\sigma = 0.25$ mm, and $\widehat{C}$ is computed such that the integral of $\widehat{q}(d_G)$ on the middle surface Ω_0 equals to one. The "effective load" has a diameter between 0.5 mm and 0.8 mm, see Fig. 2 (right), emulating the diameter of commercial microcatheters. For the experiments, we considered $h_v = 200$ μm and $h_d = 50$ μm, similar values to other shell-based models with uniform thickness [19, 20]. Young's modulus of the healthy cerebral artery is $E_v = 2$ N/mm^2 [27, 28], whereas at the dome is $E_d = 4$ N/mm^2 [29, 30], and a Poisson parameter of 0.49. Based on [31] we set the load value as 100 mmHg, a reasonable value considering the reported material parameters.

The total energy function is expressed in terms of the nodal variables $\boldsymbol{\varphi}_a$, $a = 1, 2, \ldots, N$, which is minimized with respect to the degrees of freedom given by

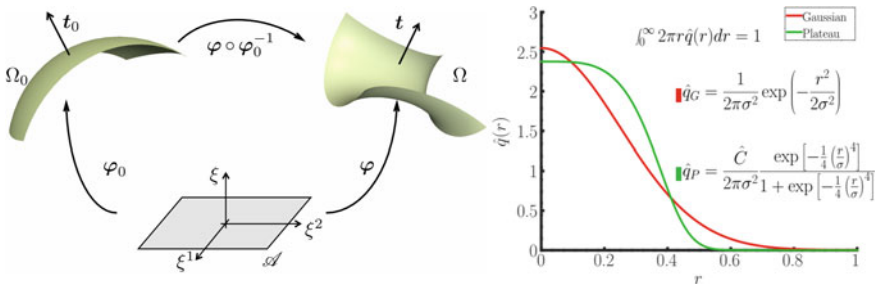

Fig. 2 Left: Sketch depicting the mappings $\boldsymbol{\varphi}_0$ and $\boldsymbol{\varphi}$ defining the middle reference and deformed surfaces Ω_0 and Ω of the shell, $\mathbf{t}_0$ and $\mathbf{t}$ are fields of normal vectors. Finally, $\mathscr{A} \subset R^2$ is the parametric space parametric domain is described by the coordinates $\{\xi^1, \xi^2, \xi\}$. Right: Gaussian (red) and *plateau* (green) load functions in polar coordinates

the deformation using the Newton–Raphson method, combined with a linear search method [23]. This is repeated until a convergence criterion is reached, following which the next load site is selected and the whole process is repeated.

3 Surfaces Mesh Treatment

Our study focuses on the region surrounding the aneurysm neck. As shown in Fig. 1, models acquired from the database have a mesh describing the blood vessel tree containing the aneurysm and there is poor mesh quality in regions with high curvature. To perform efficient numerical simulations, a pre-process was needed to obtain the final meshes, as described in Fig. 3, left. For this purpose, we developed a C++ computational framework that enables us to combine VTK (Visualization Toolkit

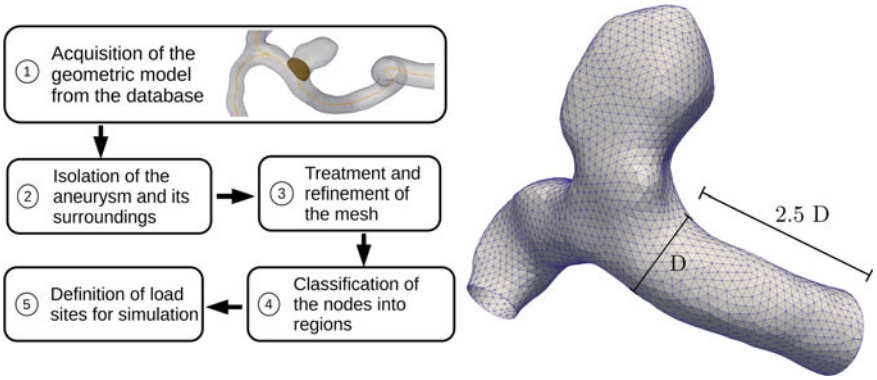

Fig. 3 Left: Mesh processing steps. Right: Example of an isolated mode (case C0005)

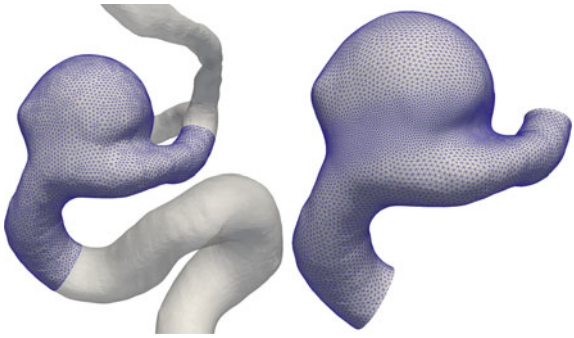

Fig. 4 Case C0034 remeshing. Left: original isolated model. Right: remeshed model, with refined neck

[32]) and CGAL libraries for mesh processing. From 40 initial cases 34 final meshes were obtained, as 6 cases presented issues at some step of the process.

As a first step, we isolated each aneurysm dome from its parent vessel by cutting at a certain distance from the neck, discarding the rest of the artery. The procedure is carried out in a semi-automated fashion, such that the user defines the distance as a multiple of the vessel's inner diameter on each side of the neck (Fig. 3, right). Here we set up the isolation distance to be 2.5 times the vessel diameter, based on analyzing the problem's behavior to different lengths. Higher values (>3 times the diameter) presented more stability but caused a flexion effect on the model and an excessive dome movement, when deformations should be localized and the aneurysm dome relatively still due to the surrounding tissue. This isolation algorithm successfully performed ~89% of the overall cuts, while the rest had to be executed manually.

After the isolation we applied a remeshing step [26], maintaining the original element edge size of 0.25 mm. Due to the impact of the neck in steps 4 and 5, (Fig. 3, left), we refined the neck area through the isotropic remeshing algorithm from CGAL's library [26]. We apply a final iteration of the Loop's subdivision surface scheme, see Fig. 4, right, generating edges of 0.0625 mm in length for the refined region around the neck and 0.125 mm for the rest of the model.

We needed to distinguish between dome and artery nodes in order to consider different material properties for each region. To this end, we developed an algorithm that finds the relative position on the surface of each node to the plane defined by the neck curve and assigns a tag correspondingly. In this step, we also used algorithms described in the section "*Triangulated Surface Mesh Shortest Paths*" of CGAL library [26], which computes geodesic paths on a triangulated surface mesh, finding the shortest distance between a node on the mesh and another node or set of nodes, retrieving the length of the resulting path. This way, we calculated the geodesic distance between each node and the curve that defines the neck (Fig. 5, left) and assigned it a positive sign if the node was located on the aneurysm or a negative sign if it was on the dome (Fig. 5, center).

The final step consisted of the definition of a region surrounding the artery in the neck area. This loading zone was defined similarly to the isolation step, but at a distance of 1 time the vessel's inner diameter (Fig. 3, right). In this region we

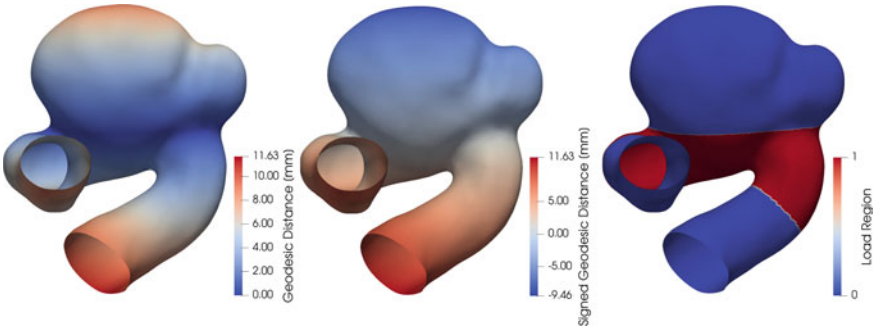

Fig. 5 Example of the associated fields to the geometric models. Left: Geodesic distance to the neck curve. Center: Signed geodesic distance. Right: Load region surrounding the neck

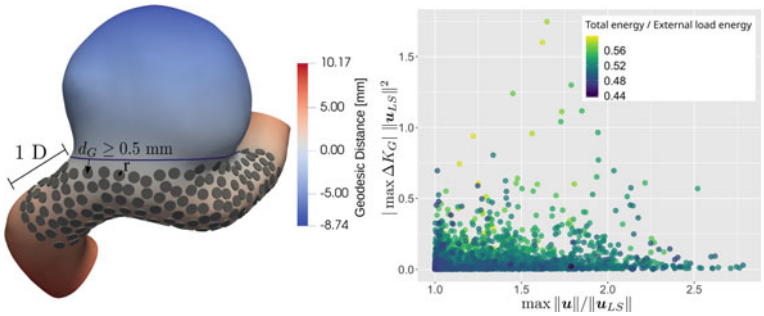

Fig. 6 Left: Case C0034, detail of load sites including parameters that determine their designation ($r = 0.25$ mm, for visualization). Right: Relationship between normalized maximum displacement and normalized maximum Gaussian curvature difference, for every load site of all 34 cases, and artery thickness equal to 200 μm, where color corresponds to normalized total energy

considered a distribution of load points or sites (Fig. 6, left). They were selected so as the minimum distance between them is 0.5 mm, keeping the density as regular as possible. In Fig. 6 we depict these sites as discs of 0.25 mm radius, for an easier visual inspection. The applied load corresponds to the function described in Sect. 2.3.

4 Experiments and Results

We conducted experiments with the long-term objective of determining which areas of an aneurysm have a higher sensitivity to localized loads and could lead to rupture. For this, we focused on establishing which biomechanical variables are involved in large perturbations of an aneurysm when pressure is applied. To achieve statistically meaningful results, all 34 ICA cases were considered. The meshes were treated as

explained in Sect. 3 obtaining, for each case, a final mesh with an associated thickness field for each node, and a distribution of load sites on the selected zone ("vest") (see Fig. 6, left), each of which are used to simulate the effect of a tool pressing in that position during an intervention. Thus, for each load site, an independent numerical experiment was performed. For the final state of the deformed mesh, a number of biomechanical observables were measured at three Gauss points inside the mesh triangles, determining the biomechanical model. These observables include displacement magnitudes, differences between the Gaussian curvature at the reference and deformed configurations of the Gauss points, as well as total, membrane and bending energies, among other variables. Given the large amount of data associated with any single load site, we summarised each variable by only keeping its maximum, minimum, and average values.

It is instructive to see the relationship between these summary metrics across all 34 selected cases. In Fig. 6 (right) we show the maximum displacement magnitude and the maximum Gaussian curvature difference between the reference and deformed configurations for all load points. The values of the former are normalized by the displacement magnitude of the load site and the latter by the square of the same magnitude. One can see that the relationship among the biomechanical variables is highly nonlinear and complex in character. To simplify the analysis, we applied a nonlinear dimensionality reduction algorithm to these variables. We selected Isomap [33], a well-established isometric feature mapping known for its ability to capture nonlinear embeddings. For each aneurysm case and for each load point in that case, we computed an embedding considering N neighbors and all continuous biomechanical variables defined in the model. The embedding's intrinsic dimension d was selected by studying the correlation dimension and the reconstruction error, finding an optimal intrinsic dimension d between 3 or 4. We chose $d = 3$ (with a reconstruction error equal to 0.009) for better visualization.

To interpret our experiments, we first focus on one case (C0034), characterized by 6779 load sites. In Fig. 7 we plot each load site's dimensions defined by the three Isomap components (left panel), colored by the normalized maximum displacement. It is possible to see non-trivial structure in the three-dimensional figure, being especially meaningful the grouping of several load sites which stand out from the bulk, with higher values of component 2, as well as component 1, to a lesser extent. To understand why these load sites appear separately from the rest, we plot the same load sites in cartesian coordinates (Fig. 7, right), coloring each point in the same manner as the left panel, finding that most load sites in the small clusters in the embedding correspond to neighboring load sites near the neck of the aneurysm, forming a small area distinct from the rest of the wall. In the center panel, we show inset figures depicting the final deformed state of the aneurysm. We have selected three load points almost contiguous to each other in Euclidean space, but each belonging to the three different clusters visible in the embedding. The three cases differ in terms of the deformation in the dome, the most prominent one corresponding to a buckling effect (bottom), i.e. a strong deformation produced after a small increase in pressure. Our result suggests that Isomap may be able to identify areas associated with large-scale deformation after pressure. Although the correlation with buckling is also present

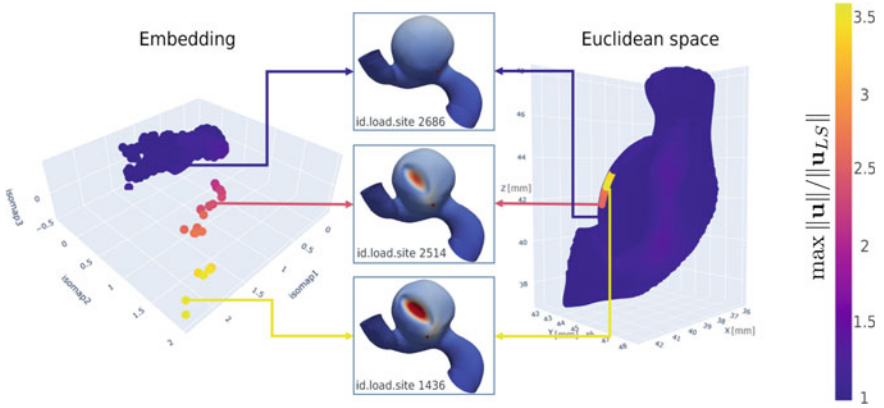

Fig. 7 Nonlinear dimensionality analysis for case C0034. Left: Isomap embedding dimensions for all load sites (N = 6779). Color refers to normalized maximum displacement. Right: Euclidean coordinates for all load sites. Center: final state after external load application for very near load sites (shown as a dot), with quite different results in terms of buckling effects. The color map represents the normalized maximum displacement associated to a given load site

in some biomechanical variables, such as the maximum curvature difference, the capacity to discriminate of these variables appears to be less straightforward than with Isomap.

Finally, we extended our dimensionality reduction analysis to four complete cases to explore the generality of the results found for case study C0034. Even though our final goal involves parsing all 34 ICA aneurysms, our preliminary results with four selected cases point to a broader applicability. In Fig. 8 we show Isomap components for all load sites belonging to cases C0090, C0034, C0014, and C0042, where we color by visually identifying presence (blue) or absence (orange) of buckling effects. The top left panel shows all Isomap components simultaneously, and the three remaining are its pairwise projections. The load sites group into two clusters with some overlap, indicating that this visualization method can be an efficient tool to classify aneurysm areas prone to large deformations related to instabilities in the aneurysm neck, and thus likely to be associated with complications during procedures. Isomap components appear as useful features to train machine learning classification models aiming at detecting areas more likely associated with buckling events. Even though a thorough study including all cases in a unique dimensionality reduction step remains open, we already see a discriminatory capability of our method, even though the embedded coordinates are drawn from separately reduced ensembles.

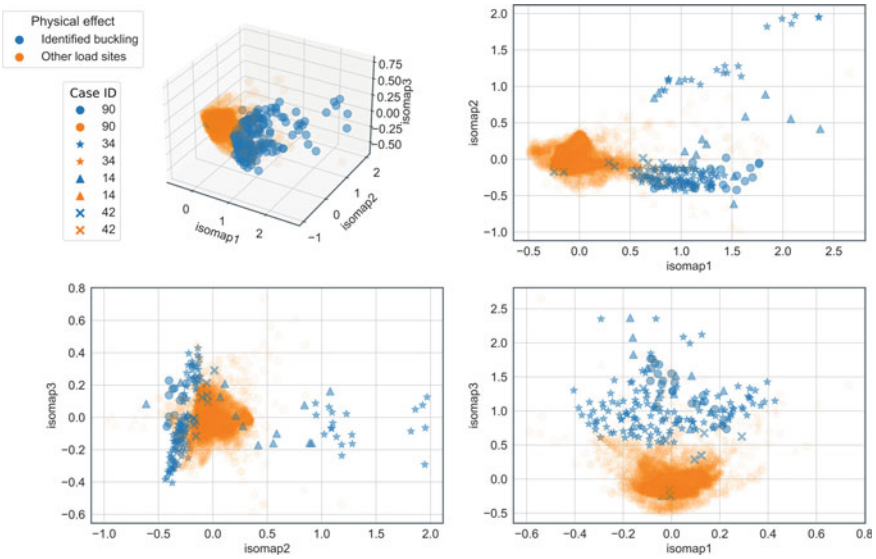

Fig. 8 Isomap components for all load sites for four selected ICA cases, colored by manual inspection of presence of buckling effects (blue) or not (orange). Top left, three-dimensional figure. Remaining panels: pairwise components projections. $N = 80$ for cases other than C0034

5 Conclusions and Future Directions

This work presents preliminary results of a thin shell model considering a smoothly-varying thickness and Young's modulus between the parent vessel and the aneurysm dome. We develop a user-assisted semi-automatic procedure to isolate and remesh the aneurysm dome and its neighboring connected parent vessels and perform simulations of the biomechanics of an endovascular intervention in a relatively large number of cases from the AneuriskWeb database. Additionally, we show that dimensionality reduction techniques can be used to visualize non-trivial areas of interest, and in particular may help avoiding sensitive load sites. In particular we find that, in the analyzed cases, the Isomap embeddings form clusters whose load sites correspond to distinct areas in the neck of the aneurysm that present extreme values in a combination of biomechanics variables. Moreover, many of the final states associated with these particular load sites show buckling effects. These areas could be associated with complications during an embolization procedure, and may possibly be related to rupture events.

In future work, we plan to improve the material model by considering a nonlinear Mooney-Rivlin incompressible material. Also, the effect of the surrounding media, which constrains natural displacements of the artery tree, will be taken into account. Finally, we envision a complete and deep study considering nonlinear dimensionality reduction techniques applied to the whole database in conjunction with morphometric descriptors, paving the path to a better intervention planning, finding "hot

spots" to avoid in the neck area which could be related to complications during the endovascular treatment, and possibly automating this analysis via machine learning classification models.

Acknowledgements This work was funded by the Investigation Projects PICTO-2016-0054 UNCuyo-ANPCyT, L028-2019 and M084-2019 SIIP UNCuyo, Argentina. We also thank Ezequiel Petra, MD. for his useful comments.

References

1. Lindgren, A. E., Koivisto, T., Björkman, J., & von und. (2016). Irregular shape of intracranial aneurysm indicates rupture risk irrespective of size in a population-based cohort. *Stroke, 47*(5), 1219–1226.
2. Wardlaw, J. M., & White, P. M. (2000). The detection and management of unruptured intracranial aneurysms. *Brain, 123*(2), 205–221.
3. Vlak, M. H. M., Algra, A., Brandenburg, R., & Rinkel, G. J. E. (2011). Prevalence of unruptured intracranial aneurysms, with emphasis on sex, age, comorbidity, country, and time period: A systematic review and meta-analysis. *Lancet Neurology, 10*(7), 626–636.
4. Van Rooij, W. J., & Sluzewski, M. (2006). Procedural morbidity and mortality of elective coil treatment of unruptured intracranial aneurysms. *American Journal of Neuroradiology, 27*(8), 1678–1680.
5. Orrù, E., Roccatagliata, L., Cester, G., Causin, F., & Castellan, L. (2013). Complications of endovascular treatment of cerebral aneurysms. *European Journal of Radiology, 82*(10), 1653–1658.
6. Lee, J. Y., Seo, J. H., Cho, Y. D., Kang, H. S., & Han, M. H. (2011). Endovascular treatment of wide-neck intracranial aneurysms using a microcatheter protective technique: Results and outcomes in 75 aneurysms. *American Journal of Neuroradiology, 32*(5), 917–922.
7. Pierot, L., & Wakhloo, A. K. (2013). Endovascular treatment of intracranial aneurysms: Current status. *Stroke, 44*(7), 2046–2054.
8. Cloft, H. J., & Kallmes, D. F. (2002). Cerebral aneurysm perforations complicating therapy with Guglielmi detachable coils: A meta-analysis. *American Journal of Neuroradiology, 23*(10), 1706–1709.
9. Robertson, A., & Watton, P. (2013). Mechanobiology of the arterial wall. In *Modeling of transport in biological media*(pp. 275–347). Elsevier.
10. Hoskins P., Lawford P., & Doyle B. (2017). *Cardiovascular biomechanics*. Springer International Publishing.
11. Humphrey, J., & Canham, P. (2000). Structure, mechanical properties, and mechanics of intracranial saccular aneurysms. *Journal of Elasticity, 61*(1–3), 49–81.
12. Savastano, L., Bhambri, A., Wilkinson, D., & Pandey, A. (2018). *Biology of cerebral aneurysm formation, growth, and rupture* (pp. 17–32). Elsevier.
13. Frösen, J. (2014). Smooth muscle cells and the formation, degeneration, and rupture of saccular intracranial aneurysm wall—A review of current pathophysiological knowledge. *Translational Stroke Research, 5*(3), 347–356.
14. Tulamo, R., Frösen, J., Hernesniemi, J., & Niemelä, M. (2018). Inflammatory changes in the aneurysm wall: A review. *Journal of Neurointerventional Surgery, 10*(Suppl 1), i58–i67.
15. Watton, P., Ventikos, Y., & Holzapfel, G. (2009). Modelling the growth and stabilization of cerebral aneurysms. *Mathematical Medicine and Biology, 26*(2), 133–164.
16. Selimovic, A., Ventikos, Y., & Watton, P. N. (2014). Modelling the evolution of cerebral aneurysms: Biomechanics, mechanobiology and multiscale modelling. *Procedia IUTAM, 10*, 396–409.

17. Bazilevs, Y., Hsu, M. C., Zhang, Y., Wang, W., Kvamsdal, T., Hentschel, S., & Isaksen, J. G. (2010). Computational vascular fluid–structure interaction: Methodology and application to cerebral aneurysms. *Biomechanics and Modeling in Mechanobiology, 9*(4), 481–498.
18. Isaksen, J. G., Bazilevs, Y., Kvamsdal, T., Zhang, Y., Kaspersen, J. H., Waterloo, K., Romner, B., & Ingebrigtsen, T. (2008). Determination of wall tension in cerebral artery aneurysms by numerical simulation. *Stroke, 39*(12), 3172–3178.
19. Zhou, X., Raghavan, M. L., Harbaugh, R. E., & Lu, J. (2010). Patient-specific wall stress analysis in cerebral aneurysms using inverse shell model. *Annals of Biomedical Engineering, 38*(2), 478–489.
20. Lu, J., Hu, S., & Raghavan, M. L. (2013). A shell-based inverse approach of stress analysis in intracranial aneurysms. *Annals of Biomedical Engineering, 41*(7), 1505–1515.
21. AneuriskWeb project website, http://ecm2.mathcs.emory.edu/aneuriskweb. Emory University, Department of Math & CS, 2012.
22. Simo, J., & Fox, D. (1989). On a stress resultant geometrically exact shell model. Part I: Formulation and optimal parametrization. *Computer Methods in Applied Mathematics, 72*, 267–304.
23. Millán, D., Rosolen, A., & Arroyo, M. (2013). Nonlinear manifold learning for meshfree finite deformation thin-shell analysis. *International Journal for Numerical Methods in Engineering, 93*(7), 685–713.
24. Cirak, F., & Long, Q. (2011). Subdivision shells with exact boundary control and non-manifold geometry. *International Journal for Numerical Methods in Engineering, 88*(9), 897–923.
25. Kadasi, L. M., Dent, W. C., & Malek, A. M. (2013). Cerebral aneurysm wall thickness analysis using intraoperative microscopy: Effect of size and gender on thin translucent regions. *Journal of Neurointerventional Surgery, 5*(3), 201–206.
26. CGAL, Computational Geometry Algorithms Library, https://www.cgal.org
27. Humphrey, J. D., & Canham, P. B. (2000). Structure, mechanical properties, and mechanics of intracranial saccular aneurysms. *Journal of Elasticity, 61*(1), 49–81.
28. Valencia, A., Contente, A., Ignat, M., Mura, J., Bravo, E., Rivera, R., & Sordo, J. (2015). Mechanical test of human cerebral aneurysm specimens obtained from surgical clipping. *Journal of Mechanics in Medicine and Biology, 15*(05), 1550075.
29. Scott, S., Ferguson, G. G., & Roach, M. R. (1972). Comparison of the elastic properties of human intracranial arteries and aneurysms. *Canadian Journal of Physiology and Pharmacology, 50*(4), 328–332.
30. Laurence, D. W., Homburg, H., Yan, F., Tang, Q., Fung, K. M., Bohnstedt, B. N., Holzapfel, G. A., & Lee, C. H. (2021). A pilot study on biaxial mechanical, collagen microstructural, and morphological characterizations of a resected human intracranial aneurysm tissue. *Scientific Reports, 11*(1), 1–15.
31. Závodszky, G., Csippa, B., Paál, G., & Szikora, I. (2020). A novel virtual flow diverter implantation method with realistic deployment mechanics and validated force response. *International Journal for Numerical Methods Biomedical Engineering, 36*(6), e3340.
32. Schroeder, W., Martin, K., & Lorensen, B. (2006). *The visualization toolkit*. Kitware.
33. Tenenbaum, J. B., De Silva, V., & Langford, J. C. (2000). A global geometric framework for nonlinear dimensionality reduction. *Science, 290*(5500), 2319–2323.

Imaging-Based Patient-Specific Biomechanical Evaluation of Atherosclerosis and Aneurysm: A Comparison Between Structural-Only, Fluid-Only and Fluid–Structure Interaction Analysis

Jessica Benitez Mendieta, Phani Kumari Paritala, Jiaqiu Wang, and Zhiyong Li

Abstract Cardiovascular diseases (CVD) are the leading cause of morbidity and mortality worldwide. Atherosclerosis is the dominating underlying cause of CVD, that occurs at susceptible locations such as coronary and carotid arteries. The progression of atherosclerosis is a gradual process and most of the time asymptomatic until a catastrophic event occurs. Similarly, an intracranial aneurysm is the bulging of the cerebral artery due to a weakened area of the vessel wall. The progression of the aneurysm could result in the rupture of the vessel wall leading to a subarachnoid haemorrhage. The formation and progression of atherosclerosis and aneurysm are closely linked to abnormal blood flow behaviour and mechanical forces acting on the vessel wall. Recent technologies in medical imaging, modeling, and computation are used to estimate critical parameters from patient-specific data. However, there is still a need to develop protocols that are reproducible and efficient. This article focuses on the methods for biomechanical analysis of the cerebral aneurysms and

All authors contributed equally to the manuscript

J. Benitez Mendieta · P. K. Paritala · J. Wang · Z. Li (✉)
School of Mechanical, Medical and Process Engineering, Queensland University of Technology (QUT), 2 George St., Brisbane, QLD 4000, Australia
e-mail: zhiyong.li@qut.edu.au

J. Benitez Mendieta
e-mail: j2.benitezmendieta@qut.edu.au

P. K. Paritala
e-mail: p.paritala@qut.edu.au

J. Wang
e-mail: jiaqiu.wang@qut.edu.au

Centre for Biomedical Technologies, Queensland University of Technology, Brisbane 4000, Australia

Z. Li
School of Biological Science and Medical Engineering, Southeast University, Nanjing 210096, China

P. M. F. Nielsen et al. (eds.), *Computational Biomechanics for Medicine*,
https://doi.org/10.1007/978-3-031-09327-2_4

atherosclerotic arteries including carotid & coronary. In this study, patient-specific 3D models were reconstructed from optical coherence imaging (OCT) for coronary and magnetic resonance imaging (MRI) for the carotid and cerebral arteries. The reconstructed models were used for computational fluid dynamics (CFD), structural-only, and fluid–structure interaction (FSI) simulations. The results of the FSI were compared against structural and CFD-only simulations to identify the most suitable method for each artery. The comparison between FSI and structural only simulations for the coronary artery showed similar mechanical stress values across the cardiac cycle with a maximum difference of 1.8%. However, the results for the carotid and cerebral arteries showed a maximum difference of 5% and 20% respectively. Additionally, with relation to the hemodynamic WSS calculated from FSI and CFD-only, the coronary artery presented a significant difference of 87%. Conversely, the results for the carotid and cerebral arteries showed a maximum difference of 9 and 6.4% at systole. Based on the results it can be concluded that the shape & location of the artery will influence the selection of the model that can be used for solving the numerical problem.

Keywords Cardiovascular diseases · Computational biomechanics · Fluid–structure interaction · Cerebral aneurysm · Carotid and coronary atherosclerosis · Wall shear stress · Principal stress

1 Introduction

Cardiovascular disease (CVD) is an abnormal condition of the arteries that occurs at regions of disturbed blood flow due to sudden directional flow changes. CVD affects cerebral, coronary, carotid, iliac, renal, and femoral arteries. From a mechanical point of view, blood vessels are exposed to multiple kinds of mechanical forces, which are exerted on the vascular wall (radial, circumferential, and longitudinal forces) or the endothelial surface (shear stress). The stresses and strains experienced by arteries influence the initiation and progression of vascular diseases such as atherosclerosis and intracranial aneurysms. These diseases result in catastrophic events such as stroke and myocardial infarction (MI), the leading causes of morbidity and mortality globally. CVD accounted for approximately 42,300 deaths and 591,000 hospitalisations in Australia in the year 2019 [3], and around 18.6 million deaths globally [45]. CVD also have an impact on health care expenditure, costing around $363.4 billion in the United States [45]. In this regard, we will be presenting methodologies and results of the patient-specific biomechanical analysis of diseased arteries including coronary, carotid (atherosclerotic plaque), and cerebral (aneurysm) in separate sections with a focus on standardized approach and numerical techniques that could enable clinical implementation in the future.

Atherosclerosis is a chronic inflammatory disease characterized by hardening or narrowing of the arteries [38] in which plaque builds up underneath the endothelium, resulting in the partial or complete occlusion of arteries such as coronary and carotid.

Plaque initiation, progression, and rupture are complex processes. Several factors like mechanical forces, plaque morphology, blood conditions, hypertension, living, and eating habits, influence the process [35]. Atherosclerotic plaque generally occurs at an arterial bend, characterized by flow separation and low shear stress [14]. This disease develops at an early age and remains silent for decades. In the progression of atherosclerosis, lipid-filled macrophages are the major component. They undergo chemical changes, and the atherosclerotic plaque will become a combination of lipids, calcification, neovascularization, and possible haemorrhage. The center of the plaque, due to the deprivation of oxygen, can further develop into a necrotic core [27]. Currently, luminal narrowing is used as a marker for high-risk plaques, however, this is not an accurate estimator of plaque size, as this measurement underestimates the atherosclerotic burden [1].

Plaque stenosis severity, combined with patient-specific risk factors, is still the primary evaluation method used as guidance for treatment decisions related to atherosclerosis. This approach leaves behind patients with moderate stenosis, and such plaques can also be vulnerable. On the other hand, patients with stable plaques and a low risk of rupture are sent to surgery, and the surgery itself has some associated risks. Hence, an additional tool to evaluate the vulnerability of atherosclerotic plaques is needed, such as biomechanical computational analysis using patient-specific data. In this way, more drastic clinical events can be reduced and lower the number of unnecessary surgeries.

Another type of CVD is the intracranial aneurysm, which is the abnormal dilation of the arteries that is fragile and could rupture due to a stretched and thin wall at the aneurysm. According to our current understanding, intracranial aneurysm formation is a gradual process influenced by genetic, environmental, and hemodynamic risk factors [18] resulting in vessel wall degeneration, contributing to the structural remodelling and aneurysm growth [40, 41]. Although the majority of aneurysms are small and are often asymptomatic [47], aneurysm rupture leads to subarachnoid haemorrhage resulting in significant morbidity and mortality [7]. Unruptured intracranial aneurysms (UIAs) develop over the life course remain unchanged for a long period before undergoing rapid growth and have an increased risk of rupture [15, 44]. Management of UIAs is currently based on risk stratification guidelines developed by large-scale clinical studies. These include PHASES (population, hypertension, age, size, earlier subarachnoid haemorrhage) score [22], UIATS (unruptured intracranial aneurysm treatment site) score [17], and the ELAPSS (earlier subarachnoid haemorrhage, location of aneurysm, age, population, size, and shape) score [4]. However, the accuracy of these scores is suboptimal due to the lack of considering quantitative factors and there is a need to develop additional tools to evaluate the risk of rupture.

Accurate information about plaque morphology and composition, aneurysm size/shape, and location in conjunction with the patient-specific flow conditions and risk factors are crucial to identify vulnerable plaques and aneurysms and the likelihood of their developing into cardiovascular events, such as stroke [39] and myocardial infarction. Non-invasive imaging modalities such as magnetic resonance imaging (MRI) and ultrasound (US) have been widely used in the characterization

of carotid plaques. Other imaging techniques such as Computed Tomography (CT) and molecular imaging have also been used to a lesser extent due to the linkage with ionizing radiation. OCT is a state-of-the-art imaging technology, it could provide cross-sectional imaging of tissue morphology with high resolution (1~15 μm could be achieved) and in real-time [16, 19, 34] for coronary arteries. In addition, the most used imaging modalities in the diagnosis, evaluation, and treatment of UIAs are, x-ray angiography, computed tomography angiography (CTA), and magnetic resonance angiography (MRA).

Vascular disease progression is associated with the biomechanical forces acting locally and the rupture is considered as a mechanical failure process. Therefore, biomechanics has the potential to evaluate plaque behaviour and predict its progression. For example, the morphological factors of a vulnerable plaque, such as a thin fibrous cap and large lipid core, will affect its mechanical behaviour, which in turn will be reflected by changes in biomechanical parameters. If a biomechanical parameter could be mapped to the current known clinical risk factors, it could be used as a biomechanical risk factor of plaque vulnerability. These biomechanical risk factors will give clinicians quantitative evidence to judge the plaque vulnerability, as an addition to the current imaging morphologies. Also, this has the potential ability to quantitatively predict the progression of the diseases, which is a supplement to current commonly used clinical risk factors.

Wall shear stress (WSS) and plaque structural stress (PSS) play a key role in the initiation and progression of atherosclerotic plaques. Hence, the evaluation of the biomechanical forces in specific geometries based on patient-specific medical imaging can give crucial insights into vulnerability. Computational analysis based on numerical methods such as the finite element method (FEM), finite volume method (FVM), finite difference method (FDM), Galerkin method, and spectral method, offer the possibility of evaluating these stresses (WSS and PSS) on specific artery geometries. The computational analysis combined with in-vivo medical imaging provides a less invasive and non-ionizing approach to identify the role of composition, morphology, and hemodynamic factors for understanding and treatment approach. In literature, various approaches such as computational fluid dynamics (CFD) [21, 31, 33, 48, 49], structural stress analysis [28–30, 37] (and fluid–structure interaction (FSI) [23, 26, 43, 46] are used to understand the vascular biomechanics. In addition, from the literature, it is understood that local flow dynamics contribute to the initiation, growth, and rupture of atherosclerotic plaques and cerebral aneurysms [2, 8, 9, 11, 13, 24, 25]. Therefore image-based patient-specific computational simulations are widely used to understand the relationship between flow parameters and anatomical variations [6, 13, 32, 42].

Even though multiple studies have explored the stresses exerted in the arteries due to blood flow, there is still a lack of understanding and standardization in analysing the stresses either by FSI or CFD simulation of the arteries. Therefore, this article focuses on comparing the FSI with CFD and structural simulations to understand if FSI is required or single physics can provide the same information with less computational expenses for certain models. It also presents a standard methodology for the

reconstruction, meshing, setup, simulation, and analysis process for carotid, coronary, and aneurysm models. Application of standard methodology and process will improve confidence in the results and enable the development of a unified approach for analysing the stresses in the arteries. This study will be a step forward towards clinical application and provide crucial insights into the differences between single-physics and multi-physics models and when they should be used for three different arteries with a specific cardiovascular disease.

2 Materials and Methods

2.1 Medical Imaging, Segmentation and 3D Reconstruction of Blood Vessels

2.1.1 Coronary Arteries

The coronary study was based on OCT and angiography imaging data acquired from the Catheterization Laboratory in The Prince Charles Hospital (Chermside, QLD, Australia). The QUT University Human Research Ethics Committee assessed this research as meeting the conditions for exemption from HREC review and approval in accordance with Sect. 5.1.22 of the National Statement on Ethical Conduct in Human Research (2007). In this study, a set of right coronary artery (RCA) imaging data from a 61-year-old male patient with acute coronary syndrome (ACS) was used. This study was approved by the internal review board and informed written consent was obtained.

The geometry for an FSI simulation contains both structure and fluid domains. From OCT the contours of the lumen and the plaque were obtained. As the intravascular-OCT is a catheter-based imaging modality, each contour must be stacked and aligned with the catheter path-line to form a 3D coronary model (Fig. 1). This required 3D baseline could be generated from the angiography data, which was used as guidance during the OCT operation. Two plane angiographic images from two different directions were selected to generate the 3D baseline of the coronary artery. The central line of the coronary artery in each angiography imaging was segmented in ImageJ (imagej.nih.gov/ij/), and outputted as a set of 2D discrete point coordinates. The coordinates from the two plane angiography data were imported into SolidWorks (Dassault Systèmes, Vélizy-Villacoublay, France). These coordinates were converted into splines in two different 2D planes and were projected to form a new spline in 3D space. Finally, the 3D spline was discretized into a set of registration points and their 3D coordinates were exported. The number of points was determined by the corresponding OCT slice number. The OCT images were recorded in the axial direction during the pullback of a catheter in the coronary artery. Each

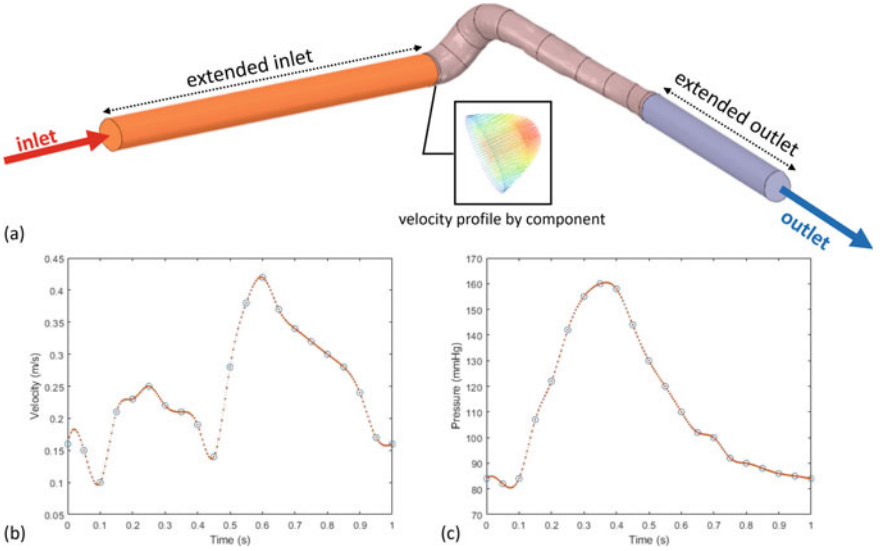

Fig. 1 **a** Coronary artery geometry with extended inlet and outlet, and the box emphasized the fully developed flow profile defined by the velocity given as inlet to the FSI simulation. **b** velocity profile prescribed at the inlet, and **c** pressure profile given to the outlet

slice provided a 2D view of the coronary lumen and vessel wall in the radial direction. In each slice, the contours of the lumen, the outer wall boundary, and plaque components were segmented by using ImageJ [46].

An in-house developed MATLAB (R2017a, MathWorks, Natick, MA, US) code package was used to register the 2D OCT contours onto the 3D angiographic baseline. The MATLAB code was designed to have several functional packages, which contains all the sub-steps in the registration processes. Because of the difference in the resolution of the OCT and angiography, the program firstly unified the scale of the point coordinates from OCT and angiography into millimetre unit. Then in each OCT slice, the centroid was defined as the midpoint on the perpendicular bisector of the longest line segment between two points on the lumen contour. Then each contour in each 2D OCT slice was moved to its position in 3D space by offsetting the centroid point onto the corresponding registration point on the 3D angiography baseline. Considering the tortuosity of coronary arteries, each OCT slice should be vertical against the local baseline curvature. A slope angle of each slice (from the normal vector of OCT slice plane to the local tangent vector of 3D baseline) was determined by calculating and applying a rotational matrix to each OCT slice. The transferred point coordinates were imported into the ANSYS SpaceClaim, a Geometry component in ANSYS Workbench (version 19.0, ANSYS, Canonsburg, PA, USA). Here the contours from each slice, including the coronary lumen, the outer boundary, and plaque component, were re-generated in a 3D space using the point coordinates. Then based on the contours, the surface of the coronary lumen,

outer wall, and plaque were created separately by blending each kind of contours. Finally, the geometric model of the coronary lumen, outer wall, and plaque were generated by solidifying their surfaces and performing a Boolean operation on the overlapped parts between the outer wall, lumen, and plaque. To save the computational consumption, the coronary model was cut off to only include the region of interest for the subsequent fluid–structure simulation. The length of the region of interest was approximately three times the length of the plaque.

2.1.2 Carotid Arteries

The study of the carotid atheroma was based on Magnetic Resonance Imaging (MRI), and was approved by the Human Research Ethics Committee at the Princess Alexandra Hospital (PAH) in Brisbane, Australia, and by the Queensland University of Technology's (QUT) Office of Research Ethics and Integrity (HREC/17/QPAH/181). The multi-contrast MR imaging study was performed on a Magnetom Prisma (Siemens Medical Solutions, Malvern, PA, USA) 3 T MR whole body system using a 64-channel head/neck coil. Four MRI contrast weighted imaging techniques were employed. The parameters used were T2-weighted (TR 4040 ms, TE 89 ms, resolution 456 × 384 × 40, FOV 213 × 180), proton density (PD) (TR 2720 ms, 29 ms, resolution 384 × 384 × 40, FOV 180 × 180), T1-weighted (TR 717 ms, 9.9 ms, resolution 320 × 320 × 40, FOV 180 × 180), and Time of Flight (TOF) (TR 21 ms, TE 3.11 ms, resolution 384 × 290 × 136, FOV 151 × 199). Additionally, 2D ECG-gated phase-contrast MRI (PC-MRI) images were acquired at three different locations (common carotid artery (CCA), maximum stenotic region, and internal carotid artery (ICA)). The scan parameters were TR 24.36 ms, TE 3.59 ms, resolution 240 × 240, FOV 111 × 111; velocity encoding (VENC) ranging from 60 $cm{\cdot}s^{-1}$ to 100 $cm{\cdot}s^{-1}$.

One patient with identified carotid stenosis (>90% based on Ultrasound (US) doppler) was scanned using MRI before carotid endarterectomy (CEA), and written consent was obtained before scanning. The patient-specific 3D geometry segmentation and reconstruction were developed using our previously established protocol [20, 33, 46]. In brief, T1 was employed to identify the plaque components focused on lipids, calcification, and arterial wall using Amira (version 6.0, FEI, Hillsboro, Oregon, USA). T2, PD, and TOF were utilised as supporting sequences for component identification. The mass flow rate was extracted from PC-MRI which also was employed in FSI analysis as an inlet at the CCA. The pressure applied to the internal region in the 3D structural-only analysis was calculated using the patient-specific pressure-arm scaled based on the mass flow rate profile. For FSI analysis this pressure was utilised as outlets at the ICA and ECA (Fig. 2). A mesh independent test was performed to identify the adequate element size for both methods, structural and fluid parts.

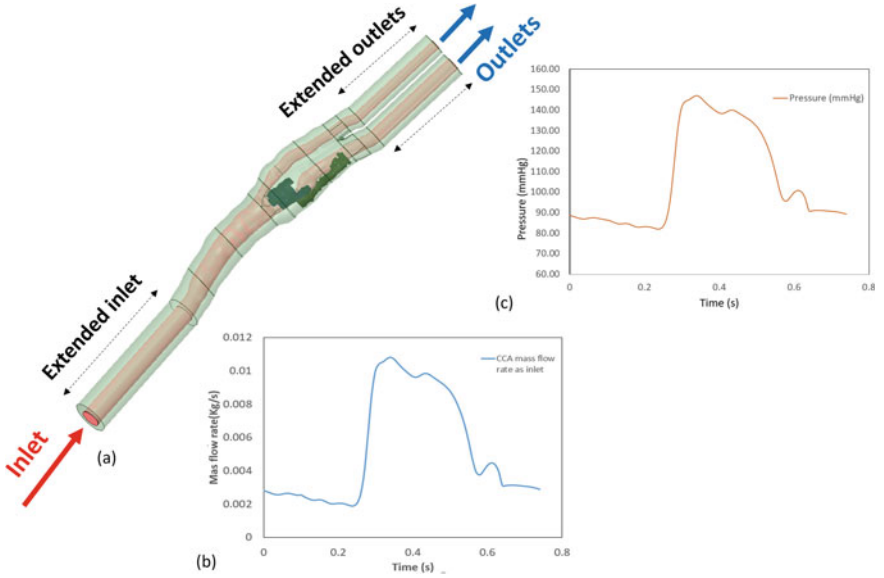

Fig. 2 **a** Carotid artery geometry including plaque components (lipids and calcification) with extended inlet and outlets. **b** Mass flow rate profile given at the inlet, **c** pressure profile given at the outlets.

2.1.3 Cerebral Arteries

For the study of a cerebral artery, the data from a patient with identified middle cerebral artery (MCA) aneurysm was employed. This study was approved by the ethics committee at Renji hospital (2017) no.093. The data included, Time of Flight (TOF) MRA and T1 scans for imaging the unruptured cerebral aneurysm. The parameters used were T1-weighted (TR 2.5 ms, TE 0.95 ms, resolution 315 × 96 × 360, FOV 308 × 352), and Time of Flight (TOF) (TR 1000 ms, TE 15 ms, resolution 320 × 320 × 240, FOV 320 × 320). The multi-contrast imaging study was performed on a Magnetom Prisma (Siemens Medical Solutions, Malvern, PA, USA) 7 T MR whole body system. TOF (MRA) and T1 of sequences were imported into an image processing software package, Amira. The region of interest corresponding to the MCA aneurysm was segmented using a thresholding technique for 3D reconstruction of the aneurysm lumen and the parent vessels. For the arterial wall, manual segmentation was performed to identify the non-uniform thickness of the wall (Fig. 3). The initial geometries created from Amira were smoothed using an open-source software Meshmixer 3.5 (2020 Autodesk, Inc) to improve the quality of the reconstruction by increasing the element density of the construction for better CFD outcomes.

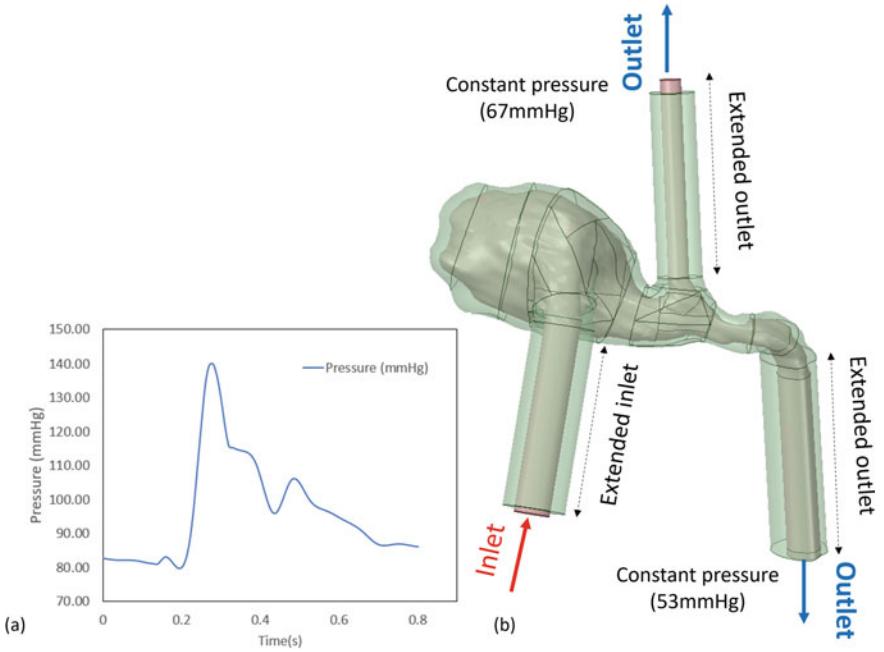

Fig. 3 **a** Pressure profile given to the inlet, and **b** middle cerebral artery geometry with extended inlets and outlets, showing the constant pressure used at the outlets

2.2 Computational Analysis

2.2.1 Structural Computational Model

The different plaque components (calcification and lipids) and arterial wall for the three models were meshed using the proximity and curvature function size with default element size and discretized with tetrahedral elements. The number of elements generated for each geometry were 890,158, 811,375, and 1,241,307 for the coronary, carotid, and aneurysm models respectively. Extensions were also added to the ends of the models to match the length of the fluid domain and allow a fully developed flow to reach the region of interest (atheroma or aneurysm). Fixed support was added to the narrow edges of the geometries at the ends of the extensions. The material properties for the vessel wall and plaque components were assumed to be isotropic elastic, with Poisson's ratio of 0.48 for all materials and Young's Modulus of 10 MPa for calcification, 0.02 MPa for lipids, and 0.6 MPa for arterial tissue [5, 20, 33, 37]. In the aneurysm, the material properties of the vessel wall were assumed as, Poisson's ratio of 0.48 and Young's Modulus of 3 MPa. The Young's modulus of cerebral aneurysms has values between approximately 0.5–5.7 MPa [12].

2.2.2 Fluid Computational Model

For all cases, blood flow was assumed to be laminar incompressible, homogenous, and Newtonian, with a viscosity of 0.00345 Pa·s and a density of 1050 kg/m^3. In the FSI simulation, the dynamic mesh function had to be enabled for the fluid domain with the diffusion and remesh functions with an interval of 1. This function allowed the motion of the boundary in the fluid participant and transfer the fluid pressure to the structural part of the FSI. Adaptive mesh with tetrahedral elements with a coarse size of 0.30 mm was selected for the fluid part. Also, inflation was added to the fluid domain boundary, 5-layer to the coronary model, and 10-layer to the carotid and aneurysms models. This mesh setup guaranteed there was no negative cell volume error when performing FSI simulation with a relatively big time step of 0.01 s for CFD and FSI for all the geometries. The number of elements generated for each geometry were 80,534, 641,749, and 1,382,850 for the coronary, carotid, and aneurysm models respectively. The interior of the lumen and the geometry were set as deforming dynamic zones and the wall was set as a system coupling zone.

2.2.3 Boundary Conditions and Co-simulation Settings

For the coronary artery, a time-dependent velocity boundary condition was prescribed at the inlet and a time-dependent pressure boundary condition was given at the outlet. The original waveforms were acquired from wave intensity analysis [10], based on the number of time points in the FSI simulation, the velocity and pressure waveforms were interpolated to a set of discrete points. As the geometry we used for the FSI simulation was only a short section of the full-long coronary model, the blood flow was not able to fully develop from the inlet. A CFD-only model with extended inlet and outlet was performed to obtain fully developed parabolic flow velocity profiles used as the boundary condition for the subsequent FSI simulation. Later the velocity profiles defined by element coordinates and velocity components were directly given to the inlet of the fluid domain in the FSI simulation (Fig. 1). The extended CFD-only model helped to provide a fully developed flow, thereby saving computational consumption in FSI simulation.

In the carotid artery model, patient-specific mass flow rate waveforms were computed using Segment (version 2.2, Medviso, R6435, Lund, Sweden) by selecting the region corresponding to the lumen of the CCA, in the PC-MRI images and integrating the axial velocity. The diastolic and systolic pressure values acquired from the patient were scaled to the mass flow rate profile. Figure 2 shows the boundary conditions in terms of pressure (as outlets at the ICA and ECA) and mass flow rate (as inlet at the CCA) profiles used for the FSI calculation as an example. Figure 2 also shows the resolved mass flow rate (MFR) at the ICA and ECA by FSI. In the aneurysm model, a time-dependent pulsatile pressure profile was defined at the inlet (MCA) and the constant pressure of 8000 and 9000 Pa was defined at the outlets. The prescribed pressure profile (80–120 mmHg) corresponds to normal blood pressure (Fig. 3).

CFD, structural, and FSI simulations were performed on ANSYS Workbench (explicit formulation) platform using the finite volume for the fluid simulation and finite element method for the structural. The time step for all the simulations was 0.01 s. The same computational power was allowed to the multi-physics and single-physics simulations (24 CPUs to the fluid participant and 8 CPUs to the structural participant). System Coupling component was used for controlling pressure/force and displacement data transferring between the two participants (Fluent and transient structural). For data transfer, the inner surface of the structural part which is in contact with the lumen was set as the fluid–solid interface. No-slip conditions and normal stress equilibrium conditions were assumed at all interfaces. The timestep in system coupling was set to 0.01 s, running for two cardiac cycles. At each timestep, the values of transferring data were ramped linearly in the first 5 coupling iterations (minimum iteration number) to help in the stability of the coupled simulation. To avoid instability of the results from the initial time steps, only the data from the second cycle were used for post-processing.

2.3 Data Analysis

To compare our FSI model with conventional structural-only, and CFD-only simulations the same geometry from FSI simulations was used. In the conventional transient structural analysis, the fluid–structure interface on the inner surface of the arterial wall was replaced by direct pressure waveform load, while other settings were kept the same as in the FSI simulation. Principal stress (stress-P1) was compared from both simulations at one location for all the time points. Stress-P1 provides information related to the normal stress at an angle on a plane where shear stress is zero. In the CFD-only simulation, the same setting was given as in the FSI model but the dynamic mesh and the system coupling interface were disabled. Wall shear stress (WSS) distribution was compared from CFD only and FSI results, using the area at which the WSS is lower than 2 Pa for the coronary and carotid arteries, and 10 Pa for the cerebral artery. The analysis was performed at systole for all the geometries.

3 Results

3.1 Coronary Artery

3.1.1 Principle Stress Comparison from Structural-only and FSI Simulations

By comparing the stress-P1 results related to the coronary artery, it was found that the values from the FSI and structural only simulation are similar. This information can

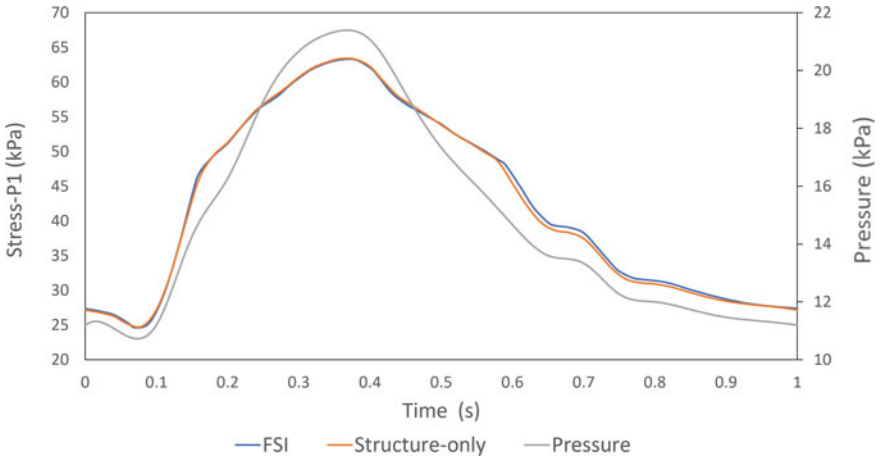

Fig. 4 Comparison of the principal stress (Stress-P1) between FSI and structural-only simulations of the coronary artery at a specific selected point. The plot also illustrates the pressure profile prescribed for calculation

be verified from Fig. 4, where the maximum difference was 820 Pa (1.8%) found after systole. Additionally, both curves followed the same trend as the pressure profile, prescribed as a boundary condition.

3.1.2 Wall Shear Stress Analysis and Comparison from CFD-only and FSI Simulations

Figure 5a, b shows the WSS contours at the 0.8 s time point, for FSI and CFD-only simulations. Additionally, Fig. 5c illustrates the change in area with WSS lower than 2 Pa across the complete cardiac cycle. From there, it can be seen that CFD-only simulation tended to provide lower values than the FSI simulation due to the non-deformable rigid wall. The maximum difference between the area of the low WSS for FSI and CFD simulations was 87%. FSI model detected more area for low WSS because the fluid domain could expand circumferentially when pressure loaded to the flexible arterial wall. Also, the area with low WSS correlates negatively to the velocity flow wave.

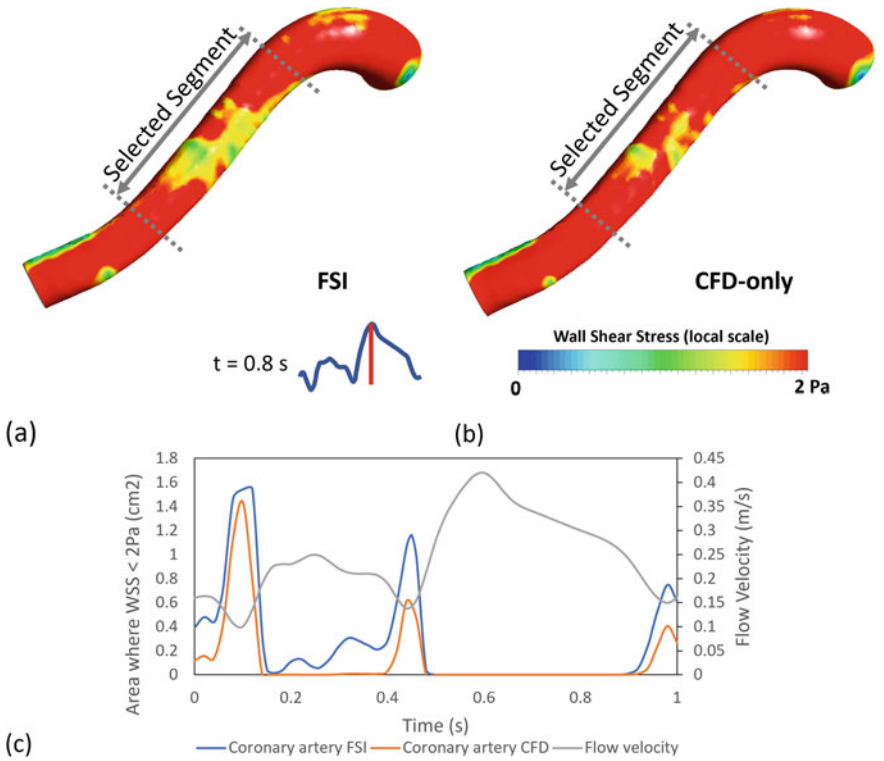

Fig. 5 Contours of WSS< 2 Pa at the 0.8 s time point, for **a** the FSI and **b** CFD-only simulations. **c** Shows the area within the coronary luminal geometry with WSS < 2 Pa across the cardiac cycle

3.2 Carotid Artery

3.2.1 Principle Stress Comparison from Structural-only and FSI Simulations

Stress-P1 was also investigated for the carotid arteries at a specific location within the carotid plaque at the level of the bifurcation. Figure 6 shows that FSI simulation tended to provide higher values than CFD-only and was more noticeable at the region of systole in the cardiac cycle. The maximum difference located at systole was 1.25 kPa which is about 5%. However, both curves followed the trend given by the prescribed pressure profile.

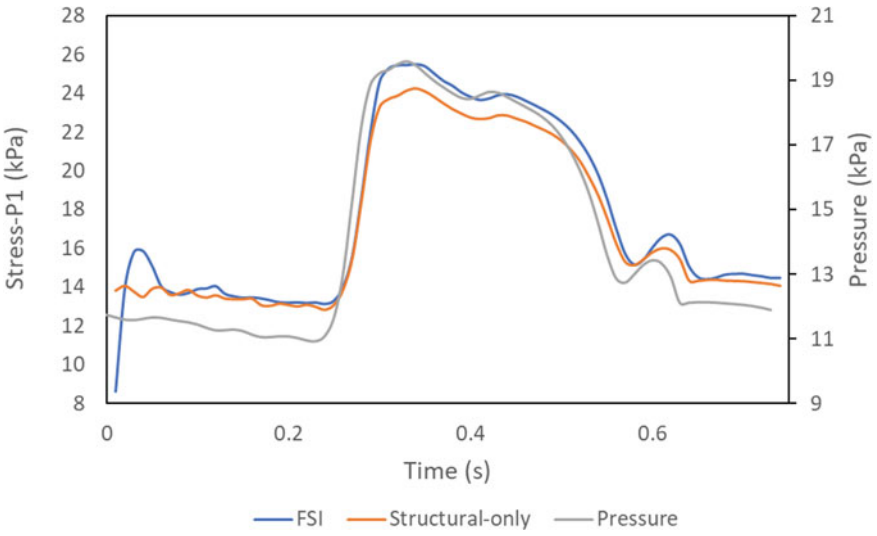

Fig. 6 Comparison of the principal stress (Stress-P1) between FSI and structural-only simulations of the carotid artery at a specific selected point. The plot also illustrates the pressure profile prescribed for calculation

3.2.2 Wall Shear Stress Analysis and Comparison from CFD-only and FSI Simulations

Figure 7a and b illustrates the low WSS contours from the CFD-only and FSI simulation for the carotid artery geometry, at the 0.34 s time point of the cardiac cycle. FSI analysis also provided higher areas across the cardiac cycle compared to CFD-only simulation (Fig. 7c) with a maximum difference of 9%. For this geometry, it is observed that the data from FSI simulation shifted to the right compared to CFD-only. Even though there is a clear difference between both sets of data, both curves followed a negatively correlated pattern with relation to the mass flowrate prescribed as a boundary condition.

3.3 Cerebral Artery

3.3.1 Principle Stress Comparison from Structural-only and FSI Simulations

Figure 8 provides the summary of the data related to the stress-P1 collected for the cerebral artery for the structural-only and FSI simulation, at the thinnest region of the arterial wall. The data presents a consistent difference across the cardiac cycle

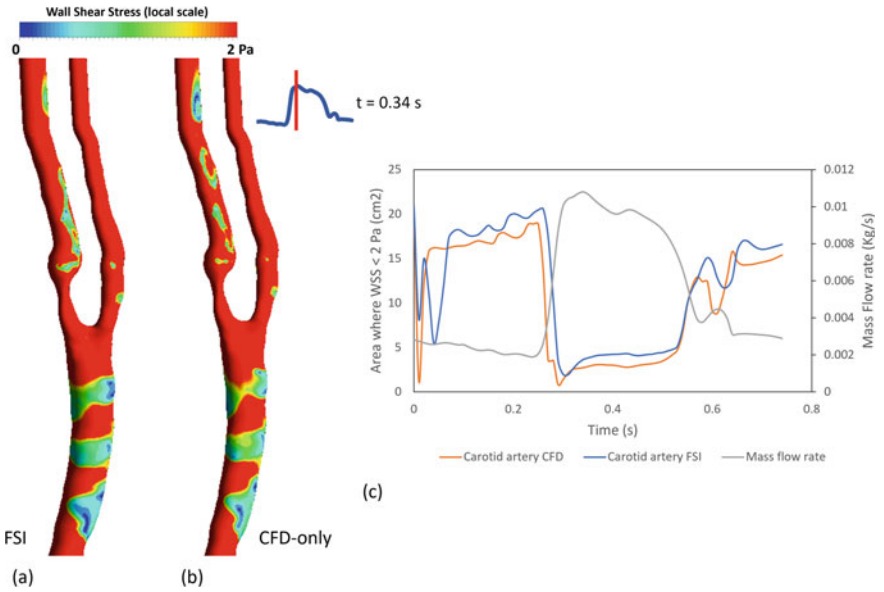

Fig. 7 Contours of WSS < 2 Pa at the 0.34 s time point, for **a** the FSI and **b** CFD-only simulations. **c** shows the area within the carotid luminal geometry with WSS < 2 Pa across the cardiac cycle

with a maximum difference of 30 kPa (20%), at systole. Both curves also followed the trend given by the pressure profile used as a boundary condition.

3.3.2 Wall Shear Stress Analysis and Comparison from CFD-only and FSI Simulations

The contours from the FSI and CFD-only simulations plotted at systole (0.28 s) are shown in Fig. 9a and b, with a maximum value of 10 Pa. Additionally, Fig. 9c presents the area of WSS lower than 10 Pa. For the cerebral artery, it is observed that both FSI and CFD-only analysis provided almost identical values across the cardiac cycle, with a maximum difference of 6.4%. The data provided by the FSI and CFD-only analysis provided a negative correlation to the pressure profile prescribed as a boundary condition.

4 Discussion

Overall, the three investigated arteries presented different patterns, for example with relation to the comparison from the structural-only and FSI simulation, the coronary artery showed similar values across the cardiac cycle, contrary to the carotid and

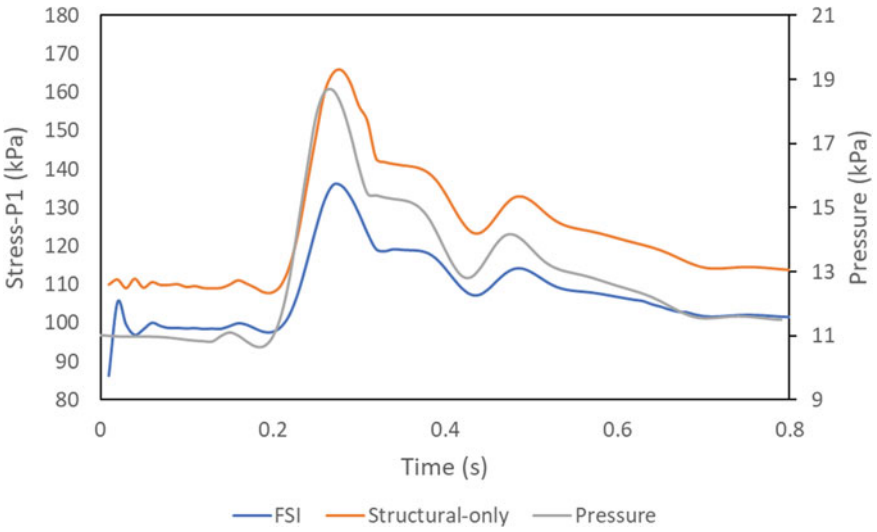

Fig. 8 Comparison of the principal stress (Stress-P1) between FSI and structural-only simulations of the cerebral artery at a specific selected point. The plot also illustrates the pressure profile prescribed for calculation

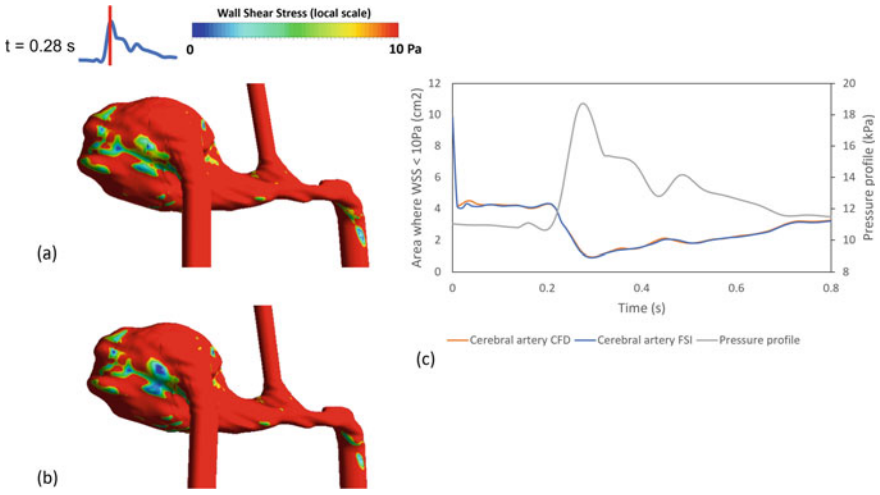

Fig. 9 Contours of WSS < 10 Pa at the 0.28 s time point, for **a** the FSI and **b** CFD-only simulations. **c** Shows the area within the cerebral luminal geometry with WSS < 10 Pa across the cardiac cycle

cerebral arteries. For these arteries, there was a noticeable difference across the cardiac cycle. This may be due to the characteristics of each model. In the case of the coronary artery, the model included lipids as a plaque component, for the carotid artery the model included lipid and calcification, for the cerebral artery the model had just the arterial tissue and the highest stress was in the thinnest region of the wall. However, in all cases, the results from the simulations followed the trend prescribed by the pressure profile set as a boundary condition. It is also important to mention that in a structural-only simulation the pressure is applied homogeneously to the internal wall of the structure, instead in the FSI simulation the force is given node by node by the CFD calculation.

With relation to the area at low WSS calculated for different geometries from FSI and CFD-only simulations, the coronary and the carotid artery presented significant difference between the values compared to the cerebral artery where the values are similar to each other. This pattern can be due to the material properties given to the arterial wall for each simulation. For example, in the case of the coronary and carotid artery, even though the models included plaque component lipids and calcification, the arterial wall was defined with Young's modulus of 0.6 MPa instead in the cerebral artery Young's modulus was 3 MPa. This value was selected due to the complexity of the geometry which allowed the acquisition of the FSI data.

Two different imaging modalities were used in this study to extract the geometries for simulation. In the case of the coronary artery the geometry was extracted from OCT, and for the carotid and cerebral arteries, the geometries were extracted from MRI. This information provides the basic framework for further studies that aimed to segment and 3D reconstructed models for FSI, structural, and CFD only simulations.

FSI is a valuable tool that can provide information in terms of structural and CFD analysis of a specific geometry. However, it is computationally expensive and time-consuming (Table 1), and in some cases, it may not reach convergence due to the complexity of the models. Therefore, this study compared the results of CFD and structural only simulations against FSI simulations to identify if single physics can provide similar information as the multi-physics approach. In the case of the coronary artery, for the structural-FSI comparison there was a small difference in terms of deformation and stress. However, the comparison between CFD and FSI simulations showed a clear difference in WSS values indicating that FSI is still required. For the carotid artery, both comparisons (structural-FSI and CFD-FSI) presented different values to each other, which suggests that for this geometry and settings there is still a necessity for the information provided by FSI. In the case of the cerebral artery, the structural–FSI comparison presented the highest difference in stress values, contrary to the CFD-FSI comparison which showed similar results. This information suggests that FSI will be needed for the structural participant of the cerebral artery. In summary, it was observed that the results from CFD, structural and FSI simulations were influenced by the type of geometry evaluated, and simulation settings.

Table 1 Computational time consumption for each geometry and method using 24 CPUs for the CFD and 8 CPUs for the structural participant

Computational time	FSI	Structural-only	CFD-only
Coronary	17 h 39 m	2 h 50 m	45 m
Carotid	41 h 50 m	2 h 4 m	1 h 3 m
Cerebral	171 h	7 h 40 m	4 h 25 m

4.1 Limitations

The results of the numerical simulations are based on the geometry of the model, the loads or boundary conditions employed, and the material properties. In this study, the geometry and the boundary conditions are patient-specific for the carotid artery; however, the material properties and the boundary conditions for the coronary and cerebral arteries are still based on previous studies [36, 46], where a linear elastic behaviour was assumed for the arterial tissue, calcification, and lipids. Further investigation is required with relation to non-linear elastic material properties to the plaque components using the proposed methods.

Another limitation of this study is that the shrinkage or zero-state pressure procedure was not performed in the geometries. Some studies have performed it using a uniform circumferential shrink and axial stretch ratio [23, 24, 43]. Even though this procedure is valuable, it was demonstrated previously that applying a method to address this issue, will not affect the results significantly [5], instead will increase the complexity of the models.

The proposed methods were only applied to one patient per location (coronary, carotid, and cerebral arteries). Future larger-scale patient studies are needed to further demonstrate the feasibility and advantage of the methods. It is also recognised that experimental validation can give further insight into the accuracy of the results.

5 Conclusions

This article presented the methods for biomechanical analysis of coronary, carotid, and cerebral arteries. The results for the hemodynamic, mechanical, and FSI simulations were compared to understand the applicability of single and multi-physics methods for different arteries. For the coronary artery, the results of the structural-only and FSI simulations were in agreement, whereas CFD-only results were significantly different from the FSI simulations. The results for the CFD-only and structural-only against FSI simulations were comparable for the carotid artery. In the cerebral artery, the comparison between structural-only against FSI simulations presented substantial differences, whereas CFD-only and FSI simulation results were in agreement. In conclusion, the shape, location of an artery, and simulation settings should be considered when selecting a computational model. Further large-scale studies are required to verify the results and propose a method for different arteries.

Funding and Acknowledgements Computational resources and services used in this work were provided by the HPC and Research Support Group, Queensland University of Technology, Brisbane, Australia. The authors would like to acknowledge the financial support from the Australian Research Council (DP200103492, DP200101970), National Nature Science Foundation of China (NSFC:11972118,11772093, 61821002), Australian Research Council (ARC) (FT140101152, DP180103009), the Prince Charles Hospital Foundation (NI2019-19), and the PA Research Foundation (PARF). The authors would also like to acknowledge the support of Dr Thomas Lloyd, Dr Christopher Raffel and Dr Chengcheng Zhu and the research team from the hospitals.

References

1. Adame, I., Van Der Geest, R., Wasserman, B., Mohamed, M., Reiber, J., & Lelieveldt, B. J. (2004). Automatic segmentation and plaque characterization in atherosclerotic carotid artery MR images. *Magnetic Resonance Materials in Physics, Biology and Medicine*, *16*(5), 227–234.
2. Asakura, T., & Karino, T. J. (1990). Flow patterns and spatial distribution of atherosclerotic lesions in human coronary arteries. *Circulation Research*, *66*(4), 1045–1066.
3. Australian Institute of Health and Welfare. (2021). Heart, stroke and vascular disease—Australian facts. Retrieved from Canberra: https://www.aihw.gov.au/reports/heart-stroke-vascular-diseases/hsvd-facts
4. Backes, D., Rinkel, G. J., Greving, J. P., Velthuis, B. K., Murayama, Y., Takao, H., Ishibashi, T., Igase, M., Agid, R., & Jääskeläinen, J. E. (2017). ELAPSS score for prediction of risk of growth of unruptured intracranial aneurysms. *Neurology*, *88*(17), 1600–1606.
5. Benitez, J., Fontanarosa, D., Wang, J., Paritala, P. K., McGahan, T., Lloyd, T., & Li, Z. (2021). Evaluating the impact of calcification on plaque vulnerability from the aspect of mechanical interaction between blood flow and artery based on MRI. *Annals of Biomedical Engineering, 49*(4), 1169–1182. https://doi.org/10.1007/s10439-020-02655-1
6. Berg, P., Voß, S., Janiga, G., Saalfeld, S., Bergersen, A. W., Valen-Sendstad, K., Bruening, J., Goubergrits, L., Spuler, A., Chiu, T. L., & Tsang, A. C. (2019). Multiple Aneurysms AnaTomy CHallenge 2018 (MATCH)—phase II: Rupture risk assessment. *International Journal of Computer Assisted Radiology and Surgery*, *14*(10), 1795–1804.
7. Brisman, J. L., Song, J. K., & Newell, D. W. (2006). Cerebral aneurysms. *New England Journal of Medicine*, *355*(9), 928–939.
8. Brown, A. J., Teng, Z., Calvert, P. A., Rajani, N. K., Hennessy, O., Nerlekar, N., Obaid, D. R., Costopoulos, C., Huang, Y., & Hoole, S. P. (2016). Plaque structural stress estimations improve prediction of future major adverse cardiovascular events after intracoronary imaging. *Circulation: Cardiovascular Imaging*, *9*(6), e004172.
9. Brown, A. J., Teng, Z., Evans, P. C., Gillard, J. H., Samady, H., & Bennett, M. R. (2016). Role of biomechanical forces in the natural history of coronary atherosclerosis. *Nature Reviews Cardiology*, *13*(4), 210–220.
10. Broyd, C. J., Davies, J. E., Escaned, J. E., Hughes, A., & Parker, K. (2017). Wave intensity analysis and its application to the coronary circulation. *Global Cardiology Science & Practice*, *2017*(1), e201705–e201705. https://doi.org/10.21542/gcsp.2017.5
11. Cebral, J. R., Detmer, F., Chung, B. J., Choque-Velasquez, J., Rezai, B., Lehto, H., Tulamo, R., Hernesniemi, J., Niemela, M., & Yu, A. (2019). Local hemodynamic conditions associated with focal changes in the intracranial aneurysm wall. *American Journal of Neuroradiology*, *40*(3), 510–516.
12. Cebral, J. R., Duan, X., Chung, B. J., Putman, C., Aziz, K., & Robertson, A. J. (2015). Wall mechanical properties and hemodynamics of unruptured intracranial aneurysms. *American Journal of Neuroradiology*, *36*(9), 1695–1703.

13. Cebral, J. R., Mut, F., Weir, J., & Putman, C. M. J. (2011). Association of hemodynamic characteristics and cerebral aneurysm rupture. *American Journal of Neuroradiology*, 32(2), 264–270.
14. Chatzizisis, Y. S., Coskun, A. U., Jonas, M., Edelman, E. R., Feldman, C. L., & Stone, P. H. (2007). Role of endothelial shear stress in the natural history of coronary atherosclerosis and vascular remodeling: Molecular, cellular, and vascular behavior. *Journal of the American College of Cardiology*, *49*(25), 2379–2393.
15. Chien, A., Liang, F., Sayre, J., Salamon, N., Villablanca, P., & Viñuela, F. J. (2013). Enlargement of small, asymptomatic, unruptured intracranial aneurysms in patients with no history of subarachnoid hemorrhage: The different factors related to the growth of single and multiple aneurysms. *Journal of Neurosurgery*, *119*(1), 190–197.
16. Dibildox, G., Baka, N., Punt, M., Aben, J. P., Schultz, C., Niessen, W., & van Walsum, T. J. (2014). 3D/3D registration of coronary CTA and biplane XA reconstructions for improved image guidance. *Medical Physics*, *41*(9), 091909.
17. Etminan, N., Brown, R. D., Beseoglu, K., Juvela, S., Raymond, J., Morita, A., Torner, J. C., Derdeyn, C. P., Raabe, A., & Mocco, J. J. (2015). The unruptured intracranial aneurysm treatment score: A multidisciplinary consensus. *Neurology*, *85*(10), 881–889.
18. Etminan, N., & Rinkel, G. J. (2016). Unruptured intracranial aneurysms: Development, rupture and preventive management. *Nature Reviews Neurology*, *12*(12), 699–713.
19. Fujimoto, J. G. (2001). Optical coherence tomography. *Comptes Rendus de l'Académie des Sciences - Series IV - Physics, 2*(8), 1099–1111.
20. Gao, H., Long, Q., Graves, M., Gillard, J. H., & Li, Z. Y. (2009). Carotid arterial plaque stress analysis using fluid-structure interactive simulation based on in-vivo magnetic resonance images of four patients. *Journal of Biomechanics, 42*(10), 1416–1423. https://doi.org/10.1016/j.jbiomech.2009.04.010
21. Gharahi, H., Zambrano, B. A., Zhu, D. C., DeMarco, J. K., & Baek, S. (2016). Computational fluid dynamic simulation of human carotid artery bifurcation based on anatomy and volumetric blood flow rate measured with magnetic resonance imaging. *International Journal of Advances in Engineering Sciences and Applied Mathematics*, *8*(1), 46–60.
22. Greving, J. P., Wermer, M. J., Brown Jr, R. D., Morita, A., Juvela, S., Yonekura, M., Ishibashi, T., Torner, J.C., Nakayama, T., & Rinkel, G. J. (2014). Development of the PHASES score for prediction of risk of rupture of intracranial aneurysms: A pooled analysis of six prospective cohort studies. *The Lancet Neurology*, *13*(1), 59–66.
23. Huang, X., Yang, C., Yuan, C., Liu, F., Canton, G., Zheng, J., & Tang, D. (2009). Patient-specific artery shrinkage and 3D zero-stress state in multi-component 3D FSI models for carotid atherosclerotic plaques based on in vivo MRI data. *Molecular & Cellular Biomechanics: MCB*, *6*(2), 121–134.
24. Koskinas, K. C., Chatzizisis, Y. S., Baker, A. B., Edelman, E. R., Stone, P. H., & Feldman, C. L. (2009). The role of low endothelial shear stress in the conversion of atherosclerotic lesions from stable to unstable plaque. *Current Opinion in Cardiology*, *24*(6), 580–590.
25. Ku, D. N., & Giddens, D. P. (1983). Pulsatile flow in a model carotid bifurcation. *Arteriosclerosis: An Official Journal of the American Heart Association, Inc.*, *3*(1), 31–39.
26. Leach, J. R., Rayz, V. L., Soares, B., Wintermark, M., Mofrad, M. R., & Saloner, D. (2010). Carotid atheroma rupture observed in vivo and FSI-predicted stress distribution based on pre-rupture imaging. *Annals of Biomedical Engineering*, *38*(8), 2748–2765.
27. Leiner, T., Gerretsen, S., Botnar, R., Lutgens, E., Cappendijk, V., Kooi, E., & Van Engelshoven, J. J. (2005). Magnetic resonance imaging of atherosclerosis. *European Radiology*, *15*(6), 1087–1099.
28. Li, Z.-Y., Howarth, S., Tang, T., Graves, M., Jean, U., & Gillard, J. H. (2007). Does calcium deposition play a role in the stability of atheroma? Location may be the key. *Cerebrovascular Diseases*, *24*(5), 452–459.
29. Li, Z.-Y., Howarth, S., Trivedi, R. A., U-King-Im, J. M., Graves, M. J., Brown, A., Wang, L., & Gillard, J. H. (2006). Stress analysis of carotid plaque rupture based on in vivo high resolution MRI. *Journal of Biomechanics*, *39*(14), 2611–2622.

30. Li, Z.-Y., Tan, F. P., Soloperto, G., Wood, N. B., Xu, X. Y., & Gillard, J. H. J. (2015). Flow pattern analysis in a highly stenotic patient-specific carotid bifurcation model using a turbulence model. *Computer Methods in Biomechanics and Biomedical Engineering*, *18*(10), 1099–1107.
31. Liu, X., Zhang, H., Ren, L., Xiong, H., Gao, Z., Xu, P., Huang, W., & Wu, W. (2016). Functional assessment of the stenotic carotid artery by CFD-based pressure gradient evaluation. *American Journal of Physiology-Heart and Circular Physiology*, *311*(3), H645–H653.
32. Lu, G., Huang, L., Zhang, X., Wang, S., Hong, Y., Hu, Z., & Geng, D. Y. (2011). Influence of hemodynamic factors on rupture of intracranial aneurysms: patient-specific 3D mirror aneurysms model computational fluid dynamics simulation. *American Journal of Neuroradiology*, *32*(7), 1255–1261.
33. Mendieta, J. B., Fontanarosa, D., Wang, J., Paritala, P. K., McGahan, T., Lloyd, T., & Li, Z. (2020). The importance of blood rheology in patient-specific computational fluid dynamics simulation of stenotic carotid arteries. *Biomechanics and Modeling in Mechanobiology*, *19*(5), 1477–1490.
34. Molina, M. C., Prause, G. P., Radeva, P., & Sonka, M. (1998). 3D catheter path reconstruction from biplane angiograms. Paper presented at the Medical Imaging 1998: Image Processing.
35. Morbiducci, U., Kok, A. M., Kwak, B. R., Stone, P. H., Steinman, D. A., & Wentzel, J. J. (2016). Atherosclerosis at arterial bifurcations: evidence for the role of haemodynamics and geometry. *Thrombosis and Haemostasis*, *115*(03), 484–492.
36. Paritala, P. K., Yarlagadda, P. K. D. V., Wang, J., Gu, Y., & Li, Z. (2018). Numerical investigation of atherosclerotic plaque rupture using optical coherence tomography imaging and XFEM. *Engineering Fracture Mechanics*, *204*, 531–541. https://doi.org/10.1016/j.engfracmech.2018.11.002
37. Paritala, P. K., Yarlagadda, T., Mendieta, J. B., Wang, J., McGahan, T., Lloyd, T., & Li, Z. (2021). Plaque longitudinal heterogeneity in morphology, property, and mechanobiology. *Cerebrovascular Diseases*, *50*(5), 510–519. https://doi.org/10.1159/000515690
38. Ross, R. (1999). Atherosclerosis—an inflammatory disease. *New England Journal of Medicine*, *340*(2), 115–126.
39. Saam, T., Ferguson, M., Yarnykh, V., Takaya, N., Xu, D., Polissar, N., Hatsukami, T. S., & Yuan, C. (2005). Quantitative evaluation of carotid plaque composition by in vivo MRI. *Arteriosclerosis, Thrombosis and Vascular Biology*, *25*(1), 234–239.
40. Sforza, D. M., Putman, C. M., & Cebral, J. R. (2009). Hemodynamics of cerebral aneurysms. *Annual Review of Fluid Mechanics*, *41*, 91–107.
41. Soldozy, S., Norat, P., Elsarrag, M., Chatrath, A., Costello, J. S., Sokolowski, J. D., Tvrdik, P., Kalani, M. Y. S., & Park, M. S. (2019). The biophysical role of hemodynamics in the pathogenesis of cerebral aneurysm formation and rupture. *Neurosurgical Focus*, 47(1), E11.
42. Steinman, D. A., Milner, J. S., Norley, C. J., Lownie, S. P., & Holdsworth, D. W. (2003). Image-based computational simulation of flow dynamics in a giant intracranial aneurysm. *American Journal of Neuroradiology*, *24*(4), 559–566.
43. Tang, D., Yang, C., Huang, S., Mani, V., Zheng, J., Woodard, P. K., & Fayad, Z. A. (2017). Cap inflammation leads to higher plaque cap strain and lower cap stress: An MRI-PET/CT-based FSI modeling approach. *Journal of Biomechanics*, *50*, 121–129. https://doi.org/10.1016/j.jbiomech.2016.11.011
44. Villablanca, J. P., Duckwiler, G. R., Jahan, R., Tateshima, S., Martin, N. A., Frazee, J., Gonzalez, N. R., Sayre, J., & Vinuela, F. V. (2013). Natural history of asymptomatic unruptured cerebral aneurysms evaluated at CT angiography: Growth and rupture incidence and correlation with epidemiologic risk factors. *Radiology*, *269*(1), 258–265.
45. Virani, S. S., Alonso, A., Aparicio, H. J., Benjamin, E. J., Bittencourt, M. S., Callaway, C. W., Carson, A. P., Chamberlain, A. M., Cheng, S., & Delling, F. N. (2021). Heart disease and stroke statistics—2021 update: A report from the American Heart Association. *Circulation*, *143*(8), e254–e743.
46. Wang, J., Paritala, P. K., Mendieta, J. B., Komori, Y., Raffel, O. C., Gu, Y., & Li, Z. (2020). Optical coherence tomography-based patient-specific coronary artery reconstruction and fluid–structure interaction simulation. *Biomechanics and Modeling in Mechanobiology*, *19*(1), 7–20.

47. Williams, L. N., & Brown, R. D. (2013). Management of unruptured intracranial aneurysms. *Neurology: Clinical Practice*, *3*(2), 99–108.
48. Xu, P., Liu, X., Zhang, H., Ghista, D., Zhang, D., Shi, C., & Huang, W. (2018). Assessment of boundary conditions for CFD simulation in human carotid artery. *Biomechanics and Modeling in Mechanobiology*, *17*(6), 1581–1597.
49. Zhao, S., Xu, X., Hughes, A., Thom, S., Stanton, A., Ariff, B., & Long, Q. J. (2000). Blood flow and vessel mechanics in a physiologically realistic model of a human carotid arterial bifurcation. *Journal of Biomechanics*, *33*(8), 975–984.

Automatic Framework for Patient-Specific Biomechanical Computations of Organ Deformation: An Epilepsy (EEG) Case Study

Saima Safdar, Benjamin Zwick, George Bourantas, Grand R. Joldes, Simon K. Warfield, Damon E. Hyde, Adam Wittek, and Karol Miller

Abstract Our motivation is to enable non-specialists to use sophisticated biomechanical models in the clinic. To further this goal, in this study, we constructed a framework within 3D Slicer for automatically generating and solving patient-specific biomechanical models of the brain. This framework allows determining automatically patient-specific geometry from MRI data, generating patient-specific computational grid, defining boundary conditions and external loads, assigning material properties to intracranial constituents and solving the resulting set of differential equations. We used the Meshless Total Lagrangian Explicit Dynamics (MTLED) algorithm to solve these equations. We demonstrated the effectiveness and appropriateness of our framework on a case study of brain tissue deformations caused by placement of electrodes on the brain surface in intracranial electroencephalography (iEEG).

Keywords Patient-specific Modelling (PSM) · Nonlinear computational biomechanics · Brain · Brain shift · Automated computations · Electrodes · Deformations

1 Introduction

We are at the verge of a new exciting era of personalized medicine based on patient-specific scientific computations. These computations usually involve solving models described by boundary value problems of partial differential equations (PDEs). The most common and useful are models of biomechanics, bioheat transfer and bioelectricity.

S. Safdar · B. Zwick · G. Bourantas · G. R. Joldes · A. Wittek · K. Miller (✉)
Intelligent System for Medicine Laboratory, The University of Western Australia, Crawley, WA 6009, Australia
e-mail: karol.miller@uwa.edu.au

S. K. Warfield · D. E. Hyde
Computational Radiology Laboratory, Department of Radiology, Boston Children's Hospital and Harvard Medical School, Boston, MA, USA

P. M. F. Nielsen et al. (eds.), *Computational Biomechanics for Medicine*,
https://doi.org/10.1007/978-3-031-09327-2_5

In this paper, we are especially interested in patient-specific biomechanics as a tool to compute soft tissue deformations for operation planning and intraoperative guidance. While the methods for patient-specific biomechanical model generation [33] and solution [9, 10, 39] exist, they are very sophisticated and require very high level of specialist expertise from the users. Therefore, the objective of the work described here is to create an automatic framework so that these sophisticated computations can be conducted in the clinic by a non-specialist.

We integrated the framework [9, 39] to automate the process of generating and solving patient-specific biomechanical models into 3D Slicer (http://www.slicer.org/), an open-source software for visualization, registration, segmentation and quantification of medical data developed by Artificial Intelligence Laboratory of Massachusetts Institute of Technology and Surgical Planning Laboratory at Brigham and Women's Hospital and Harvard Medical School [5].

We demonstrated the application of our framework using a case study of brain deformations caused by placement of electrodes on the brain surface in intracranial electroencephalography (iEEG). The case study is obtained from database of Computational Radiology Lab, Harvard Medical School. The paper is organized as follows: In Sect. 2, we presented the proposed framework. In Sect. 3, we showed our results based on the case study. Section 4 contains discussion and conclusion.

2 Proposed Framework

The four main steps of the proposed framework workflow (see Fig. 1) are as follows:

1. Image Pre-processing
   - Determining patient-specific geometry from medical images
2. Model Construction
   - Patient-specific computational grid generation
   - Defining boundary conditions and external load (displacements of the boundary)
   - Assigning patient-specific material properties to brain tissues
3. Model Solution
   - Computation of tissue deformations using Meshless Total Lagrangian Explicit Dynamics Algorithm (MTLED)
4. Image Warping, using the computed deformation field

The details of each step are given in Sects. 2.1–2.3. Image warping is done with example case study under Sect. 3.

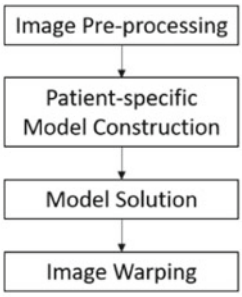

(a) Framework Workflow

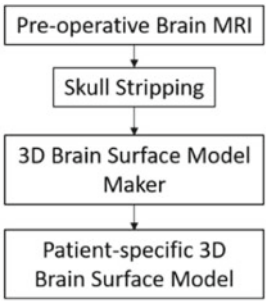

(b) Image Pre-processing

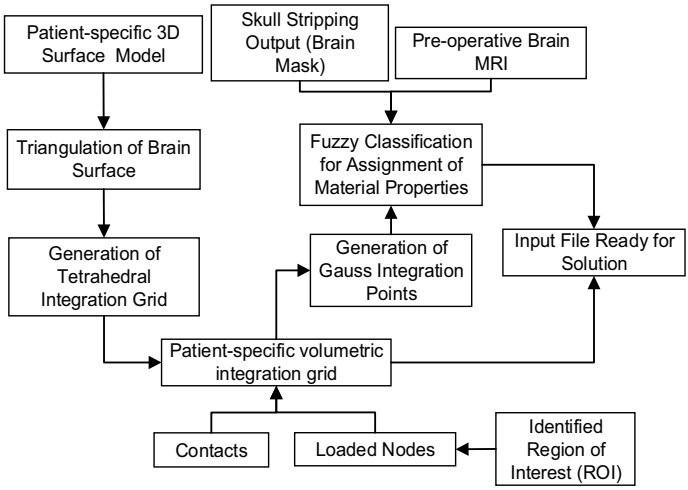

(c) Model Construction

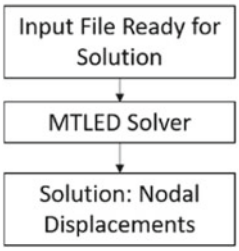

(d) Model Solution

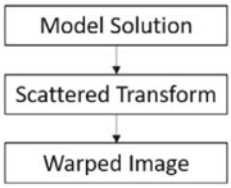

(e) Image Warping

Fig. 1 Workflow diagram for patient-specific biomechanical interpretations of organ deformations

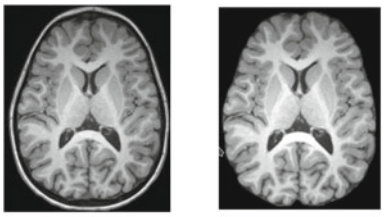

Fig. 2 Results of skull stripping for patient-specific preoperative MRI. **a** Preoperative MRI image, **b** Skull-stripped MRI

2.1 Image Pre-processing

2.1.1 Determining Patient-Specific Geometry from Medical Images

To obtain the geometry of the brain, the skull needs to be removed from the preoperative MRI. We remove the skull and extract the brain volume using FreeSurfer software (http://surfer.nmr.mgh.harvard.edu/) (see Fig. 2). It is an open source software suite for processing and analyzing human brain medical resonance images (MRIs) [3]. Watershed algorithm is used by FreeSurfer to extract the brain portion from T1-weighted MRI [27]. We wrote python-based scripted modules within 3D Slicer to execute all the remaining steps.

After extracting brain volume, we use threshold filter [23] of 3D Slicer to select the brain parenchyma (see Fig. 3). We created a three dimensional surface model based on the selected region using model maker module of 3D Slicer, see Fig. 3 (3D view) [32]. We applied 10% Laplacian smoothing to control the smoothing on model [28]. We have selected 10% smoothing to avoid volume reduction.

2.1.2 Extracting Location of Electrodes

Information about the electrode locations is necessary for biomechanical modeling of neurosurgery [39]. We extracted locations (co-ordinates) of electrodes from the segmented electrode volume (image set containing electrode segmentations) using our procedure implemented as 3D Slicer extension, "electrodes-to-markups". The procedure (see Fig. 5) consists of the following steps: (1) creating a binary label volume from segmented electrode volume, (2) splitting the binary label volume to segments corresponding to each electrode and (3) adding a point (3D space) at the centroid of segments defining each electrode. The conversion from segmented electrode volume to binary label volume (step (1)) is performed using PolySeg [24], a software library that provides automatic conversions between different representations (e.g. label map, surface) [24]. Splitting the binary label volume (step (2)) is

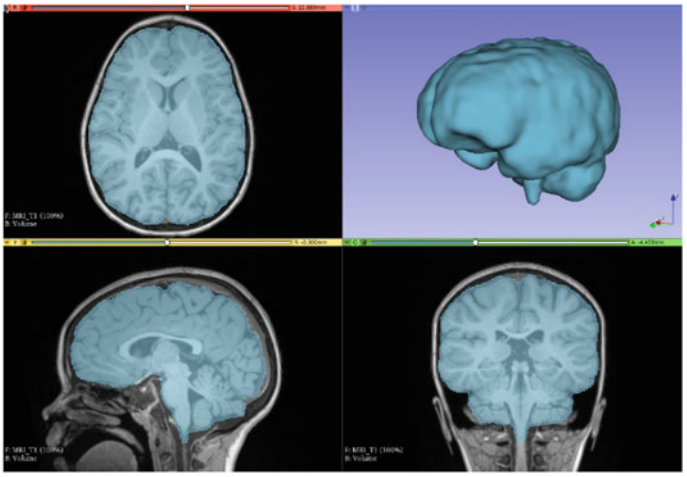

Fig. 3 Visualization of results of threshold filter along with visualization of surface geometry produced by surface model maker of 3D Slicer with 10% value of Laplacian filter. Visualization performed with 3D Slicer (www.slicer.org) [5]

performed using split island into segments and then segment statistics (step (3)) is used to get the centroid (center of mass of the segment) [24].

The intraoperative (post-implantation) positions of the electrodes were extracted (through segmentation) from the CT image (see Fig. 4) rigidly registered to the preoperative MRI. We projected the extracted electrodes (see Fig. 5c) onto the brain surface

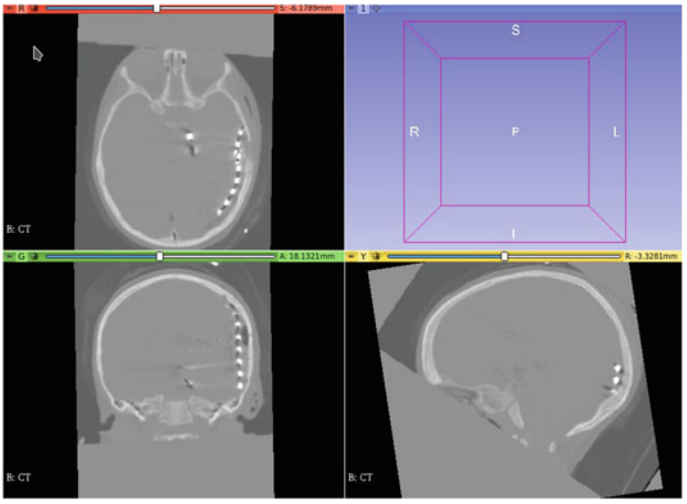

Fig. 4 CT with intracranial electrodes implanted

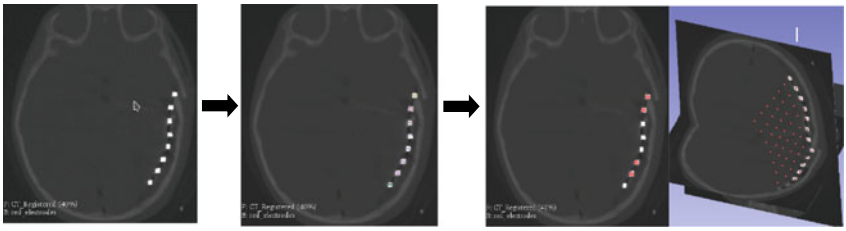

(a) Electrodes (white) on CT

(b) Electrodes selected and split into island (colors)

(c) Fiducial (3D point) placed at centroid position of each electrode. Left: Sagittal View (one slice), Right: 3D View

Fig. 5 Workflow for extracting electrodes from electrode segmented volume obtained from CT image

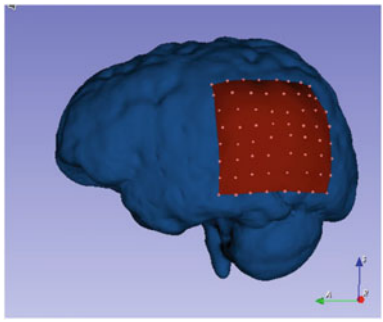

Fig. 6 3D patient-specific brain model along with electrode sheet model

segmented from the preoperative MRI to determine the points corresponding to location of electrodes (referred to as projected electrodes) in the undeformed (preoperative) brain geometry [39]. We used these points to create an electrode sheet model by means of PolyData algorithm [29] from PyVista (www.pyvista.org), Python programming language library [29] (see Fig. 6). We then selected the nodes of brain model located under electrode sheet model (see Fig. 9). We define displacements on these selected surface brain nodes (see Sect. 3 for an example on calculating prescribed displacements) and we applied contacts (see section "Boundary Conditions") on the remaining boundary nodes.

2.2 Model Construction

2.2.1 Patient-Specific Computational Grid Generation

In our method, we use unstructured cloud of nodes to discretize the geometry of interest instead of elements. In this study, we use a geometry conforming tetrahedral background grid [9, 39]. The displacements are calculated over the cloud of points

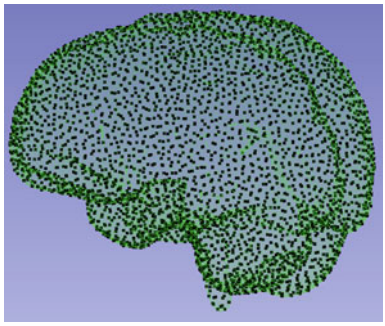

Fig. 7 Meshless discretization for simulation of brain deformation caused by surface electrodes implantation. In this example we have 21,788 nodes (black dots) and 55,470 tetrahedral integration cells with four integration points (green dots 221,880) per cell

formed by the vertices of the tetrahedra. Volumetric integration (a step in the MTLED solution method, see Sect. 3) is performed over background integration cells with four Gauss points per tetrahedral cell. Creating such background grids is fully automatic (i.e. does not require any manual correction) (see Fig. 7). It is very important to note that our tetrahedral integration grid is NOT a finite element mesh and does not need to conform to strict quality requirements demanded by the finite element method. MTLED incorporates Modified Moving Least Squares (MMLS) shape functions [11] which increases the set of admissible nodal distributions and allows very rapid generation of patient-specific discretization of acceptable quality [9]. Whereas in FEM, the linear tetrahedral elements exhibits volumetric locking, especially in case of soft tissues such as the brain, which are modelled as almost incompressible materials [36].

Our framework uses ACVD (Surface Mesh Coarsening and Resampling) [30] to construct a patient-specific triangulated brain surface (see Fig. 8b) which is then used for generating a 3D integration grid filled with tetrahedral integration cells (see Fig. 8c) using Gmsh [6]. The triangulated surface is also used for defining contacts. We automated all these steps and implemented them in 3D Slicer.

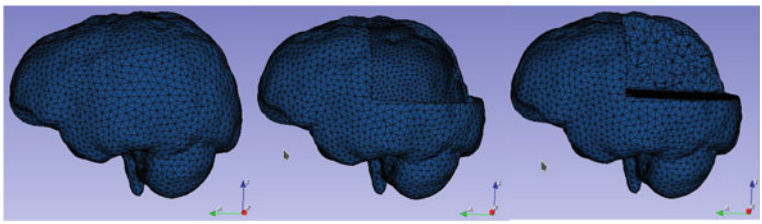

Fig. 8 **a** Patient-specific tetrahedral integration grid with triangular surface mesh, **b** Example of triangulated patient specific brain surface mesh model, **c** Example of patient specific brain volumetric integration grid filled with tetrahedral cells (geometry conforming tetrahedral cells based biomechanical model)

2.2.2 Defining Boundary Conditions and External Load

Boundary Conditions

The stiffness of the skull is several orders of magnitude higher than that of the brain. Therefore, to define the boundary conditions for nodes other than displaced nodes on the exposed surface of the brain, a contact interface is defined between the rigid interface model of the skull and the deformable brain model. Nodes on the brain surface could not penetrate the skull, but could slide without friction or separate from the skull as described in [13].

We created a skull interface using the triangulated surface cells generated as described in Sect. 2.1.2 to define contacts automatically on the surface of patient specific brain biomechanical model.

External Load

Load can be defined either through forces (prescribing natural BCs) or displacements on the boundary (prescribing essential BCs). It is rather difficult to make patient-specific measurements of forces acting on the brain during surgery but there are well-established methods for determining the displacements on the boundaries from images. Furthermore, if we use forces, to accurately compute intraoperative deformations, we need accurate information about patient-specific material properties of the brain tissues. As there is no commonly established method to accurately determine patient-specific material properties of soft tissues from radiographic (MR, CT) images, we define the load through imposed motion (essential BCs). This makes the computed deformations only very weakly dependent on uncertainty in patient specific information about tissue material properties [20, 21, 34].

To define intraoperative loading, intraoperative information is required such as measurement of the current position of the exposed surface of the brain. This can be done through cameras [17] and a pointing tool of a neurosurgical station [25].

In this study, we defined the load by prescribing displacements (essential boundary conditions) on the brain surface deformed due to EEG electrode implantation [39].

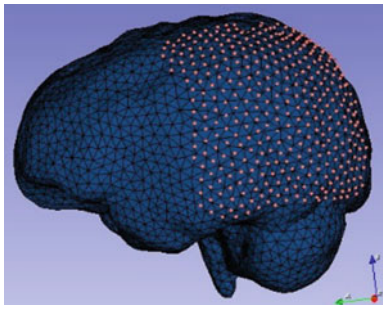

Fig. 9 Brain surface nodes (orange dots) on the surface of the patient-specific brain

The displacements were applied to the nodes located on the brain surface model directly under the electrode sheet (see Fig. 9). We applied displacements using smooth loading curve (3–4-5 polynomial) [12, 31].

2.2.3 Assignment of Patient-Specific Material Properties: Fuzzy Tissue Classification

Material properties of the intracranial constituents are assigned to integration points within the problem geometry through fuzzy tissue classification [1] algorithm. Hard segmentation of brain tissues is difficult to automate [4] and therefore it is incompatible with clinical workflows. Therefore, we integrated a fuzzy tissue classification algorithm [15, 16, 33, 38] into our framework to automatically assign material properties to brain tissues (see results in Fig. 10). Slight inaccuracies of tissue properties assignment do not affect the precision of intraoperative displacement prediction because the external load is defined though prescribed essential boundary condition motion rendering the problem Dirichlet-type [20, 38].

In this framework, a neo-Hookean constitutive model (see Table 1) was used for brain tissues with Poisson's ratio of 0.49, whereas 0.1 was used for the ventricles

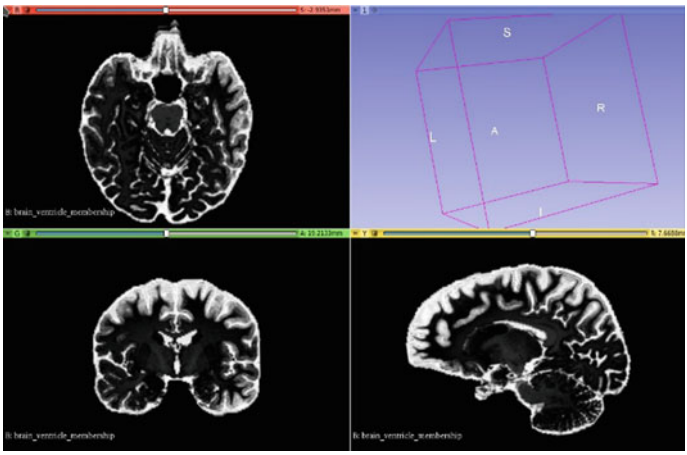

Fig. 10 Result of automatic material property assignment (Young's modulus of 3000 Pa for the brain and 100 Pa for CSF) using fuzzy tissue classification [33, 38]. Brain tissue and CSF (white) were used as cluster centers. Visualization performed with 3D Slicer www.slicer.org [5]

Table 1 Material properties of biomechanical model

Model components	Density (kg/m^3)	Young's modulus (Pa)	Poisson's ratio
Parenchyma	1000	3000 [18]	0.49 [37]
Ventricle	1000	100 [18]	0.1 [35, 37]
Skull	Rigid		

[34, 35]. This simple model is used as the simulation belongs to the special class called displacement-zero traction problems (or Dirichlet-type problems) whose solutions are known to be weakly dependent on the unknown patient-specific material properties of the tissues [2, 22, 34].

2.3 Model Solution

2.3.1 Computation of Tissue Deformations: Meshless Total Lagrangian Explicit Dynamics Algorithm

MTLED is a numerically robust and accurate meshless algorithm [7, 9]. The method computes deformations at an unstructured cloud of nodes used to discretize the geometry instead of elements as in finite element methods, which requires a high quality mesh of problem geometry [33]. The algorithm uses explicit time integration based on the central difference method. Unlike implicit time integration, this does not require solving systems of equations at every time-step making the method robust in performing calculations [7].

MTLED was evaluated extensively in computing brain deformations on problem geometry based on patient specific MRI data. The simulation results presented were within limits of neurosurgical and imaging equipment accuracy (~1 mm) [9, 19]. The method is also capable of handling very large deformations as well as cutting [8].

Meshless methods are preferred to finite element methods, due to excessive element distortion, are unreliable in scenarios where human soft tissues undergo very large strains in the vicinity of contact with a surgical tool while MTLED gives reliable results for compressive strains exceeding 70% [9].

The MTLED solver uses three input files automatically generated using our framework within 3D Slicer, which are: (1) computational grid information file, (2) material properties and (3) external load information file. All remaining parameters of MTLED are set by default (see Table 2) and are based on the experience obtained through numerous applications in computing soft continua and soft tissue deformations. The end user can change these parameters as per requirements but we recommend that a non-specialist user leave them unaltered.

3 Case Study: Intracranial Electrodes Induced Brain Shift

For the purpose of this case study, we determined prescribed displacements using a BSpline transform obtained using scattered transform module [14]. The input to scattered transform is the original electrode positions derived from CT (see Fig. 11a) and the projected electrode positions (see Fig. 11b). The output is a BSpline transform. We applied the obtained BSpline transform to the undeformed (initial) brain surface nodes located under the electrode sheet to determine position of the corresponding

Table 2 Default parameters list for MTLED simulator

MTLED parameters	Values
Mass scaling [7]	True
Integration points per tetrahedron [7]	4
Shape function type [11]	mmls
Basic function type [11]	Quadratic
Use exact derivatives [11]	True
Dilation coefficient [11]	2.5
Load file curve [7]	Smooth
Node set	Contacts
Surface	Skull
Load time for running simulation	1.0 s
Equilibrium time [12]	5 s

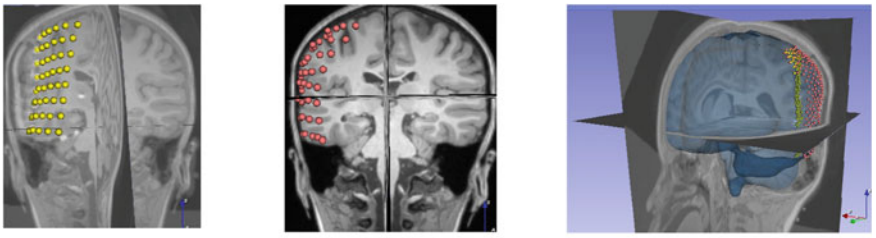

Fig. 11 External Load **a** Visualization of 3D intracranial electrodes (yellow) on a preoperative MRI rigidly aligned with CT image, **b** Visualization of projected electrodes (red) on MRI, **c** Visualization of brain nodes pre-transformed (red) and transformed (yellow) along with 3D brain model (blue with reduced opacity) on preoperative MRI rigidly aligned with CT image. Visualization performed with 3D Slicer www.slicer.org [5]

nodes in the deformed (due to electrode implantation) brain geometry (see Fig. 11c) (yellow transformed brain nodes)). We computed the prescribed displacements as a difference between the locations (coordinates) of the corresponding brain surface nodes under electrode sheet in undeformed and deformed brain geometry.

We used nodal displacements computed by MTLED (see Fig. 12) in the scattered transform module [14] in 3D Slicer to obtain a BSpline transform to warp the preoperative MRI image so that it corresponds to the brain configuration with electrodes implanted (see Fig. 12).

The simulation presented in this study was performed on a HP ProBook with Intel Core i7 2.7 GHz processor and 8 GB of physical memory. The calculation time for generating automatically a patient-specific computational model with all details, including patient-specific geometry construction, craniotomy region selection, external loading and defining contacts was 180.87 s. The execution time of the MTLED solution algorithm (i.e. obtaining the deformed model) was 762 s. The time

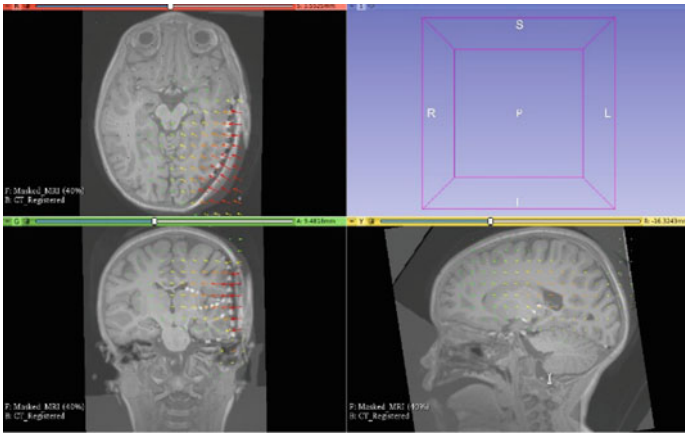

Fig. 12 Visualization of the transformed preoperative MRI using deformation field computed by MTLED registered onto a CT with implanted intracranial electrodes. Visualization performed with 3D Slicer www.slicer.org [5]

for warping the preoperative image with the deformation field extracted from the model was 0.9 s.

4 Discussion and Conclusion

In this paper we described the framework for automated solution of computational biomechanics problems described by partial differential equations of solid mechanics. We also demonstrated the effectiveness of this framework using a case study of brain deformation caused by the placement of electrodes on brain surface in intracranial electroencephalography (iEEG).

In this study, electrodes implanted brain shift is simulated with 21,788 nodes (i.e. ~65,364 differential equations are solved) and 55,470 integration cells. The model has 221,880 integration points. The patient specific biomechanical model construction, which involves defining the patient specific brain geometry from a preoperative MRI, patient-specific tetrahedral integration grid generation, defining boundary conditions and external loads, and assigning material properties to brain tissues, took 180.87 s of computer processing time. The solution of the model using our MTLED algorithm took 762 s and finally the image warping took 0.9 s.

We are interested in computation of the deformation field within the brain which is completely determined by the description of the displacement on the boundary and equations of solid mechanics. We are creating an automatic framework that facilitates such computation for wide range of neurosurgical procedures. We previously successfully validated through application in computation of the brain shift induced

by craniotomy and comparison of the predicted deformations with the intraoperative MRI [26]. In this study we present an extension of this framework to even more challenging problems of computing brain deformations induced by implantation of intracranial electroencephalography (iEEG) electrodes [39]. We showcase it through application in the analysis of an epilepsy patient undergoing such implantation. The results are very promising. Nevertheless application in computer simulation of a selected surgical procedure conducted on one patient can be regarded only as a preliminary evaluation of our framework. Therefore, we plan to apply our framework in the analysis of more patients undergoing craniotomy induced brain shift, electrode implantation for epilepsy treatment, and brain tumour resection.

Acknowledgements The funding from NHMRC grants APP1162030; APP1144519 is gratefully acknowledged. The first author acknowledges scholarship funding from University Postgraduate Award. We also wish to thank 3D Slicer on-line community https://discourse.slicer.org/ whose members have made many valuable contributions. Our special thanks go to Dr. Andras Lasso of Laboratory for Percutaneous Surgery (PerkLab).

References

1. Bezdek, J. C., Ehrlich, R., & Full, W. (1984). FCM: The fuzzy c-means clustering algorithm. *Computers & Geosciences, 10*(2–3), 191–203.
2. Ciarlet, P. G. (1988). *Mathematical elasticity*. North Hollad.
3. Dale, A. M., Fischl, B., & Sereno, M. I. (1999). Cortical surface-based analysis: I. Segmentation and surface reconstruction. *NeuroImage, 9*(2), 179–194.
4. Dora, L., Agrawal, S., Panda, R., & Abraham, A. (2017). State-of-the-art methods for brain tissue segmentation: A review. *IEEE Reviews in Biomedical Engineering, 10*, 235–249.
5. Fedorov, A., Beichel, R., Kalpathy Cramer, J., Finet, J., Fillion Robin, J.-C., Pujol, S., Bauer, C., Jennings, D., Fennessy, F., Sonka, M., Buatti, J., Aylward, S., Miller, J., Pieper, S., & Kikinis, R. (2012). 3D Slicer as an image computing platform for the quantitative imaging network. *Magnetic Resonance Imaging, 30*(9), 1323–1341.
6. Geuzaine, C., & Remacle, J. F. (2009). Gmsh: A 3-D finite element mesh generator with built-in pre- and post-processing facilities. *International Journal for Numerical Methods in Engineering, 79*(11), 1309–1331.
7. Horton, A., Wittek, A., Joldes, G. R., & Miller, K. (2010). A meshless total Lagrangian explicit dynamics algorithm for surgical simulation. *International Journal for Numerical Methods in Biomedical Engineering, 26*, 977–998.
8. Jin, X., Joldes, G. R., Miller, K., Yang, K. H., & Wittek, A. (2014). Meshless algorithm for soft tissue cutting in surgical simulation. *Computer Methods in Biomechanics and Biomedical Engineering, 17*, 800–817.
9. Joldes, G., Bourantas, G., Zwick, B., Chowdhury, H., Wittek, A., Agrawal, S., Mountris, K., Hyde, D., Warfield, S. K., & Miller, K. (2019). Suite of meshless algorithms for accurate computation of soft tissue deformation for surgical simulation. *Medical Image Analysis, 56*, 152–171.
10. Joldes, G., Wittek, A., & Miller, K. (2009). Suite of finite element algorithms for accurate computation of soft tissue deformation for surgical simulation. *Medical Image Analysis, 13*(6), 912–919.
11. Joldes, G. R., Chowdhury, H. A., Wittek, A., Doyle, B., & Miller, K. (2015). Modified moving least squares with polynomial bases for scattered data approximation. *Applied Mathematics and Computation, 266*, 893–902.

12. Joldes, G. R., Wittek, A., & Miller, K. (2011). An adaptive dynamic relaxation method for solving nonlinear finite element problems. Application to brain shift estimation. *International Journal for Numerical Methods in Biomedical Engineering, 27*(2), 173–185.
13. Joldes, G. R., Wittek, A., Miller, K., & Morriss, L. (2008). Realistic and efficient brain-skull interaction model for brain shift computation. In *Computational Biomechanics for Medicine III Workshop, MICCAI*.
14. Joldes, G. R., Wittek, A., Warfield, S. K., & Miller, K. (2012). *Performing brain image warping using the deformation field predicted by a biomechanical model* (pp. 89–96). Springer.
15. Li, M., Miller, K., Joldes, G. R., Kikinis, R., & Wittek, A. (2016). Biomechanical model for computing deformations for whole-body image registration: A meshless approach. *International Journal for Numerical Methods in Biomedical Engineering, 32*(12).
16. Li, M., Wittek, A., Joldes, G. R., & Miller, K. (2016). Fuzzy tissue classification for non-linear patient-specific biomechanical models for whole-body image registration. In G. R. Joldes, B. Doyle, A. Wittek, P. M. F. Nielsen & K. Miller (Eds.), *Computational biomechanics for medicine: Imaging, modeling and computing* (pp. 85–96). Springer International Publishing.
17. Miga, M. I., Sun, K., Chen, I., Clements, L. W., Pheiffer, T. S., Simpson, A. L., & Thompson, R. C. (2016). Clinical evaluation of a model-updated image-guidance approach to brain shift compensation: Experience in 16 cases. *International Journal of Computer Assisted Radiology and Surgery, 11*(8), 1467–1474.
18. Miller, K., Chinzei, K., Orssengo, G., & Bednarz, P. (2000). Mechanical properties of brain tissue in-vivo: Experiment and computer simulation. *Journal of Biomechanics, 33*, 1369–1376.
19. Miller, K., Horton, A., Joldes, G. R., & Wittek, A. (2012). Beyond finite elements: A comprehensive, patient-specific neurosurgical simulation utilizing a meshless method. *Journal of biomechanics, 45*(15), 2698–2701.
20. Miller, K., & Lu, J. (2013). On the prospect of patient-specific biomechanics without patient-specific properties of tissues. *Journal of the Mechanical Behavior of Biomedical Materials, 27*, 154–166.
21. Miller, K., Wittek, A., & Joldes, G. (2011). Biomechanical modeling of the brain for computer-assisted neurosurgery. In *Biomechanics of the brain* (pp. 111–136). Springer.
22. Neal, M. L., & Kerckhoffs, R. (2010). Current progress in patient-specific modeling. *Briefings in Bioinformatics, 11*, 15.
23. Otsu, N. (1979). A threshold selection method from gray-level histograms. *IEEE Transactions on Systems, Man, and Cybernetics, 9*(1), 62–66.
24. Pinter, C., Lasso, A., & Fichtinger, G. (2019). Polymorph segmentation representation for medical image computing. *Computer Methods and Programs in Biomedicine, 171*, 19–26.
25. Pruthi, S., Dawant, B., & Parker, S. L. (2020). Initial experience with using a structured light 3D scanner and image registration to plan bedside subdural evacuating port system placement.
26. Safdar, S., Joldes, G., Zwick, B., Bourantas, G., Kikinis, R., Wittek, A., & Miller, K. (2021). *Automatic framework for patient-specific biomechanical computations of organ deformation* (pp. 3–16). Springer.
27. Ségonne, F., Dale, A. M., Busa, E., Glessner, M., Salat, D., Hahn, H. K., & Fischl, B. (2004). A hybrid approach to the skull stripping problem in MRI. *NeuroImage, 22*(3), 1060–1075.
28. Sorkine, O., Cohen-Or, D., Lipman, Y., Alexa, M., Rössl, C., & Seidel, H. P. (2004). Laplacian surface editing. In *Proceedings of the 2004 Eurographics/ACM SIGGRAPH Symposium on Geometry Processing*.
29. Sullivan, C., & Kaszynski, A. (2019). PyVista: 3D plotting and mesh analysis through a streamlined interface for the Visualization Toolkit (VTK). *Journal of Open Source Software, 4*(37), 1450.
30. Valette, S., Chassery, J. M., & Prost, R. (2008). Generic remeshing of 3D triangular meshes with metric-dependent discrete Voronoi diagrams. *IEEE Transactions on Visualization and Computer Graphics, 14*(2), 369–381.
31. Waldron, K. J., & Kinzel, G. L. (2004). *Kinematics, dynamics, and design of machinery*. Wiley.
32. Lorensen, W. E., & Cline, H. E. (1987). Marching cubes: A high resolution 3D surface construction algorithm. In *SIGGRAPH Computer Graphics*, (Vol. 21, pp. 163–169). Association for Computing Machinery.

33. Wittek, A., Grosland, N., Joldes, G., Magnotta, V., & Miller, K. (2016). From finite element meshes to clouds of points: A review of methods for generation of computational biomechanics models for patient-specific applications. *Annals of Biomedical Engineering, 44*(1), 3–15.
34. Wittek, A., Hawkins, T., & Miller, K. (2009). On the unimportance of constitutive models in computing brain deformation for image-guided surgery. *Biomechanics and Modeling in Mechanobiology, 8*, 77–84.
35. Wittek, A., Joldes, G., Couton, M., Warfield, S. K., & Miller, K. (2010). Patient-specific non-linear finite element modelling for predicting soft organ deformation in real-time; Application to non-rigid neuroimage registration. *Progress in Biophysics and Molecular Biology, 103*, 292–303.
36. Wittek, A., Joldes, G. R., & Miller, K. (2019). *Finite element algorithms for computational biomechanics of the brain* (pp. 243–272). Springer.
37. Wittek, A., Miller, K., Kikinis, R., & Warfield, S. K. (2007). Patient-specific model of brain deformation: Application to medical image registration. *Journal of Biomechanics, 40*, 919–929.
38. Zhang, J. Y., Joldes, G. R., Wittek, A., & Miller, K. (2013). Patient-specific computational biomechanics of the brain without segmentation and meshing. *International Journal for Numerical Methods in Biomedical Engineering, 29*(2), 293–308.
39. Zwick, B.F., Bourantas, G.C., Safdar, S., Joldes, G.R., Hyde, D.E., Warfield, S.K., Wittek, A., & Miller, K. (2022). Patient-specific solution of the electrocorticography forward problem in deforming brain (preprint on ArXiv:2109.07164, submitted to Neuroimage).

Generating Scoliotic Computed Tomography Volumes from Finite Element Spine Models

Austin Tapp, Michael Polanco, Isaac Kumi, Sebastian Bawab, Stacie Ringleb, Rumit Kakar, Carl St. Remy, James Bennett, and Michel Audette

Abstract The use of deep learning (DL) neural networks (NN) for medical image analysis is dependent on available datasets and associated ground truths. Often, pathological image datasets, especially for the spine, are disproportionately challenging to obtain. To assist DL NN training and contribute to the pathological dataset landscape, this study presents a methodology for the generation of scoliotic computed tomography (CT) volume data. The CT data have associated ground truth segmentations of bone and select soft tissues and are produced from biomechanically based, finite element simulations of spine models. Cervical, thoracolumbar, and lumbar spine finite element (FE) models are deformed by FE analyses prior to their conversion into CT volumes, which are characterized by authentic Hounsfield units. Volumes are tested in a pre-trained vertebral segmentation DL NN to prove compatibility with image analysis methods. Further, an osseoligamentous, lumbar FE model, provides volumetric, ground truth segmentations of soft tissue structures; this affords DL NNs the opportunity to expand segmentation predictions to anatomy, like ligaments, that remain inconspicuous in CT imaging.

Keywords Finite element modeling · Synthetic computed tomography · Scoliotic pathology · Osseoligamentous spine mesh · Spine dataset

A. Tapp (✉) · I. Kumi · R. Kakar · M. Audette
Biomedical Engineering, Batten College of Engineering and Technology, Old Dominion University, Norfolk, VA 23529, USA
e-mail: atapp001@odu.edu

M. Polanco · S. Bawab · S. Ringleb
Department of Mechanical Engineering, Batten College of Engineering and Technology, Old Dominion University, Norfolk, VA 23529, USA

C. St. Remy · J. Bennett
Pediatric Orthopedic Surgery and Sports Medicine, Children's Hospital of the King's Daughters, Norfolk, VA 23507, USA

M. Audette
Department of Computational Modeling and Simulation Engineering, Batten College of Engineering and Technology, Old Dominion University, Norfolk, VA 23529, USA

P. M. F. Nielsen et al. (eds.), *Computational Biomechanics for Medicine*,
https://doi.org/10.1007/978-3-031-09327-2_6

1 Introduction

Deep learning (DL) neural network (NN) applications for medical images are almost entirely dependent on the imaging data utilized to train the NN. It is widely recognized that pre-trained models have a limited capacity to perform accordingly on outlier data during testing. These outliers often present themselves as pathological images [1]. Pathological images pose significant challenges, regardless of analysis methodology. Whether analyses are done automatically with NNs, semi-automatically, or manually, unclear image boundaries, image artifacts, traces of surgical activity and shape differences between pathological and asymptomatic anatomy result in significant image analysis complications [2]. Often, the difficulties of performing medical image analysis (MIA) on pathological data simultaneously limit the associated ground truth data determined by experts. These ground truth limitations contribute to a paradox: medical image analysis solutions lack robustness for pathology due to the absence of pathological ground truth data, which are difficult to obtain because image analysis solutions are unfavorable when applied to pathology. This paradox limits dataset availability, which suppresses research progression, and ultimately slows or halts research advancements for MIA. Pathological datasets and their ground truths are crucial components for the proper usage and advancement of artificial intelligence in medical imaging [3].

Pathological datasets occur more frequently for some anatomy. Pathological data for the brain, as both computed tomography (CT) and magnetic resonance imaging (MRI), is common, compared to pathological data for the spine. Pathologies in the spine include compressed, degenerating, or broken bone structures, sports and automobile accident injuries, and scoliosis. The imaging required for physician diagnosis and treatment of such conditions is typically provided by low resolution CT or X-rays. Even in cases of severe scoliosis, simple, biplanar X-ray images are deemed appropriate to determine correction strategies and evaluate Cobb angles [4, 5]. Thus, while asymptomatic spine CT and MRI datasets are prevalent, pathological datasets and associated ground truths are not because the perceived need for the advancement of symptomatic spine image analysis in a clinical setting is minimal. Therefore, DL NNs designed for spine applications are trained with datasets containing limited pathological images. Even the most recent MICCAI vertebral segmentation challenge provided researchers with a dataset of over 400 images, but fewer than 10 images were highly pathological, yielding poor results when these outlier images were tested using the challenge winning network [6]. Based on this outcome, which is seen in Fig. 1, more work can be done to enhance DL NNs and extend NNs' capabilities to all patient cases. Enhancing DL NNs designed for spine applications would improve diagnoses, treatments, and surgery techniques, namely scoliosis correction [7, 8].

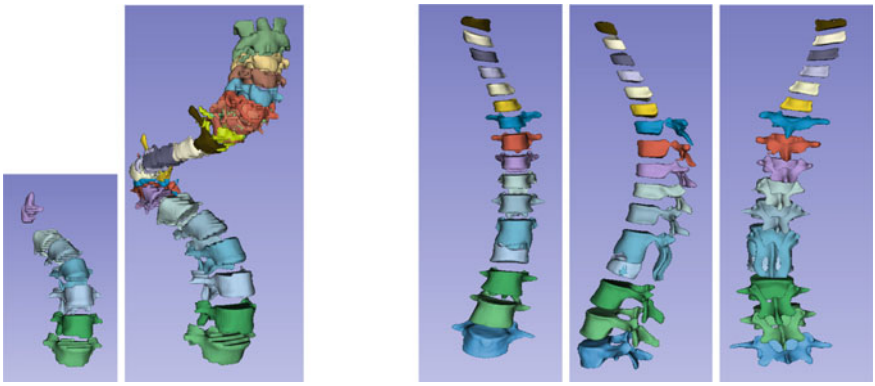

Fig. 1 Vertebrae segmentation results of the MICCAI challenge winning DL NN when run automatically on a severely pathological image (far left) versus with user assistance (second from left). Views of an automatic segmentation result on a moderately pathological image (right side)

1.1 Related Works

Curiously, making NNs more robust to pathological spine images may begin with finite element (FE) models of the spine. Many FE model studies explore spine pathology, focusing on mechanisms for scoliotic induction and lumbar degeneration [9–11]. Using biomechanical models, simulations seek to elucidate the formation or effects of a selected disease, and how the disease may be treated [12–15]. Often, FE models constructed and used in biomechanical simulations are personalized, founded on radiographs, and embody the geometry of symptomatic cases [16–18]. Most FE simulation studies evaluate symptomatic FE meshes, predicting an increase in symptomatic presentation, if treatment is forgone, or a successful correction outcome, if treatment is given [12, 14, 15]. However, it is rare that FE simulation studies explore deforming an asymptomatic spine into a symptomatic one.

The FE models, produced from patient images, have significant potential and applicability toward NN training, especially after simulations result in greater deformations. The potential held by these models is unlocked by transforming deformed FE meshes into a synthetic CT volumes. The manipulation of pathological meshes into synthetic volumes is surprisingly absent from literature. For synthetic volume creation, literature is often focused on the production of synthetic CT from other image modalities, namely MRIs. These methods range from simple algorithms to the use of conditional generative adversarial networks (cGANs) [19–21]. Methods using cGANs are computationally expensive, requiring powerful graphical processing units. The goal of these studies is to better multimodal registration, not to create more robust NN methods for pathological MIA. The CT scans produced are characterized by Hounsfield unit values derived from the original MR image, but are artificially implanted to corresponding areas of the new synthetic CT volume. Most surprisingly, soft tissues conspicuous in the MR image used to generate a synthetic CT (sCT), are

disregarded. However, the availability of soft tissue ground truths paired with sCTs would provide an invaluable asset for enhanced NN training.

This study presents a method that deforms a discretized anatomy with FE simulations to provide an anatomically faithful mesh that embodies scoliotic geometries. The mesh is converted to a synthetic CT image through deformable registration. This unique method permits the formation of pathological data, which have default ground truth segmentations. The sCT volumes are quickly produced from the scoliotic FE meshes at low computational cost and have true Hounsfield unit values. This contribution addresses the paucity of pathological datasets that characterize the current field. Additionally, because ground truths are known, the sCTs do not require analyses by experts, escaping the DL MIA advancement paradox. While this study produces data meant to mimic scoliotic patient datasets, the proposed method is ubiquitously applicable to any musculoskeletal FE modeling. More importantly, the methods presented in this study also explore the use of volumetric, 3-dimensional (3-D) ligaments within FE models of the spine. This allows for the ground truths associated with the synthetic CT data to include 3-D ligament information. The sCTs produced from the ligamentous FE models are terse about soft tissue information, as is the case with true CT images. The sCTs that have associated ligamentous ground truths are useful for the validation of ligament estimation strategies that are based on bony structures or conspicuous anatomical landmarks. The sCTs with ligament ground truths may also provide DL NNs with the ability to segment anatomy remaining inconspicuous in CT images.

2 Methods

2.1 Overview

The presented study is divided into 3 components. Component 1 used prescribed forces to displace anatomy of pre-developed, FE spine meshes, which had healthy, normal curvatures. Component 2 replaced the pre-developed, FE spine meshes with an anatomist-drawn, computer-aided designed (CAD), osseoligamentous FE spine mesh. This osseoligamentous FE spine mesh was subjected to the same prescribed force that was applied to the pre-developed, FE spine mesh. Components 1 and 2 both sought to mechanically deform their respective FE meshes, with healthy curvatures, into FE meshes, with geometrically scoliotic curvatures. Lastly, Component 3 converted the FE meshes, output from Components 1 and 2, into sCT volumes. The methodological overview is illustrated by Fig. 2.

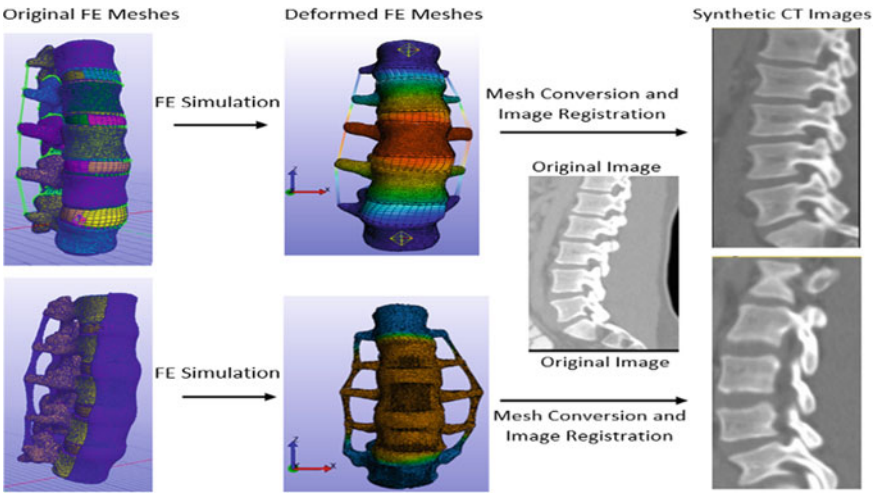

Fig. 2 An overview of presented methods. The top level shows component 1, the deformation of a pre-developed lumbar FE spine mesh. The bottom level, component 2, displays equivalent deformation applied to an osseoligamentous, lumbar FE spine mesh. Component 3 begins with mesh to image conversion, when deformed meshes are used to produce synthetic CT images

2.2 Finite Element Anatomical Meshes

Two FE spine meshes previously validated and developed for the open-source, biomechanics-based finite element analysis software program FEBio (FEBio, Salt Lake City, UT, USA) were obtained [22–24]. Component 1 utilized these three-dimensional, non-linear FE spine meshes, which were produced radiographically from healthy female subjects aged 49 and 26 years. The FE spine meshes included anatomy of the lumbar spine, from the 49-year-old, and of the cervical spine from the 26-year-old. Both FE spine meshes are of hybrid type, combining hexahedral meshes for some soft tissues, like intervertebral discs (IVDs), and linear tetrahedral meshes for bony vertebrae structures.

Component 2 utilized a healthy, osseoligamentous, generic-CAD spine mesh. This anatomist developed CAD spine mesh was tetrahedralized with PreView, a FE processing program compatible with FEBio that converts triangular surfaces to tetrahedral volumes [22]. By converting the CAD spine, two original FE spine meshes were developed: an osseoligamentous, lumbar FE spine mesh, containing 3-D ligaments, and a simplistic thoracolumbar FE spine mesh. The simplistic thoracolumbar FE spine mesh was used only for a methodological proof of concept; it is in its infancy and does not yet contain 3-D ligaments. Further, there is no reciprocal, FE spine mesh readily developed to provide an appropriate comparison. Therefore, the purpose of the thoracolumbar FE spine mesh is to provide a predictive metric that compares the extent of deformation possible during FE analyses of FE spine meshes containing more than 8 vertebrae.

The four FE spine meshes each use volumetric components for the following anatomy: cortical bone, trabecular bone, posterior bone, vertebral endplates, cartilage endplates, nucleus pulposus, annulus matrices, and annulus fibers. The pre-developed lumbar and cervical FE spine meshes represented ligaments as simplified, hand-drawn, discrete elements, namely 1-dimensional rods or springs. To the authors' knowledge, a few studies have modeled some, but never simultaneously all, spinal ligaments in 3-D [25]. The CAD-based, lumbar FE spine mesh represents all spine ligaments with tetrahedral, 4-node solids. The adjustment from simplistic to 3-D ligament representations constitutes the only differences between the two lumbar FE spine meshes; this difference is visually reflected in Fig. 3.

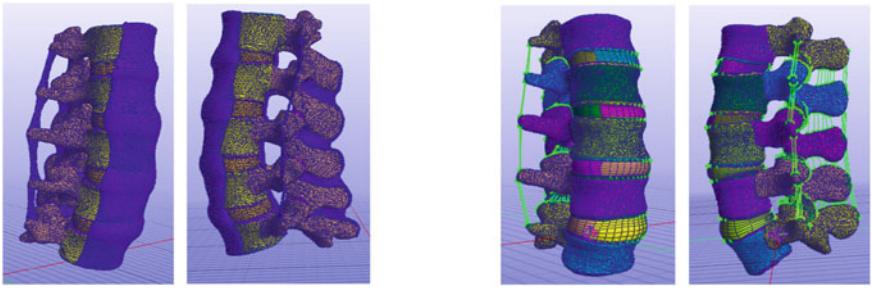

Fig. 3 The CAD-based lumbar FE spine mesh with 3-D ligaments (left side) versus the pre-developed lumbar FE spine mesh with hand-drawn spring elements as ligaments (right side)

Material properties for elements of all the FE spine meshes were derived from published studies and are shown in Tables 1 and 2 [23–28]. A neo-Hookean model represented the material of the trabecular bone, posterior bone, nucleus pulposus and both endplate types. Orthotropic elastic material represented the cortical bone. The annulus fibrosus was represented as two parts: (1) a matrix component using a

Table 1 Material property constants shared by the pre-developed and CAD-based FE meshes

Structure	Materials	Young's modulus (MPa)	Poisson's ratio	References
Cortical bone	Orthotropic elastic	$E_1 = 8000$, $E_2 = 8000$, $E_3 = 12{,}000$	$\nu_{12} = 0.4$, $\nu_{23} = 0.3$, $\nu_{31} = 0.35$	[23–25]
Trabecular bone	Neo-Hookean	$E = 100$	$\nu = 0.2$	[23–25]
Posterior bone	Neo-Hookean	$E = 3500$	$\nu = 0.3$	[23–25]
Vertebral endplate	Neo-Hookean	$E = 1000$	$\nu = 0.3$	[23–25]
Cartilage endplate	Neo-Hookean	$E = 23.8$	$\nu = 0.42$	[23–25]
Nucleus pulposus	Neo-Hookean	$E = 1$	$\nu = 0.49$	[23–25]
Facet cartilage	Neo-Hookean	$E = 30$	$\nu = 0.4$	[23–25]

Table 2 Additional shared material property constants and the material property constants exclusive to the 3-D ligaments, which are only included in the CAD-based lumbar spine FE mesh

Structure	Materials	Property constants	References
Annulus matrix	Holmes-Mow	$E = 1$ MPa, $ß^1 = 3.4$	[23–25]
Annulus fibers	Fiber-exponential-power	$\alpha^2 = 65$, $ß^3 = 2$, $\xi^4 = 0.296$ MPa	[23–25]
All 3-D Ligaments: Coupled transversely-iso-Interspinous, Liga-tropic Mooney-Rivlin menta Flava, Inter-transverse, Supraspinous, Longitudinal ligaments, and zygapophyseal joints		$c_1 = 2.1660$ MPa, $c_2 = 0$ MPa, $c_3 = 0.2677$ MPa, $c_4 = 83.0594$, $c_5 = 535.5720$, $k^5 = 436.845$ MPa, $\lambda^6 = 1.0498$	[25, 26]

1: exponential stiffening coefficient, 2: coefficient of exponential argument, 3: power of exponential argument, 4: fiber modulus, 5: bulk like modulus, 6: maximum fiber straightening stretch

compressible Holmes-Mow model and (2) fiber components that applied an exponential power law to describe the strain energy density. Only the material properties of the ligaments differed between the two lumbar FE spine meshes. The pre-developed lumbar FE spine mesh grouped simplistic ligaments and tied them to displacement-force curves, whereas experimentally derived material properties were assigned to the ligaments within the CAD-based lumbar FE spine mesh. Viscoelastic, coupled, transversely-isotropic Mooney-Rivlin material was used to define all the 3-D ligaments of the CAD-based lumbar FE spine mesh [23–26]. For simplicity, and because not every spinal ligament had experimentally determined properties, material values from the published studies were averaged and applied ubiquitously to each 3-D ligament [25, 26]. The lumbar FE spine mesh developed for FEBio contains 415,567 elements, the cervical FE spine mesh developed for FEBio contains 245,456 elements. The osseoligamentous lumbar FE spine mesh that has 3-D ligaments contains 394,040 elements, and the thoracolumbar FE spine mesh with no ligaments contains 227,961 elements (Table 3).

2.3 Displacement and Boundary Conditions Applied to FE Meshes

Components 1 and 2 of this study utilized FEBio for FE analysis because of its credibility, its capacity to solve multiphysics problems and its compatibility with the pre-developed FE spine meshes. Component 1 of the study sought to produce the geometric shape of scoliotic spines using the FE meshes originally developed for FEBio. To induce a scoliotic shape, boundary conditions were applied the FE mesh in a phenomenological manner. While previous studies have explored more complex loading regimes, such as buckling theory or asymmetric vertebral plate growth, these studies sought to determine the etiology of scoliosis [9, 11, 15, 18]. The goal of this study was to convert a FE spine mesh, having a generally scoliotic appearance, into a synthetic CT volume. Therefore, simplistic boundary conditions

Table 3 The total number of elements in each of the presented models of the pre-developed cervical spine and lumbar spine and the CAD lumbar spine and CAD thoracolumbar spine

Model	Element formulations used	Elements, nodes and faces
Pre-developed cervical FE spine mesh	8-node solid (IVDs), 4-node solid (Vertebra), triangular surface mesh (Skull Base), 2 node tension-only springs (ligaments)	245,456 71,113 93,431
Pre-developed lumbar FE spine mesh	8-node solid (IVDs), 4-node solid (Vertebra), 2 node tension-only springs (ligaments)	415,567 99,072 106,358
CAD-based lumbar FE spine with 3-D ligaments	4-node solid (Vertebra and ligaments)	394,040 117,321 50,757
CAD-based thoracolumbar spine, no ligaments	8-node solid (IVDs), 4-node solid (Vertebra)	227,961 153,667 84,990

that yielded geometrically scoliotic FE spines were utilized. First, to simulate that the FE spine meshes were part of larger spinal column, upper vertebral endplates of the most superior vertebrae and lower vertebral endplates of the most inferior vertebrae were fixed, acting as a rigid constraint. Next, a linear, prescribed, transverse displacement was applied as a boundary condition to all nodes that comprised the bony structure of the most central FE mesh's vertebra. For the cervical FE mesh, this was C4; for the lumbar FE mesh, this was L3. Component 2 of the study followed this same procedure, starting with endplate fixation. L3 of the lumbar CAD-based FE mesh and T10 of the thoracolumbar CAD-based FE mesh were subjected to boundary conditions identical to those applied in Component 1. The linear boundary conditions were continuously applied in a transient manner to all the central FE meshes' vertebra, until a subsequent time step resulted in deformations that prematurely terminated the FE model's run.

2.4 Conversion of FE Meshes to Synthetic CT Volumes

Component 3 of the study converts the FE meshes, which have undergone FE analyses to appear scoliotic, into sCT volumes. Once boundary conditions have been applied to the FE spine meshes, they are exported as triangular surface meshes. During this export, the simplistic, 1-dimensional hand drawn ligaments of the pre-developed FE spine meshes cannot be transferred. In the CAD-based FE spine meshes, all structures, including the 3-D ligaments, are exported as triangular surface meshes. Next, the surface mesh is resampled with a selected, true CT volume. This resampling uses the voxel locations of the true CT volume and the point values of the surface mesh to maintain the mesh's structure but adjust its size and spacing to match that of the true CT volume. Then, the resampled mesh is binarized. All mesh structures are

classified as foreground and empty space introduced during resampling is classified as background; this yields a binary volume of the mesh. Finally, the true CT volume is deformably registered onto the newly created mesh volume, which is structurally identical to the surface mesh it was created from. There are many available volume-to-volume deformable registration tools and multiple options were tested, including BRAINS, Elastix, ANTs and demons, but the most convenient and effective choice was a 3D Slicer plug-in of Elastix [29, 30]. Because Elastix applies intensity-based registration methods, voxels representing the conspicuous bone structures of the true CT were exceptionally aligned onto the voxels representing the foreground components of the mesh-based volume [31]. Simultaneously, this method of volume-to-volume registration consistently maintains Hounsfield unit values of the true CT. By applying a mask that obscures bone bereft portions of the true CT, the deformation field warping the true CT onto the mesh-based volume will ensure ideal bone-to-bone alignment and explicitly preserve the original image intensity values that surround bony structures of the true CT. This elegant but simple solution rapidly produces sCT volumes that have true CT equivalent Hounsfield unit (HU) intensity values for all portions of the image. Additionally, the output sCT innately has a corresponding ground truth segmentation, the original triangular surface mesh that was exported from FEBio.

If the mesh contains 3-D ligaments, like in the CAD-based FE mesh, the deformation process is slightly different. Two triangular meshes are exported, one with 3-D ligaments and one without. By exporting a triangular mesh without ligaments, the process of volume-to-volume registration is maintained. Once again, Elastix performs bone-to-bone registration but defers ligament presence in the sCTs. The meshes with ligaments can provide 3-D ligament ground truth segmentations for the sCT, if desired. Following the true CT to mesh-based volume registration, a deformation field is produced. By inverting and applying this field to the counterpart 3-D ligament mesh-based volume, an artificial ground truth segmentation containing surmised ligament positions of the true CT image can be obtained. This may be an added benefit of the proposed method, however, the positioning of the extrapolated ligaments in the artificial ground truth should be evaluated. While this evaluation is outside the scope of this study, it should be recognized that extrapolations would likely be more accurate for ligaments in closer proximity to bony structures (i.e. the anatomy prioritized by the Elastix registration process).

3 Results

For Component 1 (see Sect. 2.3), both the pre-developed lumbar and cervical spine FE meshes were deformed using prescribed displacement to create a scoliotic curve profile. The pre-developed lumbar FE mesh had its L3 vertebra displaced to 6.2 mm in the sagittal direction. The pre-developed cervical FE mesh was displaced farther, to 8.8 mm in the sagittal direction. For Component 2 (see Sect. 2.3), the CAD-based lumbar FE mesh with 3-D ligaments and the CAD-based thoracolumbar FE mesh

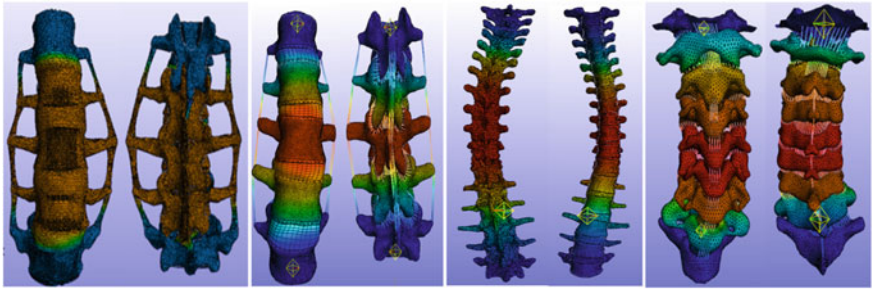

Fig. 4 All FE meshes after deformation, from left to right: the CAD-based lumbar FE spine mesh with 3-D ligaments, the pre-developed lumbar FE spine mesh with simple ligaments, the CAD-based thoracolumbar FE spine mesh without ligaments and the pre-developed cervical FE spine mesh with simple ligaments. FE mesh coloring, from blue to red, indicates the magnitude of the mesh's transverse displacement, as minimum to maximum displacement, respectively

were also deformed, with the same prescribed displacement used in Component 1, to create a scoliotic curve profile. The CAD-based lumbar FE mesh was slightly stiffer than its pre-developed lumbar FE mesh counterpart. The L3 vertebra of the CAD-based FE mesh was displaced 5.1 mm. The CAD-based thoracolumbar spine was the most successfully displaced. Although this model is unrestricted by ligaments, the number of vertebrae within the model seem to have permitted a greater degree of displacement, to 33 mm. These components' results are shown in Fig. 4.

For component 3 (Sect. 2.4), all FE meshes, pre-developed and CAD-based, were converted into 4 different sCT images, one for each mesh. Figure 5 shows coronal views of 3 out of 4 sCT images and 2 true CT counterparts, while the farthest right images of Fig. 2 display sagittal views of both lumbar sCTs. Each sCT volume had voxel intensity values that remained consistent with its true CT. sCT values ranged from −1136 to 1687 HUs. Figure 6 displays histograms of both true CTs and sCTs for lumbar and cervical volumes. The 4 resulting sCTs were processed with MICCAI's vertebral segmentation challenge winning network, which achieves an average Dice score of 91.23% on unseen, true CT images [32]. Figure 7 presents what the network observed when reading sCT images. Further, Fig. 7 demonstrates the network was successfully able to segment mildly pathological sCTs. Figure 1 reveals the difficulty of segmenting the moderately pathological thoracolumbar sCT. The network's ability to process the sCTs confirms sCT volumes may be utilized to train and test DL NNs.

4 Conclusion

This study has presented a successful method for the generation of pathological, synthetic, CT volumes, which are based on finite element spine meshes that have undergone biomechanically-driven deformations. The presented method is broadly applicable toward any kind of pathological sCT generation, provided the FE mesh is

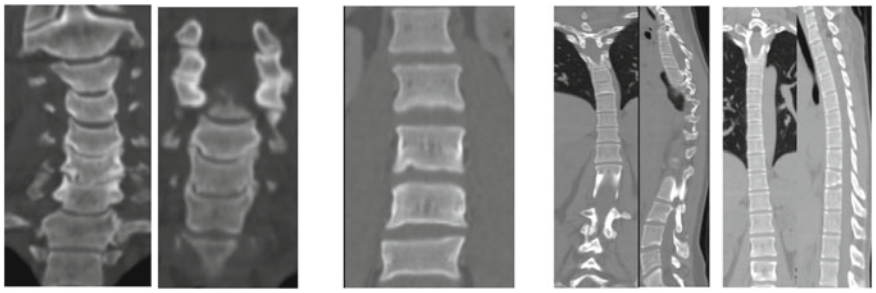

Fig. 5 Left to right: pre-developed, cervical sCT and true CT volume, only the CAD-based lumbar sCT volume (no true CT pair), and two view planes of the thoracolumbar sCT next to a true thoracolumbar CT volume

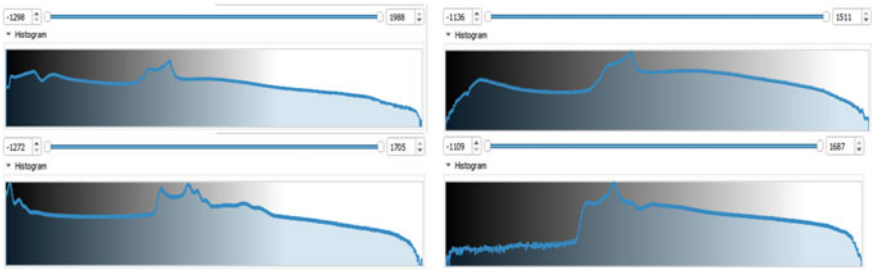

Fig. 6 Histograms of the true cervical spine CT (top left), the cervical sCT (top right), the true lumbar spine CT (bottom left) and the lumbar sCT (bottom right)

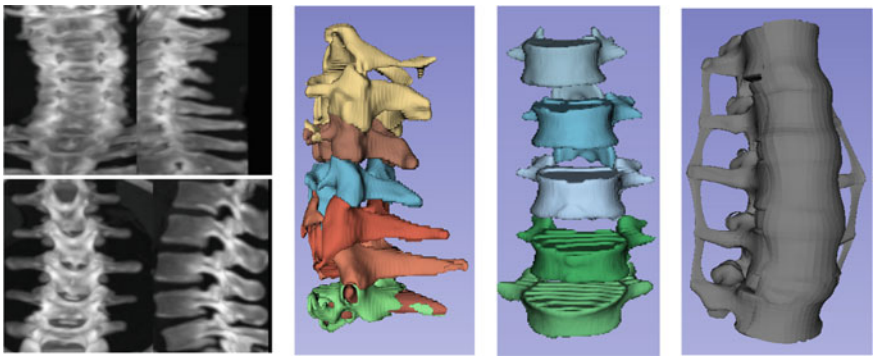

Fig. 7 (top left) The cervical sCT and (bottom left) lumbar sCT as seen by the DL NN, their output segmentations (middle), and the ligamentous ground truth of the lumbar sCT (far right)

musculoskeletal in nature and undergoes appropriate deformation. The sCT volumes produced are achieved at little computational expense, contain true Hounsfield unit values, can have associated ligamentous ground truths, and as shown, may be readily introduced to training or testing datasets for DL NNs. The deformed FE meshes were converted to volumes, whose voxel footprints have the intensity characteristics of scoliotic images, alleviating the scarcity of pathological spine datasets that constitute the current field. Ground truth segmentations of bone structures and 3-D ligaments are known, obviating the need for challenging, manual, MIA by experts. The sCTs that have associated ligamentous ground truths are useful for ligament estimation and validation of ligament positioning, when positions are surmised by conspicuous anatomical landmarks, such as bones.

References

1. Shen, D., Wu, G., & Suk, H. (2017). Deep learning in medical image analysis. *Annual Review of Biomedical Engineering, 19*, 221–248.
2. Ibragimov, B., Korez, R., et al. (2017). Segmentation of pathological structures by landmark-assisted deformable models. *IEEE Transactions on Medical Imaging, 36*(7), 1457–1469.
3. Mongan, J., Moy, L., & Kahn, C. E. (2020). Checklist for artificial intelligence in medical imaging (CLAIM): A guide for authors and reviewers. *Radiology: Artificial Intelligence*, *2*(2).
4. Illés, T., & Somoskeöy, S. (2012) The EOS™ imaging system and its uses in daily orthopaedic practice. *International orthopaedics.* Springer.
5. Mohamed, M., Trivedi, J., et al. (2020). Adolescent idiopathic scoliosis: A review of current concepts. *Orthopaedics and Trauma, 34*(6), 338–345.
6. Sekuboyina, A., Bayat, A., et al. (2020) VerSe: A vertebrae labelling and segmentation benchmark.
7. Cheung, Z. B., Selverian, S., et al. (2019). Idiopathic scoliosis in children and adolescents: Emerging techniques in surgical treatment. *World Neurosurgery, 130*, e737–e742.
8. Audette, M. A., Schmid, J., et al. (2019). Towards a deformable multi-surface approach to ligamentous spine models for predictive simulation-based scoliosis surgery planning. In *Lecture Notes in Computer Science* (Vol. 11397 LNCS, pp. 90–102).
9. Sarwark, J. F., Castelein, et al. (2019) The biomechanics of induction in adolescent idiopathic scoliosis: Theoretical factors. *Journal of Bone and Joint Surgery—American Volume.*
10. Sylvestre, P. L., Villemure, I., & Aubin, C. É. (2007). Finite element modeling of the growth plate in a detailed spine model. *Medical and Biological Engineering and Computing*, *45*(10).
11. Shi, L., Wang, D., et al. (2011). Biomechanical analysis and modeling of different vertebral growth patterns in adolescent idiopathic scoliosis and healthy subjects. *Scoliosis*, *6*(1).
12. Little, J. P., & Adam, C. (2011). Patient-specific computational biomechanics for simulating adolescent scoliosis surgery: Predicted vs clinical correction for a preliminary series of six patients. *International Journal for Numerical Methods in Biomedical Engineering*, *27*(3).
13. Chen, C. S., Cheng, C. K., et al. (2001). Stress analysis of the disc adjacent to interbody fusion in lumbar spine. *Medical Engineering and Physics, 23*(7), 485–493.
14. Abolaeha, O. A., Weber, J., & Ross, L. T. (2012). Finite element simulation of a scoliotic spine with periodic adjustments of an attached growing rod. In *34th Annual International Conference of the IEEE EMBS San Diego, California USA* (pp. 9–16).
15. Wang, W., Baran, G. R., et al. (2014). The use of finite element models to assist understanding and treatment for scoliosis: A review paper. *Spine Deformity, 2*(1), 10–27.
16. Wang, L., Zhang, B., et al. (2016). A validated finite element analysis of facet joint stress in degenerative lumbar scoliosis. *World Neurosurgery, 95*, 126–133.

17. Grunwald, A. T. D., Roy, S., et al. (2021). Assessment of adolescent idiopathic scoliosis from body scanner image by finite element simulations. *PLoS ONE*, *16*(2 February), e0243736.
18. Clin, J., Aubin, C. É., et al. (2011). A new method to include the gravitational forces in a finite element model of the scoliotic spine. *Medical & Biological Engineering & Computing, 49*(8), 967–977.
19. Chegeni, N., Birgani, M., et al. (2019). Introduction of a simple algorithm to create synthetic-computed tomography of the head from magnetic resonance imaging. *Journal of Medical Signals and Sensors, 9*(2), 123–129.
20. Mangalagiri, J. (2021). Toward generating synthetic CT volumes using a 3D-conditional generative adversarial network. (2).
21. Baydoun, A., Xu, K., et al. (2020). Dixon-based thorax synthetic CT generation using generative adversarial network. *Intelligence-Based Medicine, 3–4*, 100010.
22. Maas, S. A., Ellis, B. J., Ateshian, G. A., & Weiss, J. A. (2012). FEBio: Finite elements for biomechanics. *Journal of Biomechanical Engineering*, *134*(1).
23. Finley, S. M., Brodke, D. S., et al. (2018). FEBio finite element models of the human lumbar spine. *Computer Methods in Biomechanics and Biomedical Engineering, 21*(6), 444–452.
24. Herron, M. R., Brockmeyer, D. L., et al. (2020). FEBio finite element models of the human cervical spine. *Journal of Biomechanics.* In Press.
25. Hortin, M. (2015). Ligament model fidelity in finite element analysis of the human lumbar spine. *Mechanical Engineering*, *MS*. Retrieved from https://scholarsarchive.byu.edu/etd
26. Kim, H. J., Chun, H. J., et al. (2009). A validated finite element analysis of nerve root stress in degenerative lumbar scoliosis. *Medical and Biological Engineering and Computing*, *47*(6).
27. Peña, E., Calvo, B., et al. (2006). A three-dimensional finite element analysis of the combined behavior of ligaments and menisci in the healthy human knee joint. *Journal of Biomechanics.*
28. Weiss, J. A., Maker, B. N., & Govindjee, S. (1996). Finite element implementation of incompressible, transversely isotropic hyperelasticity. *Computer Methods in Applied Mechanics and Engineering, 135*(1–2), 107–128.
29. Wang, M., & Li, P. (2019). A review of deformation models in medical image registration. *Journal of Medical and Biological Engineering*. Springer Berlin Heidelberg.
30. Fu, Y., Lei, Y., et al. (2020). Deep learning in medical image registration: A review. *Physics in Medicine and Biology*. IOP Publishing Ltd.
31. Klein, S., Staring, M., et al. (2010). Elastix: A toolbox for intensity-based medical image registration. *IEEE Transactions on Medical Imaging, 29*(1), 196–205.
32. Payer, C., & Štern, D. (2020). Coarse to fine vertebrae localization and segmentation with spatialconfiguration-Net and U-Net. In *VISIGRAPP 2020* (Vol. 5, pp. 124–133).

Morphological Variation in an Endothelial Cell Population: A Virtual-Cell Model

Yi Chung Lim, Michael Cooling, Sue McGlashan, and David S. Long

Abstract The mechanotransmission of fluid-induced forces in endothelial cells is a focal determinant of atherosclerosis. Understanding mechanotransmission is a key step towards developing endothelial-cell based therapies for cardiac diseases. Mechanotransmission is dependent on cell morphology, yet the effect of population morphological variation on mechanotransmission has not yet been examined. We have developed a set of morphological descriptors to quantify three-dimensional morphological variation in a population of human microvascular endothelial cells. From these data we determined quantitatively how the morphology of any cell compares to the overall population. Descriptors were used to generate virtual cells representative of the population morphologies. These virtual cells can be used as the spatial domain in a finite-element analysis. To the best of our knowledge, our study is the first to examine morphological variation in an EC population using a virtual cell approach.

Keywords Cell morphology · Endothelial cells · Principal component analysis · Spatial statistics generative models · Endothelial cells

1 Introduction

Blood flow-induced wall shear stress (WSS) is a key determinant of vessel health and function. The detection and response to fluid-induced WSS is mediated by endothelial cells (ECs) in a process known as mechanotransduction [1]. Abnormal EC mechanotransduction of WSS has been postulated to be a focal determinant for the pathogenesis of atherosclerosis [2–4]. Hence EC's have untapped potential as a basis

Y. C. Lim · M. Cooling
Auckland Bioengineering Institute, University of Auckland, Auckland, New Zealand

S. McGlashan
Faculty of Medical and Health Science, University of Auckland, Auckland, New Zealand

D. S. Long (✉)
Department of Biomedical Engineering, Wichita State University, Wichita, KS, USA
e-mail: david.long@wichita.edu

P. M. F. Nielsen et al. (eds.), *Computational Biomechanics for Medicine*,
https://doi.org/10.1007/978-3-031-09327-2_7

of treatment and diagnosis of cardiac disease. However, before these therapeutic interventions can be developed more needs to be understood about the process of mechanotransduction.

Finite element models have been employed to quantify EC mechanotransmission [5], integrating three inputs: (1) boundary conditions representing haemodynamics, (2) material properties of the cell, and (3) spatial geometry of the cells (morphology). The latter input can further be categorised into idealised geometry models, which typically represent the cell as a simple geometric shape, such as a hemisphere or a simple polygon [6–8], or cell-specific models which have a geometry based on micrograph images of a cell, and therefore, typically have a higher computational cost to represent the cell [9–11]. Neither cell-specific nor idealised geometry models consider the effect of morphological variation in the population on their estimates of mechanotransmission. As such, it is uncertain whether the findings of these studies can be applied to the overall cell population. There is reason to suggest they cannot be: Ferko et al. demonstrated that the distribution of focal adhesions causes heterogenous stress/strain distributions. They also found that stresses concentrated at the interface of the nucleus and cytoplasm [10]. This suggests that varying focal adhesion and nuclei morphology would have resulted in substantially different stress/strain estimates. Caille et al. found that rounded cells had an elastic response to compression, whereas spread cells of identical elastic moduli exhibited hysteresis [9]. Taken together, these results suggest that individual endothelial morphology is an important determinant of cell mechanical behaviour. Thus, we believe it is important to consider morphological variation in the population of cells when performing single cell mechanical simulations.

EC morphology has been qualitatively described as “polygonal”, “elongated”, “ellipsoidal”, “cobblestone” [12–15]. Two-dimensional scalar quantitative measures have also been developed, such as the axis of orientation, length, area, perimeter length, width, width-length ratio, axis-interaction ratio, shape index and angle orientation with respect to the flow direction [16–18]. More advanced quantitative morphological descriptors include statistical based descriptors of the associated bivariate spatial point pattern (points are centroids of the cell, and triple points, where three neighbouring cells meet, thus capturing information about shape interaction with neighbouring cells) [19]. Another important descriptor is the hydrodynamic shape factor proposed by Barbee et al., which is the proportional constant relating shear stress to cell surface height across an entire endothelial cell layer. They found that the hydrodynamic shape factor was significantly different in populations of cells that had remodelled to align with the flow direction, hence their shape factor could characterise three-dimensional population morphology in response to WSS.

Existing morphological descriptors are insufficient for examining the effect of population morphology variation on mechanotransmission. This is because a specific cell cannot be re-created from a set of its morphological descriptors. Furthermore, a global set of morphological descriptors cannot be used to generate a virtual cell that is representative of the entire population. Hence although idealised geometries can be generated, it is not possible to generate a realistic spatial domain suitable for a finite-element model based on these morphological descriptors. Therefore, the

relationship between a cell's morphological description and its mechanotransmission behaviour has not been quantitatively assessed.

Morphological variation may have a substantial effect on the mechanotransmission of fluid-induced WSS. To quantify this effect, we first need to be able to quantify the morphological variation in a cell population. Therefore, in this study, we aim to quantify the morphological variation in an EC population. The starting point for our methods to quantify the three-dimensional morphological variation was the generative model approach, proposed by Murphy et al. [20–22]. We have developed a modified set of morphological descriptors and quantified them within a population of endothelial cells. From this data set we have generated three-dimensional virtual cells.

2 Materials and Methods

We imaged a single population of endothelial cells cultured under identical conditions (total cells, $N = 15$). The morphological variation found in the cells of this population is typical of what is observed in statically cultured endothelial cells. The nucleus, f-actin and acetylated α-tubulin components of the cytoskeleton were imaged. Shape descriptors were formulated to numerically describe the three-dimensional morphology of the nucleus and cell membrane. The statistical variation in each descriptor was analysed by creating virtual cells with a morphology based on the morphological descriptor distribution of the entire population of endothelial cells.

2.1 Cell Culture and Imaging

Unless otherwise stated all materials were obtained from Thermo Fisher Scientific. Human microvascular endothelial cells (HMEC-1 s) were cultured using previously described methods [23, 24].

The nucleus, acetylated α-tubulin and f-actin were stained and imaged. The protocol is as follows: Upon confluence cells were fixed with 4% paraformaldehyde (#158,127–100, Sigma Aldrich, St Louis, MO, USA) for 30 min at 37 °C, then washed with PBS (3 × 5 min, #00–3000). Next, cells were permeabilized in triton X-100 (0.5%, 5 min, #T9284, Sigma-Aldrich), followed by PBS wash (3 × 5 min). To image the nucleus, cells were stained with Hoechst 33258 (1:1000, #B2883, Sigma-Aldrich) for 5 min at room temperature and washed with PBS (3 × 5 min). To image acetylated α-tubulin, cells were blocked with goat serum (1:20, #G9023 Sigma-Aldrich) for 30 min at room temperature. They were then incubated overnight with 611b (1:500, #T7451 Sigma-Aldrich). This was followed by a two-hour incubation with secondary antibody goat anti mouse Alexa Fluor 594 (1:500, #A11005), and a PBS wash (3 × 5 min). To image f-actin, cells were incubated with Alexa Fluor

Phalloidin 488 (1:500, #A12379) for 30 min at room temperature, followed by PBS washes (3 × 10 min).

Next, coverslips were mounted directly onto 6-well plates using ProLong Gold (#P36934). The bottom of each well (with coverslip attached) was then removed with a heated scalpel to allow direct imaging. An Olympus FV1000 laser scanning confocal microscope with a 60 × /1.35 NA oil immersion lens was used to image the cells. Diode-pumped 405 nm (to image the nuclei nucleus), helium neon 543 nm (acetylated α-tubulin) and an argon ion multi-line 458 nm (primary cilium and f-actin) lasers were used to sequentially excite samples. Acquired image resolution acquired was 1600 pixels × 1600 pixels, with an x–y spatial resolution 0.132 μm/pixel and z spatial resolution of 0.424 μm/slice. Thus, the three-dimensional topography of cell was characterised as a stack of images, from which the morphological descriptors were extracted.

2.2 Morphological Descriptors

2.2.1 Nuclei

To quantify nuclei morphology we used a modified version of the method described by Buck et al. [20], (see Fig. 1). This method involved four morphological descriptors per nucleus: (1) median axis; (2) Nucleus width, where both (1) and (2) are $1 \times n$ vector, where n is the number of pixels in nucleus; (3) nucleus length (scalar value); and, (4) centroid vector ($3 \times n$ vector, where m is the number of z-direction slices in the nucleus).

Cells were aligned using the nuclei as the point of reference, such that the long of axis of the nuclei formed the y-direction (see Fig. 1). The median axis was defined as the point equidistant from nucleus boundary in the x-direction, left-to-right. The equidistant length was defined as the nucleus width. Nucleus length is the length of the longest possible line that can be drawn in the nucleus. Centroid vector describes the relative position of the nucleus centroid in each z-slice. A distribution for each morphological descriptor was gathered from a population of cells ($N = 15$). By sampling from this distribution, it is possible to generate nuclei representative of the entire population.

2.2.2 Cell Edge

The cell membrane was not explicitly imaged in this study. Instead, the edge of the cell was approximated as being one pixel (132 nm) beyond the edge of the f-actin and acetylated α-tubulin features. This is a reasonable assumption as f-actin is present in the actin cortex, which lies on the inner face of the cell membrane [25, 26]. The morphological descriptors of the cell membrane were adapted from Buck et al. [20].

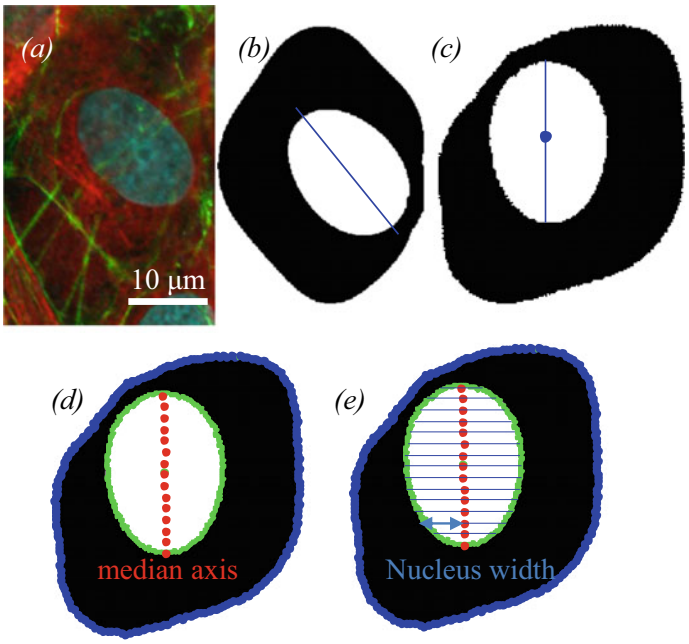

Fig. 1 Quantifying nuclei morphology using morphological descriptors. **a** Triple-labeled co-image of a human microvascular endothelial cell, with the nucleus in blue, f-actin in green and acetylated α-tubulin in red. **b** Thresholded image of cell shown in **a** with the central axis in blue. The central axis length is the nucleus length. **c** Cells were rotated so that the central axis runs top-to-bottom. **d** The median axis was found (red dots), as the point along the row (shared y coordinate) that is equally distant from either edge of the nucleus. **e** This distance is known as the nucleus width (blue lines)

First, all the cells were centered around the nuclei centroid, and aligned (see Fig. 1 b-d). The centroid of each slice was also determined, and the x and y displacement between the slice centroid and the origin was recorded. In each slice the cell boundary was detected by finding the boundary at 240 equally-angled points, radiating outwards 1.5° apart from the slice centroid (see Fig. 2). Instead of storing these points as x, y, z coordinates, they were converted to a polar coordinate system, hence only 240 radial lengths were needed (as the angle is known).

Hence the cell membrane morphological description could be stored as a $241 \times n$ cell edge vector, where n is the number of slices, being 240 radial lengths, and a single z coordinate that all the points in each slice share. Prior to calculating radial length, each x and y coordinate in the cell edge vector was normalized by the displacement of the slice centroid relative to the origin. This was repeated in all 15 cells.

Principal component analysis (PCA) was used to analyse the morphological variation in these 15 cell membrane edges. Since only a few shape modes are needed to recreate the cell (8 explains 93% variance), PCA reduces the dimensionality of the

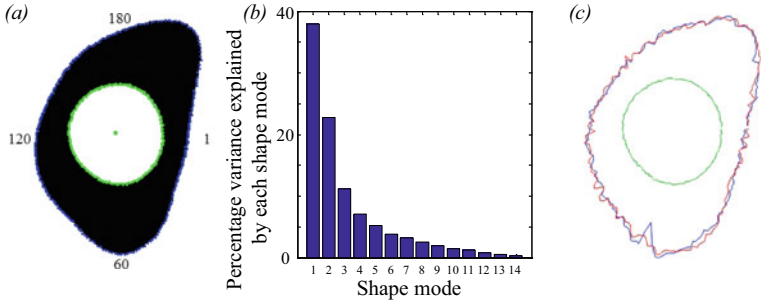

Fig. 2 Spatial descriptors of the cell edge. **a** Illustration of polar-coordinate description of the cell outline, 240 data points outlined in blue. **b** Percentage of shape variation explained by each of the shape modes found using principal component analysis on the 3D cell edge data set. The first 8 modes accounted for >93% of the total variation. **c** Goodness of fit of the results of the genetic algorithm (blue) versus the actual cell outline (red), in 2D, using 8 shape modes. The actual nucleus is shown in green

dataset [20, 27–33]. Conceptually, PCA describes each cell edge as a linear combination of the average cell edge shape and a series of shape modes multiplied by a weighting. Each specific cell is generated using a different weighting set. The PCA process is as follows: firstly, the cell edge shape in each slice is described as a 241 $\times$ n vector. This vector was converted back into Cartesian coordinates resulting in a 1 $\times$ 720n vector (n slices, each slice having 240 x, y, and z coordinates). A matrix was formed from the edge vectors of all 15 cells, 15 $\times$ 720n. Each column was centered by subtracting the average cell edge shape vector (also 1 $\times$ 720n vector). The singular value decomposition algorithm was then performed on the matrix. The resulting eigenvalues were the variance of the population of cells in the direction of each of the shape modes. The eigenvectors are the shape mode directions.

Virtual cell membrane shapes can be generated by randomly generating shape mode weightings. The square root of the eigenvalue is the standard deviation of that particular shape mode (corresponding eigenvector) in the population. Hence, the weightings can be sampled from a normal distribution with a mean (zero, as data are centered), and standard deviation, to generate "typical" cells, or sampled from three standard deviations above or below the mean to generate "atypical" cells. For example, random weightings for the kth shape mode, w_k, can be generated from a normal distribution on the interval (a, b) for one standard deviation by

$$w_k = \mathrm{a} + (b - a) \times R$$

where a is—$\sqrt{eigenvalue(k)}$, b is $\sqrt{eigenvalue(k)}$, and R is a random number between zero and one. Then virtual cell membrane shape, $cell_k$, of the kth shape mode can be generated by

$$cell_k = w_k \times PC_k$$

where, PC_k *is the* kth principal component.

To visualise the shape modes, and to assess the effect of each shape mode on morphology, virtual cells were generated to represent each mode, as follows (first mode as an example):

$$\text{first shape mode} = \text{average cell} + 1 \times \sqrt{\text{eigenvalue}(1)}$$

This was repeated for the following weightings: $2 \times \pm$ and $1 \times \pm$ the eigenvalue of the first two shape modes, and their combinations. Only the first two shape modes were analysed, as there many possible combinations ($= 3^n$, where n is the number of shape modes). Furthermore, the first two modes explained ~60% of the variance of the cell. Therefore, higher-order modes have a smaller effect on cell edge shape. To deconstruct our actual 3D cell shapes into a linear combination of shape-modes, we used the *Open Genetic Algorithm Toolbox*, implemented in MATLAB [34]. The solutions of the genetic algorithm were a 1×14 vector of shape-mode weightings. For this study 3D cell morphology was used (*i.e.*, all z-slices for each cell). However, for illustrative purposes, we describe the genetic algorithm procedure here in 2D, as seen in Fig. 2. Goodness of fit of the 3D genetic algorithm were determined between the original cell and the virtual cell recreated from genetic algorithm-fitted shape modes (data not shown).

3 Results

3.1 Spatial Descriptors

3.1.1 Nucleus

To compute the median axis, images of nuclei were automatically thresholded, and the central axis was computed (longest line that can be drawn within the nucleus). Images were rotated so that central axis ran top-to-bottom, and rotated 180° if needed, to ensure most of the cell volume was on the right-side of the central axis. All slices in a stack were rotated by same angle as the central slice. Next, the median axis was computed for each slice in the z-stack by finding the point equidistant from the nucleus boundary (in the x-direction, left-to-right). This distance is known as the nucleus width. This procedure was repeated for every row along the central axis, hence the median axis and nucleus width vectors contain n elements, where n is the number of pixel rows present in nucleus. Both median axis and nuclei curves were normalized by the length of the central axis, and fitted with a 10th-order polynomial. Finally, in every 2D slice, we defined the centroid vector: the vector between the centroid of a 2D nucleus on a given slice, and the centroid of the whole 3D nucleus. Hence any nucleus can be described by the $1 \times m$ vector of central axis lengths where m is number of slices, two $11 \times m$ vectors (fitted coefficients of a 10th-order

polynomial to describe the median axis and nuclei width) and the $3 \times m$ array of centroid vectors.

The mean centroid vector was 0 ± 1.5 pixels in both x and y, indicating that each slice of the nucleus had a centroid essentially directly above the middle slice centroid. The average nuclear length was 144 ± 20.4 pixels (mean and standard deviation). The maximum average width of the nucleus is at the centre, and is 40 pixels $\times$ 0.132 μm/pixel resolution $=$ 5.28 μm (on each side of the median axis). There is near-zero values and little variation in the median axis position. Furthermore, the nucleus width curve is symmetric. Taken together with the near-zero values and variation of the nuclei centroid vector, we suggest that the nuclei are well represented as a tri-axial ovoid. We found variation in nuclei width and length, but there are insufficient samples to determine if these descriptors are well fitted with a normal distribution, as found by Zhao and Murphy using HeLa cells [22].

Cell edge Each 3D cell in the population was de−constructed into a linear combination of shape modes using the genetic algorithm. Of the 15 cells, 5 had a first or second shape mode weighting greater than one standard deviation away from the average. Cell 7 has an atypical morphology, with a first shape mode more than 3 standard deviations away from the mean (See Table 1). There may be considerable morphological variation in a larger population that has not been captured within the 15 cell sample size. The first shape mode explains 38% of the shape variation, the first two modes represented >60% of shape variance, and the first 8 modes representing >93% of shape variance (see Fig. 2). Therefore, we have represented our cell population as n vectors of size 8×1, and 9 vectors of size $720 \times m$, where n is the number of cells in the population and m is the number of slices in the image. Using a modified PCA method, Peng and Murphy found that 20 modes were required to represent >90% of shape variance in a dataset consisting of 447 HeLa cells [21], suggesting that saving in dimensionality (that PCA enables) increases with increasing sample size. To assess the effect of morphological variation, the first two modes (Fig. 3) and their interactions (Fig. 4) were visualised. The first mode of cell shape ((−2, 0) to (2, 0) direction) increases in size and shifts centre of mass from above the nucleus centroid to below. The second mode of cell shape has fairly constant size and centre of mass position as it changes from (0, −2) to (0, 2): the bulk of the cell shifts from being adjacent left and right (0, −2) of the nucleus to being above and below (0, 2).

As PCA decomposes the cells into linear combinations, the interactions of the first two shape modes are created through linear addition. For instance, a (2, −2) shape is computed by:

$$(2, -2) = (0, 0) + \left(2 \times \sqrt{eigenvalue(1)} \times firstshapemode\right) + (-2 \times \sqrt{eigenvalue(2)} \times secondshapemode)$$

The morphological variation found in the cells of this population is typical of what is observed in statically cultured endothelial cells. Conceptually, PCA describes each cell edge as a linear combination of the average cell edge shape and a series of shape modes multiplied by a weighting. Each specific cell is generated using a different

Table 1 Shape mode weightings of all cells in the population. Eigenvalue indicates the standard deviation of each weighting in the population. Red shaded values indicate weightings that are more than one standard deviation away from the mean

Cell	1	2	3	4	5	6	7	8	9	10	11	12	13	14
1	35.3	−12.7	122.7	120.4	44.7	−58.5	−32.7	23.2	−19.2	−5.5	4.4	−12.4	5.0	3.5
2	24.1	47.6	9.0	−71.9	5.9	−30.0	15.9	−14.7	−37.9	−52.0	−45.6	1.8	13.3	−2.4
3	−35.9	42.5	30.4	−0.3	−11.5	65.8	−59.5	−4.5	−18.9	33.8	−9.2	11.4	24.8	−15.7
4	−88.3	43.7	−48.6	30.6	20.5	−59.9	35.9	−17.3	19.6	12.2	0.6	10.6	−10.8	−28.4
5	133.8	−239.1	−27.1	−9.4	60.8	7.3	30.8	−23.6	13.9	31.3	−24.1	−5.6	7.4	5.0
6	−23.5	6.9	−13.1	7.7	40.7	54.9	−10.0	2.5	−48.5	1.4	−8.6	5.2	−40.3	2.0
7	408.3	77.6	−1.2	−17.2	−36.9	0.6	16.1	9.3	−5.4	1.0	27.9	5.8	−2.3	−3.6
8	−47.4	−198.0	−51.8	−44.6	−45.6	−31.7	−71.9	−5.1	−1.0	−25.5	29.7	3.2	−5.1	−3.3
9	−34.8	110.7	−158.4	52.6	57.7	5.9	−11.5	−17.0	6.5	−12.7	18.3	11.5	14.3	15.2
10	−99.2	−0.4	130.6	−14.6	6.3	38.0	40.2	−65.1	15.8	−19.1	35.5	4.2	1.6	3.6
11	−47.3	33.9	33.5	−82.7	69.7	18.9	−3.8	77.2	46.7	−10.3	6.3	−3.5	−0.4	−2.0
12	−0.2	−37.5	−14.0	95.7	−82.4	48.7	11.5	18.3	43.5	−28.0	−31.0	1.8	−4.3	0.4
13	−44.9	80.9	−42.5	−22.2	−31.6	2.9	−2.3	−16.3	−0.5	14.0	2.5	−59.1	−1.3	−0.2
14	−147.7	−50.0	−15.0	−3.9	−57.7	−12.1	68.1	50.9	−42.7	21.3	16.8	8.5	10.1	7.7
15	−25.4	95.1	44.1	−45.1	−41.9	−51.9	−32.0	−17.7	27.0	36.5	−22.8	17.5	−10.3	17.7
Eigenvalue	129.7	100.5	70.4	56.1	48.3	40.8	38.0	33.6	29.3	25.3	23.9	18.0	14.9	11.2

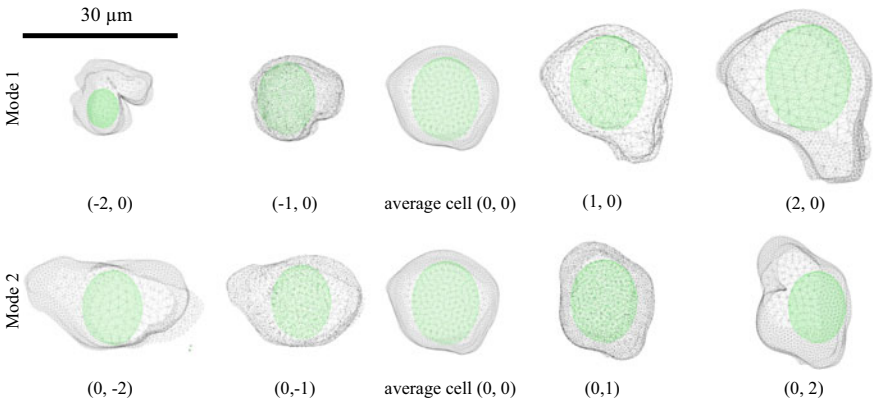

Fig. 3 The effect of first two shape modes on cell morphology. Cells are labelled (i, j), where i and j are the number of standard deviations in the first and second mode directions, respectively. The first shape mode (top row, moving left-to-right) increases in size and shifts cell volume below nucleus. The second shape mode (bottom row, moving left-to-right) shifts the bulk of cell volume from left and right of the nucleus, to above and below the nucleus

weighting set. The PCA process is as follows: firstly, as described in Cell edge section of the methods, the cell edge shape in each slice is described as a 241 $\times$ n vector. This vector was converted back into Cartesian coordinates resulting in a 1 $\times$ 720n vector (n slices, each slice having 240 x, y and z coordinates). A matrix was formed from the edge vectors of all 15 cells, 15 $\times$ 720n. Each column was centered by subtracting the average cell edge shape vector (also 1 $\times$ 720n vector). The singular value decomposition algorithm was then performed on the matrix. The resulting eigenvalues are the variance of the population of cells in the direction of each of the shape modes. The eigenvectors are the shape mode directions.

To visualise the shape modes, virtual cells were generated to represent the first and second modes, and their interactions. Details of the genetic algorithm used to fit

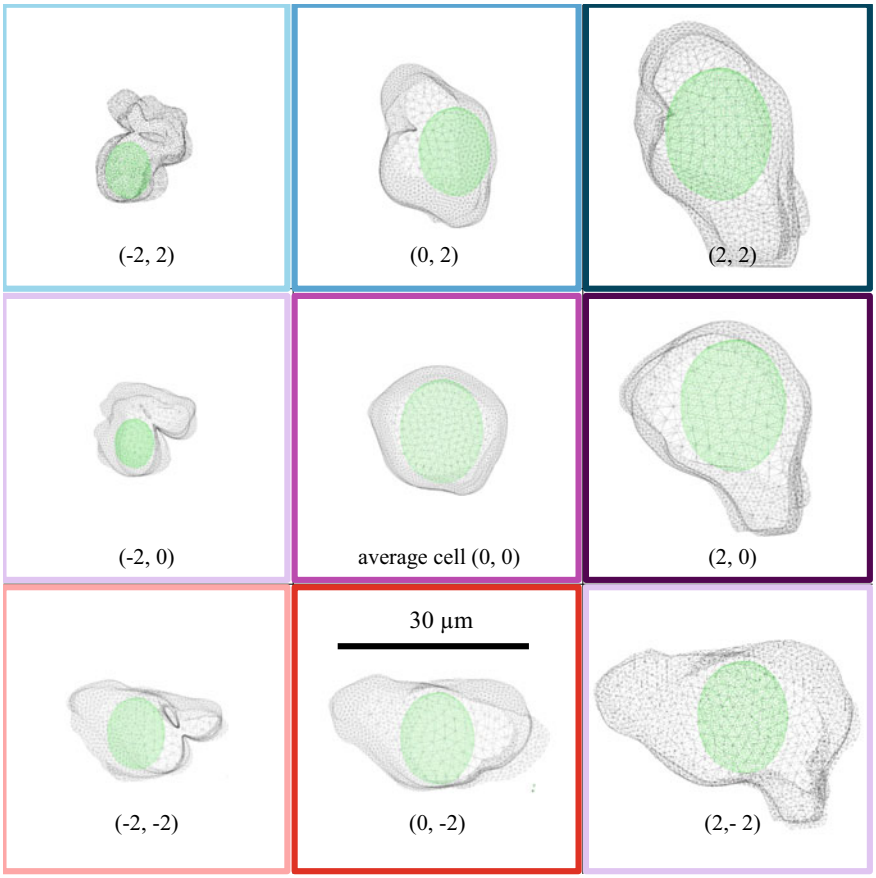

Fig. 4 Visualisation of shape modes and their interactions. This 3 × 3 grid illustrates the first two shape modes and their interactions. Cells in diagonal positions are linear combinations of cells along the axes. Cells are labelled (*i*, *j*), where *i* and *j* are the number of standard deviations in the first and second mode directions, respectively. Because two standard deviations are used to form these virtual cells, most cells exist within the region bounded by the outer 8 cells

real cells to PCA weights are outlined here. The genetic algorithm fitness function minimises the root-mean-squared difference between the 240 points in the original cell, and the 240 points of the cell created from the genetic algorithm. Fitness selection was conducted using stochastic remainder proportional selection, with the ranked scaling method. A single crossover point was used with a crossover probability of 90% and a mutation probability of 6%. Elitism was also used in the genetic algorithm (the best 10% of solutions in the previous generations were included in the next iteration, without modification).

To illustrate goodness of fit of the three-dimensional genetic algorithm, we have embedded two models: the original cell, the virtual cell recreated from genetic

algorithm-fitted shape modes. Due to file size restrictions, both models are at far lower resolution that those used in the mechanical analysis.

4 Discussion

A custom set of spatial descriptors was developed to quantify morphological variation in a population of ECs. We believe that our study is the first to examine morphological variation in an EC population using a shape descriptor and virtual cell approach. A potential drawback of using polar coordinates could occur if there is more than one intersection of the cell membrane with the radius. However, the cell population considered in the study that did not occur, and would not commonly occur with these cell type when confluent.

We have demonstrated a methodology for quantitatively comparing a specific cell morphology against the population dataset. This is important in determining if experimental results from cell-specific studies cell be generalised across the population. From our data set, we found that one cell from the population ($N = 15$) had substantially different morphology compared to the overall population. Hence, if this cell was examined, then cell-specific studies would have been incorrectly generalised. A stability analysis was also carried out to ensure that the sample size was sufficient to capture the variation in the cell population. This consisted of removing each cell, one at a time, and repeating the PCA on the remaining 14 cells. Hence PCA is carried out on 14 different populations of cells. There was very little variation between the first shape mode of all 14 cell populations, indicating that the population shape modes are not skewed by a single outlier.

Several studies have examined flow-induced remodelling of EC adhesions, intercellular junctions, actin stress fibres and microtubules [12–18]. The morphological descriptors used in this study improve on those previously used to describe the EC and subcellular components, as they are sophisticated enough to generate virtual cells. The increased sophistication will benefit future remodelling studies as they allow better comparison of effect sizes of changes in flow, chemical treatments, or experimental variables. Increased sophistication also enables the generation of virtual cells that are representative of the entire population. Virtual cells are suitable for finite-element analysis, and represent an advance in the cell-specific modelling field. Furthermore, it is possible to generate virtual cells to represent variation in a specific morphological descriptor.

While existing morphological descriptors are likely to be co-dependent (for example it is easy to imagine a relationship between alignment and length in flow-remodelled cells), this dependency has not been examined. In contrast, our PCA approach ensures that each mode is independent and thus overall cell shape is a linear combination of shape modes. This linearity allows the morphological effect of each shape mode to be separately assessed rather than having to consider their interactions. It should be noted that while each shape mode is independent the mechanotransmission effect of each shape mode can interact. Our approach allows these

mechanical interactions to be identified rather than being obscured by interactions in cell morphological descriptors. It should also be noted that a dependency may exist between overall cell shape modes and nuclear morphological descriptors. Testing the existence of this dependency is a logical extension of our study, perhaps with a regression analysis and a larger data set. To know more about the relationship between remodelling and disease, other variables could be added such as variable flow conditions during culture or mutant/diseased EC types.

Our study allows population morphology to be incorporated in mechanotransmission studies. However, to obtain a complete picture of EC mechanotransduction other subcellular components need to be examined, too. In particular, the cytoskeleton has been demonstrated as having a key role in the mechanotransmission of WSS in ECs [35]: both the actin stress fibres [36] and microtubules [37] are mechanically significant. Other important components include the focal adhesions (the inclusion of which, has already been shown to significantly affect intracellular force estimates in computational models [10]), integrins and intracellular junctions [38] which link the cell to its extracellular matrix and surrounding cells. Future inclusion of these features into our analysis will enable us to better address the question: what are the forces experienced by each type of transducer in different parts of the cell in response to a range of flow-induced WSS? Answering this question is central to determining individual transducer contributions to mechanotransduction, which, in turn, will improve understanding of the pathogenesis of EC-related disease.

Acknowledgements The authors wish to acknowledge the contribution of NeSI high-performance computing facilities to the results of this research. NZ's national facilities are provided by the NZ eScience Infrastructure and funded jointly by NeSI's collaborator institutions and through the Ministry of Business, Innovation & Employment's Research Infrastructure programme https://www.nesi.org.nz. We also thank Ms. Hilary Holloway and Ms. Jacqui Ross from the Biomedical imaging Research Unit for assistance in microscope training and image acquisition.

References

1. Aird, W. C. (2004). Endothelium as an organ system. *Critical Care Medicine, 32*(5), S271–S279. https://doi.org/10.1097/01.CCM.0000129669.21649.40
2. Davies P, F. (1995). Flow-mediated endothelial mechanotransduction. *Physiological Reviews, 75*(3), 519–560.
3. Davies, P. F. (2009). Hemodynamic shear stress and the endothelium in cardiovascular pathophysiology. *Nature Clinical Practice. Cardiovascular Medicine, 6*(1), 16–26.
4. Davies, P. F., et al. (2002). The convergence of haemodynamics, genomics, and endothelial structure in studies of the focal origin of atherosclerosis. *Biorheology, 39*(3), 299–306.
5. Lim, Y., Cooling, M., & Long, D. (2015). Computational models of the primary cilium and endothelial mechanotransmission. *Biomechanics and Modeling in Mechanobiology, 14*(3), 665–678.
6. Barreto, S., et al. (2013). A multi-structural single cell model of force-induced interactions of cytoskeletal components. *Biomaterials, 34*(26), 6119–6126.

7. Dabagh, M., et al. (2014). Shear-induced force transmission in a multicomponent, multicell model of the endothelium. *Journal of the Royal Society, Interface/The Royal Society, 11*(98), 20140431.
8. Jean, R. P., Chen, C. S., & Spector, A. A. (2005). Finite-element analysis of the adhesion-cytoskeleton-nucleus mechanotransduction pathway during endothelial cell rounding: Axisymmetric model. *Journal of Biomechanical Engineering, 127*(4), 594–600.
9. Caille, N., et al. (2002). Contribution of the nucleus to the mechanical properties of endothelial cells. *Journal of Biomechanics, 35*(2), 177–187.
10. Ferko, M., et al. (2007). Finite-element stress analysis of a multicomponent model of sheared and focally-adhered endothelial cells. *Annals of Biomedical Engineering, 35*(2), 208–223.
11. Slomka, N., & Gefen, A. (2010). Confocal microscopy-based three-dimensional cell-specific modeling for large deformation analyses in cellular mechanics. *Journal of Biomechanics, 43*(9), 1806–1816.
12. Davies, P. F., et al. (1986). Turbulent fluid shear stress induces vascular endothelial cell turnover in vitro. *Proceedings of the National Academy of Sciences of the United States of America, 83*(7), 2114–2117.
13. Dewey, J., C.F., et al. (1981). The dynamic response of vascular endothelial cells to fluid shear stress. *Journal of Biomechanical Engineering, 103*(3), 177–185.
14. Geerts, W. J. C., et al. (2011). Cobblestone HUVECs: A human model system for studying primary ciliogenesis. *Journal of Structural Biology, 176*(3), 350–359.
15. Iomini, C., et al. (2004). Primary cilia of human endothelial cells disassemble under laminar shear stress. *The Journal of Cell Biology, 164*(6), 811–817.
16. Galbraith, C. G., Skalak, R., & Chien, S. (1998). Shear stress induces spatial reorganization of the endothelial cell cytoskeleton. *Cell Motility and the Cytoskeleton, 40*(4), 317–330.
17. Nerem, R. M., Levesque, M. J., & Cornhill, J. F. (1981). Vascular endothelial morphology as an indicator of the pattern of blood flow. *Journal of Biomechanical Engineering, 103*(3), 172–176.
18. Rouleau, L., et al. (2010). Endothelial cell morphologic response to asymmetric stenosis hemodynamics: effects of spatial wall shear stress gradients. *Journal of Biomechanical Engineering, 132*(8), 081013–081013.
19. Díaz, M. E., et al. (2001). Testing abnormality in the spatial arrangement of cells in the corneal endothelium using spatial point processes. *Statistics in medicine, 20*(22), 3429–3439.
20. Buck, T. E., et al. (2012). Toward the virtual cell: Automated approaches to building models of subcellular organization "learned" from microscopy images. *BioEssays, 34*(9), 791–799.
21. Peng, T., & Murphy, R. F. (2011). Image-derived, three-dimensional generative models of cellular organization. *Cytometry.Part A : The Journal of the International Society for Analytical Cytology, 79*(5), 383–391.
22. Zhao, T., & Murphy, R. (2007). Automated learning of generative models for subcellular location: Building blocks for systems biology. *Cytometry. Part A : The Journal of the International Society for Analytical Cytology, 71*(12), 978–990.
23. Ades, E. W., et al. (1992). HMEC-1: Establishment of an immortalized human microvascular endothelial cell line. *Journal of Investigative Dermatology, 99*(6), 683–690.
24. Lim, Y., et al. (2015). Culture and detection of primary cilia in endothelial cell models. *Cilia, 4*(1), 11.
25. Riedl, J., et al. (2008). Lifeact: A versatile marker to visualize F-actin. *Nature Methods, 5*(7), 605–607.
26. Rivero, F., et al. (1996). The role of the cortical cytoskeleton: F-actin crosslinking proteins protect against osmotic stress, ensure cell size, cell shape and motility, and contribute to phagocytosis and development. *Journal of Cell Science, 109*(11), 2679–2691.
27. Ringner, M. (2008). What is principal component analysis? *Nature Biotechnology, 26*(3), 303–304.
28. Wall, M., Rechtsteiner, A., & Rocha, L. (2003). *Singular value decomposition and principal component analysis.* In D. Berrar, W. Dubitzky, & M. Granzow (Eds.). Springer US (pp. 91–109).

29. Yuan, L., et al. (2016). A role of stochastic phenotype switching in generating mosaic endothelial cell heterogeneity. *Nature Communications, 7*, 10160.
30. Chessel, A., & Carazo Salas, R. E. (2019). From observing to predicting single-cell structure and function with high-throughput/high-content microscopy. *Essays in Biochemistry, 63*(2), 197–208.
31. Brasch, M. E., Pena, A. N., & Henderson, H. (2021). Image-based cell subpopulation identification through automated cell tracking, principal component analysis, and partitioning around medoids clustering. *Medical & Biological Engineering & Computing.*
32. Ruan, X., & Murphy, R. F. (2019). Evaluation of methods for generative modeling of cell and nuclear shape. *Bioinformatics, 35*(14), 2475–2485.
33. de Back, W., Zerjatke, T., & Roeder, I. (2019). Statistical and mathematical modeling of spatiotemporal dynamics of stem cells. *Methods in Molecular Biology, 2017*, 219–243.
34. Freitas, A. L. (2012). *Open Genetic Algorithm Toolbox* (2012)
35. Helmke, B. P., & Davies, P. F. (2002). The cytoskeleton under external fluid mechanical forces: Hemodynamic forces acting on the endothelium. *Annals of Biomedical Engineering, 30*(3), 284–296.
36. Sugita, S., et al. (2011). A novel method for measuring tension generated in stress fibers by applying external forces. *Biophysical Journal, 101*(1), 53–60.
37. Deguchi, S., et al. (2009). Measurement and finite element modeling of the force balance in the vertical section of adhering vascular endothelial cells. *Journal of the Mechanical Behavior of Biomedical Materials, 2*(2), 173–185.
38. Ueki, Y., et al. (2009). Morphological responses of vascular endothelial cells induced by local stretch transmitted through intercellular junctions. *Experimental Mechanics, 49*(1), 125–134.

Fluid Mechanics

Efficient and Accurate Computation of Quantitative Flow Ratio (QFR) for Physiological Assessment of Coronary Artery Stenosis from a Single Angiographic View

George C. Bourantas, Grigorios Tsigkas, Konstantinos Katsanos, Fivos V. Bekiris, Benjamin F. Zwick, Adam Wittek, Karol Miller, and Periklis Davlouros

Abstract In this study we develop a fast (less than 30 s) method to compute the quantitative flow ratio (QFR) from angiographic images. We evaluate its diagnostic accuracy in patients with intermediate coronary stenosis through comparison with invasively measured fractional flow reserve (FFR). Our method uses a single angiographic view with minimal vessel foreshortening and overlap to compute geometrical data (vessel length, stenosis length, diameter of normal unobstructed vessel, diameter of stenosed vessel). Finally, we evaluate the diagnostic performance of our 2D-based QFR in the physiological assessment of intermediate coronary lesions.

Keywords Fractional flow reserve · Coronary artery · Stenosis · Angiography · Pressure drop · Hagen–Poiseuille

1 Introduction

Myocardial revascularization is selected by physicians mostly on the basis of visual assessment of stenosis severity by coronary angiography. However, decision making and treatment planning based on functional assessment of coronary stenoses

G. C. Bourantas (✉) · B. F. Zwick · A. Wittek · K. Miller
Intelligent Systems for Medicine Laboratory, School of Mechanical and Chemical Engineering, The University of Western Australia, 35 Stirling Highway, Perth, WA 6009, Australia
e-mail: george.bourantas@uwa.edu.au

G. Tsigkas · P. Davlouros
Cardiology Department, School of Medicine, University of Patras, Rion, Greece

K. Katsanos
Department of Interventional Radiology, Patras University Hospital, Rion, Greece

F. V. Bekiris
medLYTIC Inc, Patras, Greece

K. Miller
Harvard Medical School, Boston, MA, USA

P. M. F. Nielsen et al. (eds.), *Computational Biomechanics for Medicine*,
https://doi.org/10.1007/978-3-031-09327-2_8

improves clinical outcomes. Anatomical details obtained by X-ray coronary angiography do not completely reflect the entire physiological impact of the stenosis on the blood circulation.

Fractional flow reserve (FFR) is the gold standard for evaluating the physiological significance of non-occlusive coronary stenosis [1]. FFR is defined as the ratio of hyperaemic myocardial flow in the presence of a stenosis and the hyperaemic flow in the absence of a stenosis. FFR is obtained by measuring invasively the ratio of distal coronary pressure and the aortic pressure during maximal hyperaemia [2, 3]. Using FFR in clinical practice has been limited [4] due to various reasons, such as physician's confidence in visual assessment from coronary angiograms, the need to induce hyperaemia, and the use of a costly pressure wire. A number of coronary angiography-based computational FFR methods have been developed, combining the geometrical data obtained from coronary angiography and fluid mechanics and computational fluid dynamics (CFD) [5–7]. Among them, the quantitative flow ratio (QFR) emerged as a reliable approach for fast computation of FFR. The diagnostic performance (accuracy, sensitivity, and specificity) of QFR has been reported in numerous studies [7–13]. In all these studies, a 3D reconstruction of the coronary artery segments has been used for computational modelling. However, even if 3D vessel reconstruction appears as an easy and straightforward procedure (two angiographic views acquired with at least 25° in separation are required), an accurate 3D vessel reconstruction is not always feasible since it requires angiographic images with minimal vessel foreshortening and overlap, which is not always possible due to the curved geometry of coronary arteries.

In this study, we develop and present a method for computing QFR from a single angiographic view. We use well-established fluid mechanics principles to compute the pressure drop along the stenosed part of the vessel. We are motivated by the fast (less than 10 s) computation of QFR from a single angiographic view. Finally, we aim to evaluate the diagnostic performance of a 2D-based QFR in the physiological assessment of intermediate coronary lesions.

2 Methods

Patient cases examined in this paper were obtained from a prospective cohort, single-center study. From January 1, 2021 to May 31, 2021, patients aged at least 18 years from the University Hospital in Rion Patras, Greece, scheduled for FFR-guided percutaneous coronary intervention (PCI) of single-target lesions within one of the major epicardial coronary arteries were recruited for this study. The angiographic inclusion criteria included lesions with diameter stenosis of 30–90%, a reference vessel diameter of greater than 2 mm according to visual estimation, and the feasibility of FFR. The exclusion criteria were contraindications to adenosine, previous history of myocardial infarction, presence of an acute coronary syndrome (ACS), known impaired ejection fraction (EF) and previous coronary artery bypass graft (CABG) surgery. Patients with complex anatomy such as lesions with longitudinal

or cross-sectional eccentricity, ostial and bifurcation lesions and diffuse disease were also excluded from this study.

The study protocol was approved by the Ethics Committee of University Hospital in Patras, Greece, and all the recruited patients signed a written informed consent form before participating in the study.

2.1 Coronary Angiography

Patients first underwent routine coronary angiography. Angiographic cine images were acquired at 15 frames per second using an Allura Xper X-ray system (Philips Medical Systems). Two-dimensional quantitative coronary angiography was performed offline using a proprietary software (medLYTIC, Greece, https://medlytic.eu/). A single angiographic view (see Fig. 1a) with the least foreshortening and yielding the best depiction of the stenosis was used to compute QFR. Lumen borders of the interrogated vessel were computed, and lumen borders correction was performed manually if required. The site of minimum luminal diameter, and the proximal and distal coronary artery segments were manually identified on the angiographic view (see Fig. 1b). Minimum luminal area (MLA), percentage area stenosis, minimum luminal diameter (MLD), percentage diameter stenosis and lesion length were determined using 2D-QCA.

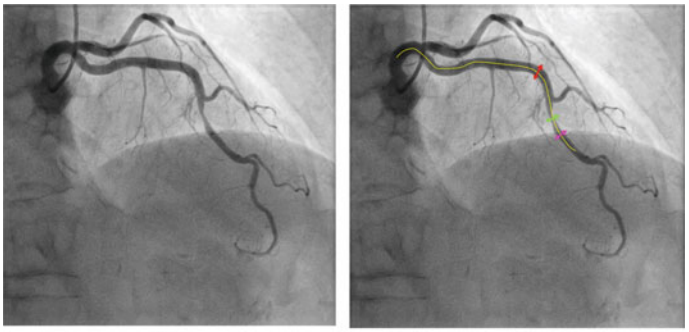

Fig. 1 **a** Single angiographic view with the least foreshortening and the best depiction of the stenosis and **b** geometrical data computed: vessel length (yellow line), diameter of the proximal part of the vessel (red), minimum luminal diameter (green), diameter of the distal part of the vessel (magenta)

2.2 FFR Measurements

Intracoronary angiography (ICA) and FFR measurements were performed using standard techniques by experienced invasive cardiologists (G.T., P.D.). A 6F angioplasty quidding catheter was used to engage the relevant coronary artery. The pressure reading obtained from the pressure sensor guidewire was then equalized with that of the guiding catheter with the sensor placed at the tip of the catheter. FFR was measured with ComboWire XT guidewire (Volcano Therapeutics, Rancho Cordova, California) or with COMET II Pressure Guidewire (Boston Scientific, Marlborough, USA). The pressure sensor was advanced to the distal part of the vessel and FFR computed during administration of intravenous adenosine (140 mg/kg/min). The proximal arterial pressure trace was also recorded and checked to ensure that there was no damping during hyperaemia. At the end of pressure measurement, the sensor was carefully pulled back, first across the lesion, and then to the tip of the guiding catheter to check for drift, confirming that both measured pressures are identical. FFR was computed as the ratio of mean coronary blood pressure distal to the stenosis and mean aortic pressure at the time of the induced hyperemia. Values of FFR ≤ 0.80 were considered as significant stenosis. The exact probe position at the measurement site was recorded on angiography.

2.3 QFR Calculations

QFR calculations were performed on X-ray angiographic images using a proprietary software (medLYTIC QFR, Greece, https://medlytic.eu/). The software allows the computation of QFR values in selected locations of the interrogated vessel. Computed QFR can then be compared with corresponding invasive FFR measurements. The algorithm uses both anatomical data and physiological models to compute QFR.

FFR was calculated via 2D quantitative coronary analysis (QCA). 2D QCA was measured in the best possible view (based on interventional cardiologist expertise) with the least foreshortening at the end-diastolic phase. Selection of optimal image projection and cine frame selection follow general guidelines [14, 15]. The patient-specific projection of X-ray angiography images was selected to obtain the size of the coronary stenosis. The external diameter of the contrast-filled catheter (6F) was used as the calibration standard for the right and left coronary arteries. Diameter stenosis, lesion length, distal diameter, and proximal diameter were selected manually, and the pixel size was converted into mm by determining a scaling factor.

From the geometrical data of the interrogated vessel (measured on the selected angiographic view) we computed the key parameters for pressure drop estimation along the interrogated vessel. We use the length of the interrogated vessel (see Fig. 1b) along with the TIMI frame count (TFC) number (see Fig. 2) to compute the mean blood velocity as $u_m = L_{vessel} \times (15/\text{TFC})$, where 15 s^{-1} are the number of angiographic frames obtained per second. Once the mean blood velocity is computed,

we can compute the baseline volumetric flow rate Q_b. The hyperaemic volumetric flow rate Q_h is computed as $Q_h = \text{CFR} \times Q_b$, with CFR being the coronary flow reserve. To compute the pressure drop along the vessel, we divided the vessel into three region: stenosis, proximal and distal to the stenosis parts. The pressure drop Δp_p and Δp_d along the proximal and distal parts of the vessel, respectively, are computed using the Hagen–Poiseuille formula as:

$$\Delta p_p = \frac{8\pi\mu L_p}{A_p}\frac{Q_h}{A_p} \tag{1}$$

and

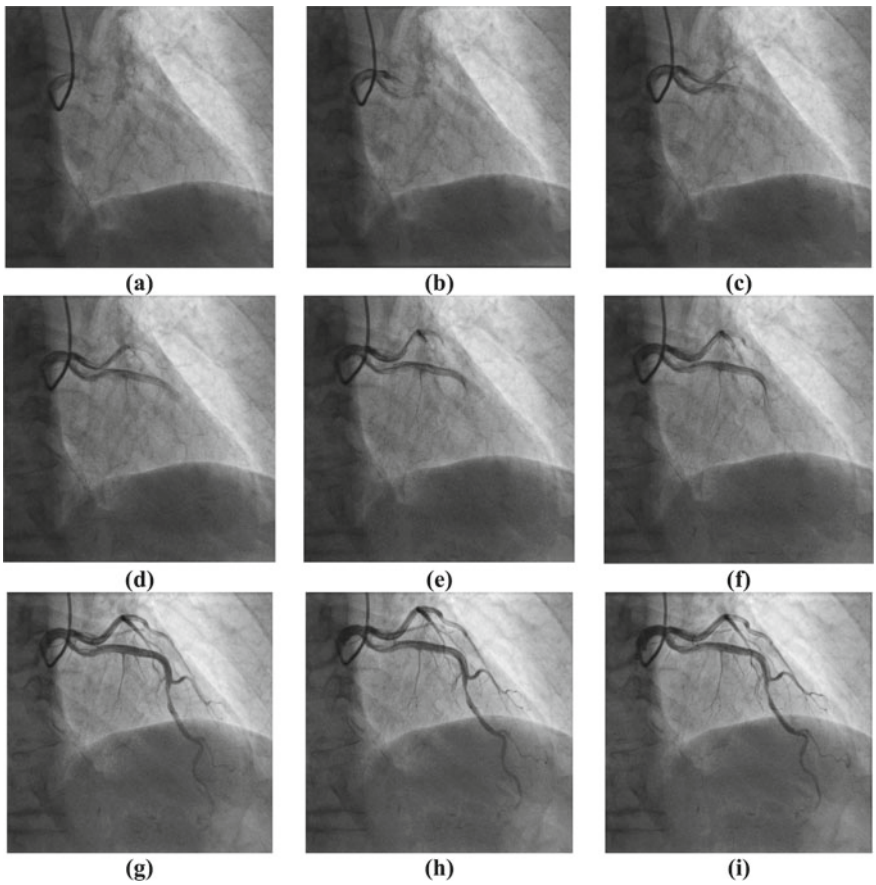

Fig. 2 TIMI frame count (TFC) to compute he mean velocity u_m and the baseline volumetric flow rate Q_b

$$\Delta p_d = \frac{8\pi\mu L_d}{A_d}\frac{Q_h}{A_d} \tag{2}$$

with L_p and L_d being the lengths of the proximal and distal parts of the vessel, respectively; and A_p and A_d being the cross-sectional area of the proximal and distal parts of the vessel, respectively. Although the Hagen–Poiseuille formula is applicable only to steady and laminar flow, it has been widely used to model physiological flows because it is easy to use and provides a fairly accurate model that relates mean pressure and flow values to the frictional resistance of the arterial segment. In the stenosed part of the vessel, the pressure drop Δp_s is computed as

$$\Delta p_s = a_v Q_h + a_t Q_h^2 \tag{3}$$

with $a_v = \frac{32\mu L_s}{D_s^2}\left(\frac{A_p}{A_s}\right)^2$ and $a_t = 1.52\frac{\rho}{2}{A_p}^2\left(\frac{1}{A_s} - \frac{1}{A_p}\right)^2$ being parameters defined in [16–19] with μ being the dynamic viscosity of the fluid, L_s the length of stenosis, A_s the minimum cross sectional lumen area inside the stenosis, D_s is the diameter corresponding to area A_s, and ρ the density of the fluid. Finally, $\mathrm{QFR_{B2D}}$ is calculated using the following equation

$$\mathrm{QFR_{B2D}} = 1 - \frac{\Delta p_p + \Delta p_s + \Delta p_d}{\mathrm{MAP}} \tag{4}$$

with MAP being the mean arterial pressure computed as [20]

$$\mathrm{MAP} = \mathrm{DBP} + \left(\frac{1}{3} + 0.0012 \times \mathrm{HR}\right) \times (\mathrm{SBP} - \mathrm{DBP}) \tag{5}$$

with DBP, SBP and HR being the diastolic blood pressure, systolic blood pressure and heart rate, respectively.

3 Numerical Results

We analysed a total of 14 vessels with both angiographic and measured FFR data from 14 patients using a proprietary code from medLYTIC Inc. QFR was successfully computed in all 14 vessels. QFR had a mean value of 0.83 ± 0.10 and a median value of 0.84. We identified FFR $\leq$ 0.80 in 9 (56%) vessels. $\mathrm{QFR_{B2D}}$ showed excellent correlation (Fig. 3a) and agreement (Fig. 3b) with measured FFR.

Using a cut-off value of $\leq$0.80 for FFR to define hemodynamically significant lesions, the vessel-level diagnostic accuracy of $\mathrm{QFR_{B2D}}$ was 93.0%, with 6 true positives, 7 true negatives, 1 false positive, and 0 false negatives.

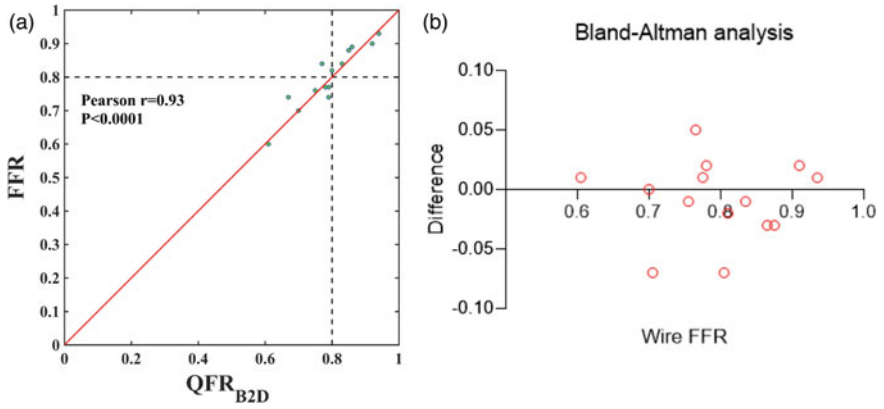

Fig. 3 The (**a**) Correlation and (**b**) agreement between QFR_{B2D} and FFR

4 Discussion

We have applied a fast method to compute QFR on coronary arteries from a single 2D angiographic view. Our method relies on limited human intervention. The computed QFR showed excellent correlation and agreement with wire-based FFR. The diagnostic accuracy of QFR $\leq$ 0.80 in predicting FFR $\leq$ 0.80 was 93%, with sensitivity of 90% and specificity of 90%. Finally, the average analysis time of QFR was 25 ± 5 s (computations were conducted using an Intel i7 quad core processor with 16 GB RAM), which appears to be significantly lower than the analysis time demonstrated by similar tools with computation times in the range of 3 to 5 min [21].

QFR computation based on the three-dimensional (3D) reconstruction of two angiographic views demonstrated a high vessel-level diagnostic accuracy (92.7%) with online in-procedure analysis and (93.3%) with offline core laboratory analysis [13]. In our study, we found that QFR had a high diagnostic accuracy by computing quantitative flow ratio based on a single 2D angiographic view without the need to perform 3D vessel reconstruction. The results are comparable with those computing quantitative flow ratio from two 2D angiographic views. The total time needed to compute FFR in both cases is similar.

A key factor on the accuracy of the QFR is that the angiographic view with optimal image quality was used for computation. Optimal exposure of the stenotic segment facilitates the quantification of the interrogated vessel geometry. One can argue that 3D angiographic reconstruction based on two angiographic views can be more accurate in the quantification of lumen area, especially in cases where the lesion(s) are eccentric. However, a second angiographic view might also introduce inaccurate computation of the vessel size, especially when there is vessel foreshortening and overlap. Our study demonstrates the diagnostic performance of QFR based on a single angiographic view, and highlights the importance of using angiographic

views with optimal exposure of all lesions in the interrogated vessel for the computation of QFR. Additional angiographic views (second or even a third one) may also be used for computing QFR. The additional 2D views will accurately compute QFR value in cases with high lesion eccentricity. Furthermore, the computed QFR using multiple 2D angiographic views is also time compatible with clinical workflow (less than 1 min), compared to the computational time provided by other methods (3 to 5 min) [21]. Finally, the quantification of contrast flow velocity in the computation of QFR based on a single angiographic view might be influenced by vessel foreshortening in individual patients. Nevertheless, previous studies demonstrated that such variation in the contrast flow velocity had negligible impact on the diagnostic accuracy of QFR [22]. The accurate reference vessel dimension would also enable more accurate 2-dimensional QCA analysis for bifurcation lesions.

In many countries, the use of FFR in clinical practice remains low [4], despite that using FFR for identifying flow limiting coronary stenosis has been recommended by guidelines [1]. A number of reasons may explain this inconsistency. Apart from the high cost of the pressure wire and the discomfort caused to patient by inducing hyperaemia, it has been reported that a major obstacle to the adoption of coronary physiological assessment in the catheterization laboratory is the physician's confidence in visual assessment of angiographic images alone [23]. Therefore, image-based computational FFR may enforce a wider adoption of coronary physiological assessment [24].

The accuracy and efficiency of computational FFR is crucial for its adoption in the catheterization laboratory. Previous studies demonstrated that that inability to acquire two satisfactory angiographic views greatly impair the feasibility of QFR analysis [11–13]. Operators were encouraged to acquire angiographic images according to recommended angiographic projections, thus increasing the feasibility of QFR in prospective validation studies [11, 13]. Computation of QFR based on a single angiographic view can result in more accurate computation of FFR, especially in patients with tortuous, sequential, or diffuse lesions where it was not always possible to obtain two angiographic views both with good exposure of all lesions in the interrogated vessels.

The present study has some limitations. Our study is a single-center, offline calculation of QFR. Therefore, the diagnostic accuracy of QFR performed by medical staff in the catheterization laboratory needs to be assessed. Furthermore, the QFR should be assessed for its accuracy and efficiency in identifying the physiological significance of all side branches. Additionally, we should assess the accuracy of the QFR on multiple stenosis in tandem configuration. These two important aspects should be addressed such that QFR can be considered as a reliable clinical tool. Therefore, further studies to validate the diagnostic accuracy of QFR are warranted.

5 Conclusion

Our data suggest that the computation of QFR from a single angiographic view has high feasibility and excellent diagnostic accuracy in identifying significant coronary stenosis. The analysis time is short (less than 30 s) and it is comparable to the physical time needed to measure FFR invasively. The accuracy and efficiency of our method, compared with the good reproducibility of QFR indicate the potential of wider adoption of physiological assessment of coronary stenosis in the catherization lab. Despite the encouraging results, our findings require appropriately powered validation in an independent multicenter cohort.

References

1. Knuuti, J., Wijns, W., Saraste, A., Capodanno, D., Barbato, E., Funck-Brentano, C., Prescott, E., Storey, R. F., Deaton, C., Cuisset, T., Agewall, S., Dickstein, K., Edvardsen, T., Escaned, J., Gersh, B. J., Svitil, P., Gilard, M., Hasdai, D., Hatala, R., Mahfoud, F., Masip, J., Muneretto, C., Valgimigli, M., Achenbach, S., Bax, J. J., & ESC Scientific Document Group. (2020). 2019 ESC guidelines for the diagnosis and management of chronic coronary syndromes: The task force for the diagnosis and management of chronic coronary syndromes of the European Society of Cardiology (ESC). *European Heart Journal, 41*, 407–477.
2. De Bruyne, B., Baudhuin, T., Melin, J. A., Pijls, N. H., Sys, S. U., Bol, A., Paulus, W. J., Heyndrickx, G. R., & Wijns, W. (1994). Coronary flow reserve calculated from pressure measurements in humans. Validation with positron emission tomography. *Circulation, 89*, 1013–1022.
3. Pijls, N. H., van Son, J. A., Kirkeeide, R. L., De Bruyne, B., & Gould, K. L. (1993). Experimental basis of determining maximum coronary, myocardial, and collateral blood flow by pressure measurements for assessing functional stenosis severity before and after percutaneous transluminal coronary angioplasty. *Circulation, 87*, 1354–1367.
4. Götberg, M., Cook, C. M., Sen, S., Nijjer, S., Escaned, J., & Davies, J. E. (2017). The evolving future of instantaneous wave-free ratio and fractional flow reserve. *Journal of the American College of Cardiology, 70*, 1379–1402.
5. Pellicano, M., Lavi, I., De Bruyne, B., Vaknin-Assa, H., Assali, A., Valtzer, O., Lotringer, Y., Weisz, G., Almagor, Y., Xaplanteris, P., Kirtane, A. J., Codner, P., Leon, M. B., Kornowski, R. (2017). Validation study of image-based fractional flow reserve during coronary angiography. *Circulation: Cardiovascular Interventions, 10*, e005259.
6. Ramasamy, A., Jin, C., Tufaro, V., Bajaj, R., Kilic, Y., Safi, H., Amersey, R., Jones, D., Torii, R., Lansky, A., Mathur, A., Bourantas, C. V., & Baumbach, A. (2020). Computerised methodologies for non-invasive angiography-derived fractional flow reserve assessment: A critical review. *Journal of Interventional Cardiology, 2020*, 6381637.
7. Tu, S., Westra, J., Yang, J., von Birgelen, C., Ferrara, A., Pellicano, M., Nef, H., Tebaldi, M., Murasato, Y., Lansky, A., Barbato, E., van der Heijden, L. C., Reiber, J. H. C., Holm, N. R., & Wijns, W. (2016). Diagnostic accuracy of fast computational approaches to derive fractional flow reserve from diagnostic coronary angiography: The international multicenter FAVOR pilot study. *JACC: Cardiovascular Interventions, 9*, 2024–2035.
8. Fearon, W. F., Achenbach, S., Engstrom, T., Assali, A., Shlofmitz, R., Jeremias, A., Fournier, S., Kirtane, A. J., Kornowski, R., Greenberg, G., Jubeh, R., Kolansky, D. M., McAndrew, T., Dressler, O., Maehara, A., Matsumura, M., Leon, M. B., De Bruyne, B., & FAST-FFR Study Investigators. (2019). Accuracy of fractional flow reserve derived from coronary angiography. *Circulation, 139*, 477–484.

9. Kaneshka, M., Laurens, J. C. V. Z., Matthew, M. B., Frank, J. H. G., Jurgen, M. R. L., Marcel, C. M. R., Miguel, E. L., Jeroen, M. W., Roberto, D., de Peter, J., Felix, Z., Nicolas, M. V. M., & Joost, D. (2020). Validation of a three-dimensional quantitative coronary angiography-based software to calculate fractional flow reserve: The FAST study. *EuroIntervention, 16*, 591–599.
10. Michail, I. P., Takashi, M., Yuki, I., Lampros, S. L., Shimpei, N., Christos, V. B., Jurgen, M. R. L., Yoshinobu, O., Mauro, E.-P., Georgia, T., Anna, K., Dimitrios, N. N., Owen, M., Robert-Jan, M. v. G., Katerina, K. N., Dimitrios, I. F., Emmanouil, S. B., Hector, M. G.-G., Javier, E., Felix, Z., Lampros, K. M., & Patrick, W. S. (2014). Fast virtual functional assessment of intermediate coronary lesions using routine angiographic data and blood flow simulation in humans: Comparison with pressure wire—fractional flow reserve. *EuroIntervention, 10*, 574–583.
11. Westra, J., Andersen, B. K., Campo, G., Matsuo, H., Koltowski, L., Eftekhari, A., Liu, T., Di Serafino, L., Di Girolamo, D., Escaned, J., Nef, H., Naber, C., Barbierato, M., Tu, S., Neghabat, O., Madsen, M., Tebaldi, M., Tanigaki, T., Kochman, J., Holm, N. R. et al. (2018). Diagnostic performance of in-procedure angiography-derived quantitative flow reserve compared to pressure-derived fractional flow reserve: The FAVOR II Europe-Japan study. *Journal of the American Heart Association, 7*, e009603.
12. Westra, J., Tu, S., Winther, S., Nissen, L., Vestergaard, M.-B., Andersen, B. K., Holck, E. N., Fox Maule C., Johansen, J. K., Andreasen, L. N., Simonsen, J. K., Zhang, Y., Kristensen, S. D., Maeng, M., Kaltoft, A., Terkelsen, C. J., Krusell, L. R., Jakobsen, L., Reiber, J. H. C., Lassen, J. F., Bøttcher, M., Bøtker, H. E., Christiansen, E. H., & Holm, N. R. (2018). Evaluation of coronary artery stenosis by quantitative flow ratio during invasive coronary angiography. *Circulation: Cardiovascular Imaging, 11*, e007107.
13. Xu, B., Tu, S., Qiao, S., Qu, X., Chen, Y., Yang, J., Guo, L., Sun, Z., Li, Z., Tian, F., Fang, W., Chen, J., Li, W., Guan, C., Holm, N. R., Wijns, W., & Hu, S. (2017). Diagnostic accuracy of angiography-based quantitative flow ratio measurements for online assessment of coronary stenosis. *Journal of the American College of Cardiology, 70*, 3077–3087.
14. Fischell, T. A., Maheshwari, A., Mirza, R. A., Haller, S., Carter, A. J., & Popma, J. J. (2005). Impact of frame selection on quantitative coronary angiographic analysis after coronary stenting. *Catheterization and Cardiovascular Interventions, 64*, 460–467.
15. Ito, S., Kinoshita, K., Endo, A., & Nakamura, M. (2019). Impact of cine frame selection on quantitative coronary angiography results. *Clinical Medicine Insights: Cardiology, 13*, 1179546819838232.
16. Kirkeeide, R. L. (1991). Coronary obstructions, morphology and physiologic significance. In J. H. C. Reiber & P. W. Serruys (Eds.), *Quantitative coronary arteriography* (pp. 229–244). Springer.
17. Stergiopulos, N., Young, D. F., & Rogge, T. R. (1992). Computer simulation of arterial flow with applications to arterial and aortic stenoses. *Journal of Biomechanics, 25*, 1477–1488.
18. Young, D. F. (1979). Fluid mechanics of arterial stenoses. *Journal of Biomechanical Engineering, 101*, 157–175.
19. Young, D. F., Cholvin, N. R., Kirkeeide, R. L., & Roth, A. C. (1977). Hemodynamics of arterial stenoses at elevated flow rates. *Circulation Research, 41*, 99–107.
20. Babakhani, H., Sadeghipour, P., Tashakori Beheshti, A., Ghasemi, M., Moosavi, J., Sadeghian, M., Salesi, M., Zahedmehr, A., Shafe, O., Shakerian, F., Mohebbi, B., Alemzadeh-Ansari, M. J., Firouzi, A., Geraiely, B., & Abdi, S. (2021). Diagnostic accuracy of two-dimensional coronary angiographic-derived fractional flow reserve—preliminary results. *Catheterization and Cardiovascular Interventions, 97*, E484–E494.
21. Wong, C. C. Y., & Yong, A. S. C. (2020). Flash-forward: The emergence of angiography-derived fractional flow reserve in the catheter laboratory. *Cardiovascular Research, 116*, 1242–1245.
22. Zhang, Y., Zhang, S., Westra, J., Ding, D., Zhao, Q., Yang, J., Sun, Z., Huang, J., Pu, J., Xu, B., & Tu, S. (2019). Automatic coronary blood flow computation: Validation in quantitative flow ratio from coronary angiography. *The International Journal of Cardiovascular Imaging, 35*, 587–595.

23. Tebaldi, M., Biscaglia, S., Fineschi, M., Musumeci, G., Marchese, A., Leone, A. M., Rossi, M. L., Stefanini, G., Maione, A., Menozzi, A., Tarantino, F., Lodolini, V., Gallo, F., Barbato, E., Tarantini, G., & Campo, G. (2018). Evolving routine standards in invasive hemodynamic assessment of coronary stenosis: The nationwide Italian SICI-GISE cross-sectional ERIS study. *JACC: Cardiovascular Interventions, 11*, 1482–1491.
24. Tu, S., Westra, J., Adjedj, J., Ding, D., Liang, F., Xu, B., Holm, N. R., Reiber, J. H. C., & Wijns, W. (2020). Fractional flow reserve in clinical practice: From wire-based invasive measurement to image-based computation. *European Heart Journal, 41*, 3271–3279.

Predicting Plaque Progression in Patient-Specific Carotid Bifurcation

Tijana Djukic, Smiljana Djorovic, Branko Arsic, Branko Gakovic, Igor Koncar, and Nenad Filipovic

Abstract Atherosclerosis is an inflammatory disease that is characterized by the accumulation of lipids and formation of plaque within the arterial wall. It would be clinically useful to analyze this inflammation process and its progress in more detail for each particular patient. In this study, fully coupled biomechanics software for plaque progression was used to simulate the growth of plaque within patient-specific carotid bifurcation. The numerical model couples computational fluid mechanics, transport of relevant molecules, inflammatory process and plaque growth. The simulation is performed using the geometry of the specific patient that is reconstructed by applying deep learning techniques to the images obtained from clinical ultrasound examination. The numerical model used can help to predict the evolution of atherosclerotic plaque which is very significant for appropriate diagnostics and treatment planning and represents one step further in applying biomechanics modeling within the concept of computer-integrated medicine.

Keywords Ultrasound examination · Three-dimensional patient-specific geometry · Numerical simulation · Plaque progression

T. Djukic (✉)
Institute of Information Technologies, University of Kragujevac, Kragujevac, Serbia
e-mail: tijana@kg.ac.rs

T. Djukic · B. Arsic · N. Filipovic
Bioengineering Research and Development Center, BioIRC, Kragujevac, Serbia
e-mail: brankoarsic@kg.ac.rs

N. Filipovic
e-mail: fica@kg.ac.rs

S. Djorovic · N. Filipovic
Faculty of Engineering, University of Kragujevac, Kragujevac, Serbia
e-mail: smiljana@kg.ac.rs

B. Arsic
Faculty of Science, University of Kragujevac, Kragujevac, Serbia

B. Gakovic · I. Koncar
Clinic for Vascular and Endovascular Surgery, Serbian Clinical Centre, Belgrade, Serbia

P. M. F. Nielsen et al. (eds.), *Computational Biomechanics for Medicine*,
https://doi.org/10.1007/978-3-031-09327-2_9

1 Introduction

Atherosclerosis is an inflammatory disease of the large arteries within the human cardiovascular system. This disease is characterized by the vessel endothelial dysfunction, accumulation of lipid, cholesterol and other elements within the arterial wall that ultimately results with the formation of plaque within the arterial wall [1]. There are several factors that can increase the progression of atherosclerosis, one being the regions with low wall shear stress (WSS) within the arterial wall. These regions are especially vulnerable to the dysfunctions of endothelium and plaque formation [2]. Another factor that contributes to the lipid accumulation within the arterial wall is the transport of atherogenic substances such as low density lipoprotein (LDL) from the lumen through the wall. It would be hence useful to analyze these processes in more detail.

Several clinical examinations can be performed to analyze the state of the patient's carotid bifurcation and inspect possible stenotic regions, including the ultrasound (US) examination. However, it would be useful to analyze the distribution of WSS or the potential growth of the currently present plaques. This can be achieved by using numerical simulations of blood flow, LDL transport and plaque progression. Of course, in order to obtain valuable conclusions for the particular patient, it is important to perform simulations using patient-specific geometries. In this study, images from US examination are used to reconstruct patient-specific geometry that is used to predict the behavior of the plaque.

There are several approaches presented in literature [3, 4] that deal with the transport of LDL and other macromolecules through the arterial wall. In this study, a complex three-dimensional (3D) model of LDL transport and plaque progression presented in [5] is used. This model was developed within an European FP7 project and validated against data from animal experiments and clinical data [6, 7]. This mathematical model consists of three parts: blood flow through the 3D reconstructed patient-specific arterial segment, which includes the distribution of WSS; the transport of macromolecules through the bloodstream and arterial wall; and the biological mechanism of the inflammation within the intima, that causes plaque generation and further growth of atherosclerotic plaque.

The paper is organized as follows: The reconstructed patient-specific geometry and the numerical model for the prediction of plaque growth are presented in Sect. 2. The results of the plaque progression simulation are presented in Sect. 3. Section 4 provides a discussion of relevant work in literature and a short conclusion.

2 Materials and Methods

In this section, first the reconstruction of the patient-specific carotid bifurcation from clinical data obtained during ultrasound examination is presented. Then, the details of the numerical model for plaque progression are discussed.

2.1 Reconstruction of the Carotid Bifurcation

The 3D reconstruction of patient-specific carotid artery was performed using the procedure presented in literature [8, 9]. Here only a brief overview of the procedure will be provided. The main goal is to use deep learning to automatically extract lumen and wall segments from the US images and then use the segmented data to perform automated 3D reconstruction. The US images obtained during clinical examination for a set of patients are annotated by the clinical experts and used to train a convolutional neural network. Afterwards, for a particular patient, the collection of longitudinal and transversal US images is imported into the deep learning module and the 3D reconstruction module to create the patient-specific geometry. The procedure described in [8] is related to the reconstruction of the lumen of the carotid bifurcation, and the same procedure is also applied for the wall reconstruction, with the only difference being in the fact that an additional set of contours for the wall is segmented from the US images. The US images for the specific patient considered within this study and the reconstructed geometry are shown in Fig. 1.

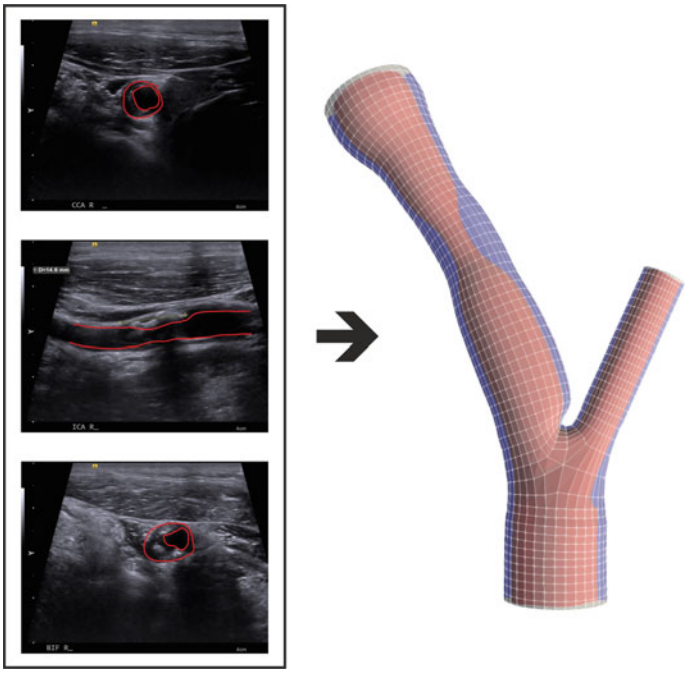

Fig. 1 Patient-specific US images used for the reconstruction (left) and the reconstructed 3D geometrical model (right) with vessel lumen colored in red and arterial wall colored in blue

2.2 Plaque Progression Modeling

In this section, the numerical model for plaque progression is presented. As already mentioned in the introductory section, the numerical model consists of three parts. The first part represents the modeling of blood flow through the patient-specific arterial segment. For this purpose the Navier–Stokes equations and the continuity equation are solved over the entire lumen domain. This way, the distribution of hemodynamic parameters is calculated. This includes the calculation of WSS distribution across the contact surface between lumen and arterial wall (the intimal area).

For an incompressible fluid, and considering that there is a non-slip boundary condition applied on the wall surface, the WSS can be calculated as:

$$\tau = -\mu \frac{\partial \mathbf{u}_t}{\partial \mathbf{n}} \tag{1}$$

where $\mathbf{u}_t$ denotes the tangential velocity and $\mathbf{n}$ denotes the unit vector of the normal to the arterial wall in the considered point of the domain.

The second part represents the modeling of transport of relevant macromolecules (primarily LDL) through the bloodstream and afterwards through the intima. Mass transfer through the bloodstream is modeled using convection–diffusion equations, Darcy law is used to model the filtration of blood and Kedem-Katchalsky equations [10, 11] are used to model the solute and flux exchanges between the lumen and the intimal area. The convection–diffusion equation for the LDL transport is given by:

$$\frac{\partial c}{\partial t} + v_x \frac{\partial c}{\partial x} + v_y \frac{\partial c}{\partial y} + v_z \frac{\partial c}{\partial z} = D\left(\frac{\partial^2 c}{\partial x^2} + \frac{\partial^2 c}{\partial y^2} + \frac{\partial^2 c}{\partial z^2}\right) \tag{2}$$

where c represents the concentration of LDL; v represents the blood velocity (subscripts x, y and z represent the components in the Cartesian coordinate system) and D is the constant representing the diffusion coefficient. The remaining equations contain many parameters and their complex explanation is omitted from this paper, but can be found in [5]. Some of the parameters of the model are used from literature and others are measured or fitted during the European FP7 project ARTreat [7].

The third part of the numerical model deals with the biological mechanism that is responsible for the generation and growth of atherosclerotic plaque. The mechanism considered within the used numerical model is briefly discussed in the sequel, while all the details of the numerical model can be found in literature [5–7]. After reaching the intimal area, it is assumed that the LDL molecules are oxidized. When a certain threshold concentration of oxidized LDL is reached, the monocytes are recruited, which further differentiate into macrophages. Further transformation of macrophages to foam cells leads to further recruitment of monocytes. This further leads to a self-support inflammatory reaction of the tissue, represented by creation of cytokines molecules that act a pro-inflammatory signal. The mentioned foam cells that are created actually induce the local increase of volume of the arterial wall. In order to model the described inflammatory process, three additional reaction–diffusion

equations are included in the system. The lumen and arterial wall are considered to be locally incompressible, which can be considered as an acceptable assumption for a large vessel like carotid bifurcation [12]. Hence, when the foam cells induce the increase of intima volume, this change produces a decrease in lumen volume and this further affects the fluid domain. This way, the full coupling of all parts of the model is achieved.

The entire system of equations is solved using finite element method [13]. In order to couple the motion of the nodes belonging to the intimal region of the arterial wall with the blood flow, the Arbitrary Lagrangian Euler (ALE) formulation is used for blood flow simulation that includes mesh moving algorithm [14]. The Navier–Stokes equation and the continuity equation is ALE formulation are written as:

$$\rho\left[v_i^* + \left(v_j - v_j^m\right)v_{i,j}\right] = -p_{,i} + \mu v_{i,jj} + f_i^B \tag{3}$$

$$v_{i,i} = 0 \tag{4}$$

where v_j^m represents the velocity components of the point of the moving surface. Fluid density, viscosity and pressure are denoted by ρ, μ and p, respectively. The body force is denoted by f_i^B. The superscript * denotes the time derivative at a considered point on the mesh.

The standard Galerkin procedure and the Gauss theorem are applied on Eqs. (3) and (4) in order to discretize the fluid domain and transform the obtained integrals. Finally, the system of equations is integrated incrementally over the defined time period using a time step Δt. For this purpose the implicit linearization with respect to time is performed [13], by appropriating all quantities using the following expression:

$$^{t+\Delta t}F = {}^{t}F + F^*\Delta t \tag{5}$$

where F represents a generic quantity (the same procedure is applied for blood velocity, pressure and concentration of macromolecules). It is considered that at time point t (at the start of the current time step) the value of the quantities is known. The entire system of equations should be satisfied at the end of time step, at i.e. at time $t + \Delta t$.

Within the presented equations, since the diffusion coefficients are low, there is a domination of the convection terms. Thus, there is a problem of the stability of the numerical solution. This problem is addressed within the developed numerical model by applying the streamline upwind/Petrov–Galerkin stabilizing technique (SUPG) [15] within the standard numerical integration scheme. The equations including diffusion are transformed into their incremental form and then all equations are summed in a system of finite element equations of balance in its incremental-iterative form.

This iterative process is repeated until the convergence is reached. The convergence criteria are defined such that the increment of the considered quantities in a time step Δt is less than the selected numerical tolerance.

3 Results

In this section, the results of the plaque progression simulation for a particular patient are presented. The mesh independence study was performed first, to determine the optimal number of nodes in the mesh. The mesh independence criterion was that the average WSS on the surface part close to the stenosis does not differ more than 2%. In this particular case, five meshes were analyzed and elements. mesh independence was reached 191,448 nodes and 177,408 elements. Figure 2 shows the reconstructed geometry with overall 5 chosen cross-sections. The model on the left is colored according to the distribution of total displacement of the nodes on the surface between lumen and intima. On the right, the change of the shape of the cross-sections of the arterial wall is shown in three specific moments in time (baseline, after 3 months and after 6 months). The change of lumen area over time for the chosen cross-sections is plotted in Fig. 3. The change is shown in percentage with respect to the baseline lumen area, to better illustrate the change in different positions of the carotid bifurcation. The obtained change of lumen area matches the clinically expected results. As it can be observed from Figs. 2 and 3, the greatest decrease of lumen area is observed at Slice#3, in the segment that was already very stenotic at baseline. The baseline stenosis was 59% and the simulated value after 6 months is predicted to be 84%. The reasoning for this behavior is that at this segment, there is a large concentration of oxidized LDL and the inflammatory process proceeds faster. On the other hand, the smallest decrease in lumen area (almost insignificant, less than 5%) can be observed in Slice#5, that is located on the external branch of the carotid bifurcation away from the stenosis, where the diameter of the vessel is constant. Segment after the stenosis (Slice#4) is also vulnerable to plaque creation and progression, since the simulation predicts that the lumen area will decrease for 25% in this cross-section.

4 Discussion and Conclusion

The WSS as an important blood flow parameter has been studied extensively in literature. Poelma et al. [20] performed experimental measurements of blood velocity and subsequently calculated WSS in the developing chicken embryo heart. The WSS distribution in microvasculature is numerically investigated in [21], where also the influence of motion of individual red blood cells on the distribution of WSS is analyzed. Blood flow simulations were performed in several patient-specific abdominal aortic aneurysms [22] in order to investigate the change of WSS magnitude, angle, and orientation in space and time in complex geometries.

Transport of LDL molecules through the bloodstream and arterial wall has also been studied in literature [3, 4]. The simplest model proposed considers the arterial wall only as a boundary condition and is called wall-free model. This model was used to simulate the mass transport in a coronary artery [16]. However, this model does

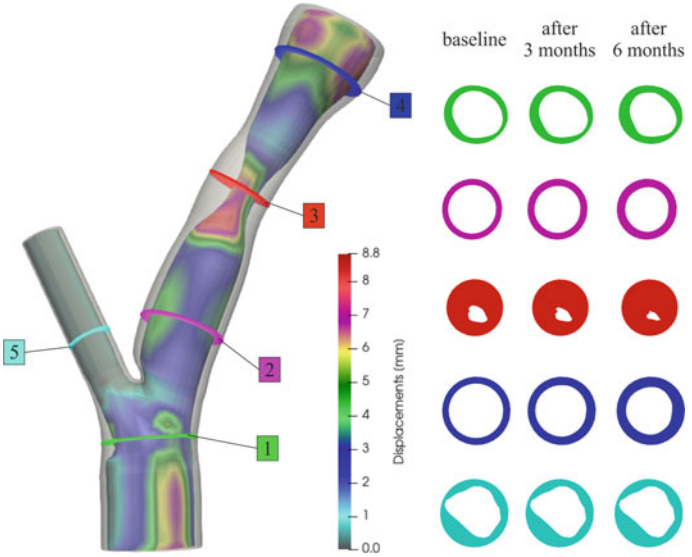

Fig. 2 The results of the plaque progression simulation. The distribution of displacement of nodes of the arterial wall (left); the change of shape of chosen cross-sections over time (right)

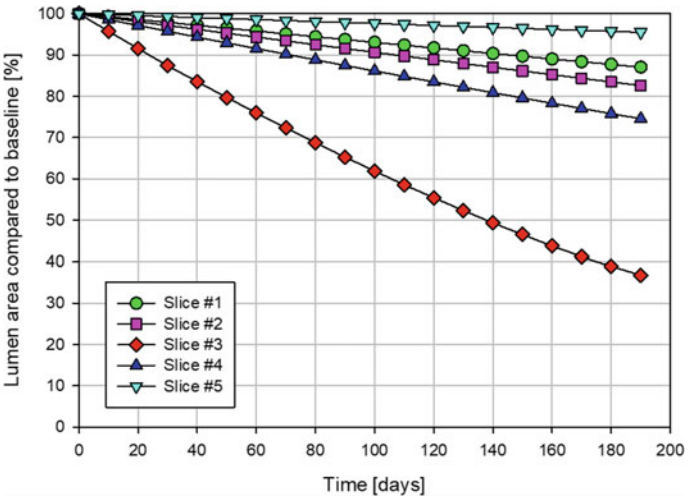

Fig. 3 Change of lumen area of 5 chosen cross-sections (from Fig. 2) over time

not analyze the transport of molecules through the wall or the dynamics of motion inside the arterial wall. The wall was modeled as a single layer porous medium in [17]. The wall was observed as a multi-layered domain, and intima and media are

represented separately in [18]. A three-pore model was used in [19], where special attention is dedicated to the influence of WSS on the transport of LDL.

In this study, fully coupled biomechanics software for plaque progression was used to simulate the growth of plaque within patient-specific carotid bifurcation. The numerical model couples computational fluid mechanics, LDL transport, inflammatory process and plaque growth. This numerical model was extensively validated against experimental and clinical data, for vessels of animals (pigs) and clinical patients [5–7]. In this study, this software is applied to perform simulation of plaque progression using the geometry of a specific patient that is reconstructed by applying deep learning techniques to the images obtained from clinical US examination. Since this research is performed within an ongoing project, the follow-up images of the patients will be collected and subsequently used in the future to compare the simulation results with clinical findings and further improve the parameters of the model.

The parameters of the numerical model are either experimentally measured in literature or fitted using the nonlinear least square method using clinically relevant patient-specific data [5–7]. These parameters were estimated for a set of patients and then their median values are applied in the simulation for the particular patient considered in this study. The fitting of parameters should be performed using patient-specific measurements, per example flow velocity and pressure at the time of the US examination. It would also be helpful to incorporate virtual histology to determine the composition of the plaque. This would enable the creation of a more detailed model for plaque progression. On the other hand, this would require additional clinical examinations, while the main goal of the presented approach was to provide clinicians with as much data as possible from a single US examination. These questions will be further considered in the future improvements of the numerical model.

Numerical simulations like the one presented in this study enable the prediction of plaque progression in time based on patient-specific geometries and this can be very useful in clinical practice for the prediction of disease progression. The US examination can be significantly improved first by the 3D computer modeling of the shape of the patient's blood vessel and exact determination of plaque location. The numerical model for plaque progression can further help to understand and predict the evolution of atherosclerotic plaque which is very significant for appropriate diagnostics and treatment planning and represents one step further in applying biomechanics modeling within the concept of computer-integrated medicine.

Acknowledgements The research presented in this study was part of the project that has received funding from the European Union's Horizon 2020 research and innovation programme under grant agreement No. 755320-2—TAXINOMISIS. This article reflects only the author's view. The Commission is not responsible for any use that may be made of the information it contains. The research is also supported by the Ministry of Education, Science and Technological Development of the Republic of Serbia [451-03-9/2021-14/200378 (Institute for Information Technologies, University of Kragujevac) and 451-03-9/2021-14/200107 (Faculty of Engineering, University of Kragujevac)].

References

1. Libby, P. (2002). Inflammation in atherosclerosis. *Nature, 420*, 868–874.
2. Loscalzo, J., & Schafer, A. I. (2003). *Thrombosis and hemorrhage* (3rd ed.). Lippincott Williams & Wilkins.
3. Tarbell, J. M. (2003). Mass transport in arteries and the localization of atherosclerosis. *Annual Review of Biomedical Engineering, 5*, 79–118.
4. Quarteroni, A., Veneziani, A., & Zunino, P. (2002). Mathematical and numerical modeling of the solute dynamics in blood flow and arterial walls. *SIAM Journal of Numerical Analysis, 39*, 1488–1511.
5. Rakocevic, G., Djukic, T., Filipovic, N., & Milutinovic, V. (2013). *Computational medicine in data mining and modeling*. Springer.
6. Parodi, O., Exarchos, T., Marraccini, P., et al. (2012). Patient-specific prediction of coronary plaque growth from CTA angiography: A multiscale model for plaque formation and progression. *IEEE Transactions on Information Technology in Biomedicine.* https://doi.org/10.1109/TITB.2012.2201732
7. Filipovic, N., Rosic, M., Tanaskovic, I., et al. (2012). ARTreat project: Three-dimensional numerical simulation of plaque formation and development in the arteries. *IEEE Transactions on Information Technology in Biomedicine.* https://doi.org/10.1109/TITB.2011.2168418
8. Djukic, T., Arsic, B., Koncar, I., & Filipovic, N. (2020). 3D reconstruction of patient-specific carotid artery geometry using clinical ultrasound imaging. Workshop computational biomechanics for medicine XV. In *23rd International Conference on Medical Image Computing & Computer Assisted Intervention (MICCAI)*
9. Djukic, T., Arsic, B., Djorovic, S., Koncar, I., & Filipovic, N. (2020). Validation of the machine learning approach for 3D reconstruction of carotid artery from ultrasound imaging. In *IEEE 20th International Conference on Bioinformatics and Bioengineering (BIBE).*
10. Filipovic, N., Meunier, N., & Kojic, M. (2010). *PAK-Athero, specialized three-dimensional PDE software for simulation of plaque formation and development inside the arteries.* University of Kragujevac.
11. Goldstein, J., Anderson, R., & Brown, M. (1979). Coated pits, coated vesicles, and receptor-mediated endocytosis. *Nature, 279*, 679–684.
12. Steinman, D. A. (2012). Assumptions in modelling of large artery hemodynamics. In *Modeling of physiological flows* (pp. 1–18). Springer.
13. Kojic, M., Filipovic, N., Stojanovic, B., & Kojic, N. (2008). *Computer modeling in bioengineering: Theoretical background, examples and software.* Wiley.
14. Filipovic, N., Mijailovic, S., Tsuda, A., & Kojic, M. (2006). An implicit algorithm within the arbitrary Lagrangian-Eulerian formulation for solving incompressible fluid flow with large boundary motions. *Computer Methods in Applied Mechanics and Engineering, 195*, 6347–6361.
15. Brooks, A. N., & Hughes, T. J. R. (1982). Streamline upwind/Petrov-Galerkin formulations for convection dominated flows with particular emphasis on the incompressible Navier-Stokes equations. *Computer Methods in Applied Mechanics and Engineering, 32*, 199–259.
16. Kaazempur-Mofrad, M. R., & Ethier, C. R. (2001). Mass transport in an anatomically realistic human right coronary artery. *Annals of Biomedical Engineering, 29*, 121–127.
17. Stangeby, D. K., & Ethier, C. R. (2002). Computational analysis of coupled blood-wall arterial LDL transport. *Journal of Biomechanical Engineering-T ASME, 124*, 1–8.
18. Ai, L., & Vafai, K. (2006). A coupling model for macromolecule transport in a stenosed arterial wall. *International Journal of Heat and Mass Transfer, 49*, 1568–1591.
19. Olgac, U., Kurtcuoglu, V., & Poulikakos, V. (2008). Computational modeling of coupled blood-wall mass transport of LDL: Effects of local wall shear stress. *American Journal of Physiology Heart and Circulatory Physiology, 294*, 909–919.
20. Poelma, C., Van der Heiden, K., Hierck, B. P., Poelmann, R. E., & Westerweel, J. (2010). Measurements of the wall shear stress distribution in the outflow tract of an embryonic chicken heart. *Journal of the Royal Society, Interface, 7*(42), 91–103.

21. Balogh, P., & Bagchi, P. (2019). Three-dimensional distribution of wall shear stress and its gradient in red cell-resolved computational modeling of blood flow in in vivo-like microvascular networks. *Physiological Reports, 7*(9), e14067.
22. Arzani, A., & Shadden, S. C. (2016). Characterizations and correlations of wall shear stress in aneurysmal flow. *Journal of Biomechanical Engineering, 138*(1), 0145031–01450310.

Imaging

Assessing Fibre Reorientation in Soft Tissues with Simultaneous Mueller Matrix Imaging and Mechanical Testing

Alexander W. Dixon, Andrew J. Taberner, Martyn P. Nash, and Poul M. F. Nielsen

Abstract The implantation of bioprosthetic heart valves constructed from heterograft soft tissue membranes, such as bovine pericardium, porcine pericardium, and porcine heart valves, is a common method of treatment for valvular heart disease. A greater understanding of the load-dependent behaviour is needed to improve durability and functional performance of these tissues in such applications. However, existing techniques that provide the required experimental data are destructive in nature. This limits measurements to pre- and post-mechanical testing states and prevents further use of the tissue in medical devices. Thus, there is a need to develop an instrument implementing wide-field non-destructive imaging techniques that can assess collagen fibre architecture in soft tissue membranes undergoing mechanical testing. In this work, a novel optomechanical system was developed that integrates a Mueller matrix imaging polarimeter with a biaxial mechanical testing instrument, suitable for characterising the mechanical material properties of soft tissue membranes. A preliminary mechanical test demonstrated that this instrument provides a non-destructive method for detecting fibre realignment along loading directions in these tissues. The additional measurements now possible with this system may offer new insights into structure–function relationships of soft tissue membranes.

Keywords Soft tissue · Tissue anisotropy · Polarisation imaging · Mechanical testing

A. W. Dixon (✉) · A. J. Taberner · M. P. Nash · P. M. F. Nielsen
Auckland Bioengineering Institute, University of Auckland, Auckland, New Zealand
e-mail: alex.dixon@auckland.ac.nz

A. J. Taberner
e-mail: a.taberner@auckland.ac.nz

M. P. Nash
e-mail: martyn.nash@auckland.ac.nz

P. M. F. Nielsen
e-mail: p.nielsen@auckland.ac.nz

A. J. Taberner · M. P. Nash · P. M. F. Nielsen
Department of Engineering Science, University of Auckland, Auckland, New Zealand

P. M. F. Nielsen et al. (eds.), *Computational Biomechanics for Medicine*,
https://doi.org/10.1007/978-3-031-09327-2_10

1 Introduction

Soft tissue membranes have uses in many important tissue engineering applications, such as in the construction of bioprosthetic heart valves for replacing diseased leaflets. Soft tissue membranes of porcine and bovine pericardium are used in the construction of bioprosthetic heart valves. However the requirements of functional performance and durability challenges the use of these tissues in such applications [1, 2].

A detailed understanding of the relationship between the tissue structure and mechanical function of membranes provides insight into their performance. Numerous studies have measured or estimated the mechanical properties of pericardium [3]. However, these types of mechanical tests are typically destructive and prevent further use of the tissue for valve construction. By considering that collagen is the main load bearing structure in pericardium [4], and that the mechanical response is dependent on the collagen fibre architecture [5], an alternative approach to mechanical testing is to non-destructively measure the fibre architecture at a macroscopic (tissue-level) scale. Such an approach requires a fundamental understanding of the structure–function relationship of these tissues.

Quantitative information on collagen fibre architecture has been used to develop important structural constitutive models that enable the prediction of mechanical behaviour of pericardial tissues at the macroscopic scale [6, 7]. These promising advancements in the understanding of the structure–function relationships of such tissues should enable structural optimisation studies of tissue selection for bioprosthetic heart valves. However, previously used structural imaging techniques, such as small-angle light scattering, have required optical clearing of pericardial tissue. This requirement prohibits further use of the imaged tissue in bioprosthetic heart valves [8] as well as limits imaging to pre- or post-mechanical testing states [9] making these techniques impractical for characterising the load-dependent behaviour of the collagen fibre architecture in these tissues. Non-destructive studies using second harmonic generation imaging have characterized the load-dependent behaviour of collagen and elastin within soft tissues at the microstructural scale [5, 10]. However, this imaging technique is currently incapable of imaging tissues at the macroscopic scale.

Thus, there is a need for the development of instrumentation that combines non-destructive imaging techniques, to measure collagen fibre architecture at a macroscopic scale in soft tissue membranes, with simultaneous mechanical testing to enable further characterisation of the structure–function relationship in these tissues. Ideally, such an imaging technique, combined with an appropriate structural constitutive model, may then enable identification and selection of suitable regions for valve leaflets within pericardial membranes to give more effective and durable bioprostheses.

Polarisation imaging techniques are a promising non-destructive optical modality that can assess the heterogeneous and anisotropic microstructure of collagen fibres over macroscopic spatial scales. Type I collagen, the primary fibrous component in pericardium [11], exhibits an intrinsic linear birefringence with an optic axis that

aligns with the collagen fibre orientation [12, 13]. Optical assessment of collagen fibre architecture in soft tissue membranes may however be confounded by the complex turbid nature of the tissue. Mueller matrix imaging is an emerging polarisation imaging technique that measures a transfer function that represents all the polarisation properties of a sample [14]. The full Mueller matrix, a 4×4 matrix of real elements, can be measured in order to characterise, without prior information, the polarisation properties of a complex turbid medium [15].

We have recently implemented a wide-field non-destructive imaging technique for measuring optical anisotropy in soft tissue membranes using Mueller matrix imaging. Calf bovine pericardium has been shown to have similar mechanical properties to adult bovine pericardium but with significantly lower thicknesses [2]. This has enabled the use of transmissive polarisation imaging on bioprosthetic heart valve materials whilst avoiding the practical limits of these imaging techniques that can occur in adult tissues [16]. In a previous study, it has been shown that for soft tissues, such as calf bovine pericardium, it is appropriate to image the full Mueller matrix of these tissues to account for polarisation properties other than those due to fibrous components [17]. In this study, we combine a mechanical testing instrument with a Mueller matrix imaging polarimeter and carry out a preliminary optomechanical test on a sample of calf bovine pericardium. We aimed to assess whether the changes in measured polarization properties indicated a change in fibre orientation that corresponded to the applied stretch in such tissues.

2 Method

A Mueller matrix imaging polarimeter has been developed and is described in detail in Dixon et al. [17]. Briefly, light from a near-infrared LED was collimated and passed through a polarisation state generator (PSG), through a sample, and then through the polarisation state analyser (PSA). Light transmitted through the PSA was focused onto a monochromatic camera, giving images with a field of view of approximately 22 mm $\times$ 18 mm at an isotropic pixel resolution of 8.9 μm.

A previously developed multiaxial mechanical testing instrument [18–20] was adapted and integrated with the polarimeter, enabling simultaneous mechanical testing and transmission Mueller matrix imaging of planar specimens (see Fig. 1). The mechanical testing instrument consisted of a circular array of eight independently controlled linear actuators (Physik Instrumente, M-226.27) with a travel range of 50 mm and minimum repeatable motion of 0.2 μm. The linear actuators were position and velocity commanded with a servo-motor controller card (NI 7350) that drove the motors via custom-built linear power amplifiers. Each linear actuator had a custom-built 1D flexure for measuring tensile force using a force sensor (Honeywell, FSS15000NST) connected to an analog input module (NI 9237) installed in a USB chassis (NI cDAQ 9174). The transducers provide a typical force sensing range of 0–6 N, dependent on the mounting for each sample. A sample was mounted in the

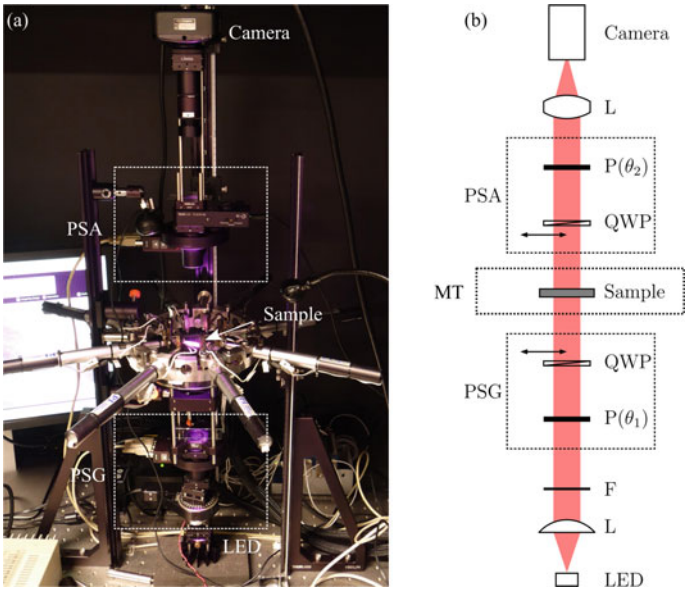

Fig. 1 Experimental setup (**a**) and schematic (**b**) of the Mueller matrix imaging polarimeter and mechanical tester. L: lens, F: filter, P: linear polariser, QWP: quarter waveplate, PSG: polarisation state generator, PSA: polarisation state analyser, MT: mechanical testing instrument

optical path between the PSG and the PSA and illuminated with a beam of approximately 22 mm diameter. The polarimeter and mechanical testing instrument were controlled via custom LabVIEW software (2018, National Instruments), to perform simultaneous optical and quasi-static mechanical tests in a fully automated manner.

A quasi-static uniaxial mechanical test was performed on a 40 mm $\times$ 10 mm sample that was cut from an excised sheet of calf bovine pericardium (Angus, 6 months old) with a CO_2 laser (Trotec, Speedy 300). The sample was glued at the ends to give a gauge length of 30 mm. Calf pericardium was stretched in steps of 0.5 mm along its long-axis dimension, at a velocity of 0.5 mm/s, with Mueller matrices measured following each displacement step. To account for stress relaxation in the tissue, a pause of 45 s was included prior to each Mueller matrix measurement.

Mueller matrices were decomposed using logarithm decomposition, which assumes that the medium exhibits co-incident, as opposed to a layered sequence of, polarisation properties. A detailed description of the decomposition procedure is given in Dixon et al. [17, 21]. A number of polarisation properties, accumulated across the thickness of the sample, were calculated from the decomposed Mueller matrices: linear retardance, fast axis orientation, and circular retardance.

3 Results and Discussion

The force and stretch data for the pericardial sample is shown in Fig. 2. The sample exhibited a nonlinear stress–strain response that is typical of soft tissues. This behaviour has been previously explained by considering that when a tensile load is applied to pericardial tissue, it is initially supported by elastin fibres allowing a high deformation at low stress. As the load increases, the initially crimped collagen fibres are extended and straightened sequentially to support the tensile load with a stiffer mechanical response. This collagen fibre recruitment leads to transitional behaviour of the tissue between elastin-controlled and collagen-controlled phases that give rise to the nonlinear mechanical response of the tissue [2, 4, 22]. Note that mechanical results are presented here with force (as opposed to stress) due to unknown variations in thickness across the pericardial sample. In future studies, we plan to map unloaded sample thicknesses using optical coherence tomography.

The Mueller matrix images for the pericardium sample in an unloaded state and at a stretch ratio of 1.15 are shown in Figs. 3 and 4, respectively. In the unloaded state, the tissue exhibited strong linearly birefringent properties, as demonstrated by the large signal in all elements of the lower-right 3×3 submatrix. When stretched, the signal in the Mueller matrix elements became more heterogeneous across the sample, indicating spatially non-uniform changes in the linearly birefringent structures. This may be associated with a recruitment of fibrous structures that varies across the sample.

The direct quantification of polarisation properties from the Mueller matrix is not possible for complex and turbid media, such as pericardial tissue, that exhibit simultaneous linear retardance, circular retardance, and depolarisation [17]. The spatial heterogeneity of these samples also makes qualitative interpretations of Mueller matrix images somewhat difficult. Logarithm decomposition was thus performed on all imaged regions of the pericardium at the different states of loading.

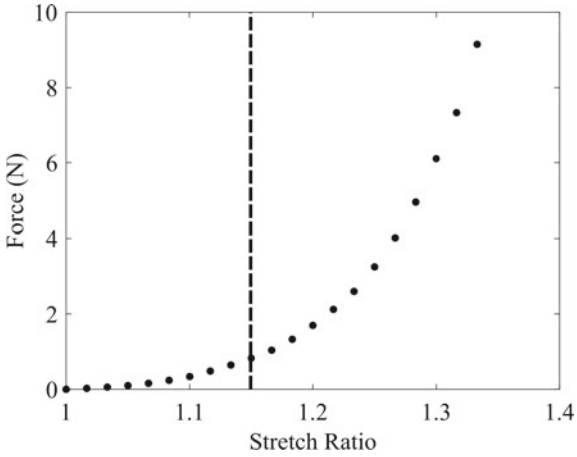

Fig. 2 Force-stretch curve for uniaxial testing of a calf bovine pericardial sample. The vertical dashed line indicates the stretch ratio at which the imaging analysis is demonstrated

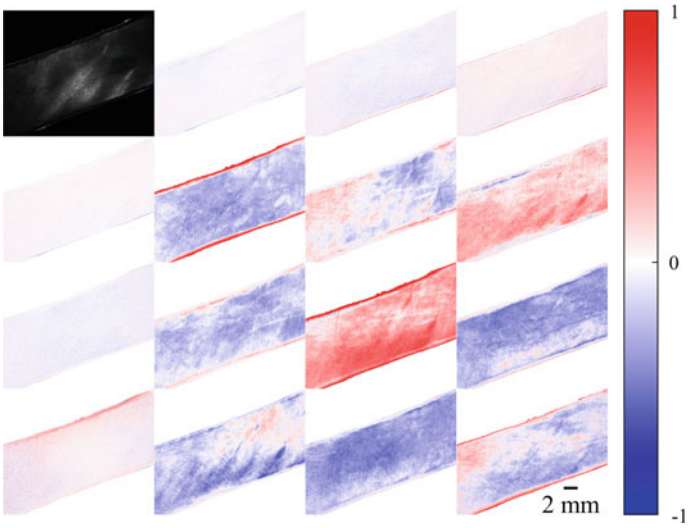

Fig. 3 Mueller matrix images for a sample of calf bovine pericardium mounted at +22.5° to the horizontal axis in a uniaxial tester in an unloaded state. Note the upper-left matrix element shows the average transmission across the sample. The color bar indicates the intensity of each Mueller matrix element, normalised with respect to the average transmission across the sample

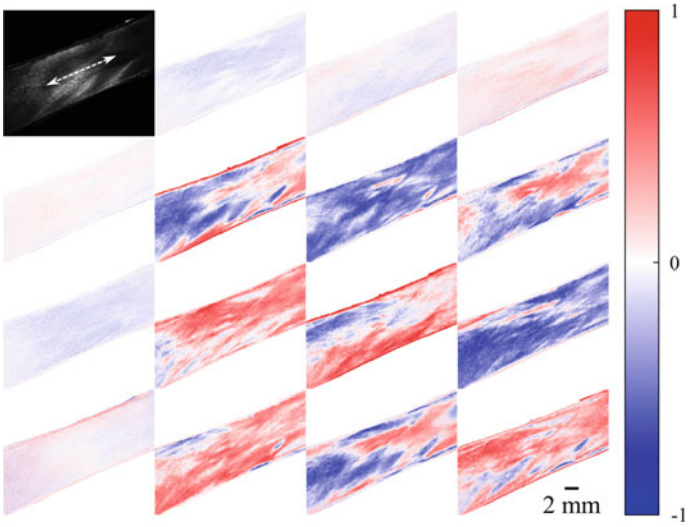

Fig. 4 Mueller matrix images for a sample of calf bovine pericardium mounted in a uniaxial tester at a stretch ratio of 1.15. The direction of stretch is indicated by white arrow in the upper-left element of the Mueller matrix

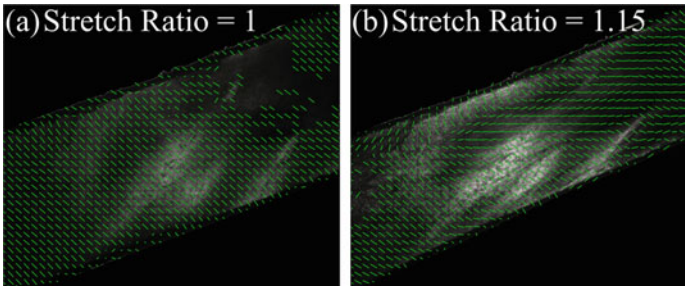

Fig. 5 Anisotropy maps for uniaxially stretched calf bovine pericardium at a stretch ratio of 1 (**a**) and a stretch ratio of 1.15 (**b**). Line segments in each subregion (0.5 mm × 0.5 mm) are oriented with the local circular mean optic axis orientation and length normalised to the corresponding local circular variance. Subregions with more than 75% undefined values have been omitted

The measured linear retardance from logarithm decomposition, which is given by the accumulated linear birefringence over the sample thickness, exhibited large strain-induced changes when stretched. This was likely associated with reorganisation of the collagen fibre architecture in response to loading. Recalling that Type I collagen exhibits a positive intrinsic linear birefringence, with an optic axis that aligns with the collagen fibre orientation, the axis of optical anisotropy corresponds to the slow axis (perpendicular to the fast axis) of linear retardance in these tissues.

The linear retardance and axis of optical anisotropy are presented as maps of tissue optical anisotropy in Fig. 5 as overlaid lines in each subregion (approximately 0.5 mm × 0.5 mm), with orientation and length corresponding to the local circular mean of the (slow) optic axis orientation and normalised local circular variance, respectively. It is important to note that retardance (linear + circular) measurements in the polarimeter were limited to π radians and that, beyond this limit, phase wrapping effects occur in the measurements. Phase wrapping was present in the unloaded measurements of the pericardial sample. Correcting the offset in the fast axis due to phase wrapping resulted in maps of optical anisotropy that indicated the tissue had a uniform fibre orientation of approximately $-40°$ when unloaded (see Fig. 5a). In general, the fibre orientation realigned toward the direction of applied stretch, particularly in the upper right region of the sample (see Fig. 5b). This was expected, since anisotropic fibrous structures are the main load bearing components in these tissues [4, 23].

4 Conclusion

This study presented the first combined Mueller matrix imaging and mechanical testing of calf bovine pericardium. Preliminary optomechanical testing was carried out with a novel instrument that will enable better understanding of the mechanical behaviour of industry standard bioprosthetic heart valve materials, such as calf and adult bovine pericardium. The imaging technique presented here was non-destructive

as it required no chemical treatment of the tissue, thus enabling further use of analysed tissue. It is worth noting that as the imaging approach adopted in this work was wide-field, the field of view could be increased to image larger tissue samples, thus enabling its use in other tissue engineering applications.

A phase wrapping issue that hinders interpretation of measurements of optical anisotropy in these tissues was noted. This issue was particularly confounding during mechanical testing, where large strain-induced changes in the birefringence occurred, likely due to collagen fibre realignment in response to loading. This issue must be addressed prior to more comprehensive optomechanical studies of these tissues.

Biaxial (as opposed to uniaxial) mechanical testing is required to characterise the mechanical behaviour of these soft tissue membranes due to the anisotropic and heterogeneous nature of their collagen fibre architecture. A distinct advantage of the developed mechanical instrument is the 4 independent stretching axes within the test plane compared to typical commercial biaxial mechanical testers, with just 2 stretching axes. This can induce a richer set of strain states, and hence load-deformation data, with which to characterise the mechanical behaviour of membranes. Moreover, no prior knowledge of preferential fibre direction in membranes will be required when mounting samples.

The measurements now possible with the optomechanical instrument developed in this study may offer new insights into structure–function relationships of soft tissue membranes. This is significant because the implemented non-destructive imaging of collagen fibre architecture can provide information on the bulk tissue function in tissue engineering applications, whilst leaving the tissue intact for further use, such as in the manufacture of bioprosthetic heart valves.

References

1. Rodriguez Gabella, T., Voisine, P., Puri, R., et al. (2017). Aortic bioprosthetic valve durability: Incidence, mechanisms, predictors, and management of surgical and transcatheter valve degeneration. *Journal of the American College of Cardiology, 70*, 1013–1028. https://doi.org/10.1016/j.jacc.2017.07.715
2. Caballero, A., Sulejmani, F., Martin, C., et al. (2017). Evaluation of transcatheter heart valve biomaterials: Biomechanical characterization of bovine and porcine pericardium. *Journal of the Mechanical Behavior of Biomedical Materials, 75*, 486–494. https://doi.org/10.1016/j.jmbbm.2017.08.013
3. Aguiari, P., Fiorese, M., Iop, L., et al. (2016). Mechanical testing of pericardium for manufacturing prosthetic heart valves. *Interactive Cardiovascular and Thoracic Surgery, 22*, 72–84. https://doi.org/10.1093/icvts/ivv282
4. Zioupos, P., & Barbenel, J. C. (1994). Mechanics of native bovine pericardium: II—A structure based model for the anisotropic mechanical behaviour of the tissue. *Biomaterials, 15*, 374–382. https://doi.org/10.1016/0142-9612(94)90250-X
5. Alavi, S. H., Ruiz, V., Krasieva, T., et al. (2013). Characterizing the collagen fiber orientation in pericardial leaflets under mechanical loading conditions. *Annals of Biomedical Engineering, 41*, 547–561. https://doi.org/10.1007/s10439-012-0696-z

6. Sacks, M. S. (2003). Incorporation of experimentally-derived fiber orientation into a structural constitutive model for planar collagenous tissues. *Journal of Biomechanical Engineering, 125*, 280–287. https://doi.org/10.1115/1.1544508
7. Fan, R., & Sacks, M. S. (2014). Simulation of planar soft tissues using a structural constitutive model: Finite element implementation and validation. *Journal of Biomechanics, 47*, 2043–2054. https://doi.org/10.1016/j.jbiomech.2014.03.014
8. Goth, W., Yang, B., Lesicko, J., et al. (2016). Polarized spatial frequency domain imaging of heart valve fiber structure. *Proceedings of SPIE*, 971019. https://doi.org/10.1117/12.2212812
9. Goth, W., Potter, S., Allen, A. C. B., et al. (2019). Non-destructive reflectance mapping of collagen fiber alignment in heart valve leaflets. *Annals of Biomedical Engineering, 47*, 1250–1264. https://doi.org/10.1007/s10439-019-02233-0
10. Krasny, W., Morin, C., Magoariec, H., & Avril, S. (2017). A comprehensive study of layer-specific morphological changes in the microstructure of carotid arteries under uniaxial load. *Acta Biomaterialia, 57*, 342–351. https://doi.org/10.1016/j.actbio.2017.04.033
11. Naimark, W. A., Lee, J. M., Limeback, H., & Cheung, D. T. (1992). Correlation of structure and viscoelastic properties in the pericardia of four mammalian species. *The American Journal of Physiology, 263*, H1095–H1106.
12. Tuchin, V. V. (2016). Polarized light interaction with tissues. *Journal of Biomedical Optics, 21*, 071114. https://doi.org/10.1117/1.JBO.21.7.071114
13. Wolman, M., & Kasten, F. H. (1986). Polarized light microscopy in the study of the molecular structure of collagen and reticulin. *Histochemistry and Cell Biology, 85*, 41–49. https://doi.org/10.1007/BF00508652
14. He, H., Liao, R., Zeng, N., et al. (2019). Mueller matrix polarimetry—An emerging new tool for characterizing the microstructural feature of complex biological specimen. *Journal of Lightwave Technology, 37*, 2534–2548. https://doi.org/10.1109/JLT.2018.2868845
15. Alali, S., & Vitkin, A. (2015). Polarized light imaging in biomedicine: Emerging Mueller matrix methodologies for bulk tissue assessment. *Journal of Biomedical Optics, 20*, 61104. https://doi.org/10.1117/1.JBO.20.6.061104
16. Dixon, A., Taberner, A., Nash, M., & Nielsen, P. (2018). Extended depth measurement for a Stokes sample imaging polarimeter. *Proceedings of SPIE,* 1049718. https://doi.org/10.1117/12.2289311
17. Dixon, A. W., Taberner, A. J., Nash, M. P., & Nielsen, P. M. F. (2021). Quantifying optical anisotropy in soft tissue membranes using Mueller matrix imaging. *Journal of Biomedical Optics, 26*. https://doi.org/10.1117/1.JBO.26.10.106001
18. Nielsen, P. M. F., Malcolm, D. T. K., Hunter, P. J., & Charette, P. G. (2002). Instrumentation and procedures for estimating the constitutive parameters of inhomogeneous elastic membranes. *Biomechanics and Modeling in Mechanobiology, 1*, 211–218. https://doi.org/10.1007/s10237-002-0019-7
19. Kvistedal, Y. A., & Nielsen, P. M. F. (2009). Estimating material parameters of human skin in vivo. *Biomechanics and Modeling in Mechanobiology, 8*, 1–8. https://doi.org/10.1007/s10237-007-0112-z
20. Jor, J. W. Y., Nash, M. P., Nielsen, P. M. F., & Hunter, P. J. (2011). Estimating material parameters of a structurally based constitutive relation for skin mechanics. *Biomechanics and Modeling in Mechanobiology, 10*, 767–778. https://doi.org/10.1007/s10237-010-0272-0
21. Dixon, A. W. (2020). *Polarisation imaging of soft tissue membranes.* Ph.D. thesis. https://hdl.handle.net/2292/58120
22. Dixon, A. W. (2015). *An optomechanical instrument for pericardial tissue selection in bioprosthetic heart valves.* Master's thesis.
23. Sacks, M. S., Chuong, C. J. C., & More, R. (1994). Collagen fiber architecture of bovine pericardium. *ASAIO Journal, 40*, M632–M637. https://doi.org/10.1097/00002480-199407000-00075

A Direct Geometry Processing Cartilage Generation Method Using Segmented Bone Models from Datasets with Poor Cartilage Visibility

Faezeh Moshfeghifar, Max Kragballe Nielsen, José D. Tascón-Vidarte, Sune Darkner, and Kenny Erleben

Abstract We present a method to generate subject-specific cartilage for the hip joint. Given bone geometry, our approach is agnostic to image modality, creates conforming interfaces, and is well suited for finite element analysis. We demonstrate our method on ten hip joints showing anatomical shape consistency and well-behaved stress patterns. Our method is fast and may assist in large-scale biomechanical population studies of the hip joint when manual segmentation or training data is not feasible.

Keywords Cartilage generation · Hip joint · Finite element analysis

1 Introduction

The femur and pelvic bones come together in the hip joint (HJ), where the femoral head articulates within the acetabulum's lunate surface. The lunate surface and all of the femoral head, except the fovea pit, are covered by cartilage tissue allowing unhindered motion in the HJ [27]. The stress distribution on these articular surfaces is often analyzed experimentally [10, 11], using finite element (FE) analysis [2, 14,

F. Moshfeghifar (✉) · M. K. Nielsen · J. D. Tascón-Vidarte · S. Darkner · K. Erleben
Department of Computer Science, University of Copenhagen, Copenhagen, Denmark
e-mail: famo@di.ku.dk

M. K. Nielsen
e-mail: max@di.ku.dk

J. D. Tascón-Vidarte
e-mail: jota@di.ku.dk

S. Darkner
e-mail: darkner@di.ku.dk

K. Erleben
e-mail: erleben@di.ku.dk

P. M. F. Nielsen et al. (eds.), *Computational Biomechanics for Medicine*,
https://doi.org/10.1007/978-3-031-09327-2_11

24], or discrete element analysis [28, 30, 32]. The analysis results provide valuable information for studying both healthy and dysplastic hips [16, 24, 28, 31, 32]. The accuracy of these results is highly dependent on the HJ geometries.

HJ morphology is segmented directly from computed tomography (CT) [2, 9, 24, 28, 31] and magnetic resonance imaging (MRI) images [6]. CT and MRI scans contain high-contrast images of the bones with clearly visible interfaces. However, it is difficult to identify cartilage tissue due to the tight space in HJ [8] or low image resolution [29]. CT arthrography and manual traction enhance the cartilage visibility and increase the joint space at the cost of being an invasive intervention [9, 24].

This work presents a method to generate subject-specific cartilage models where cartilage segmentation is not feasible. Our method uses only the bone geometries coming together at the HJ and reconstructs the articulating cartilage surfaces based on bone curvature measures and distance measures. Our solution is fast, is independent of image modality, and preserves anatomical properties compared to previous methods. We validated our method by comparing the anatomical properties to other works, as detailed in Sect. 4 [1, 15, 20, 25]. Additionally, we tested their performance in a FE analysis setup. Our goal is to obtain consistent and stable cartilage models for FE analyses. For now, patients with HJ atypical geometries or pathology are out of the scope of this method.

2 Related Work

The femur and pelvis can be segmented using manual [2, 24], semi-automatic [9, 18, 28], or fully automated approaches [6, 17, 31].

When cartilage is manually segmented, the thickness and interfaces are either delineated from the images, assigned uniformly, or approximated by a radius representing the smoothed joint space mid-line [2, 24, 28]. This manual process is time-consuming and is limited by the users' clinical expertise and image resolution. Our method ensures conforming surfaces and computes the thickness directly from bone locality without needing for clinical expertise.

In semi-automated segmentation approaches, the initial cartilage geometry is delineated automatically, starting from user-defined landmarks. Additional refinement is needed to eliminate rough surfaces, holes, and irrelevant connected tissues [9, 28]. In contrast, our method only relies on bone surfaces and does not need landmarks or refinement.

With the advancements in computational morphometrics, automated cartilage segmentation is possible by combining bone statistical shape models with population-averaged cartilage thickness maps [30] or geometric constraints [6]. Automatic segmentation is a cost-effective approach and reduces the need for pre-processing data [30]. However, segmented data and prior information is needed to train such models. In contrast, our method does not require training data and is agnostic to data-shift problems.

Other approaches simplify the joint to a perfect ball in socket joint and fit the bone-cartilage and cartilage-cartilage interfaces to spheres or rotational conchoids [2, 21, 32]. These simplifications can affect the cartilage contact pressure and contact area [2]. Our work provides non-uniform cartilage thickness while maintaining conforming interfaces.

3 Methodology

The proposed cartilage generation method is based only on bone geometry and distance measures. Thus, the algorithm is sensitive towards the quality of the segmented bone mesh, which we assume has been preprocessed to remove irregularities and segmentation artifacts. We will focus on the hip joint and generate cartilage with respect to either the pelvis or femur, depending on which bone the cartilage attaches to. We will need to generate cartilage twice: once for the femur and once for the pelvis. We define the geometry of each bone as the vertices and faces $(\mathcal{V}, \mathcal{F})$ of a triangle mesh, where $\mathcal{V} \in \mathbb{R}^{N\times 3}$ and $\mathcal{F} \in \mathbb{Z}_{0+}^{K\times 3}$ for a mesh consisting of N vertices and K faces. We refer to the bone where cartilage attaches as the *primary bone*, $(\mathcal{V}_P, \mathcal{F}_P)$, and the other bone as the *secondary bone*, $(\mathcal{V}_S, \mathcal{F}_S)$. The generated cartilage will be a triangle surface mesh $(\mathcal{V}_C, \mathcal{F}_C)$. Our method can be summarized as the steps:

Distance Filtering: Select an initial subset of the primary bone as the *bone-attached* cartilage region based on the distance to the secondary bone;

Curvature-Based Region Filling: Apply our curvature-based region filling approach to ensure the bone-attached cartilage region extends to anatomical lines;

Extrusion: Extrude a subset of the bone-attached region towards the secondary bone;

Harmonic Boundary Blending: Interpolate between the boundary of the extruded and bone-attached regions to create a soft blend.

3.1 Distance Filtering

For now, we will focus on the femoral side of the hip joint and describe the femur as the primary bone and the pelvis as the secondary. We select faces on the primary bone, which will serve as an initial guess of the bone-attached cartilage region. We base our choice on the distance between the face barycenters of the primary bone and the secondary bone vertices. That is, provided the distance parameter, δ, we construct the set of faces,

$$\{\mathbf{f} \in \mathcal{F}_P : \min_{\mathbf{v}\in\mathcal{V}_S} \|\mathbf{BC}(\mathbf{f}) - \mathbf{v}\| \leq \delta\} \tag{1}$$

where $\mathbf{BC}(\mathbf{f})$ is the barycenter of face $\mathbf{f}$. We refer to this subset of faces and vertices as $\mathcal{F}_C^D$ and its corresponding vertices as $\mathcal{V}_C^D$. The distance filter parameter, δ, should

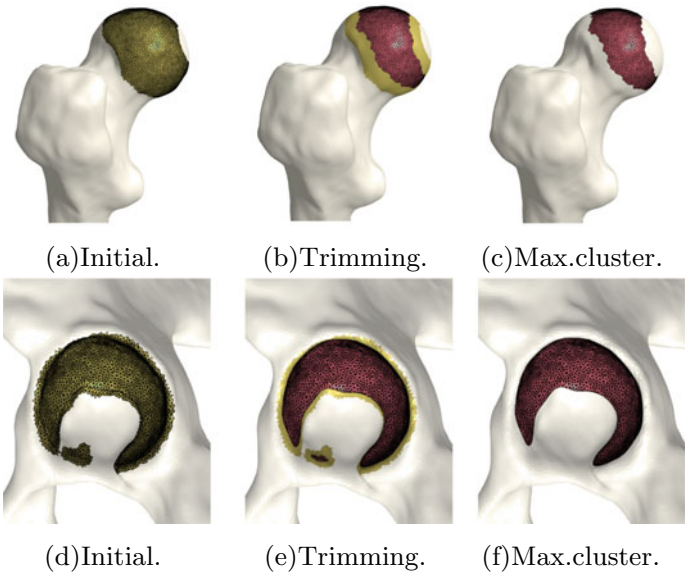

Fig. 1 Computing initial bone-cartilage interface for the femur (**a–c**) and the pelvis (**d–f**). Initially, in **a** and **d**, triangles on the surface of the femur and pelvis are selected based on the distance to the opposite bone (Eq. 1). Afterwards, in **b** and **e**, the initial sets are trimmed to remove triangles that only have one neighbor. The trimmed region can be seen in red on top of the initial guess in yellow. Finally, we select the biggest cluster of triangles as our initial estimate of the bone-attached region for both femur and pelvis (**c** and **f**)

be based on the gap between the femur and pelvis, as it determines the initial approximation quality. The femur's initial estimate must be located above the anatomical line of the femoral head (Fig. 1a). Otherwise, we do not enforce any restrictions on δ. To provide additional robustness to the initial guess, we trim the outer boundary by removing layers from its outer rim and discarding faces with two boundary edges. The trimming helps ensure the initial estimate does not become too large and, in particular, makes it simpler to avoid selecting triangles crossing the natural ridges of the bone.

The pelvis is more sensitive to the distance filtering parameter than the femur, as most of the cartilage exists in a plateau in the pelvic socket. This implies the bone-attached region does not require any additional refining, as the initial estimate accurately aligns with anatomical lines (Fig. 1d). The distance filtering step typically results in fragmented bone-attached regions, and before we proceed, we discard all but the largest of these regions (Fig. 1f). We can safely discard the smaller regions, as we grow the cartilage during the next step of our algorithm to incorporate all triangles within an area of similar curvature.

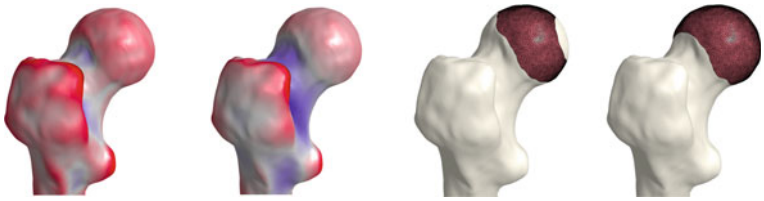

(a) $\mathcal{N} = 10$. (b) $\mathcal{N} = 20$. (c) Ten iterations. (d) End result.

Fig. 2 **a–b** The effect of changing the neighborhood size, $\mathcal{N}$, in terms of mean curvature. Red regions correspond to positive curvature directions, while blue regions correspond to negative directions. Note that smaller variations in the surface geometry influence the curvature measure less as the neighborhood size increases. **c–d** Observe in Fig. 1c the initial estimate of the bone-attached region, in **c** the bone-attached region after ten iterations of Eq. (2), and in **d** the final result, when no more faces satisfy Eq. (2)

3.2 Curvature-Based Region Filling

The initial estimate of the bone-side femoral cartilage does not yet fully cover the cartilage zone on the femoral head (Fig. 1c). The femoral cartilage border is observed as a change in the curvature between the femoral head and the neck. In this work, the principal curvatures, κ_{min} and κ_{max}, are computed by fitting local frames to a neighborhood around each vertex [23]. This method approximates the Laplace-Beltrami operator in the immediate neighborhood of each vertex to save computation time. The neighborhood size, $\mathcal{N}$, can be used as a scaling factor to control how many smaller variations to include in the curvature estimation (Fig. 2), and when $\mathcal{N}$ is sufficiently large, we will arrive at the same curvatures as can be computed using the mesh laplacian.

Denoting the boundary of $\mathcal{F}_C^D 0$ as Γ_C^D, we grow the cartilage such that,

$$\mathcal{F}_C^D \leftarrow \mathcal{F}_C^D \cup \left\{ \mathbf{f} \in \Gamma_C^D : \kappa_1 \leq \kappa_{\mathbf{f}} \leq \kappa_2 \right\} \tag{2}$$

where κ_1 and κ_2 denote the minimal and maximal curvature of the region at the femoral head and $\kappa_{\mathbf{f}}$ is the curvature of face $\mathbf{f}$. We grow the cartilage iteratively using Eq. (2) until the region contains all faces in $\mathcal{F}_C^D$ (Fig. 2d).

3.3 Extrusion

As this is a trait of healthy cartilage, we expect the generated geometry to have a high degree of congruence. We extrude vertices based on the minimal distances between the bones and choose the midpoint as the extrusion height to guarantee congruence. This approach ensures the conformity of the cartilage-cartilage interface. We want

the shape to thin out as we get further away from the contact center to mimic the real cartilage shape. The faces to extrude, are chosen to be a copy of the bone-attached estimate, $(\mathcal{V}_C^D, \mathcal{F}_C^D)$, and are denoted by $(\mathcal{V}_C^E, \mathcal{F}_C^E)$: the extruded geometry. We assign height to each vertex in the extrusion region, $\mathbf{v} \in \mathcal{V}_C^E$, based on the smallest distance to the second bone as,

$$\mathbf{v} \leftarrow \mathbf{v} + \frac{1}{2}\mathbf{n} \min_{\mathbf{v}_S \in \mathcal{V}_S} \|\mathbf{v} - \mathbf{v}_S\|_2 \tag{3}$$

where $\mathbf{n}$ is the unit outward normal direction of vertex $\mathbf{v}$. For the pelvis, the faces we extrude are a copy of the bone-attached region. As the pelvic bone-attached region does not need growing, we shrink the set of faces to be extruded by applying the same trimming approach as described in Sect. 3.1. We then extrude the reduced set of faces (Eq. 3), using the distances from the pelvis to the femur.

3.4 Harmonic Boundary Blending

The final step of the cartilage generation is to connect the bone-attached region, $(\mathcal{V}_C^D, \mathcal{F}_C^D)$, and the extruded surface, $(\mathcal{V}_C^E, \mathcal{F}_C^E)$. Referring back to Sect. 3.3 we know that $\mathcal{F}_C^E \subset \mathcal{F}_C^D$. We create a copy of the set $\mathcal{F}_C^D \setminus \mathcal{F}_C^E$ and denote it as $\mathcal{F}_C^H$. This new set will connect the bone-attached region to the extruded surface and consists of the faces from the bone-attached region not initially selected for extrusion. To create a smooth blend between the disjoint surfaces, we apply a *biharmonic weighting* scheme. We compute the blended extrusion thickness between the two regions by minimizing the Laplacian energy on the boundary of the domain, Γ. The extrusion thickness is then the minimizers of,

$$\arg\min_{\mathbf{w}} \sum_{w_j \in \mathbf{w}} \frac{1}{2} \int_{\Gamma} \|\Delta w_j\|^2 dV \tag{4}$$

subject to constraints enforcing interpolation between the boundary of the bone-attached region and the boundary of the extruded region. The Laplacian energy is discretized using the FE method and subsequently solved using an active set method [22]. For more details, we refer the reader to [12]. The resulting displacements $\mathbf{w}$ are then applied to the vertices of $\mathcal{V}_C^H$ as,

$$\mathbf{v}_j \leftarrow \mathbf{v}_j + \mathbf{n}_j w_j, \quad \forall \mathbf{v}_j \in \mathcal{V}_C^H \,. \tag{5}$$

That is, we extrude each vertex $\mathbf{v}_j$ in the direction of its normal by the displacement w_j. As a final step, we invert the bone-attached face normals before collecting the three disjoint sets of faces and vertices into a single mesh, $(\mathcal{V}_C, \mathcal{F}_C)$. Observe in Fig. 3 the cartilage sub-surfaces combined into a single mesh.

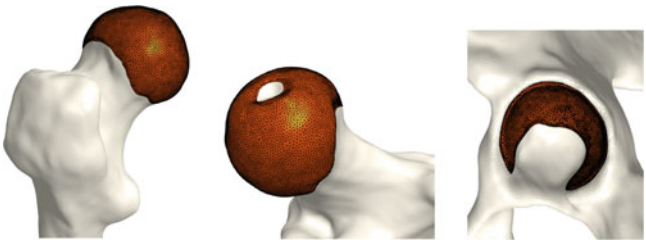

(a) Femoral cartilage. (b) Femoral cartilage. (c) Pelvic cartilage.

Fig. 3 The final cartilage generated by our method for a femur (**a, b**) and a pelvis (**c**). Notice how the cartilage aligns with the anatomical lines

4 Results

We use five CT scans from the TCGA-BLCA collection publicly available at the Cancer Imaging Archive [3]. These subjects are in a supine position and have no diagnosed disease related to the HJ. Each dataset contains a left and right HJ summing up to ten HJs. We generate pelvic and femoral cartilages for all ten joints.

Our algorithm is implemented in Python using the Libigl library [13]. To quantify the speed of our method, we timed the generation of femoral and pelvic cartilages for all ten joints. All cartilages are generated on a MacBook Pro 2018 with a 2.7 GHz quad-core Intel i7. The initial bone geometries for the ten HJs consist of a similar number of triangles (65 k triangles on average). We include all steps described in Sect. 3 in the computation time and exclude the time needed for segmentation and preprocessing the bone models. We observe that, on average, femoral cartilage reconstruction takes 39.90 s and pelvic cartilage reconstruction takes 12.82 s. These results show that the time needed to construct the femoral cartilage is significantly higher than for the pelvic cartilages—a factor of three times higher. The femoral cartilage is the only cartilage where the initially trimmed layer (shown in Fig. 1b) needs to be grown, explaining the difference in time. It should be noted that while generating a single piece of cartilage takes less than a minute, generating a *good* model of the cartilage takes significantly longer. The time needed to generate such a cartilage model includes the time required to calibrate the free parameters of our model. In our experience, the parameters for one patient generally translate well to other models, which means that only minimal tuning is required once a good set of parameter values have been found for a single patient. See supplementary material for the parameters used to generate the cartilage models.

We have qualitatively verified that the articulating surfaces in all the ten HJs are detected correctly regardless of their anatomical variance using visual inspection of overlays as shown in Fig. 4. As desired, we observe a high degree of congruence between the opposing joint surfaces, meaning no gaps or overlaps in the cartilage-cartilage interface. Moreover, we observe a smooth transition towards the bone geometries as expected from the correct anatomy. The parameter values used

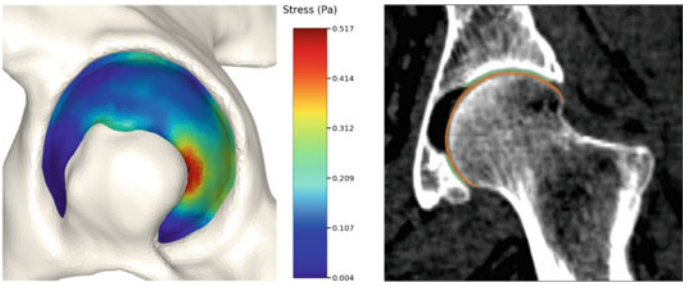

(a) The von Mises stress. (b) The CT scan overlay.

Fig. 4 The von Mises stress patterns (**a**) and the generated cartilage imposed on the CT scan from which the bone was extracted (**b**). Notice the high level of congruence in the cartilage-bone interfaces and cartilage-cartilage interface

to generate the cartilage from Fig. 5a. The free parameters are the neighborhood-size used to estimate the curvature of the bone ($\mathcal{N}$); the minimum and maximum curvature in the cartilage region ($\kappa_{\min}, \kappa_{\max}$; Eq. 2); the distance parameter in mm (δ; Eq. 1); and the number of times the outer boundary should be trimmed (N_{trim}). Here, the curvature-based parameters ($\mathcal{N}, \kappa_{\min}, \kappa_{\max}$) are only used for the femur. See supplementary material for more visual comparisons.

Further, we quantitatively compare values of our cartilage's geometric measures to data obtained from the literature to assess that we agree with state-of-the-art reported values. Results are in Table 1. We observe that our method agrees with the range of values from both manual and semi-automated approaches [1, 15, 20, 25].

Table 1 Geometric measure comparison between our method and literature

Measure	Study	# of hip joints	Femur	Pelvis
Mean thickness (mm)	Our	10	0.81 ± 0.08	1.05 ± 0.06
	[1]	1	1.5 ± 0.5	1.6 ± 0.4
	[20]	26	1.18 ± 0.06	1.26 ± 0.04
	[15]	11	1.0	1.8
	[25]	23	–	3.5 ± 0.9
	[2]	–	1.28	1.28
Bone coverage area (mm^2)	Our	10	5349.41 ± 660.51	2848.98 ± 351.86
	[25]	23	–	1634 ± 400
Bone coverage percentage	Our	10	–	$39\% \pm 7$
	[7]	16	–	34%
Contact area (mm^2)	Our	10		1732.01 ± 281.06

Next, we analyze the simulation quality of the generated models in an FE analysis setup. We use the Tetgen package to generate a volumetric mesh with tetrahedral elements for each geometry [26]. Using a displacement-controlled simulation in the FEBio software package [19], we push the pelvis on top of the femur, representing a pseudo stance position. Considering the stance position, the distal femur is fixed in the x, y, and z-directions. The pelvis is moved in the z-direction by 1 mm towards the femur. We simplified the mechanical behavior of all the tissues to isotropic and linearly elastic. The material properties are based on the review in [29]. The bone-cartilage interfaces are modeled as *Tied contacts*. An augmented surface contact algorithm with friction-less tangential interaction is applied to the cartilage-cartilage interfaces allowing unhindered motion in the HJ.

Figure 4 visualizes the von Mises stress pattern on the pelvic cartilage for one HJ. More are shown in the supplementary material. We have verified that no spurious stress peaks appear and that stress values change gradually and smoothly across the cartilage. Further, the high-stress areas are located in the up-direction, as we expect from the applied displacements. The stress values and patterns are not to be confused with those from a real stance. They only serve as a verification test of simulation properties. For such a simulation, we require ligaments and muscles to stabilize the girdle and a correction from sublime pose bias.

5 Discussion and Conclusion

The results show our method produces similar cartilage to manual segmentation and adheres to our clinical assumptions about cartilage morphology [27]. The high congruence level prevents potential spikes and peak stresses in the articulating surfaces, resulting in continuous stress distribution in the HJ.

Our subjects are in a supine position, which means the cartilage is under a horizontal load. In this case, the bones are not in an unloaded position, causing the generated cartilages to be in a pre-load state. The supine position explains the difference between the cartilage thickness and contact area compared to other studies. One solution is to relocate the bone geometries to the desired position before generating the cartilages or optimizing the rest shape used in the FE analysis. Moreover, as we measure the contact area before running any simulations, our results differ from other studies reporting this value as a simulation result in different gait cycles.

As we rely on the bone curvatures for cartilage-bone interface definition, accurate bone geometries are crucial for realistic results. If the segmented bones are too smooth or coarse, the final product will not agree with real cartilage anatomy. We want to investigate further detailed geometric validation of our method; however, no public databases contain segmented cartilage for hip joints to the best of our knowledge. We leave this for future work.

The FE analysis results show that the generated models produce smooth stress patterns in a pseudo stance without any geometry-related convergence issues. As mentioned in Sect. 4, these results only serve as a verification test of simulation

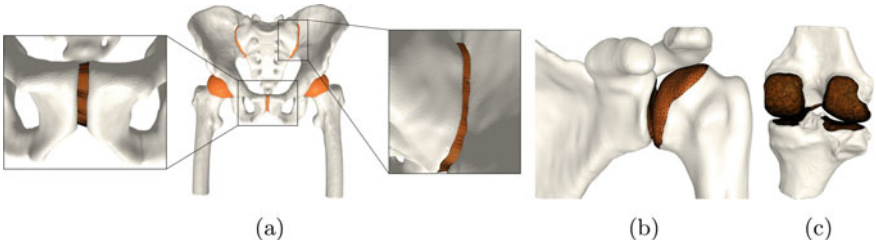

Fig. 5 **a** All generated cartilages. Zoom boxes highlight the pubic and sacroiliac joint cartilages. **b** Shoulder joint cartilage. **c** Femoral and tibial cartilage in the knee joint. Bone models are acquired from available datasets [3–5]

properties. We need a more advanced simulation setting to model a real stance position. We leave this for future work. Moreover, we believe that minor modifications will estimate the shoulder joint cartilage since it has a similar ball-in-socket structure. Figure 5 shows early evidence of generalization. In contrast, other joints, such as the knee joint, are challenging. We leave other joint types for future work.

In conclusion, we have created a method to automate the reconstruction of healthy subject-specific HJ cartilages independent from clinical images. The proposed method is fast and preserves the anatomical properties of the cartilage tissue. The proposed method generates high-quality cartilage without the need for any manual segmentation or training data. We have shown the cartilage models can be used in FE analysis and believe our method will enable large-scale population studies. Future work will extend the geometric principles to abnormal HJs and other joints such as the shoulder and knee joint. Our code is open-source and available from https://github.com/diku-dk/CarGen.

Supplementary Material

See Figs. 6, 7, 8 and Table 2.

Finite Element Analysis Details

The bone geometries are discretized using triangle meshes. The pelvic and femoral cartilages inherit the same triangle size of their corresponding bones. These values are chosen for the “master” and “slave” domains in the HJ contacting zones to ensure coarser meshes on the pelvis side. We generate 4-node tetrahedral quality volume meshes using the Tetgen package [26]. The resulting files are exported as VTK-files to the FEBio solver package [19]. FEBio is an open-source non-linear finite element solver widely used in biomechanical applications.

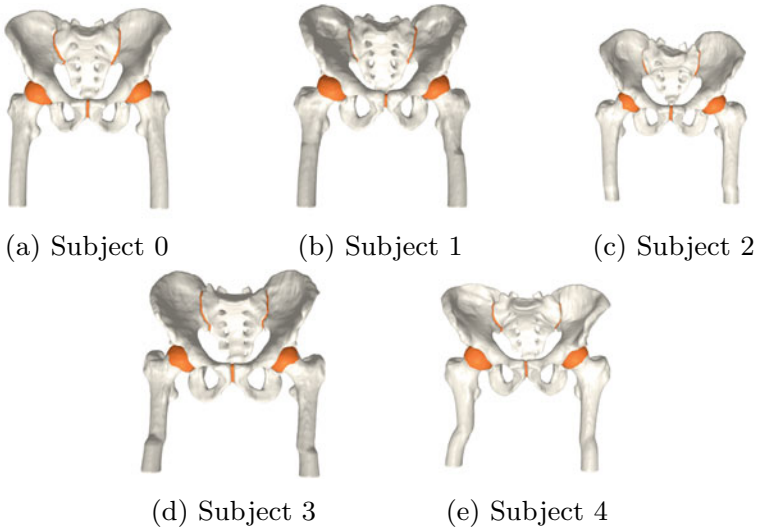

(a) Subject 0 (b) Subject 1 (c) Subject 2

(d) Subject 3 (e) Subject 4

Fig. 6 Cartilage generated for the five subjects in our test set

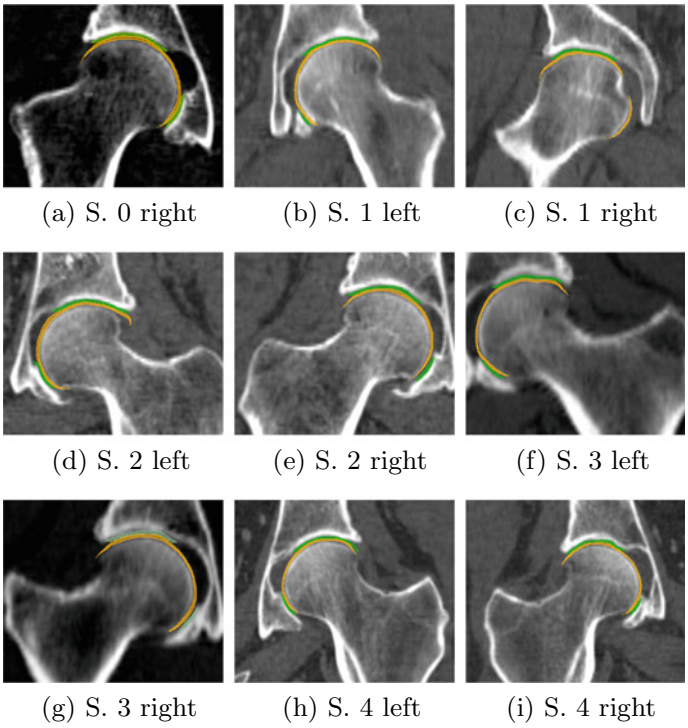

(a) S. 0 right (b) S. 1 left (c) S. 1 right

(d) S. 2 left (e) S. 2 right (f) S. 3 left

(g) S. 3 right (h) S. 4 left (i) S. 4 right

Fig. 7 CT scans overlaid with cartilage and bones for the remaining subjects

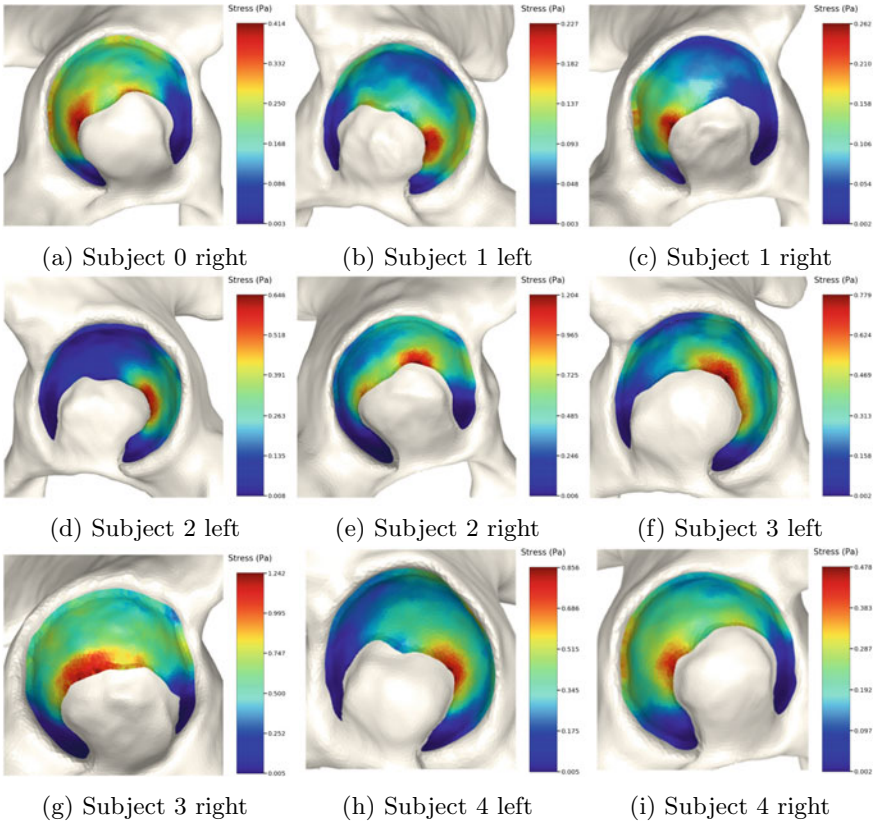

(a) Subject 0 right (b) Subject 1 left (c) Subject 1 right

(d) Subject 2 left (e) Subject 2 right (f) Subject 3 left

(g) Subject 3 right (h) Subject 4 left (i) Subject 4 right

Fig. 8 Von Mises stress patterns on the pelvic cartilage of the right side of the subject shown in Fig. 4 (top left) and the remaining four subjects. We show the left and right pelvic-side cartilage during a simulation identical to the one described in Sect. 4 of the main paper for each subject

Table 2 The parameter values used to generate the cartilage from Fig. 5a. The free parameters are the neighborhood-size used to estimate the curvature of the bone ($\mathcal{N}$); the minimum and maximum curvature in the cartilage region ($\kappa_{\min}, \kappa_{\max}$; Eq. 2); the distance parameter in mm (δ; Eq. 1); and the number of times the outer boundary should be trimmed (N_{trim}). Here, the curvature-based parameters ($\mathcal{N}, \kappa_{\min}, \kappa_{\max}$) are only used for the femur

Cartilage	Parameter				
	$\mathcal{N}$	$\kappa_{\min}$	$\kappa_{\max}$	δ	N_{trim}
Femoral cartilage	20	0.026	Inf	4.2	7
Pelvic cartilage	–	–	–	3	2
Sacroiliac	–	–	–	4.6	0
Pubic	–	–	–	6	1

We care about observing smooth stress transitions in the cartilage-cartilage interfaces. Hence, for our validation purpose it suffices that the mechanical behavior of all the tissues are set to be homogeneous isotropic linear-elastic material. The material properties are based on the review in [29]. The Young's modulus and Poisson's ratio is 17 GPa and 0.3 for bones and 12 MPa and 0.45 for the cartilages. The bone-cartilage interfaces are modeled as *Tied facet-on-facet* type of contact in FEBio. A *Sliding facet-on-facet* type of contact is applied to the cartilage-cartilage interface. This is solved as an augmented Lagrangian model with friction-less tangential interaction allowing unhindered motion in the HJ.

The HJ behavior is analyzed under a quasi-static loading condition. Therefore, the pelvis and the femur is expected to be in an equilibrium state. We use a displacement-controlled simulation where we push the pelvis on top of the femur, representing a pseudo stance position. We prescribe the nodal displacement field and the load will be given implicitly during the simulation. Considering the stance position, the distal femur is fixed in the x, y, and z-directions. The pelvis is moved in the z-direction towards the femur.

Acknowledgements This project has received funding from the European Union's Horizon 2020 research and innovation programme under the Marie Sklodowska-Curie grant agreement No. 764644. This paper only contains the author's views, and the Research Executive Agency and the Commission are not responsible for any use that may be made of the information it contains. This project has also received funding from Independent Research Fund Denmark (DFF) under agreement No. 9131-00085B.

References

1. Anderson, A. E., Ellis, B. J., Maas, S. A., Peters, C. L., & Weiss, J. A. (2008). Validation of finite element predictions of cartilage contact pressure in the human hip joint. *Journal of Biomechanical Engineering, 130*(5).
2. Anderson, A. E., Ellis, B. J., Maas, S. A., & Weiss, J. A. (2010). Effects of idealized joint geometry on finite element predictions of cartilage contact stresses in the hip. *Journal of Biomechanics, 43*(7), 1351–1357.
3. Clark, K., Vendt, B., Smith, K., Freymann, J., Kirby, J., Koppel, P., Moore, S., Phillips, S., Maffitt, D., Pringle, M., et al. (2013). The cancer imaging archive (tcia): Maintaining and operating a public information repository. *Journal of Digital Imaging, 26*(6), 1045–1057.
4. Dzialo, C. M., Pedersen, P. H., Jensen, K. K., de Zee, M., & Andersen, M. S. (2019). Evaluation of predicted patellofemoral joint kinematics with a moving-axis joint model. *Medical Engineering & Physics, 73*, 85–91.
5. Dzialo, C., Pedersen, P., Simonsen, C., Jensen, K., de Zee, M., & Andersen, M. (2018). Development and validation of a subject-specific moving-axis tibiofemoral joint model using mri and eos imaging during a quasi-static lunge. *Journal of Biomechanics, 72*, 71–80.
6. Gilles, B., & Magnenat-Thalmann, N. (2010). Musculoskeletal mri segmentation using multi-resolution simplex meshes with medial representations. *Medical Image Analysis, 14*(3), 291–302.
7. Harris, M. D., Anderson, A. E., Henak, C. R., Ellis, B. J., Peters, C. L., & Weiss, J. A. (2012). Finite element prediction of cartilage contact stresses in normal human hips. *Journal of Orthopaedic Research, 30*(7), 1133–1139.

8. Henak, C. R., Anderson, A. E., & Weiss, J. A. (2013). Subject-specific analysis of joint contact mechanics: Application to the study of osteoarthritis and surgical planning. *Journal of Biomechanical Engineering, 135*(2).
9. Henak, C. R., Carruth, E. D., Anderson, A. E., Harris, M. D., Ellis, B. J., Peters, C. L., & Weiss, J. A. (2013). Finite element predictions of cartilage contact mechanics in hips with retroverted acetabula. *Osteoarthritis and Cartilage, 21*(10), 1522–1529.
10. Ipavec, M., Brand, R., Pedersen, D., Mavčič, B., Kralj-Iglič, V., & Iglič, A. (1999). Mathematical modelling of stress in the hip during gait. *Journal of Biomechanics, 32*(11), 1229–1235.
11. Ipavec, M., Iglič, A., Iglič, V. K., & Srakar, F. (1996). Stress distribution on the hip joint articular surface during gait. *Pflügers Archiv, 431*(6), R275–R276.
12. Jacobson, A., Baran, I., Popovic, J., & Sorkine, O. (2011). Bounded biharmonic weights for real-time deformation. *ACM Transactions on Graphics, 30*(4), 78.
13. Jacobson, A., Panozzo, D., et al. (2018). *libigl: A simple C++ geometry processing library*. https://libigl.github.io/
14. Jorge, J., Simões, F., Pires, E., Rego, P., Tavares, D., Lopes, D., & Gaspar, A. (2014). Finite element simulations of a hip joint with femoroacetabular impingement. *Computer Methods in Biomechanics and Biomedical Engineering, 17*(11), 1275–1284.
15. Lazik, A., Theysohn, J. M., Geis, C., Johst, S., Ladd, M. E., Quick, H. H., & Kraff, O. (2016). 7 tesla quantitative hip mri: T1, t2 and t2* mapping of hip cartilage in healthy volunteers. *European Radiology, 26*(5), 1245–1253.
16. Li, F., Chen, H., Mawatari, T., Iwamoto, Y., Jiang, F., & Chen, X. (2018). Influence of modeling methods for cartilage layer on simulation of periacetabular osteotomy using finite element contact analysis. *Journal of Mechanics in Medicine and Biology, 18*(02), 1850018.
17. Lindner, C., Thiagarajah, S., Wilkinson, J. M., Wallis, G. A., Cootes, T. F., arcOGEN Consortium, et al. (2013). Accurate bone segmentation in 2d radiographs using fully automatic shape model matching based on regression-voting. In *International Conference on Medical Image Computing and Computer-Assisted Intervention* (pp. 181–189). Springer.
18. Lopes, D. S., Pires, S. M., Barata, C. D., Mascarenhas, V. V., & Jorge, J. A. (2020). The hip joint as an egg shape: A comprehensive study of femoral and acetabular morphologies. *Computer Methods in Biomechanics and Biomedical Engineering: Imaging & Visualization, 8*(4), 411–425.
19. Maas, S. A., Ellis, B. J., Ateshian, G. A., & Weiss, J. A. (2012). Febio: Finite elements for biomechanics. *Journal of Biomechanical Engineering, 134*(1), 011005.
20. Mechlenburg, I., Nyengaard, J. R., Gelineck, J., & Soballe, K. (2007). Cartilage thickness in the hip joint measured by mri and stereology-a methodological study. *Osteoarthritis and Cartilage, 15*(4), 366–371.
21. Menschik, F. (1997). The hip joint as a conchoid shape. *Journal of Biomechanics, 30*(9), 971–973.
22. Nocedal, J., & Wright, S. (2006). *Numerical optimization*. Springer Science & Business Media.
23. Panozzo, D., Puppo, E., & Rocca, L. (2010). Efficient multi-scale curvature and crease estimation. *Proceedings of Computer Graphics, Computer Vision and Mathematics (Brno, Czech Rapubic), 1*(6).
24. Russell, M. E., Shivanna, K. H., Grosland, N. M., & Pedersen, D. R. (2006). Cartilage contact pressure elevations in dysplastic hips: A chronic overload model. *Journal of Orthopaedic Surgery and Research, 1*(1), 6.
25. Schmaranzer, F., Helfenstein, R., Zeng, G., Lerch, T. D., Novais, E. N., Wylie, J. D., Kim, Y. J., Siebenrock, K. A., Tannast, M., & Zheng, G. (2019). Automatic mri-based three-dimensional models of hip cartilage provide improved morphologic and biochemical analysis. *Clinical Orthopaedics and Related Research, 477*(5), 1036.
26. Si, H. (2015). Tetgen, a delaunay-based quality tetrahedral mesh generator. *ACM Transactions on Mathematical Software, 41*(2), 11:1–11:36.
27. Standring, S. (2020). *Gray's anatomy e-book: The anatomical basis of clinical practice*. Elsevier.

28. Tsumura, H., Kaku, N., Ikeda, S., & Torisu, T. (2005). A computer simulation of rotational acetabular osteotomy for dysplastic hip joint: Does the optimal transposition of the acetabular fragment exist? *Journal of Orthopaedic Science, 10*(2), 145–151.
29. Vafaeian, B., Zonoobi, D., Mabee, M., Hareendranathan, A., El-Rich, M., Adeeb, S., & Jaremko, J. (2017). Finite element analysis of mechanical behavior of human dysplastic hip joints: A systematic review. *Osteoarthritis and Cartilage, 25*(4), 438–447.
30. Van Houcke, J., Audenaert, E. A., Atkins, P. R., & Anderson, A. E. (2020). A combined geometric morphometric and discrete element modeling approach for hip cartilage contact mechanics. *Frontiers in Bioengineering and Biotechnology, 8*.
31. Yokota, F., Okada, T., Takao, M., Sugano, N., Tada, Y., Tomiyama, N., & Sato, Y. (2013). Automated ct segmentation of diseased hip using hierarchical and conditional statistical shape models. In *International Conference on Medical Image Computing and Computer-Assisted Intervention* (pp. 190–197). Springer.
32. Yoshida, H., Faust, A., Wilckens, J., Kitagawa, M., Fetto, J., & Chao, E. Y. S. (2006). Three-dimensional dynamic hip contact area and pressure distribution during activities of daily living. *Journal of Biomechanics, 39*(11), 1996–2004.

Development of an Open Source, Low-Cost Imaging System for Continuous Lung Monitoring

Samuel Richardson, Andrew Creegan, Alex Dixon, Llewellyn Sim Johns, Haribalan Kumar, Kelly Burrowes, Poul M. F. Nielsen, J. Geoffrey Chase, and Merryn H. Tawhai

Abstract A lost-cost open-source electrical impedance tomography (EIT) device was equipped with a novel lidar based workflow to extract torso and electrode position which was then used in the EIT image reconstruction. EIT data was gathered from 9 healthy volunteers (5 male, 4 female) whilst undergoing a controlled breathing protocol. Four different reconstruction configurations were undertaken: a subject specific lidar based mesh versus a generic oval mesh, and subject specific lidar based electrode placements versus generic equal spaced electrode placements. Our

Samuel Richardson and Andrew Creegan—Authors acknowledge joint first authorship.

S. Richardson (✉) · A. Creegan · A. Dixon · L. S. Johns · H. Kumar · K. Burrowes · P. M. F. Nielsen · M. H. Tawhai
Auckland Bioengineering Institute, University of Auckland, Auckland, New Zealand
e-mail: sam.richardson@auckland.ac.nz

A. Creegan
e-mail: acre018@aucklanduni.ac.nz

A. Dixon
e-mail: adix022@aucklanduni.ac.nz

L. S. Johns
e-mail: lsim070@aucklanduni.ac.nz

H. Kumar
e-mail: h.kumar@auckland.ac.nz

K. Burrowes
e-mail: k.burrowes@auckland.ac.nz

P. M. F. Nielsen
e-mail: p.nielsen@auckland.ac.nz

M. H. Tawhai
e-mail: m.tawhai@auckland.ac.nz

P. M. F. Nielsen
Department of Engineering Science, University of Auckland, Auckland, New Zealand

J. G. Chase
Department of Mechanical Engineering, University of Canterbury, Christchurch, New Zealand
e-mail: geoff.chase@canterbury.ac.nz

P. M. F. Nielsen et al. (eds.), *Computational Biomechanics for Medicine*,
https://doi.org/10.1007/978-3-031-09327-2_12

results showed that torso shape error and electrode position errors can be drastically reduced with the lidar-based method allowing for the future utilization of patient-specific information. Good correlation was observed between volume delta and the EIT difference image.

Keywords COVID-19 · EIT · Electrical impedance tomography · Lidar · Spectra

1 Introduction

Critically ill COVID-19 patients usually require mechanical ventilation (MV). This particularly challenging patient group may have large 'patches' of pneumonia that make the lung stiffer and unable to exchange gas, and they frequently have underlying respiratory or cardiac conditions. There is currently no routinely used imaging method for continuously monitoring lung status or health in these critically ill patients. Patient management in the Intensive Care Unit (ICU) largely relies on assessing patient status using intermittent physiological data or external data that indirectly indicates lung function. Electrical impedance tomography (EIT) provides a non-invasive method by which lung ventilation can be continuously monitored. Despite the availability of several commercial EIT systems and its effectiveness for bedside monitoring of lung aeration [1–4], it has not had widespread uptake into clinical management due to the cost and lack of clarity in clinical interpretation [5, 6]. Commercially available EIT ventilation monitoring devices typically cost from USD45000 and are thus not well suited for large scale deployment. EIT images are generated by solving for conductivity from the measured boundary voltages, as an inverse problem. Given the anisotropy of the body being imaged, additional anatomical information can enhance EIT reconstruction and reduce the mismatch between the reconstructed image and characteristics of the original body being imaged. Furthermore, changes in the boundary shape and electrode position introduces significant errors in EIT imaging. Difference EIT reconstructs a map of conductivity change by subtracting dataframes between current time and a reference time [4]. Difference imaging obtained this way are known reduce the errors to some extent, but not eliminate it. In an ICU setting, technologies to obtain additional information about patient chest wall and electrode movement without interfering with routine ventilation workflows are limited. This project aims to develop and validate a novel torso shape extraction technology paired with a low cost EIT device paired and test its application to imaging lungs.

2 Methodologies

2.1 EIT Measurement

Spectra is an open-source EIT system from Mindseye Biomedical that is based around the ADUCM350 from Analogue Devices [7]. This device can be purchased for USD1295. It has a small form factor and comes with simple firmware installed, making it useful for initial studies. The data rate of the ADUcm350's dedicated complex impedance measurement engine is only 160 kHz. With 4096 samples per measurement, 192 measurements per image, when using 16 electrodes, this limits the device's frame rate to 0.2 fps. This was sufficient for our purposes to test and validate the workflow to extract torso and electrode position.

EIT measurements were made using the Spectra system shown in Fig. 1. The Spectra was set up to run in 16 electrode mode which sits in a sweet spot for image resolution and scanning time: any more electrodes and the scanning time becomes unmanageable; any fewer and the resolution becomes too low. The EIT system was connected to the subjects using traditional ECG electrodes (Phillips). The Spectra was worn around the subject's torso in a neoprene belt, which was manufactured to simplify cable management and reduce any strain on the electrode attachment clips that might produce movement artifacts. A 4-pole, 16 electrode EIT scheme was used for scanning the subjects. Each pair of driving electrodes was spaced 3 electrodes apart. Experiments were run, data was collected, and analysis was performed using python programs developed for this project.

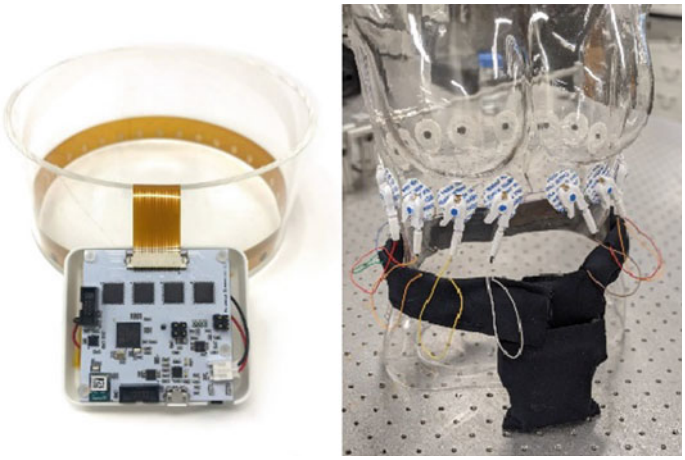

Fig. 1 Left, spectra EIT system. Right, EIT system and electrode mounted on a mannequin

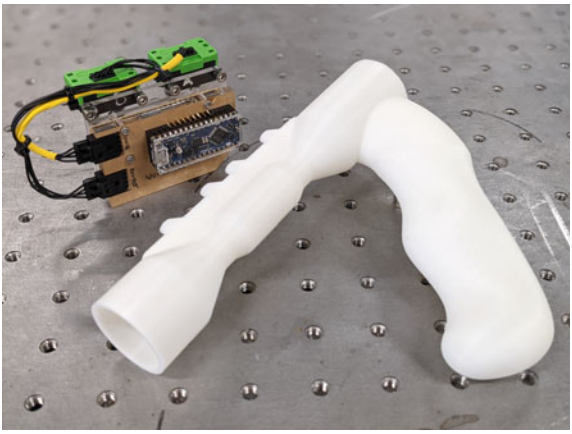

Fig. 2 Bidirectional venturi spirometer

2.2 Reference Volume Measurement

To obtain a reference volume change measurement against which to evaluate the EIT reconstruction, respiratory volume was measured using a custom bidirectional venturi spirometer (see Fig. 2) with volume measurements errors of less than 1% of the measurement tested over a range of 10 L. The venturi device consists of two venturi tubes joined in series, in opposite orientations, enabling monitoring of flow rates in both directions, from which volumes were derived.

2.3 Lidar Scanning and Mesh Generation

To enable accurate reconstruction of the subject's torso shape and the electrode locations, a novel torso shape detection system was developed. This system helped extract patient-specific torso shape, belt location on the torso, and electrode position. Each subject in the study was scanned using an Intel RealSense L515 lidar camera after the electrodes had been placed around their torsos. The electrode locations were identified and mapped to a plane parallel with the subject's transverse plane. The electrodes were blue which made isolating them a simple task of colour thresholding. The electrode positions were saved as a list of two-dimensional coordinates so that they could be used later in the EIT reconstruction. The boundary of the subject's chest was obtained by determining the intersection of the lidar point cloud with a plane fitted through the electrodes, calculated using a k-d tree approach to find the closest point cloud points to the surface points. This boundary was used to generate a 2D mesh representing the EIT imaging plane. Each subject's mesh was saved for use in reconstruction. An illustration of this process can be seen in Fig. 3. An additional

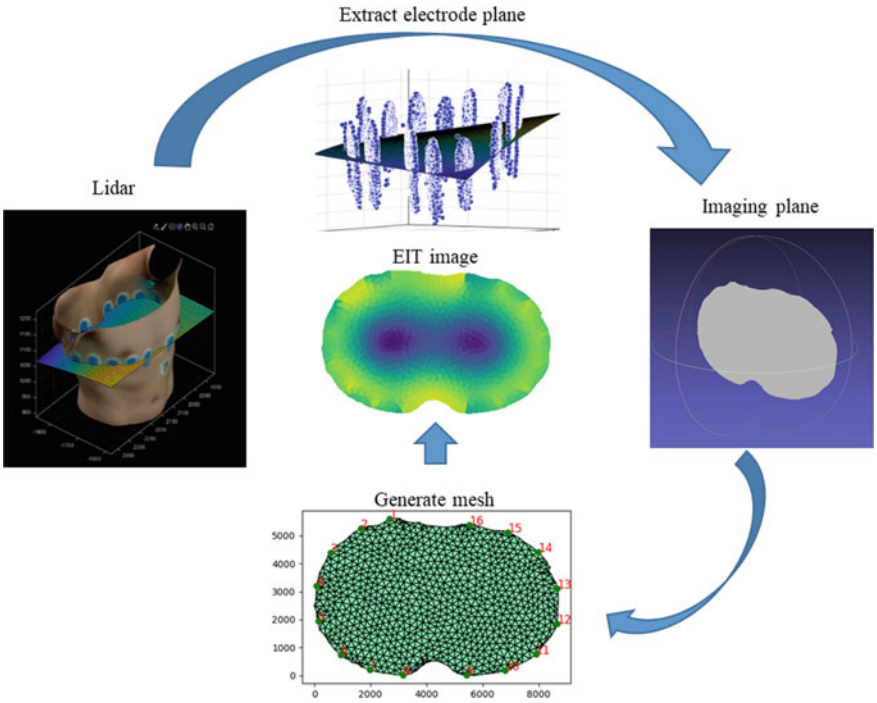

Fig. 3 A graphical illustration of the methods used to generate subject specific meshes

mesh was generated using a boundary described by an ellipse with a ratio of semi-major to semi-minor diameters being 1.5. This mesh was used as a generic mesh during reconstruction. Each mesh was generated with approximately 2000 faces.

2.4 Test Procedure

EIT data was gathered from 9 healthy volunteers (5 male, 4 female) approved by the Auckland Health Research Ethics Committee (AH252). The test procedure for each subject was as follows: First, the subject's height, age, weight, and spirometry measurements were taken as seen in Table 1.

Next the electrodes were attached to the subject, at the height of the 5th intercostal space. Each volunteer then received a 3D lidar scan of their chest. The electrodes were placed in a ring approximately parallel to the subject's transverse plane, equally spaced with additional space of one electrode width at the subject's sternum and spine. This strategy was used for both male and female subjects.

After the electrodes had been attached and imaged, the Spectra EIT system was attached, and subjects were instructed to breathe through the venturi spirometer. The EIT system was used to image at breath-hold. The test protocol involved the subject

Table 1 Subject data

Subject information					
Subject	Height (m)	Mass (kg)	BMI (kg/m^2)	Age (year)	Gender
K	1.615	66	25.3	38	F
M	1.525	61.5	26.4	30	F
J	1.76	67	21.6	30	M
A	1.7	73	25.3	30	M
L	1.75	71	23.2	31	M
S	1.78	77	24.3	30	M
W	1.8	64.5	19.9	24	F
H	1.8	99	30.6	27	M
V	1.64	66	24.5	32	F

inhaling maximally, waiting for an EIT frame to be captured, then exhaling a small amount (approximately 200 mL). This was repeated over a series of seven to ten cycles, each time increasing the volume exhaled. Figure 4 shows the exhaled volume during the test for one subject, with red crosses showing the time when a complete EIT frame was received.

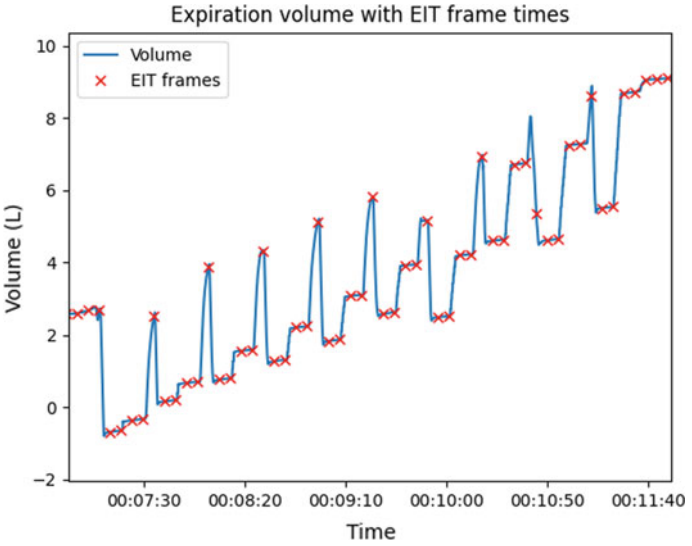

Fig. 4 Subject expiration volume with EIT frame times. Blue is the volume measurement with red crosses showing the time at which a complete EIT frame was received

3 Reconstruction and Results

Data was analysed in pairs, with EIT difference images comparing maximal inspiration to the image taken after exhalation, being compared to the expired volume measured with the venturi spirometer, the results for this can be seen in Fig. 7. Reconstruction was done using the open source pyEIT python package [8]. The functionality of pyEIT was expanded by adding the ability to read custom meshes and assign arbitrary electrode positions. We used the NOSER algorithm for difference imaging, with a p-value of 0.5, see [9]. A total of four different reconstruction configurations were undertaken, analysing the full set of volunteer data for each:

(1) A generic oval mesh with generic equal spaced electrode placements
(2) A generic oval mesh with subject specific lidar based electrode placements
(3) A subject specific lidar based mesh with generic equal spaced electrode placements
(4) A subject specific lidar based mesh with subject specific lidar based electrode placements.

Figure 5 illustrates each of these configurations for a single subject.

Table 2 shows a comparison between lidar generated and generic oval shape meshes, and a comparison between equal spaced and lidar generated electrode placements. It illustrates the difference between the reconstruction configurations. The

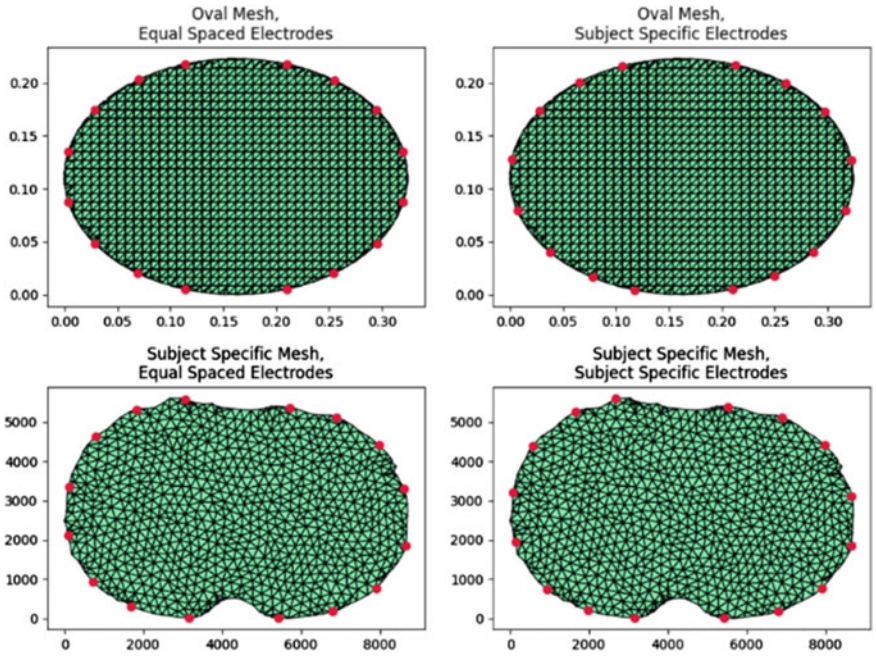

Fig. 5 Four configurations of mesh and electrodes for subject A

second column shows the area mismatch between an oval shape and LiDAR generated shape. The third column shows the average angular error (in radians) in electrode position between even spacing and lidar based spacing.

The EIT images were quantified by rendering a threshold image with the following procedure: each EIT image was considered as a matrix representing the n × n pixel grid. Pixels of value greater than 0.15 of the maximum were counted. The threshold value of 0.15 was selected as a compromise to detect the most visually significant effects. This procedure is similar to that used by Adler in [10]. This count was normalised by dividing it by the total number of pixels in the EIT image. Figure 6 shows a reconstructed image versus a threshold image for a single subject, using the subject specific mesh.

Table 2 Comparison between lidar generated and generic oval shape showing differences between mesh types and electrode spacings

Subject	Ratio between lidar mesh area and oval mesh area	Average difference between even spacing and lidar spacing of electrodes (rad)
K	1.21	0.19
V	1.26	0.2
M	1.27	0.54
J	0.94	0.24
A	0.96	0.04
L	1.27	0.08
S	1.04	0.07
W	1.01	0.37
H	1.11	0.12
Average (SD)	1.12 (0.136)	0.21 (0.164)

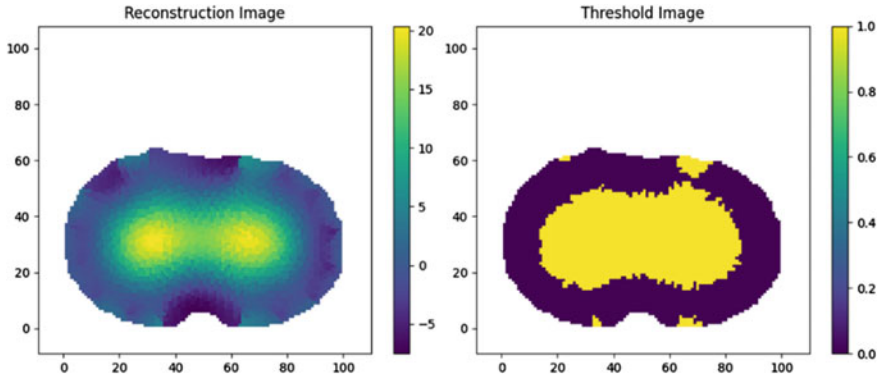

Fig. 6 Reconstruction image (left) and threshold image (right) for subject A with subject specific mesh

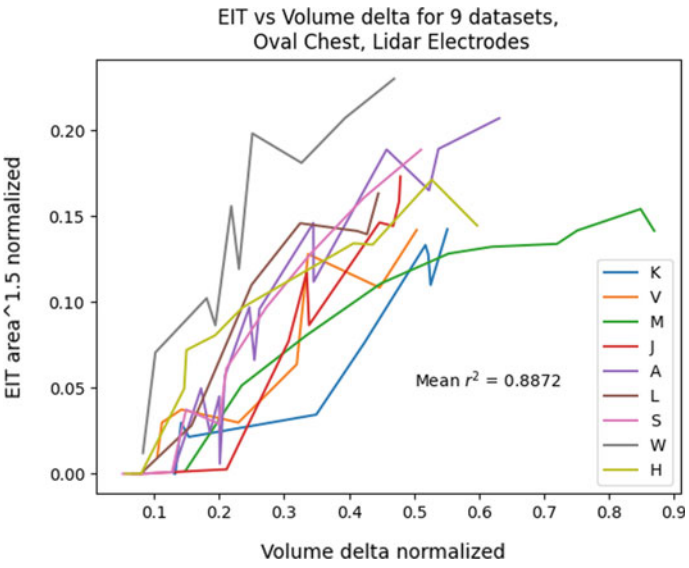

Fig. 7 Performance comparison for 9 subjects for oval reconstruction with lidar electrode spacing configuration

It was necessary to linearize the relationship between the EIT image and the exhaled volume, since the EIT represented a two-dimensional slice of the subject's chest. This was done by raising the thresholded EIT area measurement to the power of 3/2 (which is the relationship between volume and area).

The volume change was normalized by dividing it by the subject's Vital Capacity.

The correlation between the EIT measurement and the volume change measurement, as described above, was computed using a linear least-squares regression. The r^2 value (i.e., the square of the Pearson's correlation coefficient) was used to quantify the goodness of fit.

Figure 7 shows the results of a single configuration. The EIT measurement as processed above was plotted against the normalized volume measurement. This shows a general positive correlation.

Table 3 shows the mean coefficient of determination (r^2) value for each configuration. We conducted a Student's T-test to determine whether there were any statistically significant difference between the results for each of the reconstruction configurations. No statistically significant differences between configurations were found.

- The p-value for the t-test between Oval Chest, Equal Spaced Electrodes and Oval Chest, lidar Electrodes was 0.4665.
- The p-value for the t-test between Oval Chest, Equal Spaced Electrodes and Subject Lidar Chest, Equal Spaced Electrodes is 0.8591.

Table 3 Mean coefficient of determination (r^2) for all nine subjects, for the four configurations

Chest mesh	Oval chest mesh	Lidar chest mesh
Electrode positioning		
Equal spaced	0.87	0.86
Lidar generated	0.89	0.87

- The *p*-value for the *t*-test between Oval Chest, Equal Spaced Electrodes and Subject Lidar Chest, lidar Electrodes is 0.8992.

4 Discussion

In this work, we have demonstrated that lidar based torso and electrode position technology generates meshes that are different across the test subjects. This method has the potential to pave way for development of a patient-specific lung ventilation monitoring device. Optical-based methods are gaining popularity in the field of EIT image reconstruction [11]. Although the application of our technology in ICU still needs to be evaluated, our technology is useful as a testbed for extracting information about torso shape and electrode placement during EIT application. Although in our testing, electrodes were placed carefully with the aim of achieving an even electrode spacing, the average error in this approach was 0.21 radians (SD = 0.164 radians), indicating that achieving even spacing in practise is difficult. This may have deleterious impacts on reconstructions if not accounted for during image reconstruction. Furthermore, our results indicate a shape mismatch of 12% in area (SD = 13.6%) with a range of 1–27% difference compared to a generic oval shape. One previous study showed that shape mismatch beyond 4% leads to unacceptable quality of reconstruction [12]. Hence there is a considerable gain in adding anatomical and electrode position information.

The results from the healthy volunteer study showed a good correlation between the expired volume measured using the spirometer, and the volume change calculated using EIT (e.g. for the configuration of Oval mesh with lidar measured electrodes, the mean r^2 value was 0.89, indicating that 89% of the variation in the EIT measurement could be explained by the measured volume change), which agrees well with published EIT studies of lung ventilation measurement [13].

5 Conclusions

The results of this study indicated that a small form factor ‘wearable’ EIT device could be used to measure changes in lung ventilation at the bedside. The good correlation between measured expiration and volume change calculated using EIT

data. confirmed this. Further work needs to be undertaken to test these approaches on a device which is optimised for real time imaging across human torsos.

References

1. Costa, E. L. V., Gonzalez Lima, R., & Amato, M. B. P. (2009). Electrical impedance tomography. In *Yearbook of intensive care and emergency medicine* (pp. 394–404). Springer. https://doi.org/10.1007/978-3-540-92276-6_38
2. Mazzoni, M. B., et al. (2017). Electrical impedance tomography in children with community acquired pneumonia: Preliminary data. *Respiratory Medicine, 130*, 9–12. https://doi.org/10.1016/j.rmed.2017.07.001
3. Victorino, J. A., et al. (2004). Imbalances in regional lung ventilation: A validation study on electrical impedance tomography. *American Journal of Respiratory and Critical Care Medicine, 169*(7), 791–800. https://doi.org/10.1164/rccm.200301-133OC
4. Brown, B. H. (2003). Electrical impedance tomography (EIT): A review. *Journal of Medical Engineering and Technology, 27*(3), 97–108. https://doi.org/10.1080/0309190021000059687
5. Gong, B., Krueger-Ziolek, S., Moeller, K., Schullcke, B., & Zhao, Z. (2015). Electrical impedance tomography: Functional lung imaging on its way to clinical practice? *Expert Review of Respiratory Medicine, 9*(6), 721–737. Taylor and Francis Ltd. https://doi.org/10.1586/17476348.2015.1103650
6. Tomicic, V., & Cornejo, R. (2019). Lung monitoring with electrical impedance tomography: Technical considerations and clinical applications. *Journal of Thoracic Disease, 11*(7), 3122–3135. AME Publishing Company. https://doi.org/10.21037/jtd.2019.06.27
7. Analog Devices. 'Data Sheet ADuCM350'.
8. Liu, B., et al. (2018). SoftwareX pyEIT: A python based framework for electrical impedance tomography. *SoftwareX, 7*, 304–308. https://doi.org/10.1016/j.softx.2018.09.005
9. Adler, A., Dai, T., & Lionheart, W. R. B. (2007). Temporal image reconstruction in electrical impedance tomography. *Physiological Measurement, 28*(7), S1–S11. https://doi.org/10.1088/0967-3334/28/7/S01
10. Adler, A., et al. (2009). GREIT: A unified approach to 2D linear EIT reconstruction of lung images. *Physiological Measurement, 30*(6), S35–S55. https://doi.org/10.1088/0967-3334/30/6/S03
11. de Gelidi, S., et al. (2018). Torso shape detection to improve lung monitoring. *Physiological Measurement, 39*(7), 074001. https://doi.org/10.1088/1361-6579/aacc1c
12. Grychtol, B., Lionheart, W. R. B., Bodenstein, M., Wolf, G. K., & Adler, A. (2012). Impact of model shape mismatch on reconstruction quality in electrical impedance tomography. *IEEE Transactions on Medical Imaging, 31*(9), 1754–1760. https://doi.org/10.1109/TMI.2012.2200904
13. Jang, G. Y., et al. (2019). Integrated EIT system for functional lung ventilation imaging. *BioMedical Engineering Online, 18*(1), 83. https://doi.org/10.1186/s12938-019-0701-y

Measuring Three-Dimensional Surface Deformations of Skin Using a Stereoscopic System and Intrinsic Features

Amir HajiRassouliha, Debbie Zhao, Dong Hoon Choi, Emily J. Lam Po Tang, Andrew J. Taberner, Martyn P. Nash, and Poul M. F. Nielsen

Abstract Measurement of three-dimensional (3D) surface deformations is an important step in characterising mechanical properties and developing computational models of skin. Compared to two-dimensional (2D) measurements, the ability to acquire 3D information involves extra levels of complexity, particularly during calibration and reconstruction. Furthermore, the addition of speckle patterns to the skin is typically required to enhance surface contrast. We have developed a method that uses a calibrated four-camera stereoscope to accurately measure 3D surface deformations of skin without requiring the addition of extrinsic surface features. To validate the method, a flat, rigid disc was reconstructed in 3D, at different orientations, and subsequently compared against its known dimensions. The root mean squared error of our method in measuring geometric features on the disc was 44 μm ± 25 μm over a 100 mm × 100 mm field of view. Our method could accurately measure disc displacements, with a maximum error of 7.8 μm (relative error 0.0031) at an applied translation of 2500 μm. Deformations of a uniaxially stretched rubber membrane were also measured, showing close agreement with the expected values, assuming a homogenous and linear stress/strain response. Finally, we demonstrated 3D deformation measurement of unpatterned post-mortem pig skin subject to uniaxial stretch using four cameras oriented as the edges of an octahedron with 90º angles between their optical axes. The ability to measure 3D full-field deformations of unpatterned skin, at wide camera angles, enables our method to be used in various skin experiments, including tissue indentation and dissection.

Keywords Skin · Deformation · Stereoscopy · Digital image correlation

A. HajiRassouliha and D. Zhao joint first authorship.

A. HajiRassouliha · D. Zhao · D. H. Choi · E. J. L. P. Tang · A. J. Taberner · M. P. Nash · P. M. F. Nielsen (✉)
Auckland Bioengineering Institute, University of Auckland, Auckland, New Zealand
e-mail: p.nielsen@auckland.ac.nz

A. J. Taberner · M. P. Nash · P. M. F. Nielsen
Department of Engineering Science, University of Auckland, Auckland, New Zealand

P. M. F. Nielsen et al. (eds.), *Computational Biomechanics for Medicine*,
https://doi.org/10.1007/978-3-031-09327-2_13

1 Introduction

The development of realistic biomechanical models of soft tissue deformation requires characterisation of the tissue biomechanical properties. With such information, biomechanical models of the skin have been developed for a variety of applications, including facial animation [1], plastic surgery [2], and high-performance clothing [3].

Skin is a complex tissue consisting of three main layers: the epidermis, dermis, and hypodermis [4]. Being nonlinear, anisotropic, heterogeneous, and viscoelastic, such tissues require robust methods and tools to identify their mechanical properties. Furthermore, measurements must be sufficiently rich and precise in order to develop realistic computational models that can be used to study the relationship between structure and mechanical function [5].

Measurements of the mechanical properties of skin have been performed using various experimental approaches, including biaxial testing [5], suction [6], and indentation [7], with *in-vivo* experiments proving to be more challenging than *ex-vivo* investigations. Lanir and Fung [8, 9] were among the first to analyse the mechanical behaviour of skin using an *ex-vivo* biaxial tension test, where rabbit skin deformations were measured by tracking markers on the skin surface using a single camera [9]. To date, several devices have been developed to assist with measuring skin properties *in-vivo,* including a micro-robot [10], a motion capture system [11], and a polarised LED sphere with a macro camera [1].

Common methods for characterising skin are based on measuring two-dimensional (2D) or three-dimensional (3D) surface deformations from camera images. 2D systems using a single camera, such as those described in the works of Dai et al. [7] and Sasaki and Hashimoto [12], cannot capture sufficiently rich data to quantify the complexity of skin deformation. On the other hand, multi-camera stereoscopic systems enable the measurement of surface deformations in 3D, thus providing more reliable estimates of deformation magnitude. However, it is challenging to capture deformation data using stereoscopic camera systems due to the skin's surface typically possessing insufficient features for 3D reconstruction. The ability to achieve high precision is critical since the accuracy of measurements is a key factor in determining how well a computational model can describe the biomechanical behaviour of the skin.

To avoid the complexity of designing and calibrating a stereoscopic system, Buganza Tepole et al. [13] used a multi-view stereo technique and a software tool developed by Autodesk (123D Catch) to reconstruct 3D deformations of pig skin *in-vivo.* Furthermore, Buganza Tepole et al. [13] used a ruler visible in the images to provide a known scale, as well as a superimposed grid and application of artificial patterns to the pig skin to improve feature identifiability in the images.

Digital image correlation (DIC) [14] is a widely used technique for surface reconstruction and deformation measurement. In 2D DIC methods, images are divided into smaller subimages, within which individual local deformations are measured. 2D

DIC methods suffer from the geometric assumptions associated with 2D measurements and are unable to account for out-of-plane motion. To create a rich texture to assist DIC algorithms in estimating deformations, a random speckle pattern is usually applied to the surface of the object of interest. The work of Ní Annaidh et al. [4] is an example of the use of 2D DIC to measure deformations *ex-vivo* by spraying and tracking a speckle pattern on excised samples of human skin.

2D DIC can be extended to 3D DIC with the use of stereoscopic camera systems. In 3D DIC, cameras of the stereoscopic system are first calibrated to obtain their intrinsic and extrinsic parameters. Features are then identified and matched between the views of the different cameras of the system. In the last step, matched features are triangulated using the camera parameters obtained from the calibration process. Requirements to apply speckle patterns to tissues, and the need for cameras oriented at narrow angles, limit the practical application of these methods.

In the present study, we designed a four-camera stereoscopic system to measure 3D surface deformations of samples of soft material. We demonstrate the use of widely angled cameras with highly accurate and robust camera calibration and 3D DIC deformation measurement techniques. The system was first validated by computationally reconstructing objects with known dimensions, followed by a series of uniaxial stretch tests for which measured and expected displacement values were compared. Finally, the system was used to measure 3D deformations of a single sample of unspeckled post-mortem pig skin, relying on only its intrinsic features for calculating the displacement field.

2 Method

2.1 Stereoscopic Imaging Device

The design of an appropriate stereoscopic device for this study involved considering the mechanical structure of the supporting rig, as well as the camera specifications and performance. We used Flea3 1.3 MP Mono USB3 Vision cameras (FL3-U3-13Y3M-C from FLIR, formerly Point Grey Research), which exhibit sufficient sensitivity, resolution, and speed for dynamic experiments on skin. As analyses concerning colour were not of interest, the omission of colour filters in the chosen monochrome cameras also permitted a higher sensitivity and spatial resolution.

A single camera pair is often unable to capture the kinematic complexity of soft tissues undergoing large deformations, particularly when experiments involve tools required for indentation or cutting of the sample. Increasing the number of cameras enables the measurement of features that may be occluded in some camera views. Unfortunately, this significantly increases the number of computations required for calibration, reconstruction, and deformation measurement. To capture images of skin samples from four different viewpoints, our system was constructed with four synchronised cameras to provide sufficient coverage of the imaged test samples

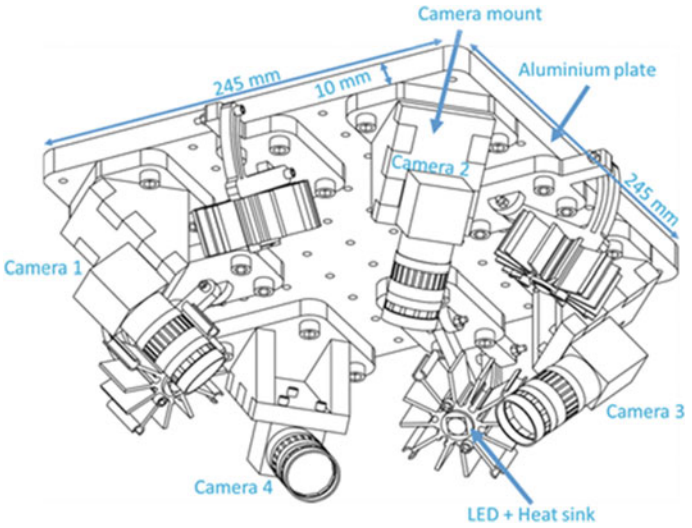

Fig. 1 Stereoscopic imaging device with four cameras and green LEDs, fixed to 10 mm thick acrylic supports on an aluminium optical breadboard of 245 mm × 245 mm (field of view = 100 mm × 100 mm)

while reducing redundant computational effort. A 90º angle between opposite pairs of camera axes was established to achieve isotropic stereoscopic resolution.

To enable high measurement accuracy, the stereoscopic imaging device required high structural rigidity. As the object is imaged by each camera in a designated fixed pose, any deviations in the cameras' relative positions result in errors during 3D reconstruction. To achieve the required rigidity, the four cameras were first fixed to camera mounts bolted to an aluminium optical breadboard with surface dimensions of 245 mm × 245 mm and thickness of 10 mm (Fig. 1). Reprojection errors of the cameras, calculated using a calibration dataset, were used as an experimental measure of the stability of the camera positions.

2.2 Multi-Camera Calibration

Multi-camera calibration of a stereoscopic system is the process of identifying intrinsic parameters (relating an object to its image in the camera plane) and extrinsic parameters (which define the 3D positions and orientations of each camera in a global coordinate system) of the cameras. For our device, the accurate multi-camera calibration method of HajiRassouliha et al. (detailed in [15]) was conducted to ensure the accuracy of the identified parameters and subsequent 3D reconstructions.

2.3 Measuring Deformations Using 3D DIC

A highly accurate and robust registration algorithm using a phase-based subpixel registration algorithm and Savitzky-Golay differentiators (hereafter referred to as the PB-SG-GC algorithm [16]) was adapted to perform 3D DIC. In previous tests, the PB-SG-GC algorithm was employed to track 2D human skin motion *in-vivo* using only intrinsic features [17].

The 3D reconstruction method was based on the method explained in [15]. 2D images of the sample, viewed from different positions, were acquired simultaneously by the four cameras in the stereoscopic system. The images were first corrected for lens distortion and perspective effects between the different views using approximately 15 control points manually selected in the camera images. The corrected images provided initial estimates of corresponding material points across images. The locations of corresponding points were found (i.e., 'matched') using the PB-SG-GC algorithm [16]. Accurate 3D locations of each matched point in the common global coordinate system were then determined by triangulation using the camera parameters derived from the calibration process. During the deformation, triangulated points were tracked across consecutive stereoscopic image sets (i.e., images of the sample in the same state taken from different perspectives) over time using 64 pixel × 64 pixel subimages. Finally, surface displacements were calculated for each material point by observing the difference in 3D locations at each time step, with reference to the original reference configuration.

All computations were implemented in MATLAB (v16, Mathworks, Natick MA, USA), and performed using a single thread of an Intel® 4th Generation Core™ i7 CPU on a PC running Windows7 (Dell Optiplex 9020).

2.4 Validation Tests for Geometry and Translational Shifts

To validate the stereoscopic system, we first imaged a rigid disc with patterns of known geometries with dimensions of 5 mm, 10 mm, and 12 mm (Fig. 2), followed by digital reconstruction of the disc in 3D. By comparing the 3D reconstructed geometries to those of the physical disc, it was possible to quantify the accuracy of the measurements. Algorithm reproducibility was assessed by estimating the magnitudes of a, b, and c (illustrated in Fig. 2) for different disc orientations. In total, 20 measurements were made using the reconstructed surface (5 for a, 10 for b, and 5 for c) to examine the accuracy.

To test the algorithm's ability to track objects in 3D, a series of controlled rigid-body translations was applied using a manual linear translation stage. As it was not practically feasible to achieve controlled deformations of soft materials, we applied small known translations to a rigid object to enable method validation. The translations ranged between 500 μm and 2500 μm (in 500 μm increments) and were controlled by a Vernier micrometre screw, with 2 μm resolution, that was attached to

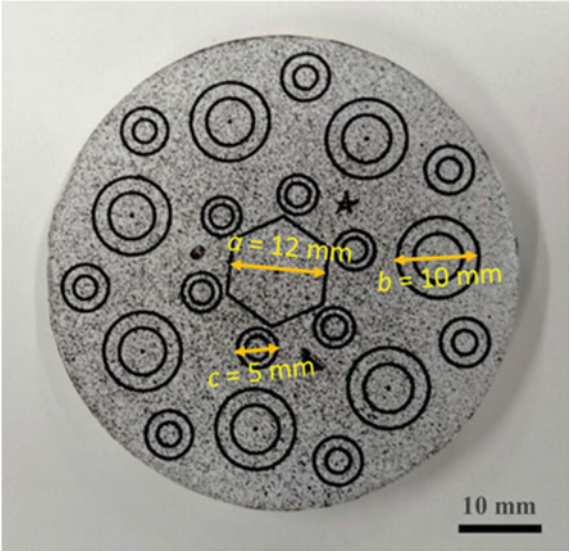

Fig. 2 The flat, rigid disc used for validation of the proposed algorithm in reconstructing 3D surfaces and tracking motion in 3D

the translation stage. To measure the translational shift, the mean and variance of the measured displacements of all matched points were calculated for each image set. The measured 3D displacements were then compared to the known applied translational shifts to quantify the accuracy of the stereoscopic system.

2.5 Practical Experimentation of the System on Membranes

Uniaxial stretch tests were carried out on soft membrane samples clamped at two opposing edges. For each sample, two experiments were conducted, using small and large deformations. For each experiment, one edge of the sample was fixed to the translation stage, and the position of the other edge was adjusted. A set of images was taken to capture each deformation state of the sample using all four cameras of the system. Details for each experiment are described below.

2.5.1 Speckled Rubber Dam Membrane

For the initial test, a commercially available rubber dam membrane was selected as a relatively trivial case of soft material deformation involving isotropic, linear elastic material properties, and structural homogeneity. As the rubber membrane exhibited no intrinsic features nor textures that could be effectively tracked, a fine speckle pattern was applied using an airbrush and black acrylic ink (Fig. 3). The sample was clamped between acrylic plates, and double-sided tape was applied to the surfaces to

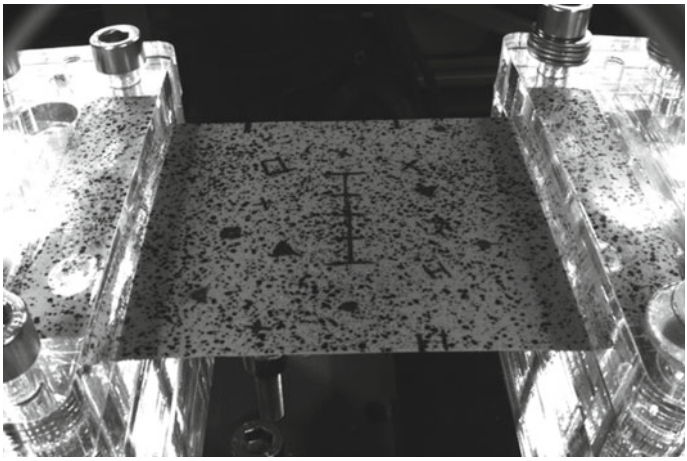

Fig. 3 Experimental setup of the speckled rubber membrane clamped between acrylic plates, showing the view from a single camera with 1280 pixel × 1024 pixel (1.3 MP) resolution

prevent slippage. This provided an area of approximately 60 mm × 60 mm between the clamped edges in the unstretched reference state.

2.5.2 Unspeckled Post-Mortem Pig Skin

Pig skin preparation involved isolating the skin layer (excised from the belly area, earlier than 72 h post-mortem) from the underlying tissues, cutting out a rectangular sample, and securely fixing the sample between acrylic plates with pins (Fig. 4). Testing was performed on a single pig skin sample only. No speckle patterning was applied.

3 Results

The root mean squared reprojection error following calibration of the stereoscopic system ranged between 0.103 pixel and 0.214 pixel, with an average reprojection error of 0.145 pixel across the 4 cameras. The computation time (approximately 15 min) varied slightly for each experiment due to differences in the sizes of the selected regions of interest, the distances between the subimages, and the number of matched points used to compose the reconstructed geometry.

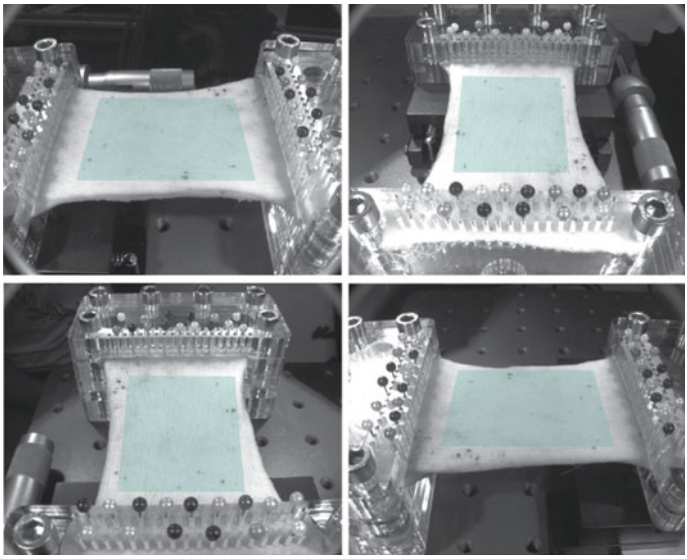

Fig. 4 Stereoscopic view (from individual cameras) of the unspeckled post-mortem pig skin sample, showing the experimental setup, and the selected area of interest (shaded). Lighting variations and perspective distortions are apparent between cameras

3.1 Validation Tests for Reconstructed Geometry and Translation

The mean absolute error across the 20 measurements of *a*, *b*, and *c* from the flat disc object (Fig. 2) was 44 μm, with a standard deviation of 25 μm. It should be noted that these measurements were performed using sparse 3D points from the reconstructed surface, which added a quantisation error to the analysis.

The results for the translational shifts of the disc are presented in Table 1. The mean displacements calculated from reconstruction data were consistently within 10 μm of the prescribed values. The largest error of 7.8 μm (relative error 0.0031) occurred at an applied translation of 2500 μm. An increase in the translation magnitude (from 500 μm to 2500 μm) was accompanied by an increase in the standard deviation of the measured displacements (from 1.1 μm to 3.5 μm).

Table 1 Use of the stereoscopic system to measure prescribed rigid translations (displacements) with the corresponding standard deviations and errors

Applied translation (μm)	500	1000	1500	2000	2500
Mean displacement (μm)	492.7	998.3	1501.7	1997.3	2492.2
Error (μm)	7.3	1.7	1.7	2.7	7.8
Standard deviation (μm)	1.1	1.5	2.2	2.7	3.5

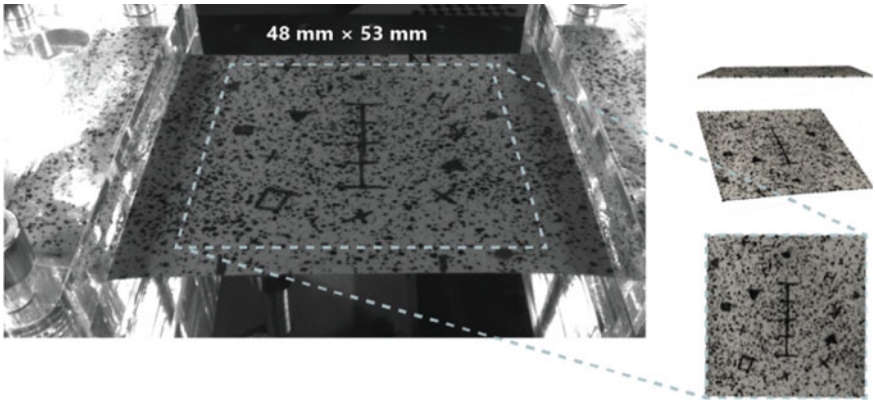

Fig. 5 The selected area of interest for a speckled rubber membrane and various views of the corresponding 3D geometry (reconstructed) in the reference state

3.2 Soft Material Experiments

3.2.1 Speckled Rubber Dam Membrane

The reconstructed surface closely resembled the texture of the flat speckled membrane surface upon visual inspection (Fig. 5). A comparison with the true geometry was not possible since independent measurements of the actual membrane geometry were not available for this study.

The membrane was stretched using the uniaxial apparatus. By tracking material points in 3D between each increment of stretch, dense spatial arrays of displacement vectors were calculated. The deformations of the membrane in the absence of stretch, and for a 2 mm stretch and a 4 mm stretch, are illustrated in Fig. 6. The maximum displacement was smaller than the overall applied stretch as the borders of analysed area were some distance away from the edges of the clamps as shown in Fig. 5 (i.e., the approximate width of the membrane was 60 mm, while the width of the reconstructed region was 53 mm). The ratio of the length of the reconstructed part of the membrane to the distance between the clamps was 53 mm/60 mm ≈ 0.883. This ratio is in accordance with the ratio of the maximum measured displacement (i.e., 3.5 mm) to the applied stretch of 4 mm (i.e., 3.5 mm/4 mm $= 0.875$). We expected these ratios to be similar under the assumption that the rubber dam exhibited homogeneous strain, and hence linear variations in displacement.

3.2.2 Unspeckled Post-Mortem Pig Skin

Figure 7 shows the reconstructed 3D surface of the pig skin sample, and the measured 3D displacements for 1 mm and 4 mm stretches, with discontinuities apparent near the upper and lower edges of the displacement field.

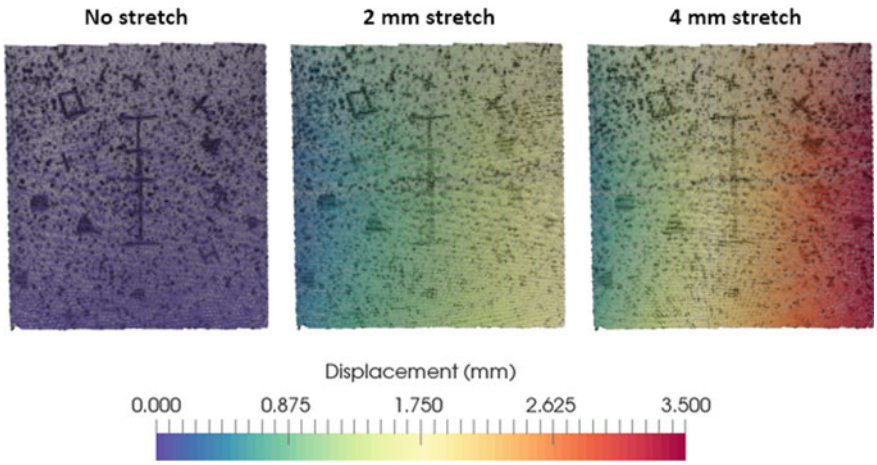

Fig. 6 Measured deformation fields across the rubber membrane surface (with left edge fixed) in the absence of stretch, and at 2 mm stretch and 4 mm stretch

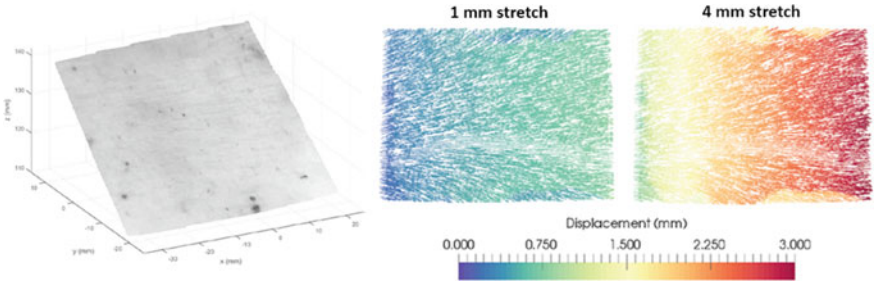

Fig. 7 Reconstructed material points of unspeckled post-mortem pig using only intrinsic surface features such as fine wrinkles and pigment spots (left), with corresponding deformation fields for stretches of 1 mm and 4 mm

4 Discussion

In this study, we demonstrate the use of a custom-built 3D DIC stereoscopic device to measure 3D surface deformations of samples of post-mortem pig skin. In comparison to existing DIC methods, our approach offers two significant advantages when concerning biological soft tissues.

Firstly, unlike previous methods that require the application of a speckle pattern (such as [4] and [18]), we successfully measured 3D surface deformations of pig skin by tracking only its intrinsic surface features. This advantage, provided by the PB-SG-GC subpixel registration algorithm, makes our method suitable for a variety of soft tissue experiments for which pattern application is not practical. Because this is an inherently contactless measurement technique, using only intrinsic features can

be an important advantage in physiological experiments where the application of speckle patterning on sensitive biological samples is not feasible or would otherwise disrupt the local mechanical response of the system.

Secondly, the ability to orient the cameras at relatively wide angles is also advantageous as it provides better depth resolution and leaves sufficient space at the centre for interventions (e.g., indentation or dissection), which require tools that may obscure sub-regions from certain cameras. Such experiments could be used to provide information about the mechanical response of soft tissues under various scenarios. Although the wide angles provide more space, the camera views of the target object are generally quite different due to perspective distortions. Hence, the 3D deformation measurement process becomes significantly more challenging than small-angle stereo-pair camera configurations. In our study, this was overcome by employing advanced camera calibration and 3D DIC techniques.

The initial tests showed that our stereoscopic system with widely angled cameras accurately reconstructed known geometries between 5 mm and 12 mm to within 44 μm ± 25 μm across 20 measurements. Mean measured displacements were within 10 μm of prescribed translational shifts of up to 2500 μm (Table 1). Stretch tests using a rubber membrane illustrated that our system measured surface deformation to high resolution, although it was not feasible to validate these measurements. Furthermore, the method produced a homogenously varying displacement field, representing uniaxial stretching of the synthetic membrane (Fig. 6). In comparison, a heterogeneous displacement field (showing discrete patches of high and low displacements) was obtained when imaging the biological sample, potentially owing to intrinsic heterogeneous structures (e.g., scars, fat deposits) of the post-mortem pig skin (Fig. 7). Further experimentation is needed to verify this finding.

Despite having only demonstrated displacement measurements of relatively flat samples, our studies using obliquely oriented surfaces enabled us to examine and verify the 3D capability of the technique (i.e., the ability to measure displacements with respect to a 3D coordinate system), albeit in the absence of potential confounding effects of surface curvature. Nevertheless, this test is a reasonable approximation for many practical applications where the curvature of skin is relatively small over the regions spanned by the registration subimages.

Keeping in mind that skin is a complex tissue, the ability to reconstruct and subsequently measure the full-field displacements of soft tissue is very useful. Furthermore, the ability to obtain material displacements with high accuracy and precision will subsequently benefit derived measurements such as strain and stiffness, which are very sensitive to errors in measured displacements. By designing a stereoscopic system around the needs of biomechanical experimentation (i.e., without the requirement for pattern application and allowing sufficient room for interventions), we present here novel tools to facilitate progress towards a comprehensive understanding and characterisation of complex soft tissue behaviour.

References

1. Nagano, K., Fyffe, G., Alexander, O., Barbič, J., Abhijeet, L., & Paul, G. (2015). Skin microstructure deformation with displacement map convolution. *ACM Transactions on Graphics, 34*(4), 1–10.
2. Pawlaczyk, M., Lelonkiewicz, M., & Wieczorowski, M. (2013). Age-dependent biomechanical properties of the skin. *Advances in Dermatology Allergologii, 5*(5), 302–306.
3. Lee, H., Hong, K., & Lee, Y. (2014). Ergonomic mapping of skin deformation in dynamic postures to provide fundamental data for functional design lines of outdoor pants. *Fibers and Polymers, 14*(12), 2197–2201.
4. Ní Annaidh, A., Bruyère, K., Destrade, M., Gilchrist, M. D., & Otténio, M. (2012). Characterization of the anisotropic mechanical properties of excised human skin. *Journal of the Mechanical Behavior of Biomedical Materials, 5*(1), 139–148.
5. Benítez, J. M., & Montáns, F. J. (2017). The mechanical behavior of skin: Structures and models for the finite element analysis. *Computers & Structures, 190*, 75–107.
6. Diridollou, S., et al. (2000). In vivo model of the mechanical properties of the human skin under suction. *Skin Research and Technology, 6*(4), 214–221.
7. Dai, A., Wang, S., Zhou, L., Wei, H., Wang, Z., & He, W. (2019). In vivo mechanical characterization of human facial skin combining curved surface imaging and indentation techniques. *Skin Research and Technology, 25*(2), 142–149.
8. Lanir, Y., & Fung, Y. C. (1974). Two-dimensional mechanical properties of rabbit skin—I. Experimental system. *Journal of Biomechanics, 7*(1), 29–34.
9. Lanir, Y., & Fung, Y. C. (1974). Two-dimensional mechanical properties of rabbit skin—II. Experimental results. *Journal of Biomechanics, 7*(2), 171–182.
10. Flynn, C., Taberner, A. J., Nielsen, P. M. F., & Fels, S. (2013). Simulating the three-dimensional deformation of in vivo facial skin. *Journal of the Mechanical Behavior of Biomedical Materials, 28*, 484–494.
11. Mahmud, J., Evans, S. L., & Holt, C. A. (2012). An innovative tool to measure human skin strain distribution in vivo using motion capture and delaunay mesh. *Journal of Mechanics, 28*(02), 309–317.
12. Sasaki, A., & Hashimoto, H. (2013). Measurement of hand skin deformation in dexterous manipulation. In *IECON 2013 - 39th annual conference on IEEE industrial electronics society*, (pp. 8306–8311).
13. Tepole, A. B., Gart, M., Gosain, A. K., & Kuhl, E. (2014). Characterization of living skin using multi-view stereo and isogeometric analysis. *Acta Biomaterialia, 10*(11), 4822–4831.
14. Pan, B. (2011). Recent progress in digital image correlation. *Experimental Mechanics, 51*(7), 1223–1235.
15. HajiRassouliha, A., Lam Po Tang, E. J., Taberner, A. J., Nash, M. P., & Nielsen, P. M. F. (2019). A method for three-dimensional measurements using widely angled stereoscopic cameras. In *2019 IEEE international instrumentation and measurement technology conference (I2MTC)* (pp. 1–5).
16. HajiRassouliha, A., Taberner, A. J., Nash, M. P., & Nielsen, P. M. F. (2018). Subpixel phase-based image registration using Savitzky-Golay differentiators in gradient-correlation. *Computer Vision and Image Understanding, 170*, 28–39.
17. HajiRassouliha, A., Taberner, A. J., Nash, M. P., & Nielsen, P. M. F. (2017). Subpixel measurement of living skin deformation using intrinsic features. In *Computational biomechanics for medicine: From algorithms to models and applications*, (pp. 91–99).
18. Maiti, R., et al. (2016). In vivo measurement of skin surface strain and sub-surface layer deformation induced by natural tissue stretching. *Journal of the Mechanical Behavior of Biomedical Materials, 62*, 556–569.

Index

P. M. F. Nielsen et al. (eds.), *Computational Biomechanics for Medicine*,
https://doi.org/10.1007/978-3-031-09327-2